**Charles University**

**Faculty of Science**

**Institute of Geology and Paleontology**

Study programme: Geology


**Reza Syahputra**

# Mechanisms and time scales of formation of ribbon continents

Ph.D. dissertation

Supervisor: prof. RNDr. Jiří Žák, Ph.D.

Prague, 2022

Prohlašuji, že jsem tuto dizertační práci zpracoval samostatně a že jsem použil pouze zde citované informační zdroje uvedené v seznamu literatury. Tato práce ani její podstatná část nebyla předložena k získání jiného nebo stejného akademického titulu.

V Praze, 21. prosince 2022 ..... podpis autora

I declare that I prepared this dissertation thesis independently under the guidance of my supervisor, and that I used only the sources I quote and include in the list of references. This thesis, or a substantial part of it, has not been submitted to obtain another or the same academic title.

In Prague, December 21st 2022 ..... signature of the author

# Table of contents

**Abstract**

Investigation into the ribbon continents has started since the 1980s; however, most studies focued on oceanic closure phase, involving the subduction, accretion, and collision. The formation of ribbon continents has received little attention, perhaps because it has less recent examples. This thesis is designed to address several possible scenarios for the formation of ribbon continent by investigating the tectonics, magmatism, and sedimentation of the former Avalonian–Cadomian belt during the break-up of the peri-Gondwana terranes and transition from the active- to passive-margin settings. The data originated from three different locations within the Bohemian Massif, the Czech Republic, which can also be viewed as a Cambro–Ordovician crustal evolution from the lower crust to the surface level: (1) intermediate to felsic of the Kdyně pluton in the Plzeň region, (2) the continental Příbram–Jince basin in the Central Bohemian region, and (3) metagranites and granitic orthogneisses of the Moldanubian zone in Pardubice and Vysočina regions. The methods used involve the integration of structural mapping, microstructural analysis, stratigraphic and sedimentological analysis, and in particular the anisotropy of magnetic susceptibility (AMS) accompanied by an examination of magnetic mineralogy using thermomagnetic measurements. Moreover, the third location contains geochronologic dating (U–Pb on zircons) measured using laser ablation–inductively coupled plasma–mass spectrometry (LA–ICP–MS).

The most important results from each study case can be summarized as follows. (1) The Kdyně pluton was an apical part of a domal structure in the upper crust and was primarily controlled by magma buoyancy rather than tectonic deformation through rapid (at ca. 524–523 Ma) and multiple emplacement processes (magma wedging and lateral expansion with minor stoping mechanism). The deformation during the pluton emplacement was partitioned into simple shear-dominated zones that delimited pure shear-dominated belts. This rapid heat input into the former accretionary complex of Blovice was perhaps due to slab break-off, indicating the initial stage of extension in the Teplá–Barrandian unit. (2) The Příbram–Jince basin was influenced mainly by synsedimentary faulting (a series of horsts and grabens) and dominated by continental conglomerates, coarse-grained sandstones, and thin tuffaceous layers deposited in alluvial fans, flood plains, and river channels. The tectonic setting evolved from pure shear dominated with the sediment sourced from pre-Cambrian terranes to a pull-apart dextral transtension with its source coming from the local material of Blovice accretionary complex during ca. 511 Ma. This tectonic setting was coeval with the separation of the Avalonian–Cadomian belt from the northern Gondwana margin and the initial opening of the Rheic Ocean. (3) The slab break-off in the Teplá–Barrandian unit was followed by lithospheric thinning that caused emplacement of granitic magma in the Moldanubian zone (Moldanubian orthogneisses) due to basalt underplating in the extended crust. This event was coeval with the Avalonia ribbon terrane's rift–drift transition and opening of the Rheic Ocean (at ca. 485 Ma).

In summary, using the above mentioned case examples, it can be shown that the formation of a ribbon continent is mainly governed by the thermal budget within the lithosphere. In the Bohemian Massif, it was shown that the lower crust was weakened first due to slab break-off, followed by stretching of the upper crust. This inference is compatible with the Type III-A/C extension model. Furthermore, the break-up and drift of a ribbon continent is also highly dependent on the presence or absence of an inherited suture or discontinuity.

**Abstrakt**

Koncept lineárních mikrokontinentů (v angličtině "ribbon continents") se v literatuře objevil v 80. letech minulého století, většina výzkumů se však soustředila na jejich akreci a kolizi s kontinentálními okraji. Naopak iniciální fáze jejich vývoje a podmínky jejich vzniku jsou do značné míry stále neobjasněny. Tato disertační práce se zaměřuje na vznik lineárních mikrokontinentů na příkladu teránů, které se odtrhly od původního avalonsko–kadomského orogenního pásma na severním okraji Gondwany během mladšího neoproterozoika až spodního ordoviku. Data získaná v této disertační práci pochází ze tří různých částí Českého masivu, které reprezentují různá stádia iniciální extenze a vzniku mikrodesek a rovněž reprezentují různé krustální úrovně: (1) kdyňský pluton v jihozápadní části tepelsko–barrandienské jednotky, (2) příbramsko–jinecká pánev v její centrální části a (3) metagranity a ortoruly v moldanubické jednotce. tyto různé jednotky byly zkoumány pomocí různých terénních a analytických metod, jež zahrnovaly strukturní mapování, stratigrafickou a sedimentologickou analýzu a zejména anizotropii magnetické susceptibility (AMS) doplněnou termomagnetickými analýzami. Metagranity a ortoruly byly datovány pomocí metody U–Pb na zirkonech metodou ICP-MS.

Hlavní závěry disertační práce jsou následující. (1) Kdyňský pluton reprezentuje apikální část dómovité struktury a byl vmístěn kombinací různých procesů (žíly, laterální expanze, stoping) během deformačního členění korového měřítka do zón jednoduchého a čistého střihu. Tato deformace a magmatismus reprezentuje terminální fázi kadomské orogeneze v důsledku odtržení subdukované desky. (2) Kontinentální klastická sedimentace (v prostředí aluviálních vějířů, aluviálních plošin a říčních koryt) příbramsko-jinecké pánve byla silně ovlivněna synsedimentárními zlomy, jež vytvořily sérii hrástí a příkopů. Sedimentace v této pánvi začala v prostředí čistého střihu a přínosu materiálu od V a JV a přešla v režim pravostranné transtenze a přínosu lokálního materiálu z podloží pánve na JZ. Tento tektonický režim reprezentuje vzdálenou odezvu na iniciální separaci Avalonie od Gondwany. (3) Pokračující extenze a ztenčení litosféry vedlo ke krátkodobé epizodě granitického magmatismu mezi 490 a 480 Ma (moldanubické ortoruly) a posléze ke změně na bazaltický vulkanismus odrážející dekompresní tavení litosférického pláště, současně s přechodem Avalonia od stádia riftu ke kontinentálnímu driftu.

Tyto závěry a širší srovnání s avalonskými terány ukazují na klíčovou roli termální a reologické struktury litosféry při vzniku lineárních mikrokontinentů: v případě Avalonie kontrolovala pre-existující sutura její úplné oddělení od Gondwany, zatímco kadomské terány, včetně tepelsko–barrandienské a moldanubické jednotky, zaznamenaly komplikovaný několik desítek miliónů let trvající vývoj litosférické extenze a pravděpodobně zůstaly součástí perigondwanského šelfu během celého spodního paleozoika.

**Acknowledgements**

This thesis was supported by the Grant Agency of Charles University (GAUK) through project no. 952220 (to Reza Syahputra), by an Internal Research Project (IRP) from the Institute of Geology and Paleontology, Faculty of Science, Charles University, and by the Charles University Cooperatio Programme (Research Area GEOL) and Center for Geosphere Dynamics (UNCE/SCI/006). Significant support was provided by the Czech Science Foundation through project No. 20-13644S (to Lukáš Ackerman).

Countless gratitude is given to my principal supervisor Jiří Žák for supporting all my fieldwork and desk studies, managing endless discussions and questions, and mentoring me throughout the last four years. My laboratory colleagues are highly appreciated for their ideas, discussions, and jokes: Petr Vitouš, Lucia Pellerey, Irena Olšanská, Jonah Jonathan, Roland Nádasky, Tatiana Tkáčiková, and Dominika Linzerová. Great teachers that have been involved in deep discussions are also appreciated: Václav Kachlík, Oldřich Fatka, Filip Tomek, Jakub Trubač, Kryštof Verner, and Richard Damian Nance. Jiří Sláma performed the U–Pb zircon geochronology included in one of the chapters. I would also acknowledge our institute secretaries, Irena Libišová and Rudolf Trnka, for assisting with complicated administration and technical issues.

I am very grateful to my Indonesian friends who had supported me when I was confused looking for ideas to write (Rudi, Gentha, Ali, Angga, Vichi, Robert, Toha, Jaka, Viri), when I was hungry (Mr. and Mrs. Tasmuri and Mahasti who is always loyal to provide their highly delicious food), and when I wanted to hang out (Thufail, Taufik, Angga, Erwin, Faisal, Clarissa).

And I am deeply indebted to the most important person in my life, my wife Radhiyatam Mardhiyah, who patiently awaited my doctoral study completion and taking care of our triplet smart, funny, soleh and solehah children (Rafifa, Raqima, and Rasyad). My parents are thanked as well for their prayers throughout the night and day for my success.

**Preface**

This thesis examines the interaction between tectonics, magmatism, and sedimentation during continental extension (rifting), transition from active- to passive-margin settings, and formation of ribbon continents. An essential goal is also to study the role of tectonic inheritance in rifting and subsequent basin inversion/orogeny. The data collected in this work originated from several locations within the Teplá–Barrandian and Moldanubian units, Bohemian Massif, the Czech Republic, which were part of the former Avalonian–Cadomian belt and may represent an intriguing example of the initial stages of its break-up and ribbon continent formation. First, the Kdyně intrusive complex consists of the earliest plutonic bodies that intruded after the end of the Cadomian orogeny. The pluton is an important indicator of the early extensional regime in the upper crust and an essential key to study the initial cause of active to-passive margin transition. Second, the Cambrian Příbram–Jince basin is an excellent example of the subsequent stage of rifting and associated volcanism on the surface. Third, the orthogneisses from the Moldanubian zone represent an intracrustal magmatic response during even later stages of rifting. New U–Pb zircon geochronology with existing data on magmatism and basin subsidence in the Prague basin then allowed a comprehensive evaluation of the timing and mechanisms of the Cambro–Ordovician rifting on a lithospheric scale.

In this thesis, a combination of various field and analytical methods (including sedimentology, structural geology, optical microscopy, anisotropy of magnetic susceptibility-AMS, and U–Pb zircon geochronology) was used as a robust approach to fulfil the research objectives.

The thesis is written in a monograph format and is divided into six sections. The introduction evaluates the research's principal goals and critical issues and briefly summarizes the current state of knowledge. The data and results that were derived from several separate

locations are described in sections 2 and 4, discussion is presented in section 5, and the most important findings of the thesis are highlighted in the Conclusions and executive summary.

**List of publications stemming from the thesis**

**Research articles (author contribution is specified in the supervisor´s evaluation)**

- **Syahputra, R.**, Žák, J., Tomek, F., Kachlík, V., *under review*. Hot plutonism in a cold accretionary wedge: what terminated the Cadomian orogeny in the Bohemian Massif? Precambrian Research.
- **Syahputra, R.**, Žák, J., Nance, R. D., **2022**. Cambrian sedimentary basins of northern Gondwana as geodynamics markers of incipient opening of the Rheic Ocean, Gondwana Res. 105, 492–513. https://doi.org/10.1016/j.gr.2021.10.004.
- Žák, J., Sláma, J., **Syahputra, R.**, Nance, R. D., *under review*. Dynamics of Cambro–Ordovician rifting of the northern margin of Gondwana as revealed by the timing of subsidence and magmatism in rift-related basins, International Geology Review.
- Žák, J., Kraft, P., Hajná, J., Vacek, F., Svojtka, M., Kachlík, V., Ackerman, L., Verner, K., Zulauf, G., Dörr, W., Tomek, F., Janoušek, V., Trubač, J., Lehnert, O., **Syahputra, R.**, Pašava, J., *under review*, The Teplá–Barrandian unit: a fascinating archive recording >600 My of evolution of European crust. In: U. Linnemann (Ed.) Geology of the Central European Variscides, Regional Geology Reviews, Springer.

**Presentations at international conferences**

- **Syahputra, R.** and Žák, J., 2021. Basin evolution during incipient rifting of ribbon terranes: an example from the Bohemian Massif. 35$^{th}$ International Association of Sedimentologist (IAS) meeting of Sedimentology, June 21–25, Prague, poster.
- **Syahputra, R.** and Žák, J., 2022. A protracted and multiphase transition of the Cadomian active margin to a failed rift setting in northern Gondwana. 23$^{rd}$ International Conference on Deformation Mechanisms, Rheology and Tectonics, July 4–10, Catania (Italy), poster.

# 1. INTRODUCTION

## 1.1. The concept of ribbon continents

Ribbon continents are linear, thus relatively long and narrow, belts composed of juvenile or recycled crust that form by a lithospheric extension (rifting) from larger continental masses. Given their geometry, ribbon continents require a specific mechanism of formation. Sengör (2004) suggested that ribbon continents mainly form as migrating arcs above retreating subduction zones (e.g., the Kipchak Arc of the Altaids, the Cimmerian continent rimming the former Tethys Ocean) or by slicing of continental margin by transtensional faulting (e.g., Baja California) or re-rifting (e.g., Lomonosov Ridge). Therefore, the primary factors that differentiate the ribbon continents from other types of continental blocks and terranes are the rifting distribution, dimensions, and geometry. For instance, ribbon continent dimensions of Siberia, Alaska, Yukon, and British Colombia (SAYBIA; Johnston, 2001), Cimmerian (Sengör, 1984), Sibumasu in Southeast Asia (Metcalfe, 1984), and Iberian in western Europe (Shaw and Johnston, 2016) could reach up to 9000 km long and 600 km wide. The concept of ribbon continents emerged in the 1980s, thus relatively late in the history of plate tectonic theory (e.g., Lister et al., 1986; Monger, 1989), yet ribbon continents are now being increasingly recognized as playing a crucial role in the closure of oceanic domains, continental assemblies, growth of continental crust, large-magnitude strike-slip terrane displacements, and the development of oroclines (Johnston et al., 2013; Sengör, 2004; van der Voo, 2004; Keppie et al., 2010). The formation of the ribbon continents often involves multiple deformational events and plutonic and volcanic activity at the periphery of an exterior ocean (e.g., Morley, 2018; Nance et al., 2002; van der Voo, 2004). Except for the Mesozoic Cordilleran "terrane wreck" in the paleo-Pacific realm (Johnston, 2001), most published examples are those derived successively from the northern margin of the supercontinent Gondwana: the Neoproterozoic

Avalonia–Cadomian belt (e.g., von Raumer et al., 2003; Stampfli et al., 2011; Nance et al., 2010; Linnemann et al., 2014; Shaw and Johnston, 2016) incorporated into the Variscan orogen, the disputed Cimmerian ribbon continent (e.g., Sengör, 1984; Gutiérrez-Alonso, 2008; cf. Topuz et al., 2013), and several continental slivers related to the closure of the Tethyan oceanic realm that now make up the tectonic collage of southeastern Asia (e.g., Sibumasu: Metcalfe, 2013; Morley, 2018). A few other examples also include Zealandia (Lord Howe Rise and New Zealand, e.g., Johnston, 2004; Klingerhoefer et al., 2007; Sutherland et al., 2010), the Elan Bank microplate in the Southern Indian Ocean (Borissova et al., 2002; Frey et al., 2000), and the Southern and Baja California (e.g., Hildebrand and Whalen, 2014).

The "lifetime" of ribbon continents typically includes four main stages: (1) rifting and rift–drift transition, (2) drift, (3) collision and reworking, and (4) late-stage oroclinal rotation and/or strike-slip slicing, although their evolution may be incomplete and arrested in any of these stages (e.g., Johnston, 2008; Morley, 2018). Several studies assigned an essential role to a pre-existing lithospheric weakness during Stage 1 (e.g., Molnar, 2018; Murphy et al., 2006) and noted that the travel time for drift depends strongly on the angular velocity and, hence, the location of the Euler pole (e.g., Molnar, 2018). It is also apparent that, during the drift (Stage 2), ribbon continents may lose continuity and break-up into several smaller displaced fragments and that the final attachment involves collisional orogeny and magmatic activity. Subduction, exhumation, shortening/transpression, and plutonism will probably affect the collisional domain during Stage 3. The collision duration may be prolonged; for example, the Cordilleran ribbon continent was attached progressively to the North American plate between ca. 150 and 50 Ma. Finally, the collision may be followed by significant orogen-parallel displacement, shortening and oroclinal buckling, leading to complex juxtaposition, rotation, and "derailment" of individual ribbon fragments (e.g., Johnston, 2008; Morley, 2018).

### 1.2. Possible geodynamic causes of ribbon continent formation

In most cases, the available studies focus on the accretional to collisional stages of the ribbon continent evolution, which is only the final stage of an oceanic closure. Therefore, the geodynamic causes and time scale for the initial ribbon continent development are unclear and poorly explored in many instances. Several models for the initial ribbon continent formation have been proposed, ranging from the impingement of a mantle plume into a continental margin (e.g., Müller et al., 2001) through asthenospheric convection (e.g., Ziegler and Cloetingh, 2004) to a large-scale plate reorganization (e.g., Whittaker et al., 2016). The details of the rifting processes are also uncertain. The ribbon geometry requires rather specific conditions, which generally involve a cold and narrow rift, perhaps with significant vertical crustal discontinuities linked to tectonic inheritance and pre-existing sutures (Murphy et al. 2006).

Other largely unexplored issues related to ribbon continent formation include the exact mode of rifting (pure shear, simple shear, combined), the role of crustal thickness and rheological stratification, the evolution of topography and basin subsidence and its sedimentary record, and the role of syn-break-up crustal magmatism. The rates and duration of ribbon development also remain elusive.

### 1.3. Ribbon continent formation in the Avalonian–Cadomian belt

Plate convergence to form Gondwana during mid- to late Neoproterozoic was recorded two types of orogenic belts, interior collisional belts that amalgamated the continental plates, and peripheral accretionary belts that were governed by subduction and accretion of oceanic material (e.g., Johnston, 2008; Linnemann et al., 2014; Morley, 2018; O´Brien, 2001; Stampfli et al., 2013; von Raumer et al., 2013, 2003). The former, which includes the Pan-African and Brasiliano orogens, were unaffected by rifting until the Jurassic break-up of Pangea. In contrast, the latter, called the peri-Gondwana terranes, consisting of the Avalonian–Cadomian,

Carolinian and Terra Australis belts, was characterized by a continuous transition from subduction to extension and rifting (e.g., Cawood, 2005; Davy et al., 2008; Nance and Murphy, 1994, 1991; Willan and Kelley, 1999).

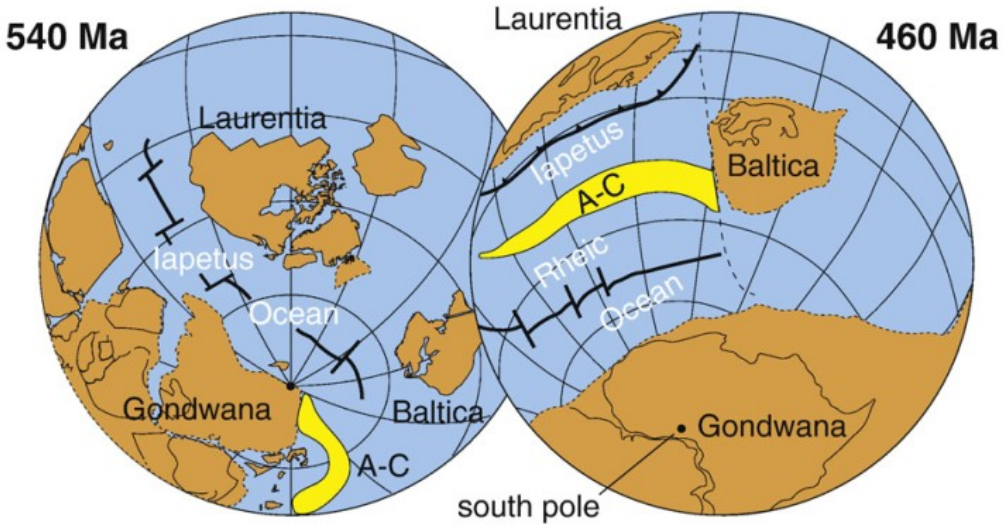


**Figure 1.** *The opening and closure of the Paleozoic oceans during active to passive margin transformation between Gondwana, Laurentia, and Baltica. Note that the Avalonia–Carolina (A–C) had separated from Gondwana as the Rheic Ocean opened at ca. 460 Ma (modified from Nance et al., 2010).*

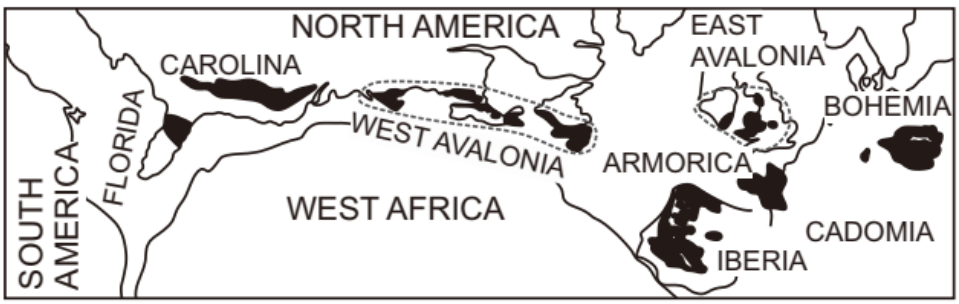


**Figure 2.** *Peri-Gondwana terranes along the Avalonian–Cadomian belt during the late Paleozoic (redrawn from Nance et al., 2002).*

The Avalonian–Cadomian belt (Fig. 2) developed as a collage of accretionary wedges, island arcs, and sedimentary basins straddling the northern margin of Gondwana for some 8,000–10,000 km length in the late Neoproterozoic (Murphy and Nance, 1989; Nance et al., 2008, 2010). The belt thus started its evolution as an active plate margin, but subsequently evolved into a ribbon continent during the Cambrian. In turn, the accretionary orogeny, which

represented a key geodynamic event at the end of the Precambrian, evolved into widespread lithospheric extension followed by the early Ordovician diachronous opening of the Rheic Ocean (Linnemann et al., 2010; Nance et al., 2002, 2008; Sánchez-García et al., 2010; Žák et al., 2013).

The transformation from active to passive margin was indicated by the Rheic Ocean's initial rifting in the northern margin of Gondwana in the mid-to-late Cambrian (e.g., Nance et al., 2002; Sánchez-García et al., 2003, 2008). During that time, the Iapetus Ocean had opened (e.g., Cawood et al., 2001) and positioned to the north as a wide ocean (Fig. 1). The transition process of the northern Gondwana margin into a passive margin involved the protracted subduction–accretion that followed by several diachronous magmatism and eventually the rifting of the Rheic Ocean in the early Ordovician (ca. 460 Ma), leading to the separation of peri-Gondwana terranes (e.g., West and East Avalonia, Cadomia; Fig. 2).

The break-up occurred in two contrasting modes along the belt. The western (Avalonian) segment was completely rifted off (Fig. 1) from the Grenville crust (ca. 1.2–1.0 Ga) along a pre-existing suture, whereas the eastern (Cadomian) part of the belt was in contact with the Paleoproterozoic (ca. 2.2–1.9 Ga) basement of the West African craton (Mallard and Rogers, 1997; Murphy et al., 2000, 2006; Nance and Murphy, 1994) and remained partially attached to Gondwana during entire Early Paleozoic (e.g., Linnemann et al., 2004; Murphy et al., 2002; Robardet, 2003; Romer and Kroner, 2019; Servais and Sintubin, 2009; Stephan et al., 2019a; ; Syahputra et al., 2022 Žák and Sláma, 2018).

The geodynamic causes of break-up of these two distinct terrane assemblages remain unclear. The kinematics, styles, magnitudes, and temporal histories of rifting, continental break-up, and development of passive margins are controlled by multiple parameters, and several models for continental extension and rift propagation were postulated to account for this variability (see Mohriak et al., 2013; Festa et al., 2020; Jakob et al., 2019 for reviews). The

models essentially evolved from a symmetric, pure shear mode accommodated by normal faults/shear zones (McKenzie, 1978) through an asymmetric, simple shear mode with a dominant role of trans-lithospheric listric detachments (Wernicke and Burchfiel, 1982) to a most extreme hyperextension mode leading to crustal boudinage and even exhumation of the subcontinental mantle (Peron-Pinvidic et al., 2019; Pérez-Gussinyé, 2012). While the general principles regarding the rifting mechanisms and processes are laid out, many outstanding issues still need to be addressed in detail. For instance, the role of crustal thickness and rheological stratification, the evolution of topography and basin subsidence and its sedimentary record, and the role of syn-break-up crustal magmatism.

### 1.4. Main focus of the thesis

Huismans and Beaumont (2014) showed that the rifting process is essentially non-uniform, with unequal amounts of extension and thinning for the crust and mantle, either the crust or mantle is preferentially removed during the development of passive margins. Consequently, it has been found that rifted continental margins may exhibit a rather complex architecture, with a significant along- and across-strike segmentation (Jakob et al., 2019). This segmentation and differences in the rifting style, localization, and partitioning of deformation could result from the presence of heterogeneities (Brune et al., 2017; Cappelletti et al., 2013), structural and thermal gradient of the continental lithosphere (e.g., Duretz et al., 2016), and especially from the inherited mechanical anisotropy and tectonic structures (Petri et al., 2019). The latter issue has been hotly debated and remains poorly understood. The tectonic inheritance may result in syn-rift faults that are not perpendicular to the far-field extension vectors, complex, polyphase fault patterns, and rift segmentation and variations in rift orientation along strike (e.g., Samsu et al., 2019). Furthermore, it has been suggested that the reactivation of the basement-inherited structures during rifting has an enormous influence on the architecture and

evolution of younger orogenic belts (e.g., Brovarone et al., 2013; Epin et al., 2017; Mohn et al., 2014, 2011).

Therefore, the thesis was designed to examine the interaction between tectonics, sedimentation, and magmatism during continental extension (rifting) and transition from active- to passive-margin settings. The main focus of the thesis is to decipher the mechanism and time scale of the formation of ribbon continents, which involved multiple geodynamic processes from the crustal to the surface, using the particularly telling example of the Cadomian basement and associated (meta-)plutonic complexes and overlaying sedimentary basins in the Teplá–Barrandian and Moldanubian units of the Bohemian Massif.

### 1.5. Tectonic and geological setting of the Bohemian Massif during the end of Cadomian orogeny and Cambro–Ordovician rifting

The Avalonian–Cadomian belt started to break up diachronously during the latest Neoproterozoic to early Ordovician and recorded evolution from the convergent/accretionary margin switched to widespread lithospheric extension, resulting in the formation of an extensive passive margin (e.g., Etxebarria et al., 2006; Hajná et al., 2018; Keppie et al., 2003; Nance et al., 2002). The Avalonian terranes extended from New England and Atlantic Canada (West Avalonia) into southern Britain (East Avalonia), whereas the Cadomian terranes include the Iberian, Armorican, and Bohemian massifs (e.g., Nance et al., 2002). Among other Cadomian terranes, the Bohemian Massif is the most critical puzzle to unravel more than 600 million of years of European crustal evolution since its upper crustal Cadomian units were essentially unaffected by the Variscan deformation (Figs. 3 and 4)

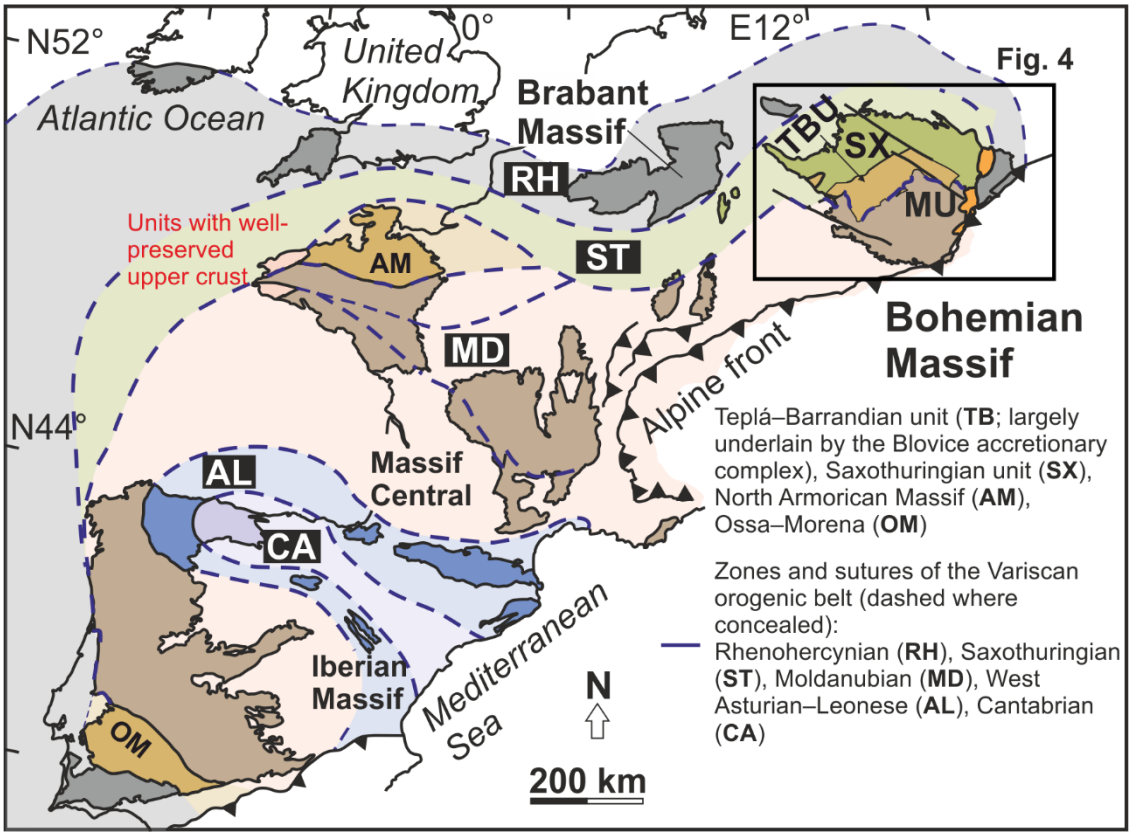


**Figure 3.** *Overview of Cadomian crustal fragments along the Variscan orogenic belts in Europe (compiled from Martínez Catalán, 2011).*

### *1.5.1. The Teplá–Barrandian unit*

The well-preserved units in the Bohemian Massif consist of Neoproterozoic to Paleozoic successions of the Saxothuringian Zone and the Teplá–Barrandian unit (Fig. 4). Even though these two units share similar geotectonic histories, the Teplá–Barrandian unit excels in several aspects. First, the archive of the oldest orogen in the Bohemian Massif was recorded in the Teplá–Barrandian unit from the plate scale tectonic through the plutonic and volcanic activities to the surface sedimentation processes. Second, most of the Teplá–Barrandian unit is still preserved with their original structure, weakly or even unaffected by the Variscan orogeny. Third, excellent stratigraphic and paleontological record occurs in several sedimentary basins, especially the Lower Paleozoic successions. The Teplá–Barrandian unit occupies a central position in the Bohemian Massif with the exposed units present in central and western Bohemia

(Fig. 4), fault-bounded by the Saxothuringian Zone to the NW and the Moldanubian zone to the SE. The boundaries in the SE with the Moldanubian zone are obscured by Variscan Central Bohemian Plutonic Complex (CBPC).

The most important lithotectonic elements of the Teplá–Barrandian unit comprise (1) the Cadomian basement, (2) Cambro–Ordovician plutonic to volcanic complexes and sedimentary basins, (3) Ordovician to early Silurian volcano and sedimentary deposits, (4) late Silurian to early Devonian massive carbonate rocks, (5) middle Devonian Variscan flysch, and (6) late Devonian to early Carboniferous plutonic complex. Therefore, the present-day structure of the Teplá–Barrandian unit is a combination of three superposed tectonometamorphic events: the Cadomian accretionary orogeny, early Paleozoic extension and rifting, and Variscan collisional orogeny.

Of six the lithotectonic elements above, the break-up of Avalonian–Cadomian belt involves only the first two, the end of Cadomian orogen (its magmatism) and Cambro–Ordovician extension and rifting, thus, provide an essential key to decipher the formation of the ribbon continent.

The Cadomian basement of the Teplá–Barrandian unit is similar to the Armorican Massif (Zulauf et al., 2000; Patočka and Štorch, 2004; Zoubek et al., 1988) and characterized by higher density of Cadomian crust (positive gravity anomaly from Blížkoský et al., 1986; Edel and Weber, 1995). The basement was formed by late Neoproterozoic (Ediacaran) accretionary orogen as the earliest crustal growth mechanism in the Teplá–Barrandian unit and the neighbouring unit (except a few volumetrically negligible and reworked crustal slivers in the Moldanubian Zone, e.g., Friedl et al. 2000, 2004; Wendt et al. 1993), and represented by coherent graywacke-dominated successions, intra- and back-arc basin turbidites, and volcanic complexes (Fig. 4). This Cadomian subduction–accretion terminated at ca. 540 Ma in the Armorican Massif and Saxothuringia (e.g., Ballèvre et al., 2001; Chantraine et al., 2001;

Linnemann and Romer, 2002; Linnemann et al., 2008), but continued in the Ossa Morena Zone (Iberian Massif) and the Teplá–Barrandian unit until at least the early to middle Cambrian (ca. 527 Ma based on Hajná et al., 2013, 2014, 2017).

After the Cadomian orogeny in the Teplá–Barrandian unit ceased, the Neoproterozoic accretionary complex was intruded by multiple plutonic bodies at ca. 524–522 Ma (Fig. 5). These large volumes of plutonic material were emplaced into a generally 'cold' fore-arc setting at the trench. Dörr et al. (2002) proposed that the driver of this plutonism was presumably a slab break-off or slab tear. Another possible scenario could be steepening and rollback of the still subducting oceanic slab, creating hot mafic magma underplated below the overriding plate. These Cambrian plutons are getting younger toward the northern of the Teplá–Barrandian unit with the remnant of ophiolite positioned at the northwestern edge, indicating that the subducting slab was coming from N or NW of the present-day TBU. Geochemical data show that the plutons originated as volcanic arc granites (Dörr et al., 1998) and were emplaced at an upper-crustal level in a tilted crustal block during the ENE–WSW dextral transtension (Zulauf, 1997; Zulauf et al., 1997; Zulauf and Helferich, 1997).

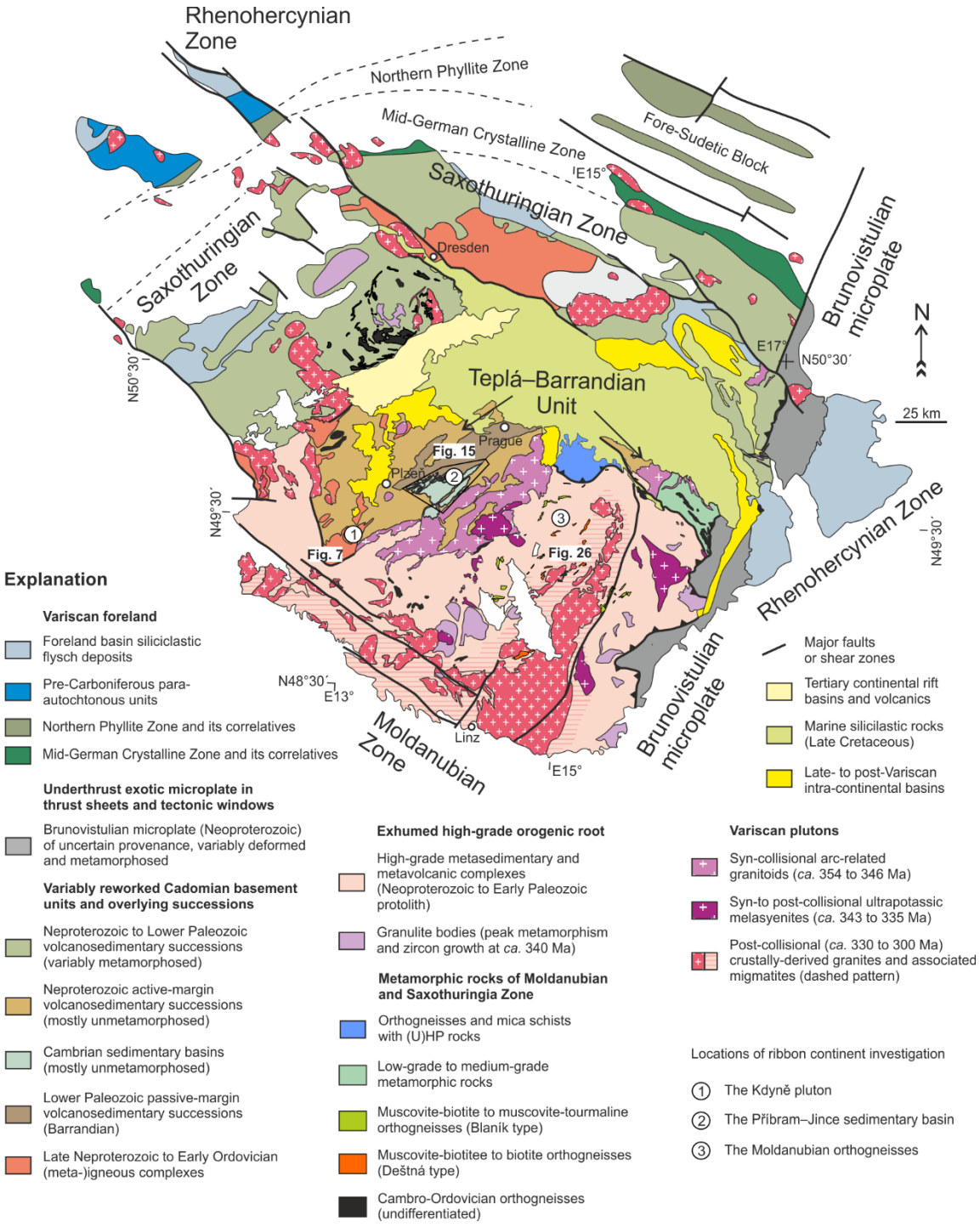


**Figure 4.** *Simplified geologic map of the Bohemian Massif with principal lithotectnic units. Background geology based on Cháb et al. 2007.*

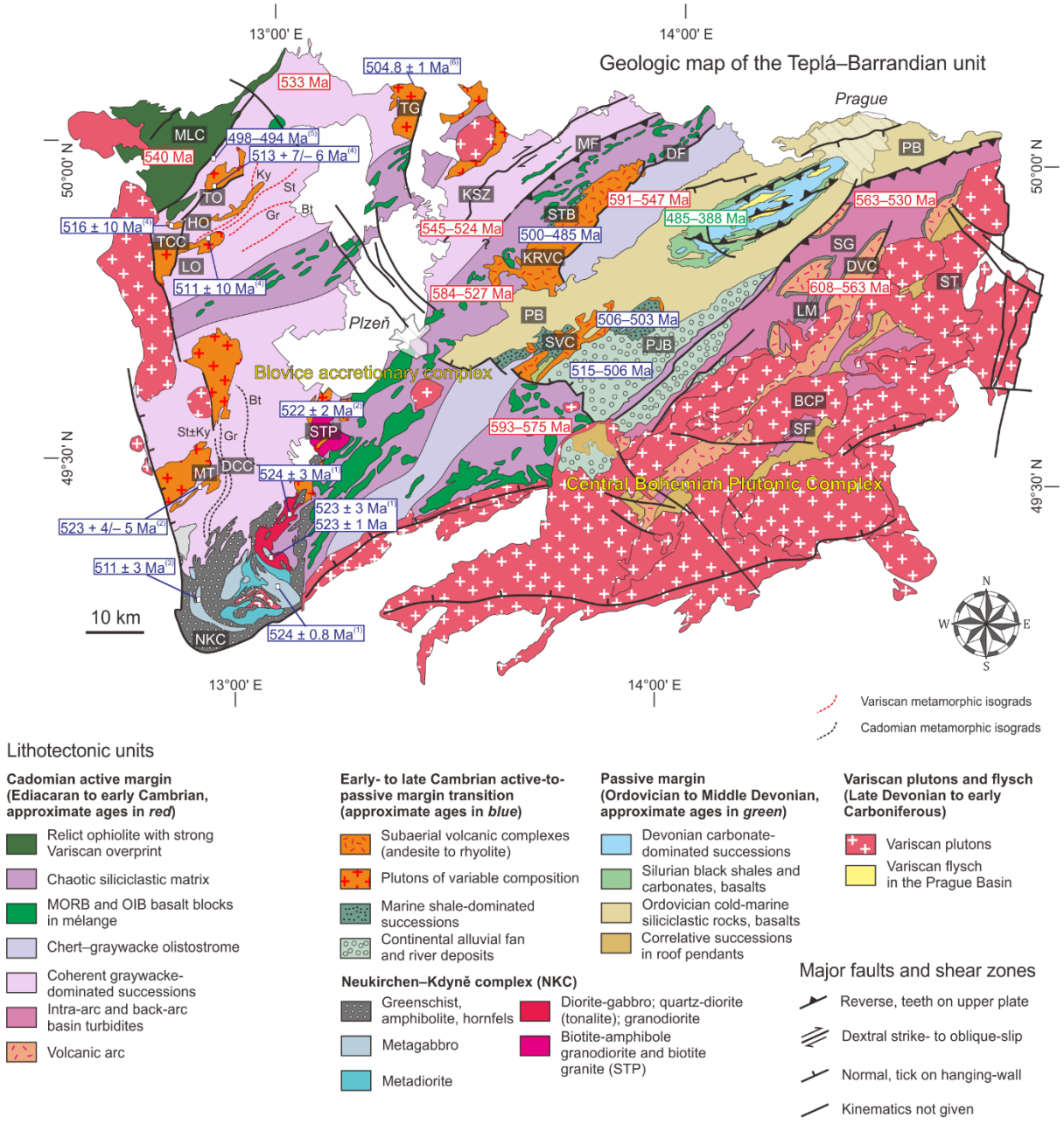


**Figure 5.** *Simplified geologic map of the Teplá-Barrandian unit on geological map 1:50,000 scale, published by the Czech Geological Survey. The ages were compiled from the existing geochronologic data for the Neoproterozoic (red rectangles), Cambrian (blue rectangles), and Ordovician (green rectangles). Metamorphic isograds attributed to Cadomian (Vejnar 1966, 1982; Zulauf, 1997; Zulauf et al., 1997) and Variscan (Zulauf, 2001) orogenic cycles differ in orientation in the western part of the Teplá–Barrandian unit. Geochronological data sources: Hajná et al., 2017, 2018. Geochronological data sources with errors: (1) Dörr et al. (2002), (2) Zulauf et al. (1997), (3) Gebauer (1993), (4) Dörr et al. (1998), (5) Timmermann et al. (2006), (6) Venera et al. (2000). Cadomian units: DF Družec fault, DVC Davle volcanic complex, LM Lečice Member, MF Městečko fault, MLC Mariánské Lázně complex, SF Svrchnice Formation, SG Štěchovice Group; Cambrian–Ordovician plutons and volcanic complexes: TCC Teplá crystalline complex, HO Hanov orthogneiss, KRVC Křivoklát–Rokycany volcanic complex, LO Lestkov orthogneiss, DCC Domažlice crystalline complex, MT Mračnice trondhjemite,*

The emplacement of Cambrian plutons was partly coeval with the development of sedimentary basins that created an angular unconformity with the Cadomian basement. Most sedimentary basins in the Teplá–Barrandian unit are pervasively deformed and metamorphosed during the Variscan orogeny, except for two basins preserved in their original stratigraphy and sedimentary record in the north-central and southeastern parts of the Teplá–Barrandian unit (Fig. 5). They are represented by a thick continental deposit briefly interrupted by marine transgression and associated volcanic complexes during the middle to late Cambrian. The continental depositional record within the sedimentary basin was controlled primarily by synsedimentary faults (Havlíček, 1971), which resulted from dextral transtension, indicating the initial rifting of the Rheic Ocean.

Both the Cadomian basement and mid- to late Cambrian basins are unconformably overlain by the Prague Basin, which represents a narrow, fault-bounded graben (e.g., Havlíček, 1981), interpreted to be a failed rift branch within the extensive peri-Gondwanan passive margin in the southern realm of the Rheic Ocean (Fig. 5; Tasáryová et al. 2018; Žák et al. 2013). The Prague Basin is filled with a continuous volcano-sedimentary marine succession ranging in age from the earliest Ordovician (Tremadocian) to Middle Devonian (Givetian) with minimum and maximum cumulative thicknesses estimated at ~1,200 and 5,100 m, respectively (e.g., Fatka and Mergl, 2009; Chlupáč, 1988; Chlupáč et al., 1998; Štorch et al., 1993). The succession consists of: (1) Ordovician siliciclastic rocks (shales, siltstones, sandstones; up to ~3,700 m thick in total) interpreted to be cold-water continental shelf deposits (e.g., Brenchley and Štorch, 1989; Štorch, 2006), (2) conformably overlying Silurian tuffitic and graptolite black shales that were deposited in an oxygen-poor environment and pass upward into warm-water carbonates (maximum total thickness ~630 m; e.g., Kříž, 1992; Lehnert et al., 2007;

Vacek et al., 2018), (3) up to ~570 m (in total) of Lower to Middle Devonian warm-water carbonates including reef and carbonate platform facies (e.g., Bábek et al., 2018a; Bábek et al., 2018b; Chlupáč, 2003; Weinerová et al., 2020), and (4) a capping succession (~250 m thick) of Givetian flysch siliciclastics (shales, siltstones, sandstones) that mark the onset of basin inversion during initial stages of the Variscan orogeny (e.g., Strnad and Mihaljevič, 2005; Vacek and Žák, 2019).

The entire Ordovician to Middle Devonian succession is interfingered with submarine basaltic volcanic complexes, dikes, and sills, with the main peaks of volcanic activity occurring in the Middle Ordovician (Floian–Sandbian) and early to late Silurian (Wenlock–Ludlow; e.g., Chlupáč et al., 1998; Tasáryová et al., 2018; Žák et al., 2013).

The subsidence patterns in the Prague Basin from Chlupáč et al. (1998) indicates an initial, steady drop of the basin floor from *ca.* 485 to *ca.* 458 Ma, reaching an apparent subsidence of about 800 m, and continues with an abrupt drop below 3000 m within a short time span of about 5 M.y. (*ca.* 458–453 Ma). A small fall is recorded at the Ordovician/Silurian boundary, following which there is very little subsidence until the next fall at *ca.* 430–423 Ma. Finally, steady slow subsidence takes place until the Givetian (488 Ma) with a small drop at *ca.* 410–408 Ma. Interestingly, the Ordovician peak in submarine basalt volcanism preceded the rapid subsidence event by *ca.* 15 My, whereas the Silurian peak overlaps with the *ca.* 430–423 Ma drop.

### *1.5.2. Moldanubian unit*

In contrast to the Teplá–Barrandian unit, the Moldanubian unit occupies an inboard position within the Variscan orogenic belt and was pervasively overprinted by Variscan metamorphism and deformation during the Late Devonian and early Carboniferous (Fig. 4; e.g., Finger et al., 2007; Lardeaux et al., 2014; Petri et al., 2014; Schulmann et al., 2005). This unit mostly comprises the Monotonous and Varied series of meta-sedimentary complexes. The

former included the Neoproterozoic to Early Paleozoic siliciclastic protoliths (e.g., Košler et al., 2014; René, 2006), and now represented by low- and middle-pressure–high-temperature, commonly sillimanite- and cordierite-bearing, migmatitic biotite paragneisses (Fig. 4). The latter consisted abundant lenses of marble, quartzite, and amphibolite and are, at least partly, Early Palaeozoic in age (e.g., Košler et al. 2014). In terms of their protoliths, the metasedimentary successions are broadly correlative with the unmetamorphosed successions preserved in the Ordovician sedimentary basin of the Teplá–Barrandian unit (the Prague Basin).

The Moldanubian unit also contains lenses and larger bodies of (U)HP eclogite- to granulite-facies and mantle rocks (Fig. 4; e.g., Faryad and Kachlík, 2013; Franěk et al., 2011; Janoušek and Holub, 2007; Kotková, 2007; Medaris et al., 2005). Together with various types of migmatites and migmatized granite gneisses, these rocks have been collectively termed ‘the Gföhl assemblage’ (e.g., Cooke and O´Brien, 2001; Petrakakis, 1997), and are interpreted to record deep burial during early stages of the Variscan orogeny (e.g., Faryad and Cuthbert, 2020; Faryad et al., 2015; Nahodilová et al., 2014).

The metaclastic successions in the Moldanubian unit host a number of scattered but regionally widespread granite plutons, several hundreds of meters to a few kilometers across, now metamorphosed to metagranites and orthogneisses (location 3 in Fig. 4). In domains with a lesser degree of Variscan overprint, contact-metamorphic assemblages, migmatite xenoliths, and local anatexis indicate that at least some of the orthogneiss bodies may represent deformed relicts of intrusive sheets rather than allochtonous slivers tectonically mixed with the metaclastic rocks (e.g., Klomínský et al., 2010).

### 1.6. Key issues

The outstanding issues that have been described above can be solved through the following integrative approach:

- A rigorous distinction of syn-rift structures from the pre-and post-rift (i.e., orogenic, post-orogenic) structures eventually led to the structural identification and characterization of the very initial stage of rifting of the Rheic Ocean.
- The evolution of the sedimentary fill and syn-rift magmatism. The sedimentary fill mechanism was examined by exploring the thickness variations, depocenters shifting, facies distribution, provenance analysis, and paleo-current directions within the sedimentary basin. The rift-related magmatism is best approached by structural differentiation and mechanism of pre-, syn-, and post-plutonic emplacement.
- Investigation of the crustal thinning mechanisms by exploring the influence of volcanisms, basin subsidence, and pre-existing heterogeneities on the architecture and evolution of the rift in a more regional context. This way, the timing, styles, and kinematics that govern the failure or success of a ribbon continental break-up will be established.

# 2. SPECIFIC FIELD AREAS EXAMINED IN THE THESIS

The aims and goals of the thesis were tested on three different locations within the Bohemian Massif, Czech Republic (Fig. 4). These locations represent continental rifting processes from middle−upper crust intrusion to the sedimentary basin at the surface level during the active to passive margin transition from early Cambrian to Ordovician. Each location is briefly introduced with respect to its contribution to the ribbon continent break-up.

## 2.1. The Kdyně pluton

The Kdyně pluton is located in the Plzeň region in the southwestern margin of the Czech Republic. It is considered a rapid intrusive series of intermediate to felsic plutonism (granite, granodiorite, tonalite, trondhjemite, gabbro-diorite, diorite) that occurred during the early Cambrian (524–522 Ma; Dörr et al., 2002). This pluton intruded the Cadomian accretionary wedge/forearc (Blovice accretionary complex; Hajná et al., 2017; Žák et al., 2020) with a high temperature, representing the earliest plutonism after the end of Cadomian accretion in the Teplá−Barrandian unit. Subsequently, several mid to late Cambrian plutonism also occurred generally toward the northwestern (Teplá crystalline complex) and northern (Tis granite) margins, creating an oblique direction to the former accretionary complex. Geochemical data shows these plutons formed in an orogenic setting classified as volcanic arc granite groups (Dörr et al. 1998). Their occurrence indicates an initial extensional process that may develop from an influx of hot asthenosphere beneath the Blovice accretionary complex due to slab break-off (Dörr et al. 2002), indicating the very initial break-up of the Rheic Ocean.

## 2.2. The Příbram–Jince basin

Of the two preserved sedimentary basins in the Teplá–Barrandian unit, the Příbram–Jince basin is the biggest and has a well exposed stratigraphy. The Příbram–Jince basin is situated in the Central Bohemian region, about 50 km southwest of Prague, and represents a

complete stratigraphy record of syn-rift deposits during the Cambrian, dominated by coarse grain sediments (the clasts are up to boulders in size). The sedimentary provenance came from the pre-Cambrian volcanic arc, metamorphic basement, and local source area. As the basin matured, those sources experienced a dynamic redirection from basin axis-oblique to basin axis-parallel, indicating the onset of dextral transtension in response to oblique rifting at ca. 511 Ma. This sedimentary deposit was controlled by fault (horst-graben) due to continental rifting, marking the separation of the Avalonian–Cadomian belt from northern Gondwana and the initial opening of the Rheic Ocean.

### 2.3. The Moldanubian orthogneisses

Metagranites and granitic orthogneisses of the Moldanubian zone are located in the Pardubice and Vysočina regions, about 60 km to the southeast of Prague. This case study is the last puzzle piece to unravel the active to passive margin transition in the Bohemian Massif. The combination of age constraints from U–Pb zircon and magma composition, as well as the basin subsidence in Prague Basin, were performed to identify the mechanisms and time scales of the lithospheric extension during the Cambro–Ordovician. The orthogneiss protoliths originated from the deformed relicts of intrusive sheets (e.g., Klomínský et al. 2010) within a deeper plutonic system. After mid- to late Cambrian plutonic emplacement in the Teplá−Barrandian unit, the late Cambrian granitic magma emplacement (now the Moldanubian orthogneisses) occurred in the Moldanubian zone due to basaltic underplating below extending continental crust. This process was coeval with the rift-drift transition of Avalonia from Gondwana and the opening of the Rheic Ocean.

# 3. METHODS

In terms of the methods used, this thesis is multidisciplinary and involves mainly field mapping, macro- and micro-structural analysis, and stratigraphic and sedimentological analysis (including paleocurrent analysis). Measurement of structural features (bedding, foliation, lineation, stratigraphic contacts) was conducted precisely and spatially close distributed as much as possible given the outrop situation. Sample collection was performed carefully to find the best representative character of the particular rock formation. Detailed petrographical analysis from thin sections was performed an optical microscope and presented in high-quality images. Together with the new U−Pb zircon analysis (done as external contract by Dr. J. Sláma of the Institute of Geology of the Czech Academy of Sciences using laser ablation–inductively coupled plasma–mass spectrometry - LA–ICP–MS) and geochronological data from existing studies. Yet, a robust and relatively inexpensive method of the anisotropy of magnetic susceptibility (AMS) was measured in the laboratory of Rock Magnetism at the Institute of Geology and Paleontology, Charles University, Prague and chosen as the most crucial method in studies of both plutonic and sedimentary rocks, thus it is described in detail below.

## 3.1. Anisotropy of magnetic susceptibility (AMS)

Magnetic susceptibility is the ability of a substance to be magnetized by an applied magnetic field, symbolized by $k$, which is equal to the ratio of magnetization $M$ within the material to the applied magnetic field strength $H$, or expressed as $k = M/H$ (SI unit are used throughout the thesis). Low field (<1 mT) anisotropy of magnetic susceptibility (AMS, e.g., Borradaile and Henry, 1997; Borradaile and Jackson, 2004, 2010; Bouchez, 1997; Hrouda, 1982; Rochette et al., 1992; Tarling and Hrouda, 1993) was used throughout the thesis to quantitatively analyse the symmetry, intensity, and orientation of the magnetic fabric. Every

mineral inside a rock has a different magnetic property. Therefore, all rocks should be considered anisotropy and divided into three groups based on their magnetic susceptibility.

The magnetic minerals in rocks will be aligned parallel to the Earth's magnetic field as the temperature decrease below Curie temperature. Those minerals are called ferromagnetic (magnetite, maghemite, and other iron oxides) and have high susceptibility ($10^{-3}$– $10^{-2}$). On the other hand, the paramagnetic minerals (e.g., muscovite, biotite, amphibole, olivine) also tend to align parallel to the direction of the magnetic field but with much smaller magnetic susceptibility ($10^{-5}$–$10^{-4}$) than ferromagnetic minerals (e.g., Hrouda and Kahan, 1991). In contrast to all the above types, the diamagnetic minerals (e.g., quartz, calcite) have an opposite direction to the applied magnetic field, thus, have a negative magnetic susceptibility ($-10^{-5}$). The mineral contribution to the bulk susceptibility of rock may vary significantly, depending on their intrinsic susceptibility as well as on their concentration (Fig. 6a); for instance, if a rock contains paramagnetic minerals as the mineral constituents (ca. 10%) with mean susceptibility range from $10^{-4}$ to $10^{-3}$, its susceptibility and anisotropy are affected by the paramagnetic and ferromagnetic fractions.

In order to define which degree predominates the magnetic susceptibility of a rock sample, measurement of susceptibility variations with temperature are conducted from the temperature of liquid nitrogen (–196 °C) up to 700 °C and back (thermomagnetic curves). For example, a 'normal' magnetite curve usually forms a box-like curve with a Curie temperature (520–560 °C) and Verwey transition (ca. –150 °C). In contrast, the paramagnetic minerals show a hyperbolic decrease curve of magnetic susceptibility as the temperature increase.

Anisotropy of magnetic susceptibility (AMS) is easier to be visualized by its ellipsoid with three orthogonal principal axes (Fig. 6b), which are the longest, intermediate, and shortest axis corresponding to maximum ($k_1$), intermediate ($k_2$), and minimum ($k_3$) principal susceptibilities, respectively (e.g., Hrouda, 1982; Tarling and Hrouda, 1993). AMS is utilized

to perform a petrofabric analysis, where $k_1$ represents magnetic lineation, and $k_3$ is the normal (pole) to magnetic foliation.

Three parameters are used to characterize the magnetic fabrics (e.g., Hrouda, 1982):

(1) the bulk susceptibility, $k_m = (k_1 + k_2 + k_3)/3$ (Nagata, 1961; Janák, 1965), represents the proportion and composition of diamagnetic, paramagnetic, and ferromagnetic minerals in a measured specimen.

(2) The degree of anisotropy, $P = k_1/k_3$ (Nagata, 1961), reflects the eccentricity of the AMS ellipsoid and thus may indicate the intensity of the preferred orientation of the magnetic minerals.

(3) The shape parameter, $T = 2\ln(k_2/k_3)/\ln(k_1/k_3) - 1$ (Jelínek, 1981), indicates the shape of the AMS ellipsoid (Fig. 6c). For $-1 \leq T < 0$, the ellipsoid is prolate; for $T = 0$ it is triaxial or transitional between linear and planar magnetic fabric; for $1 \geq T > 0$ it is oblate.

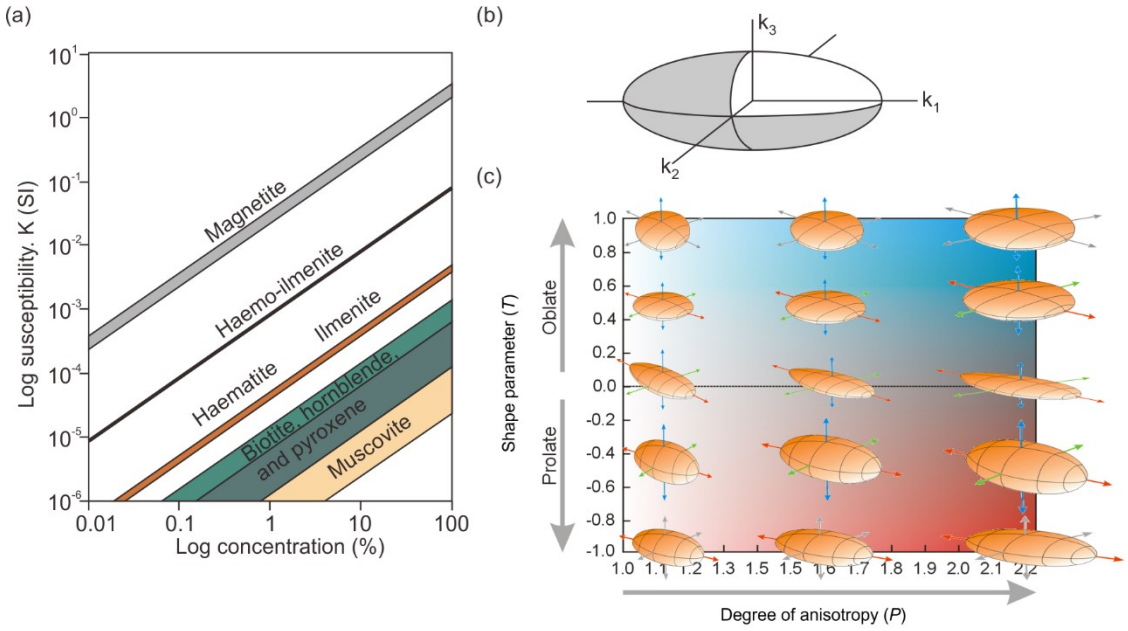


**Figure 6.** *(a) Mineral contribution to the bulk susceptibility of rock (after Hrouda and Kahan, 1991). (b) Ellipsoid of principal magnetic susceptibility. (c) Jelinek plot shows a relationship between shape parameter (T) and degree of anisotropy (P).*

### 3.2. Why is AMS important to this thesis?

The AMS used in this thesis involved sedimentary, shallow plutonic, and low-grade metamorphic rocks within the Czech Republic. The AMS is essential to recognize invisible magnetic fabrics that behave as a sedimentary depositional structure, plutonic emplacement marker, and tectonic deformation during and after the formation of rocks. The primary fabrics of clastic sediments are predominantly formed during the deposition of particles from suspension in water or air, whereas the petrofabric in igneous rocks may develop during crystal aligment within magmatic flow at higher temperatures. These primary sediment and igneous fabrics could turn into secondary fabrics through metamorphic processes. Thus, the distinction between primary and secondary fabrics in the metamorphic rock depends on the orientation of the magnetic fabric and the recognition of its ellipsoidal characteristic, whether they are related to geologically plausible stress or strain fields during the rock formation (Tarling and Hrouda, 1993).

In sedimentary rocks, the magnetic lineations or maximum susceptibility axis ($k_1$) can be used to infer sedimentary grain transport direction, especially for paleocurrent analysis (e.g., Felletti et al., 2016; Hrouda et al., 2009; Soto et al., 2016; Veloso et al., 2007). A laboratory experiment conducted by Rees and Woodal (1975) demonstrated the deposition of sediment grains in still water produced a magnetic foliation ($k_3$) parallel to the bedding and a relatively scattered magnetic lineation ($k_1$). The shape parameter of those fabrics is predominantly occupied by oblate grains with their long axes parallel to the plane of depositional surface or bedding plane, whereas the long axes of prolate grains tend to lie randomly. On an inclined surface, the prolate grains tend to roll downslope. As a result, the long grain axes (magnetic lineation) create a perpendicular angle along the strike as the slope increases, resembling the fabrics formed in the presence of water current. Those fabric's behaviour indicates that not only gravitational and hydrodynamic forces determine the fabric, but also the size, shape, and

mass of the detrital grains and the velocity of the medium (e.g., Rees, 1966, Rees and Woodall, 1975; Taira and Scholle, 1979; Stachowska et al., 2020 and references therein). Therefore, interpreting the magnetic lineations in the sedimentary rocks is not more complex than mesoscopic paleocurrent indicators. In cases where lineations are subhorizontal and scattered more or less symmetrically about opposite trends, the calculated site-mean lineation, and thus the inferred paleocurrent direction, may be strongly affected by the statistical distribution of individual specimens and may point to the opposite direction. Hence, the AMS-derived paleocurrent directions must be cautiously interpreted together with the mesoscopic paleocurrent measurement.

In contrast, shallow plutonic rock tends to be more magnetically foliated than lineated (Brown et al., 1964; Symons, 1967; Tarling and Hrouda, 1993). Hence, the AMS in these rocks has been proven as an extremely sensitive indicator of a strain capable of recording the plutonic emplacement time and style, and 'invisible' deformational fabrics (e.g., Hrouda et al., 2009; Johnson et al., 2003; Paterson et al. 1998; Paterson and Fowler, 1993; Žák and Paterson, 2005). The majority studies of the primary magnetic fabrics on plutonic rocks have dealt with granites rather than basic or ultrabasic rocks. Granitic rocks are divided into ferromagnetic and paramagnetic (Bouchez, 1997; Ellwood and Wenner, 1981; Ishihara, 1977; Ishihara et al., 2002). The higher susceptibilities between $10^{-3}$ and $10^{-2}$ usually belong to the ferromagnetic granites that mainly consist of magnetite and/or magnetite with ilmenite, whereas the paramagnetic granites have lower susceptibilities between $10^{-5}$ and $10^{-4}$ that largely carried by ilmenite and/or haemo-ilmenites (Tarling and Hrouda, 1993). Therefore, the magnetic minerals within the plutonic rocks generally reflect their origin and nature. The direction of magnetic lineations could be either parallel or perpendicular to the magmatic flow (e.g., Burton-Johnson et al., 2019; Venera et al., 2000; Žák et al., 2005), thus, requiring a combination interpretation with macro and microstructural data.

The low-grade metamorphic rocks in this thesis involve the graywackes, which are the host rock of the Kdyně pluton that was heated within high temperature and low-pressure conditions. By comparing any other similar age rocks, the orientation of magnetic fabrics can be characterized through the magnetic foliation and lineation to differentiate between the primary (initial) and secondary (deformed) sedimentary fabrics. Using basic information from a laboratory experiment on sedimentary rocks from early studies (Rees and Woodal, 1975), the magnetic foliation generally lies within 15° of the bedding plane and has an oblate shape parameter, thus fabrics that fall outside these ranges have been considered as secondary. A low degree of anisotropy ($P < 1.05$) has also been suggested by Dvořák and Hrouda (1975) as the additional constraint in primary fabric recognition.

# 4. DATA AND RESULTS

## 4.1. Cambrian plutonism

Voluminous plutonism during Cambrian marked the termination of Cadomian subduction from active to passive margin (e.g., Bues et al., 2002; Dörr et al., 2002; Hajná et al., 2018; Sláma et al., 2008a; Vítková and Kachlík, 2001; Zulauf et al., 1997, 1999). In the early to middle Cambrian, the previously formed Cadomian accretionary wedge was intruded by a number of compositionally diverse, mafic to felsic calc-alkaline plutons, interpreted to record remelting of the arc-derived crust in response to slab break-off (Fig. 5, e.g., Bues et al., 2002; Dörr, et al., 2002, 1998; Timmermann et al., 2006; Zulauf et al., 1997, 1999; Zulauf and Helferich, 1997).

The Cambrian magmatism occurred in several different locations marking a shift of magmatic activity throughout the western part of the Teplá–Barrandian unit. The onset of plutonism is represented by the Neukirchen–Kdyně and Stod complexes in the southwestern part of the Teplá–Barrandian unit (Všepadly granodiorite, U–Pb on zircon 524 ± 3 Ma, Dörr et al., 2002; Smržovice quartz-diorite, U–Pb on zircon 523 ± 3 Ma, Dörr et al., 2002; Smržovice amphibole gabbro, U–Pb on zircon 523 ± 1 Ma, Dörr et al., 2002; Orlovice diorite, U–Pb on zircon 524 ± 0.8 Ma, Dörr et al., 2002; Těšovice granite in Stod pluton, U–Pb on zircon, 522 ± 2 Ma, Zulauf et al., 1997). To the W, the Domažlice crystalline complex (DCC in Fig. 1c) comprises the Mračnice trondhjemite intrusion (U–Pb on zircon, 523 + 4/–5 Ma, Zulauf and Helferich, 1997) that intruded Cadomian metagraywackes intercalated with basic meta-volcanic units. Farther to the NW, younger granitoid plutons (ca. 516–511 Ma in age) intruded the Teplá crystalline complex (TCC in Fig. 5; all ages acquired from U–Pb on zircon; Hanov orthogneiss, 516 ± 10 Ma, Teplá orthogneiss, 513 + 7/–6 Ma; Lestkov granite, 511 ± 10 Ma, Dörr et al., 1998), broadly coeval with the Neukirchen amphibolite in the southwestern Teplá–

Barrandian unit (U–Pb on zircon, 511 ± 3 Ma, Gebauer, 1993). Finally, the extensive Tis granite intruded the northern part of the unit at 504.8 ± 1 Ma (Pb–Pb on zircon, Venera et al., 2000).

Among these Cambrian plutons, the Neukirchen–Kdyně complex including the Všepadly granodiorite and Smržovice tonalite and gabbro (Figs. 5, 7a) experienced only weak post-plutonic ductile deformation (e.g., Bues et al., 2002; Dörr et al. 2002) and, given their ages, thus may provide an important record of the earliest stages of the active to passive margin transition in former northern Gondwana.

The ~524–522 Ma Neukirchen–Kdyně complex is the oldest and also one of the largest Cambrian intrusions in the entire west-central Bohemian Massif, covering an area of about 300 $km^2$ (Fig. 5). The complex intruded the Cadomian (late Neoproterozoic to early Cambrian) siliciclastic successions with U–Pb detrital zircon ages as young as ca. 527 Ma (the Blovice accretionary complex; Hajná et al., 2017; Žák et al., 2020).

The Neukirchen–Kdyně complex is internally zoned from outer mafic members (olivine gabbro, gabbro, gabbrodiorite, and pyroxene-diorite) to inner intermediate members (quartz–diorite to granodiorite; Bues et al., 2002). The latter is referred to as the Kdyně pluton in this study, composed of diorite–gabbro, biotite–amphibole granodiorite, quartz–diorite, and amphibole gabbro (Fig. 7). The pluton forms a crescent-shaped body, consisting of a northern domain elongated NE–SW, a transitional, middle domain, and a southern domain elongated NW–SE (Fig. 7a). The whole pluton is thus concave toward the E, with a total length of ca. 21 km and a maximum width of ca. 3 km (Fig. 7).

The host rocks around the complex are mostly medium- to fine-grained meta-graywackes of the Blovice accretionary complex, locally intercalated with meta-tuffs, variably contact metamorphosed from epidote- to pyroxene-bearing hornfelsic rocks (Fig. 5, 7a). The

western, southern, and southeastern boundaries of the Neukirchen–Kdyně complex are tectonic (Variscan shear zones, Fig. 1c; Bues et al., 2002; Dörr and Zulauf, 2010).

At the end of the Cadomian orogeny, but before the onset of plutonic activity, the accretionary complex underwent Barrovian-type metamorphism, with metamorphic isograds oriented roughly ~N–S (Fig. 1c; Vejnar 1966, 1982; Zulauf, 1997; Zulauf et al., 1997). The Barrovian metamorphism was explained as a result of a collision of an unknown microplate or magmatic arc with the Blovice complex (Zulauf et al., 1999). Zulauf et al. (1997) described the metamorphic grade increasing from the lowermost greenschist facies in the east to amphibolite facies in the west (biotite, garnet, staurolite ± kyanite zones), suggesting crustal tilting after the Barrovian metamorphism but before emplacement of the early Cambrian granitoids (Zulauf et al., 1999). The Mračnice trondhjemite, Stod pluton, and presumably also the Poběžovice pluton (Fig. 5) were syn-kinematically emplaced into the tilted crust along ~ENE–WSW-trending dextral transtensional zones (Zulauf et al., 1997).

#### *4.1.1. Host rock structures*

The mesoscopic fabrics in the host rock are classified here based on their relative temporal relationships to the regional and contact metamorphic processes and, hence, to the timing of emplacement of the Kdyně pluton (Fig. 7a). Furthermore, the fabrics also vary in their intensity and spatial distribution among the northern, middle, and southern domains of the pluton/host rock system (Fig. 7a).

##### *4.1.1.1.Pre-emplacement fabric*

On outcrops, the pre-emplacement fabric typically includes compositional banding, defined by alternating millimeter-thick mica-rich and quartzofeldspathic bands, and a foliation preserved in metagraywackes (Fig. 8a), mostly occurring in the northern and middle structural domains. The pre-emplacement foliation dips moderately to steeply and appears to be folded

into open to tight upright folds of tens to hundreds of meters wavelength (Fig. 7c). As a result, its strike varies from sub-parallel to almost perpendicular to the NE–SW pluton axis (Fig. 7a).

*4.1.1.2.Syn-emplacement fabric*

The syn-emplacement, high-temperature fabric is defined by mafic–felsic compositional banding (up to 1–2 cm thick bands) and planar shape-preferred orientation of both mafic (amphibole, biotite, and/or pyroxene) and felsic (recrystallized plagioclase and quartz) mineral grains and aggregates. Unlike the above type, this foliation is widespread around the whole pluton as well as in the host rock screens and blocks in its interior (Fig. 7a). In the northern domain, the foliation dips moderately to steeply to the NW and SE, i.e., subparallel to intrusive contacts and pluton axis. In weak, tuffitic lithologies, the syn-emplacement foliation becomes subvertical and defines narrow (typically tens of meters thick), steep tabular zones parallel to the pluton margin (Figs. 7c and 8b). In the middle and southern domains, however, the foliation dips to the SSW to SSE and is thus at an angle to the local intrusive contact in some places. Especially at the southeastern tip of the pluton, the foliation appears to be truncated by the intrusive contact (Fig. 7a).

Stretching lineation associated with the syn-emplacement high-T foliation, if present, is mostly defined by stretched grains and aggregates amphibole, biotite, pyroxene, and recrystallized plagioclase. The lineation plunges shallowly to moderately, trending either NW–SE or WNW–ESE with a few exceptions (Fig. 7b).

In a kinematic (lineation-parallel and foliation-perpendicular) section, the quartzofeldspathic bands are in places thinned into pinch-and-swell structures and boundins that are mostly symmetric (Fig. 8c). Asymmetric structures are scarce except for lenses and rootless asymmetric folds that experienced a top-to-the-northeast sense of shear (Fig. 8d) but do not show regionally consistent kinematics.

#### *4.1.1.3. Post-emplacement structures*

The post-emplacement, low-temperature structures overprint the syn-emplacement foliation and are developed as centimeter- to meter-scale asymmetric open folds (Fig. 7c). Their axial surfaces are gently to moderately inclined (between 16° and 54°) with a gently plunging fold axes (Fig. 7b). Along the eastern pluton margin, localized shear bands and spaced cleavage develop parallel to the fold axial planes and dip moderately to steeply away from the pluton (Fig. 8e, f). Altogether, these folds resemble outward-verging cascading folds associated with normal kinematics in metamorphic core complexes (e.g., Jolivet et al., 2004).

Late-stage quartz veins, up to several centimeters thick, are common in all structural domains and cut across the syn-emplacement foliation and even the post-emplacement folds in some cases. The veins dip predominantly to the WSW or ENE (Fig. 7b).

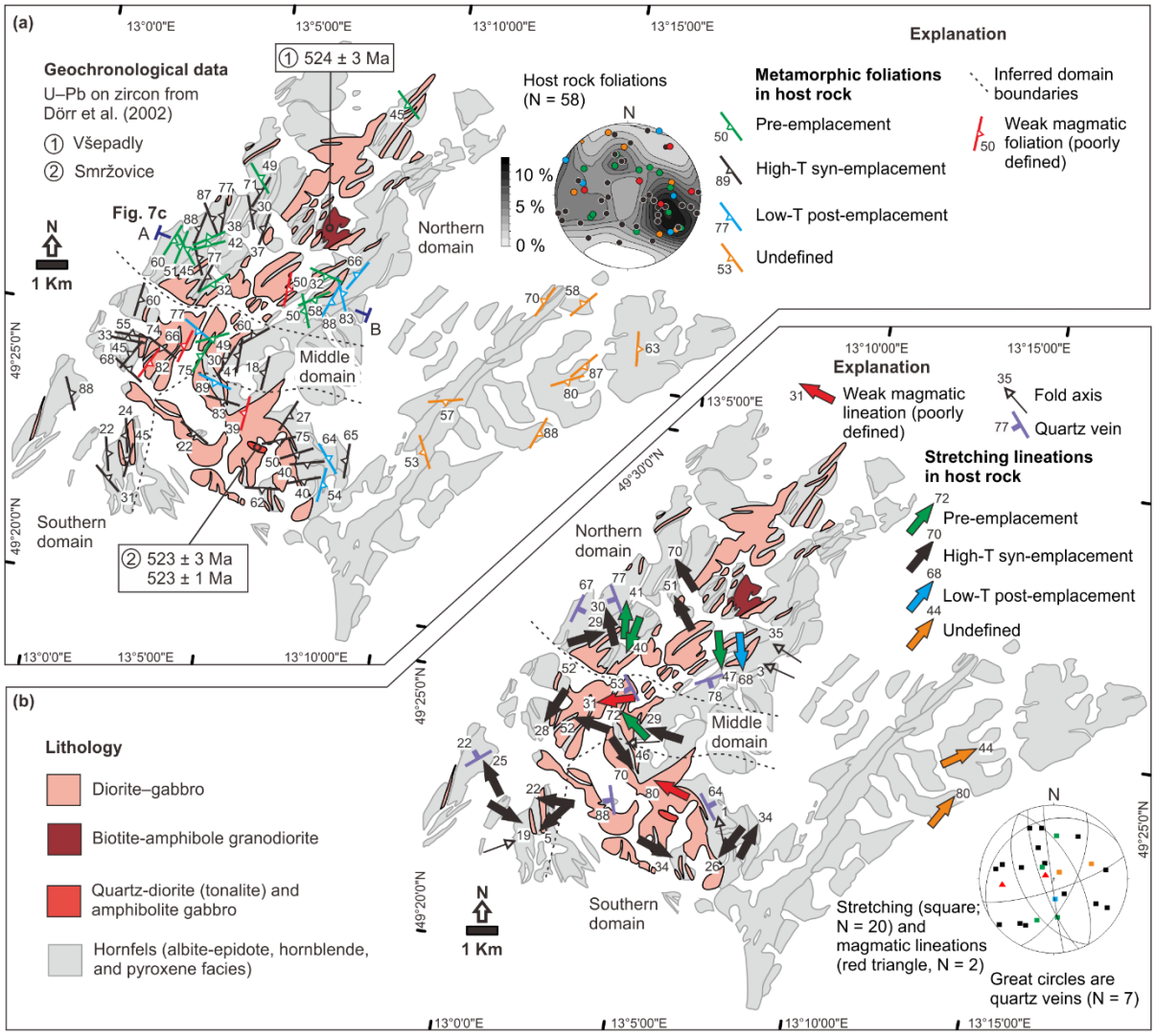
(a)
Geochronological data
U–Pb on zircon from Dörr et al. (2002)
① Všepadly
② Smržovice
① 524 ± 3 Ma
② 523 ± 3 Ma
523 ± 1 Ma
Fig. 7c
Northern domain
Middle domain
Southern domain
Host rock foliations (N = 58)
10 %
5 %
0 %
Explanation
Metamorphic foliations in host rock
Pre-emplacement
High-T syn-emplacement
Low-T post-emplacement
Undefined
Inferred domain boundaries
Weak magmatic foliation (poorly defined)
Weak magmatic lineation (poorly defined)
Fold axis
Quartz vein
Stretching lineations in host rock
Pre-emplacement
High-T syn-emplacement
Low-T post-emplacement
Undefined
Stretching (square; N = 20) and magmatic lineations (red triangle, N = 2)
Great circles are quartz veins (N = 7)
1 Km
13°0'0"E
13°5'00"E
13°10'00"E
13°15'00"E
49°25'0"N
49°20'0"N
49°30'0"N
(b)
Lithology
Diorite–gabbro
Biotite-amphibole granodiorite
Quartz-diorite (tonalite) and amphibolite gabbro
Hornfels (albite-epidote, hornblende, and pyroxene facies)

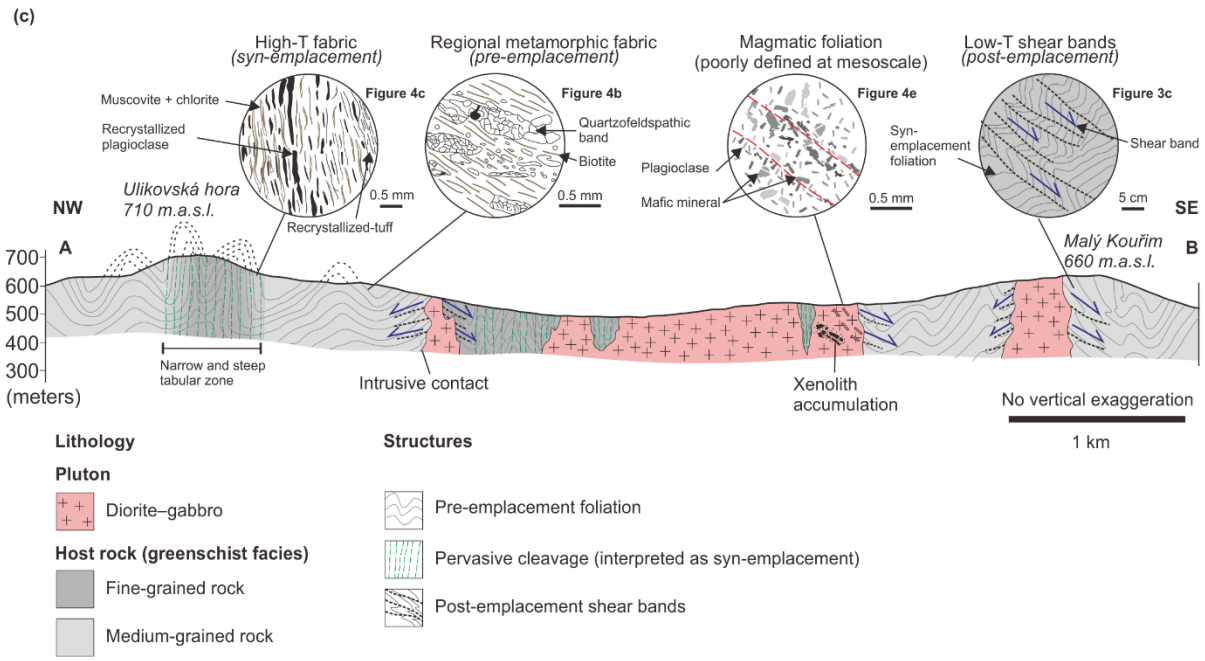
(c)
High-T fabric (syn-emplacement)
Regional metamorphic fabric (pre-emplacement)
Magmatic foliation (poorly defined at mesoscale)
Low-T shear bands (post-emplacement)
Figure 4c
Figure 4b
Figure 4e
Figure 3c
Muscovite + chlorite
Recrystallized plagioclase
Recrystallized-tuff
Quartzofeldspathic band
Biotite
Plagioclase
Mafic mineral
Syn-emplacement foliation
Shear band
0.5 mm
5 cm
NW
SE
Ulikovská hora
710 m.a.s.l.
Malý Kouřim
660 m.a.s.l.
A
B
700
600
500
400
300
(meters)
Narrow and steep tabular zone
Intrusive contact
Xenolith accumulation
No vertical exaggeration
1 km
Lithology
Pluton
Diorite–gabbro
Host rock (greenschist facies)
Fine-grained rock
Medium-grained rock
Structures
Pre-emplacement foliation
Pervasive cleavage (interpreted as syn-emplacement)
Post-emplacement shear bands

**Figure 7.** *Structural data from the Kdyně pluton and its host rock (a, b). The metamorphic foliations and stretching lineations are divided based on pre-, syn-, and post plutonic emplacement within the northern, middle, and southern domains. Geochronological data were taken from Dörr et al. (2002): location 1 is Všepadly granodiorite, location 2 is Smržovice quartz–diorite. The background geologic map was compiled from Bues et al. (2002) and geological maps 1:25,000 published by the Czech Geological Survey. (c) Schematic cross-section along the line A–B (location shown in Fig. 7a). Stereonets are equal area, lower hemisphere projection.*

---

### *4.1.2. Structure of the Kdyně pluton*

On a map scale, the northern domain Kdyně pluton is internally sheeted, with the thin and often irregular host rock screens alternating with thin plutonic sheets, whereas the southern domain is internally more homogeneous and largely devoid of host rock blocks (Fig. 7). The pluton margins are interpreted as largely discordant to the pre-emplacement fabric in the host rock to produce sharp and irregular intrusive contacts (Fig. 7c).

The pluton interior appears isotropic on most outcrops and macroscopically discernible magmatic foliation and lineation are rather rare and only weakly developed (Fig. 3h), defined by the shape-preferred orientation of plagioclase and mafic minerals (amphibole, biotite, and/or pyroxene). Nevertheless, magmatic foliation strikes NNE–SSW to NE–SW with a variable dip in all structural domains (Fig. 7a), whereas magmatic lineation plunges to the WSW (at 31°) or the NW (at 80°) (Fig. 7b).

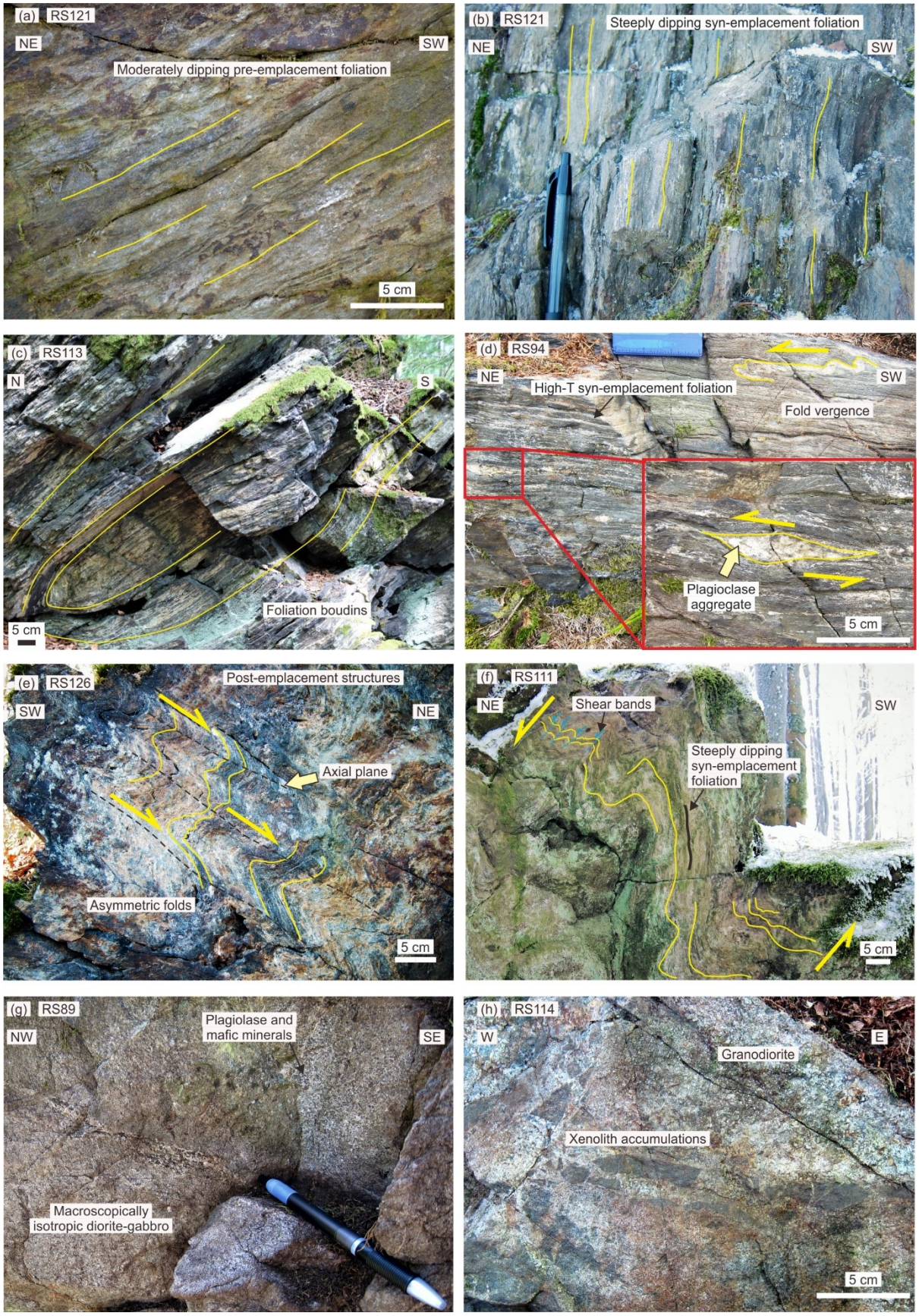


**Figure 8.** *Field photographs to show principal features of the Kdyně pluton and its host rock. (a) Medium-grained metagraywacke with moderately-dipping pre-emplacement foliation; Úlíkov [WGS84 coordinates:*

*49°25'51.916"N, 13°3'43.717"E]. (b) Fine-grained metagraywacke with recrystallized tuff bands forms a steep syn-emplacement foliation; Úlíkov [WGS84 coordinates: 49°25'47.894"N, 13°3'45.036"E]. (c) Sigmoidal foliation around boundins in hornfels; Hora [WGS84 coordinates: 49°24'31.896"N, 13°4'46.108"E]. (d) Asymmetric NE-vergent folds and plagioclase aggregates within the high temperature syn-emplacement foliation; Soběnec [WGS84 coordinates: 49°22'20.963"N, 13°7'47.285"E]. (e) Folded hornfels with foliation dipping to the NE, i.e., away from the pluton; Skalice [WGS84 coordinates: 49°25'58.148"N, 13°7'43.431"E]. (f) Folded metagraywacke with a shear band toward the NE overprinting the steeply-dipping syn-emplacement foliation; Koráb [WGS84 coordinates: 49°23'57.350"N, 13°4'20.151"E]. (g) Isotropic diorite–gabbro dominated by plagioclase and mafic minerals (amphibole); U Linharta [WGS84 coordinates: 49°25'49.414"N, 13°5'57.958"E]. (h) Xenolith accumulation in the Kdyně granodiorite; nearby Kreslova studánka [WGS84 coordinates: 49°24'35.197"N, 13°3'26.281"E].*

---

### *4.1.3. Microstructures*

Eighteen oriented and four non-oriented thin-section samples were collected in the Kdyně pluton and its host rock. The microstructures were examined in the lineation-parallel and foliation-perpendicular sections.

#### *4.1.3.1 Host rocks*

The pre-, syn-, and post-emplacement microstructures as defined in the field (section 4.1.1. and 4.1.2.) are described on representative samples below.

The pre-emplacement microstructure is defined by a regional metamorphic mineral assemblage and is exemplified by metagraywacke sample RS121A (Fig. 9a). The metagraywacke is composed of alternating quartzofeldspatic bands that alternate with mica-rich bands composed of biotite and fine-grained chlorite–muscovite matrix. The quartz–plagioclase bands are fine- to medium-grained (grain size typically varies from 0.1 to 0.5 mm) and may be folded into asymmetric microfolds or disrupted into asymmetric lenses and microboudins (Fig. 9a). Inside the bands, quartz grains exhibit an elongated to irregular shape and lobate grain boundaries (Fig. 9a), indicating dynamic recrystallization (e.g., Heilbronner and Tullis, 2002).

The high-T syn-emplacement microstructure is exemplified by a metatuff sample 121B (Fig. 9c), which exhibits bands composed of plagioclase aggregates alternating with mica-rich bands (mostly chlorite and muscovite). The plagioclase aggregates are frequently replaced by pyroxene (Fig. 9b) and recrystallized under high-temperature conditions, flattened together with fine-grained amphibole (actinolite) aggregates, recrystallized dark biotite (indicating the involvement of Ti), muscovite, and chlorite. Quartz grains have a uniform size and lack undulose extinction.

Higher intensity of contact metamorphism is recorded in hornfelses (sample RS137, Fig. 9c) that are composed of subhedral to anhedral, very fine- to fine-grained (up to 0.1 mm) aggregates of amphibole (actinolite or hornblende), fine-grained biotite, and muscovite that form bands or lenses. The dominant amphibole aggregates overprint the pre-existing relict fabric and fill the space between larger recrystallized grains (Fig. 9c). These aggregates exhibit a polygonal texture with the individual grains having an equant size and creating straight boundaries and triple points.

The low-T (retrograde) post-emplacement microstructure (representative sample in RS94, Fig. 9d) is characterized by localized shear planes that cut obliquely across the pre-existing high-T syn-emplacement foliation defined by bands and lenses of recrystallized plagioclase (albite–oligoclase) and pressure shadows of altered amphibole (actinolite). The late-stage mineral reactions also include the replacement of idiomorphic cordierite porphyroblasts (in the syn-emplacement foliation) by a mixture of muscovite, biotite, and chlorite (pinitization; yellow-greenish aggregates in Fig. 9d) and a transformation of epidote into clinozoisite.

*4.1.3.2. The Kdyně pluton*

The most widespread lithology in the pluton is diorite to gabbro, which vary from very fine- to medium-grained (from 0.3 up to more than 1 mm grain size, respectively). Figure 9e

shows a typical example of gabbrodiorite consisting of plagioclase, amphibole, both clino- and orthopyroxene, biotite, opaque minerals (magnetite, pyrrhotite), and some quartz. Plagioclase (albite–oligoclase) grains are dominated by subhedral to euhedral shapes and exhibit a blocky or elongated to skeletal form, albite, and Karlsbad twinning. In some places, plagioclase grains are enclosed by pyroxene, creating a subophitic texture (Fig. 9f). Pyroxene exhibits a fibrous texture and is replaced by chlorite and sometimes by hornblende (a sample from the southern domain in Fig. 9f). Typically, these rocks show no evidence of pervasive solid-state deformation, in some samples, the plagioclase laths are aligned and define magmatic foliation (Fig. 9e).

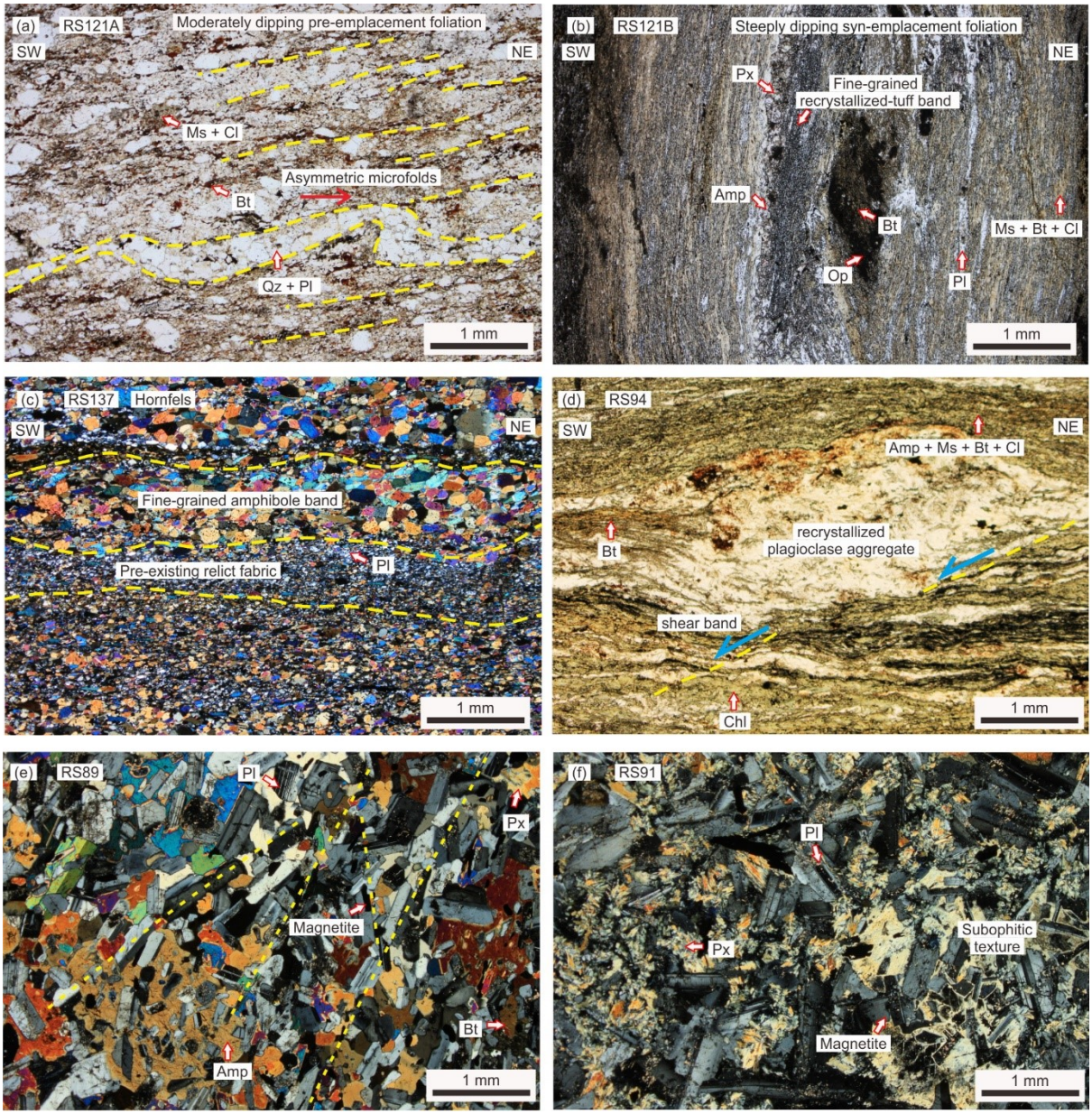


**Figure 9.** *Representative microstructures and fabric types of the Kdyně pluton and its host rock. (a) Pre-emplacement foliation with recrystallized plagioclase and quartz forming bands with asymmetric microfolds; Úlíkov [WGS84 coordinates: 49°25'51.916"N, 13°3'43.717"E]. (b) Syn-emplacement fabric composed of biotite, chlorite, and a thin layer of recrystallized plagioclase, the protolith was presumably a fine-grained recrystallized tuff. Minerals grains are aligned due to the syn-emplacement deformation; Úlíkov [WGS84 coordinates: 49°25'47.894"N, 13°3'45.036"E]. (c) Fine-grained amphibole and layer of recrystallized plagioclase overprinted the original fabric (probably a mafic rock); Bezný [WGS84 coordinates: 49°22'31.225"N, 13°2'6.450"E]. (d) Slightly asymmetric recrystallized plagioclase aggregate cross-cut by shear planes (blue arrows), indicating the post-emplacement deformation. The hornfelsic rock consists of amphibole, muscovite, altered biotite, and chlorite indicate the pinitization; Soběnec [WGS84 coordinates: 49°22'20.963"N, 13°7'47.285"E]. (e) and (f) are diorite–gabbro samples dominated by elongated to skeletal plagioclase, pyroxene, and amphibole. No solid-state deformation was observed. (e) Aligned magnetite grains within a strong plagioclase foliation (yellow dashed*

*line); U Linharta [WGS84 coordinates: 49°25'49.414"N, 13°5'57.958"E]. (f) A subophitic texture defined by skeletal plagioclase. Abundant pyroxene is found between grain contacts and transformed into chlorite; Špandava [WGS84 coordinates: 49°23'27.726"N, 13°5'17.002"E]. Mineral abbreviations: Amp = amphibole, Bt = biotite, Chl = chlorite, Ms = muscovite, Pl = plagioclase, Px = Pyroxene, Qz = quartz; photomicrographs in (c), (e), and (f) were taken with crossed polars, (a), (b), and (d) in plane-polarized light.*

---

### *4.1.4. Material and sampling strategy of AMS*

The AMS samples were collected using a hand-held gasoline-powered drill at 6 stations in the Kdyně pluton and 14 stations in the host rock. The oriented cores were cut into 94 (Kdyně pluton) and 126 (host rocks) standard cylindrical specimens (2.1 cm high and 2.5 cm in diameter), corresponding to 4–22 specimens per station. Note that the number of specimens depends on outcrop conditions such as the intensity of fracturing and weathering.

The specimens were measured in the Laboratory of Rock Magnetism, Institute of Geology and Paleontology, Charles University, Prague, using an Agico MFK1-A Multi-function Kappabridge, which was supported by the Safyr 7.0 instrument control software and analyzed using the Anisoft 5 software (Chadima and Jelínek, 2008; Jelínek, 1978; Hrouda et al., 1990). A complete list of the measured AMS parameters can be found in the Tab. 1 and 2.

**Table 1.** *AMS parameters on each specimen of the host rock.*

| Station | Specimen | *P* | *T* | $K_m$ | $K_1$-*Dec* | $K_1$-*Inc* | $K_3$-*Dec* | $K_3$-*Inc* |
|---|---|---|---|---|---|---|---|---|
| **RS87** | RS87-1-1 | 1.0183 | 0.0163 | 4.09E-04 | 11.7 | 65 | 160.5 | 21.7 |
| | RS87-1-2 | 1.0153 | -0.2493 | 3.87E-04 | 11.8 | 59.6 | 142.1 | 20.8 |
| | RS87-2-1 | 1.0237 | 0.4502 | 4.27E-04 | 248.9 | 48.3 | 138.1 | 17.5 |
| | RS87-2-2 | 1.0133 | 0.361 | 2.49E-04 | 250.4 | 29.5 | 146.4 | 23 |
| | RS87-3-1 | 1.0195 | -0.0158 | 3.18E-04 | 274 | 52.7 | 163.7 | 14.8 |
| | RS87-3-2 | 1.0184 | 0.2752 | 3.46E-04 | 260.6 | 31.5 | 162.2 | 13.5 |
| | RS87-4-1 | 1.0188 | -0.1863 | 4.17E-04 | 22.8 | 66.9 | 152.7 | 15.3 |
| | RS87-4-2 | 1.015 | 0.0138 | 3.33E-04 | 40.7 | 44.9 | 154 | 21.6 |
| | RS87-5-1 | 1.018 | 0.3654 | 3.61E-04 | 15.6 | 63.6 | 139.7 | 15.6 |
| | RS87-5-2 | 1.0179 | -0.0042 | 4.16E-04 | 15.2 | 59.9 | 132.1 | 14.7 |
| **RS94** | RS94-1-1 | 1.099 | 0.8028 | 8.32E-04 | 122.3 | 46.6 | 297.9 | 43.3 |
| | RS94-1-2 | 1.1661 | 0.3603 | 9.39E-04 | 133.9 | 48.8 | 304.4 | 40.8 |
| | RS94-1-3 | 1.2348 | 0.1752 | 1.17E-03 | 134.4 | 50.7 | 306.4 | 39 |

| | | | | | | | | |
|---|---|---|---|---|---|---|---|---|
| | RS94-1-4 | 1.1444 | 0.4908 | 9.47E-04 | 143.9 | 47.4 | 300.1 | 40 |
| | RS94-1-5 | 1.0912 | 0.8327 | 7.77E-04 | 128.7 | 44.8 | 298.7 | 44.7 |
| | RS94-2-1 | 1.2188 | 0.0534 | 1.06E-03 | 126.6 | 56.2 | 322.8 | 32.8 |
| | RS94-2-2 | 1.3885 | -0.2287 | 2.26E-03 | 139 | 62.5 | 336 | 26.5 |
| | RS94-2-3 | 1.3565 | -0.0118 | 2.10E-03 | 141.9 | 58.7 | 333.9 | 30.8 |
| | RS94-2-4 | 1.2859 | -0.0655 | 1.53E-03 | 126.1 | 57.6 | 332 | 29.7 |
| | RS94-2-5 | 1.0791 | 0.6785 | 8.27E-04 | 118.9 | 62.4 | 329.1 | 24.3 |
| **RS99** | RS99-1-1 | 1.4633 | -0.1467 | 3.03E-03 | 75.8 | 55.3 | 282.9 | 31.6 |
| | RS99-I-1-1 | 1.1314 | -0.4539 | -4.18E-03 | 22.3 | 23.5 | 287.8 | 10.4 |
| | RS99-I-1-2 | 1.0728 | -0.3273 | -4.48E-03 | 317.5 | 68 | 144.7 | 21.8 |
| | RS99-I-2-1 | 1.3096 | -0.3476 | -4.05E-03 | 270.9 | 50.8 | 37.5 | 25.9 |
| | RS99-I-2-2 | 1.1935 | -0.6454 | -3.58E-03 | 250 | 51 | 121.9 | 26.5 |
| | RS99-I-3-1 | 1.1013 | 0.0167 | -6.43E-03 | 33.1 | 35.1 | 290.1 | 17.8 |
| **RS100** | RS100-1-1 | 2.1397 | 0.9283 | 1.83E-05 | 169.7 | 31.7 | 65.6 | 21.5 |
| | RS100-1-2 | 1.2071 | 0.5638 | -2.23E-03 | 348.4 | 0.8 | 78.6 | 15.3 |
| | RS100-1-3 | 1.0753 | -0.7172 | -5.52E-03 | 213.6 | 0.7 | 123.3 | 22.1 |
| | RS100-2-1 | 1.0816 | -0.097 | 7.34E-03 | 325.9 | 47.9 | 102.1 | 33.1 |
| | RS100-3-1 | 2.3187 | 0.4545 | 3.73E-05 | 342.3 | 67.6 | 238 | 5.8 |
| | RS100-3-2 | 3.2466 | -0.5734 | -1.12E-03 | 185.5 | 23.3 | 92 | 8.1 |
| | RS100-4-1 | 3.3062 | 0.0216 | -1.86E-03 | 236.1 | 31 | 139 | 11.8 |
| | RS100-5-1 | 1.1454 | -0.014 | 1.95E-05 | 272.1 | 78.8 | 142.7 | 7.2 |
| **RS104** | RS104-1-1 | 1.2203 | 0.9265 | 2.81E-04 | 227.2 | 47.6 | 135.1 | 1.9 |
| | RS104-1-2 | 1.2044 | 0.8818 | 2.62E-04 | 226.2 | 32.5 | 134.5 | 2.7 |
| | RS104-1-3 | 1.1887 | 0.9266 | 2.45E-04 | 226 | 18.9 | 135.9 | 0.2 |
| | RS104-1-4 | 1.1649 | 0.8798 | 1.29E-04 | 224.2 | 21.3 | 133.8 | 1.2 |
| | RS104-1-5 | 1.1623 | 0.8697 | 1.16E-04 | 219.6 | 20.3 | 310.6 | 2.8 |
| | RS104-1-6 | 1.1558 | 0.9102 | 1.15E-04 | 44.8 | 26.8 | 311.6 | 6.2 |
| | RS104-1-7 | 1.1222 | 0.9274 | 8.82E-05 | 225.4 | 7.1 | 315.8 | 3.6 |
| | RS104-2-2 | 1.1502 | 0.943 | 9.89E-05 | 217.8 | 48.3 | 124 | 3.4 |
| | RS104-2-3 | 1.1562 | 0.8953 | 1.35E-04 | 212.1 | 17.8 | 121.9 | 0.8 |
| | RS104-2-4 | 1.1533 | 0.8127 | 1.09E-04 | 27.7 | 77.2 | 118.6 | 0.2 |
| | RS104-2-5 | 1.1437 | 0.8274 | 8.20E-05 | 27.5 | 53.3 | 117.8 | 0.2 |
| **RS110B** | RS110B-1-1 | 1.1655 | 0.236 | 6.29E-04 | 111.9 | 64.6 | 207.8 | 2.8 |
| | RS110B-1-2 | 1.178 | 0.2942 | 7.65E-04 | 116.8 | 61.6 | 207.4 | 0.3 |
| | RS110B-1-3 | 1.1792 | 0.2007 | 8.12E-04 | 117.2 | 68.8 | 210.8 | 1.4 |
| | RS110B-1-4 | 1.1802 | 0.1614 | 9.92E-04 | 113.9 | 69.8 | 210 | 2.2 |
| | RS110B-2-1 | 1.1903 | 0.1308 | 8.44E-04 | 194.1 | 58.3 | 291.4 | 4.5 |
| | RS110B-2-2 | 1.1627 | 0.2357 | 6.08E-04 | 218.6 | 65.7 | 118 | 4.8 |
| | RS110B-2-3 | 1.1165 | 0.3162 | 3.59E-04 | 218.9 | 68.1 | 113.8 | 6 |
| | RS110B-2-4 | 1.1167 | 0.4288 | 3.16E-04 | 217.4 | 68.1 | 108.1 | 7.6 |
| **RS113** | RS113-1-1 | 1.1295 | 0.4462 | 3.46E-04 | 341.7 | 33.5 | 129 | 51.8 |
| | RS113-1-2 | 1.0601 | 0.527 | 3.69E-04 | 312.2 | 43.9 | 117.4 | 45.1 |
| | RS113-1-3 | 1.0545 | 0.5152 | 3.42E-04 | 323.3 | 38.6 | 120.8 | 49.2 |
| | RS113-2-1 | 1.069 | -0.5138 | 3.82E-04 | 345 | 35.8 | 137 | 50.7 |
| | RS113-2-2 | 1.084 | 0.5795 | 3.72E-04 | 333.4 | 35.9 | 123.4 | 50.2 |

| | | | | | | | | |
|---|---|---|---|---|---|---|---|---|
| | RS113-2-3 | 1.0329 | 0.6864 | 3.28E-04 | 307.9 | 38.9 | 120.4 | 50.9 |
| | RS113-2-4 | 1.0228 | 0.4723 | 3.25E-04 | 341.8 | 16.5 | 177.6 | 72.9 |
| | RS113-2-5 | 1.046 | 0.6004 | 3.61E-04 | 312.6 | 35.8 | 130.2 | 54.2 |
| | RS113-2-6 | 1.0484 | 0.5105 | 2.82E-04 | 297.6 | 36.5 | 129.2 | 52.9 |
| **RS117** | RS117-I-1-1 | 1.0231 | 0.286 | 5.93E-04 | 328 | 58.6 | 125.5 | 29.5 |
| | RS117-I-2-1 | 1.0176 | 0.8034 | 5.28E-04 | 223.2 | 51.7 | 59.7 | 37.1 |
| | RS117-I-2-2 | 1.0136 | -0.0833 | 4.52E-04 | 357.9 | 67.1 | 216.8 | 18.2 |
| | RS117-I-3-1 | 1.0212 | 0.4177 | 4.98E-04 | 267.8 | 34.7 | 24.5 | 33 |
| | RS117-I-3-2 | 1.023 | -0.2948 | 5.76E-04 | 6.4 | 52.8 | 159.2 | 34 |
| | RS117-II-1-1 | 1.0175 | -0.5124 | 5.80E-04 | 141.6 | 40.6 | 253.9 | 23.8 |
| | RS117-II-2-1 | 1.0153 | -0.4656 | 5.31E-04 | 331.2 | 67.4 | 229.8 | 4.7 |
| | RS117-II-2-2 | 1.0153 | 0.3486 | 4.69E-04 | 279.9 | 58.9 | 39.3 | 16.4 |
| | RS117-II-3-1 | 1.0224 | -0.3738 | 6.03E-04 | 265.9 | 55.9 | 44.2 | 26.8 |
| | RS117-II-3-2 | 1.023 | 0.0757 | 5.80E-04 | 259.7 | 73.7 | 110.9 | 14 |
| **RS121A** | RS121A-1-1 | 1.130 | 0.4828 | 2.42E-04 | 118.8 | 42.9 | 271.5 | 43.7 |
| | RS121A-1-2 | 1.112 | 0.2766 | 2.48E-04 | 137.5 | 30 | 273.4 | 51.3 |
| | RS121A-1-3 | 1.095 | 0.4496 | 2.39E-04 | 135.9 | 34.1 | 258.5 | 38.5 |
| | RS121A-1-4 | 1.099 | 0.5695 | 2.24E-04 | 137.3 | 33.2 | 259.9 | 39.4 |
| | RS121A-1-5 | 1.098 | 0.5596 | 2.16E-04 | 139.7 | 35 | 270.3 | 43 |
| | RS121A-1-6 | 1.111 | 0.5662 | 2.27E-04 | 118.9 | 44.2 | 266.2 | 40.9 |
| | RS121A-1-7 | 1.166 | 0.5839 | 1.95E-04 | 137.7 | 29.4 | 255.5 | 39.6 |
| | RS121A-2-1 | 1.131 | 0.4888 | 1.70E-04 | 131.9 | 35.3 | 274.8 | 48.4 |
| | RS121A-2-2 | 1.128 | 0.6061 | 1.71E-04 | 126.4 | 38.2 | 268.3 | 45 |
| | RS121A-2-3 | 1.125 | 0.6523 | 1.75E-04 | 123.5 | 35.1 | 269.9 | 49.9 |
| | RS121A-2-4 | 1.131 | 0.709 | 1.68E-04 | 120.8 | 39.1 | 267.2 | 45.7 |
| | RS121A-2-5 | 1.131 | 0.5908 | 2.12E-04 | 118.6 | 45.6 | 264.6 | 39 |
| | RS121A-2-6 | 1.118 | 0.4427 | 1.79E-04 | 117.3 | 43.8 | 257.2 | 38.6 |
| | RS121A-2-7 | 1.165 | 0.2104 | 3.10E-04 | 132.3 | 32.4 | 260.2 | 44 |
| **RS121B** | RS121B-1-1 | 1.105 | 0.3729 | 5.31E-04 | 35.6 | 61.9 | 293 | 6.6 |
| | RS121B-1-2 | 1.119 | -0.3122 | 4.96E-04 | 42.5 | 70.1 | 256.1 | 16.8 |
| | RS121B-1-3 | 1.078 | 0.5667 | 4.83E-04 | 29 | 56.4 | 285.1 | 9.1 |
| | RS121B-1-4 | 1.069 | 0.613 | 4.48E-04 | 34.4 | 57.9 | 287.7 | 10.2 |
| | RS121B-1-5 | 1.060 | 0.3261 | 4.26E-04 | 23.9 | 48.9 | 283.3 | 9.2 |
| | RS121B-2-1 | 1.093 | 0.2746 | 4.56E-04 | 26.6 | 70.7 | 280.4 | 5.6 |
| | RS121B-2-2 | 1.115 | 0.5208 | 4.50E-04 | 32.6 | 70.7 | 277.8 | 8.3 |
| | RS121B-2-3 | 1.102 | 0.3762 | 4.74E-04 | 36.6 | 67.4 | 288.5 | 7.4 |
| | RS121B-2-4 | 1.087 | 0.5644 | 4.58E-04 | 30 | 53.7 | 281.8 | 12.9 |
| | RS121B-2-5 | 1.091 | 0.5779 | 5.12E-04 | 29.6 | 56 | 284 | 10.3 |
| | RS121B-2-6 | 1.094 | 0.8282 | 3.26E-04 | 21.3 | 49.4 | 280.3 | 9.3 |
| **RS126** | RS126-1-1 | 1.7616 | 0.8607 | 6.34E-03 | 59.3 | 18.5 | 186 | 60.8 |
| | RS126-1-2 | 1.8857 | 0.7822 | 7.39E-03 | 86.4 | 9.8 | 195.9 | 62.7 |
| | RS126-1-3 | 1.8778 | 0.8516 | 8.63E-03 | 97.4 | 8.2 | 203.9 | 63.1 |
| | RS126-1-4 | 1.8066 | 0.8892 | 6.84E-03 | 115.1 | 2.7 | 209.8 | 60.2 |
| | RS126-2-1 | 1.81 | 0.9379 | 5.96E-03 | 267.2 | 10 | 161.6 | 56.7 |
| | RS126-2-2 | 1.8469 | 0.7601 | 7.92E-03 | 279.1 | 12.8 | 163.2 | 62.5 |
| | RS126-2-3 | 1.8272 | 0.6953 | 9.08E-03 | 285.6 | 14.3 | 164.1 | 64 |

| | | | | | | | | |
|---|---|---|---|---|---|---|---|---|
| | RS126-2-4 | 1.8484 | 0.5874 | 7.44E-03 | 285.6 | 11.6 | 167.2 | 66.7 |
| | RS126-2-5 | 1.7741 | 0.5165 | 8.94E-03 | 280.9 | 14.8 | 163.3 | 60.3 |
| **RS132** | RS132-I-1-1 | 1.0629 | -0.2018 | 4.94E-04 | 285.6 | 59.5 | 193 | 1.5 |
| | RS132-I-2-1 | 1.0857 | 0.2153 | 6.50E-04 | 294.5 | 55.5 | 203.1 | 0.9 |
| | RS132-I-2-2 | 1.0836 | -0.064 | 5.66E-04 | 303.1 | 54.4 | 168.4 | 26.8 |
| | RS132-I-3-1 | 1.076 | 0.1016 | 6.24E-04 | 300.4 | 65.5 | 192 | 8.2 |
| | RS132-I-4-1 | 1.0827 | 0.1302 | 8.08E-04 | 289.2 | 43.9 | 175.8 | 22.3 |
| **RS136** | RS136-1-1 | 1.069 | 0.3103 | 1.62E-04 | 3.9 | 1 | 273.8 | 1.2 |
| | RS136-1-2 | 1.0827 | 0.4116 | 1.33E-04 | 177.9 | 3.4 | 87 | 13.5 |
| | RS136-2-1 | 1.0745 | 0.6527 | 1.84E-04 | 12.6 | 0.5 | 282.6 | 6.3 |
| | RS136-2-2 | 1.0947 | 0.7292 | 1.38E-04 | 10.9 | 9.7 | 280.1 | 4.5 |
| **RS138** | RS138-1-1 | 2.1625 | 0.8049 | 5.91E-03 | 191.6 | 3.6 | 92.1 | 69.2 |
| | RS138-1-2 | 1.9713 | 0.7874 | 7.53E-03 | 195.6 | 8.5 | 88.9 | 62.5 |
| | RS138-1-3 | 1.5919 | 0.9203 | 5.70E-03 | 251.2 | 30 | 75 | 59.9 |
| | RS138-1-3 | 1.7373 | 0.8098 | 6.97E-03 | 251 | 23.7 | 63.3 | 66.1 |
| | RS138-1-4 | 1.6305 | 0.5616 | 3.83E-03 | 202.2 | 8.4 | 96 | 62.2 |
| | RS138-1-4 | 1.6888 | 0.9284 | 4.62E-03 | 193 | 10.2 | 83.9 | 61.2 |
| | RS138-2-1 | 1.6312 | 0.8026 | 3.82E-03 | 205.7 | 21.2 | 81.4 | 55.5 |
| | RS138-2-2 | 1.611 | 0.7137 | 6.87E-03 | 191.1 | 12 | 81.3 | 57.8 |
| | RS138-2-5 | 1.6659 | 0.8416 | 4.73E-03 | 191.1 | 8.6 | 87.6 | 57.1 |
| | RS138-2-6 | 1.7059 | 0.7258 | 1.10E-02 | 6.6 | 1.9 | 100.1 | 61.4 |

**Table 2.** *AMS parameters on each specimen of the pluton.*

| Station | Specimen | *P* | *T* | $K_m$ | $K_1$-*Dec* | $K_1$-*Inc* | $K_3$-*Dec* | $K_3$-*Inc* |
|---|---|---|---|---|---|---|---|---|
| **RS78** | RS78-1-1 | 1.0333 | 0.4778 | 3.79E-04 | 326 | 51.9 | 124.1 | 36.1 |
| | RS78-1-2 | 1.0145 | -0.098 | 3.87E-04 | 276.6 | 27.1 | 167.2 | 33 |
| | RS78-1-3 | 1.0125 | 0.7619 | 3.73E-04 | 306.6 | 54.3 | 169.7 | 27.7 |
| | RS78-1-4 | 1.0142 | 0.7047 | 3.53E-04 | 340.5 | 61 | 164.3 | 29 |
| | RS78-2-1 | 1.0201 | 0.1221 | 3.48E-04 | 291.4 | 53.9 | 132.5 | 34.2 |
| | RS78-2-2 | 1.0109 | 0.0598 | 3.73E-04 | 273.9 | 18.5 | 168 | 39.4 |
| | RS78-2-3 | 1.0135 | 0.5332 | 3.90E-04 | 353.3 | 54.4 | 160.3 | 34.9 |
| | RS78-2-4 | 1.0154 | 0.5322 | 3.41E-04 | 322.3 | 54.3 | 160.9 | 34.2 |
| | RS78-2-5 | 1.0183 | 0.5122 | 3.19E-04 | 312.5 | 56.8 | 162.9 | 29.4 |
| **RS89** | RS89-1-1 | 1.0083 | -0.1135 | 3.96E-04 | 318.1 | 38.5 | 55.2 | 8.8 |
| | RS89-1-2 | 1.01 | -0.1506 | 4.39E-04 | 282.2 | 37.3 | 109.3 | 52.5 |
| | RS89-2-1 | 1.006 | 0.4392 | 4.82E-04 | 315.9 | 32.2 | 219.1 | 10.7 |
| | RS89-2-2 | 1.0047 | -0.9632 | 5.34E-04 | 53.4 | 15.5 | 187.3 | 68.2 |
| | RS89-2-3 | 1.0077 | 0.5589 | 4.10E-04 | 246.1 | 27.9 | 48 | 60.9 |
| | RS89-2-4 | 1.0094 | 0.0989 | 4.12E-04 | 210.8 | 21.7 | 68.6 | 63.3 |
| | RS89-2-5 | 1.0105 | -0.0046 | 3.79E-04 | 259.9 | 26.3 | 47.7 | 59.7 |
| | RS89-3-1 | 1.0063 | -0.2729 | 4.61E-04 | 263.3 | 4 | 169.9 | 39.6 |
| | RS89-3-2 | 1.0079 | 0.398 | 4.51E-04 | 315.4 | 13 | 51.3 | 24.1 |
| | RS89-3-3 | 1.0049 | 0.344 | 3.34E-04 | 332.2 | 13.9 | 71.9 | 34 |

| | | | | | | | | |
|---|---|---|---|---|---|---|---|---|
| **RS91** | RS91-2-1 | 1.0235 | 0.0242 | 6.22E-04 | 246.3 | 26.3 | 337.1 | 1.7 |
| | RS91-2-2 | 1.0279 | -0.015 | 6.58E-04 | 236.9 | 20.2 | 332.4 | 14.4 |
| | RS91-2-3 | 1.0306 | 0.2929 | 6.00E-04 | 235.2 | 6.4 | 325.8 | 5.4 |
| | RS91-2-4 | 1.0332 | 0.4723 | 6.82E-04 | 243 | 25.9 | 333.3 | 0.7 |
| | RS91-2-5 | 1.0297 | 0.5608 | 5.95E-04 | 236.4 | 16 | 327.6 | 4.2 |
| | RS91-2-6 | 1.0317 | 0.5415 | 5.87E-04 | 238.4 | 10.4 | 328.7 | 1.7 |
| | RS91-2-7 | 1.0469 | 0.7343 | 6.27E-04 | 249 | 21.6 | 340.3 | 3.2 |
| | RS91A-1-1 | 1.0052 | 0.6819 | 5.39E-04 | 29.4 | 0.7 | 299.2 | 11.7 |
| | RS91A-1-3 | 1.0146 | 0.144 | 5.79E-04 | 208.9 | 63.4 | 6.1 | 24.8 |
| | RS91A-1-4 | 1.0092 | 0.4979 | 4.73E-04 | 211.2 | 37.3 | 306.4 | 6.8 |
| | RS91A-1-5 | 1.0064 | 0.6048 | 5.43E-04 | 192.4 | 44.4 | 288 | 5.6 |
| | RS91A-1-8 | 1.0075 | 0.3938 | 5.82E-04 | 177.2 | 46 | 289.7 | 20.3 |
| | RS91A-1-9 | 1.0053 | 0.6999 | 5.64E-04 | 191.9 | 37.6 | 281.9 | 0 |
| | RS91A-2-1 | 1.0046 | -0.8836 | 5.06E-04 | 173.4 | 37.1 | 79.9 | 4.7 |
| | RS91A-2-3 | 1.0082 | 0.3066 | 5.31E-04 | 231.8 | 48.9 | 130.4 | 9.8 |
| | RS91A-3-1 | 1.0054 | -0.1782 | 4.95E-04 | 187.7 | 31.4 | 282.2 | 7.3 |
| | RS91A-3-2 | 1.0083 | 0.3191 | 5.33E-04 | 175.9 | 2.5 | 266.3 | 11.2 |
| | RS91A-4-1 | 1.0058 | 0.0401 | 5.42E-04 | 231.5 | 26.2 | 340.3 | 33.2 |
| **RS119** | RS119-1-1 | 1.0712 | 0.5964 | 6.67E-05 | 39.9 | 60.7 | 248.7 | 26.2 |
| | RS119-1-2 | 1.0863 | 0.4509 | 6.42E-05 | 43.9 | 59 | 250.9 | 28.2 |
| | RS119-1-3 | 1.1036 | 0.5903 | 6.32E-05 | 32.9 | 53.1 | 248.3 | 31.4 |
| | RS119-1-4 | 1.0843 | 0.4408 | 5.52E-05 | 35.9 | 55.2 | 240.4 | 32.3 |
| | RS119-1-5 | 1.079 | 0.2834 | 5.46E-05 | 44.3 | 54.3 | 250 | 32.9 |
| | RS119-1-6 | 1.0787 | -0.0644 | 6.12E-05 | 59.9 | 55.1 | 265.5 | 32.2 |
| | RS119-1-7 | 1.0681 | 0.2595 | 4.88E-05 | 57.1 | 57 | 245.7 | 32.7 |
| | RS119-2-1 | 1.1042 | 0.4749 | 3.41E-05 | 37.9 | 51.5 | 245.7 | 35.2 |
| | RS119-2-2 | 1.1493 | 0.7389 | 3.47E-05 | 25.9 | 45.5 | 249.2 | 35.6 |
| | RS119-2-3 | 1.1641 | 0.8614 | 3.79E-05 | 7.9 | 36.3 | 250.8 | 31.8 |
| | RS119-2-4 | 1.1064 | 0.6319 | 2.60E-05 | 35.4 | 48.8 | 255.3 | 33.9 |
| **RS144** | RS144-1-1 | 1.0128 | -0.106 | 3.64E-04 | 238.7 | 55.5 | 100.8 | 27 |
| | RS144-1-2 | 1.0172 | 0.305 | 2.75E-04 | 246.9 | 62.6 | 90.6 | 25.3 |
| | RS144-1-3 | 1.0164 | 0.237 | 3.47E-04 | 215.3 | 57.7 | 87.6 | 21.1 |
| | RS144-1-4 | 1.0136 | 0.4914 | 5.11E-04 | 256.6 | 72.6 | 87 | 17.2 |
| | RS144-1-5 | 1.0137 | 0.5822 | 5.58E-04 | 219.6 | 53.7 | 87.6 | 26.2 |
| | RS144-1-6 | 1.0138 | 0.2327 | 4.40E-04 | 239.2 | 21.1 | 84.8 | 66.8 |
| | RS144-2-1 | 1.0126 | -0.7 | 5.06E-04 | 142.9 | 60.9 | 256.7 | 12.7 |
| | RS144-2-2 | 1.0163 | -0.2821 | 4.91E-04 | 155.1 | 66.9 | 0.3 | 21.1 |
| | RS144-3-1 | 1.0081 | -0.3775 | 5.40E-04 | 290.4 | 36 | 117.7 | 53.8 |
| | RS144-3-2 | 1.0058 | -0.2023 | 3.30E-04 | 301.9 | 33.7 | 169.3 | 45.4 |
| **RS145** | RS145-1-1 | 1.2688 | 0.3406 | 2.03E-03 | 286.1 | 60.4 | 50.1 | 17.6 |
| | RS145-1-2 | 1.1485 | 0.3599 | 1.55E-03 | 240.2 | 51.9 | 126 | 17.8 |
| | RS145-1-3 | 1.111 | 0.1128 | 1.85E-03 | 233.3 | 26.2 | 116.2 | 42.8 |
| | RS145-1-4 | 1.1304 | -0.8681 | 1.62E-03 | 244.8 | 46.2 | 1.1 | 23 |
| | RS145-1-5 | 1.1282 | -0.7471 | 1.49E-03 | 237.6 | 54.1 | 329.7 | 1.5 |
| | RS145-1-6 | 1.1431 | -0.1707 | 1.35E-03 | 220.2 | 26.2 | 25.1 | 63 |
| | RS145-1-7 | 1.1082 | -0.4206 | 1.07E-03 | 243.8 | 44.1 | 33.3 | 41.7 |

| | | | | | | | | |
|---|---|---|---|---|---|---|---|---|
| | RS145-2-1 | 1.1186 | 0.1981 | 8.72E-04 | 189.8 | 7.1 | 97.9 | 14.5 |
| | RS145-2-2 | 1.0127 | 0.1392 | 9.38E-04 | 219.2 | 26 | 4 | 59.2 |
| | RS145-2-3 | 1.0142 | 0.0988 | 8.56E-04 | 210.7 | 33.6 | 328 | 34.6 |
| | RS145-2-4 | 1.0132 | -0.6417 | 8.70E-04 | 188.8 | 36.7 | 29.6 | 51.4 |
| | RS145-2-5 | 1.0454 | -0.5756 | 1.04E-03 | 225.9 | 47 | 124.5 | 10.4 |
| | RS145-2-6 | 1.0399 | -0.651 | 8.51E-04 | 192.5 | 30.4 | 95 | 12.6 |
| | RS145-3-1 | 1.1584 | -0.0023 | 7.46E-04 | 219.3 | 42.1 | 18 | 45.9 |
| | RS145-3-2 | 1.1816 | -0.1236 | 7.78E-04 | 214.9 | 43.4 | 22.4 | 45.9 |
| | RS145-3-3 | 1.1855 | -0.1313 | 7.15E-04 | 219.2 | 42.1 | 24.7 | 47 |
| | RS145-3-4 | 1.1644 | -0.3058 | 5.19E-04 | 228.8 | 43.4 | 16 | 41.7 |
| | RS145-3-5 | 1.1551 | -0.4531 | 5.21E-04 | 236.6 | 47.5 | 13.7 | 33.9 |
| | RS145-4-1 | 1.1753 | -0.3609 | 5.73E-04 | 207.7 | 51.6 | 357.8 | 34.5 |
| | RS145-4-2 | 1.1611 | -0.3114 | 5.55E-04 | 207.9 | 51.5 | 346.8 | 30.9 |
| | RS145-4-3 | 1.1469 | -0.1593 | 5.60E-04 | 212.4 | 47.8 | 3.3 | 38.4 |
| | RS145-4-4 | 1.1395 | -0.2212 | 5.44E-04 | 212.8 | 43.1 | 352.2 | 39.1 |

#### *4.1.5. Scalar AMS parameters and their statistical distribution*

The mean (bulk) susceptibility of the measured specimens (from both the pluton and its host rock) ranges from $-10^{-3}$ to $10^{-3}$, but is dominated by $10^{-5}$ (N=18, 8 % of the total) and $10^{-4}$ values (N=151, 69 % of the total), corresponding to paramagnetic minerals. Forty-one specimens (19 % of the total) exhibit bulk susceptibility on the order of $10^{-3}$ (Fig. 10a) corresponding to ferromagnetic minerals. The remaining 9 specimens (4 % of the total) are specific for their negative bulk susceptibilities, corresponding to diamagnetic minerals.

The *P*–*T* data for the host rock specimens can be divided into the low-*P* and high-*P* groups based on their degree of anisotropy: the low degree of anisotropy ($P < 1.5$) is associated with oblate to prolate AMS ellipsoids and low bulk susceptibility, whereas the higher-*P* group (> 1.5) is characterized by highly oblate ($T > 0.5$) AMS ellipsoid and high bulk susceptibility (Fig. 5b). In the pluton, the low-*P* group (< 1.05) ranges from oblate to prolate and low bulk susceptibility, whereas the high-*P* group (>1.05) has a wide range of shape parameter and bulk susceptibility values (oblate to prolate AMS ellipsoid; Fig. 10b).

In general, the *P* and *T* parameters on the map do not show any noticeable gradient over the sampled area. It can only be observed that the degree of anisotropy increases with increasing bulk susceptibility in the host rock of the middle and southern domains (specimens RS113, RS110B, RS94) and that the low degree of anisotropy and oblate ellipsoids are dominant in the Kdyně pluton (Fig. 11).

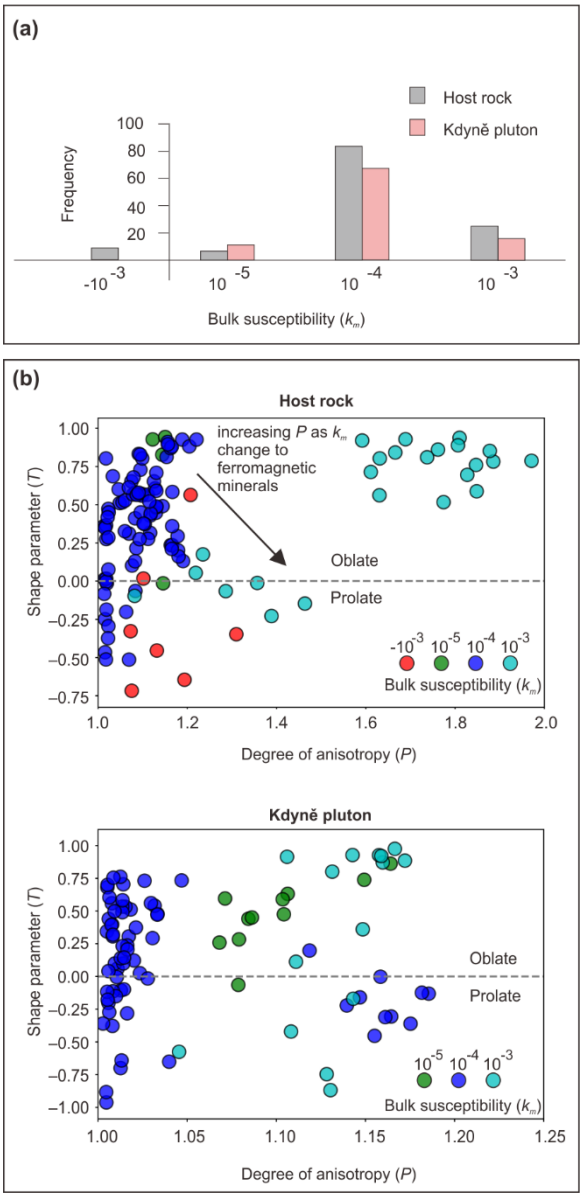


***Figure 10.*** *(a) Histogram of the mean (bulk) susceptibility of all specimens taken in the Kdyně pluton and its host rock. (b) The Jelínek P–T plot of all specimens taken in the Kdyně pluton and its host rock color-coded according to the bulk susceptibility.*

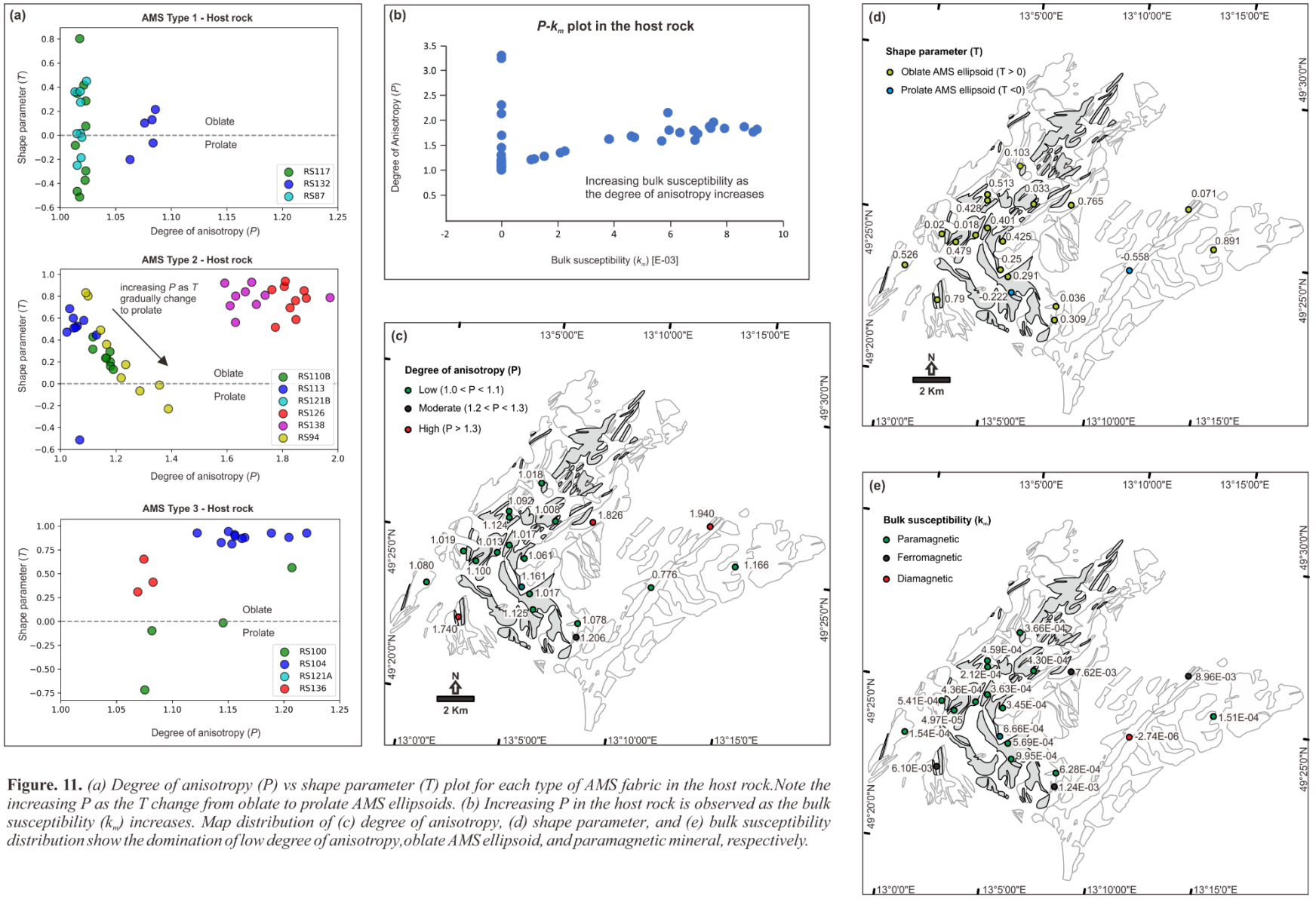


**Figure. 11.** *(a) Degree of anisotropy (P) vs shape parameter (T) plot for each type of AMS fabric in the host rock.Note the increasing P as the T change from oblate to prolate AMS ellipsoids. (b) Increasing P in the host rock is observed as the bulk susceptibility ($k_m$) increases. Map distribution of (c) degree of anisotropy, (d) shape parameter, and (e) bulk susceptibility distribution show the domination of low degree of anisotropy,oblate AMS ellipsoid, and paramagnetic mineral, respectively.*

### *4.1.6. Magnetic mineralogy*

The AMS carriers were investigated in detail through thermomagnetic measurements, and the results of this analysis are plotted as temperature–bulk susceptibility ($T$–$k_m$) curves. The measurements were performed using the CS-L Cryostat and the CS4 furnace units connected to an MFK1-A Kappabridge (Hrouda, 1994; Hrouda et al., 1997; Jelínek & Pokorný, 1997). The Saphyr 7 program (www.agico.com; Hrouda et al., 1997) was used to measure and monitor the bulk susceptibility of representative specimens in three steps over a temperature range between ca. –196 °C and 700 °C. The first step consisted of cooling the specimens down to ca. –196 °C using the liquid nitrogen and subsequent spontaneous heating to approximately 5 °C. The second step included heating the specimens from room temperature to ~700 °C and then cooling them back down to ~40 °C at an approximate controlled rate of 14 °C/min in an argon atmosphere to minimize mineral oxidation. The final step involved cooling to –196 °C again using liquid nitrogen.

Six specimens for thermomagnetic analysis were selected to cover both host rock and plutonic samples and also to cover a wide range of the $P$, $T$, and $k_m$ values (Fig. 10b). In the host rock, specimen RS94-1-4 represents the most common paramagnetic lithology ($k_m = 10^{-4}$) with a relatively low degree of anisotropy ($P = 1.144$) and oblate ($T = 0.490$) AMS ellipsoid. Another specimen (RS100-1-1) was selected for its intriguing high degree of anisotropy ($P = 2.140$) at the bulk susceptibility on the order of $10^{-5}$ and highly oblate AMS ellipsoid ($T = 0.928$). A weakly ferromagnetic specimen RS94-1-3 ($k_m = 1.7 \times 10^{-3}$) with $P = 1.235$ and $T = 0.175$ was also measured. In the Kdyně pluton, specimens RS144-1-2 and RS145-4-4 have bulk susceptibility of $10^{-4}$. The former has a low degree of anisotropy ($P = 1.017$) and oblate AMS ellipsoid ($T = 0.305$), while the latter specimen has a higher degree of anisotropy ($P = 1.139$) and prolate ellipsoid shape ($T = –0.221$). Another measured specimen was RS119-1-4,

which has a low bulk susceptibility ($k_m = 10^{-5}$), low degree of anisotropy ($P = 1.084$), and oblate AMS ellipsoid ($T = 0.441$).

The temperature vs. magnetic susceptibility plots ($T$- $k_m$) show the dominant of the hyperbolic decrease curves during the heating stage (Fig. 12). An increase of magnetic susceptibility on the heating and cooling curves occurred as the Curie temperature of magnetite approached (between 483 and 538 °C). This bulk susceptibility increment is much higher during cooling than heating (except in RS145-4-4), suggesting artificial growth of new magnetite (Fe–Ti phase) during the experiment in all specimens. Meanwhile, the hyperbolic curve with elevated bulk susceptibility during the heating stage at 302–310 °C is related to the Curie temperature of pyrrhotite mineral (e.g., Martín-Hernández et al., 2008; Pucher et al., 1994). This pyrrhotite naturally occurred in the specimens as no magnetic susceptibility increase (at ca. 300 °C) was detected during the cooling stage, suggesting the destruction of pyrrhotite during heating. The heating curves involving two magnetic susceptibility increments responsible for magnetite and pyrrhotite occurrence indicate an admixture of ferromagnetic and paramagnetic as depicted in the host rock (RS94-1-3 and RS94-1-4) and Kdyně pluton (RS145-4-4) specimens. Specimen RS100-1-1 shows a hyperbolic magnetic susceptibility curve (–196 to 5 °C) of nearly diamagnetic lithology, thus indicating a mixture of diamagnetic (weakly) and paramagnetic minerals.

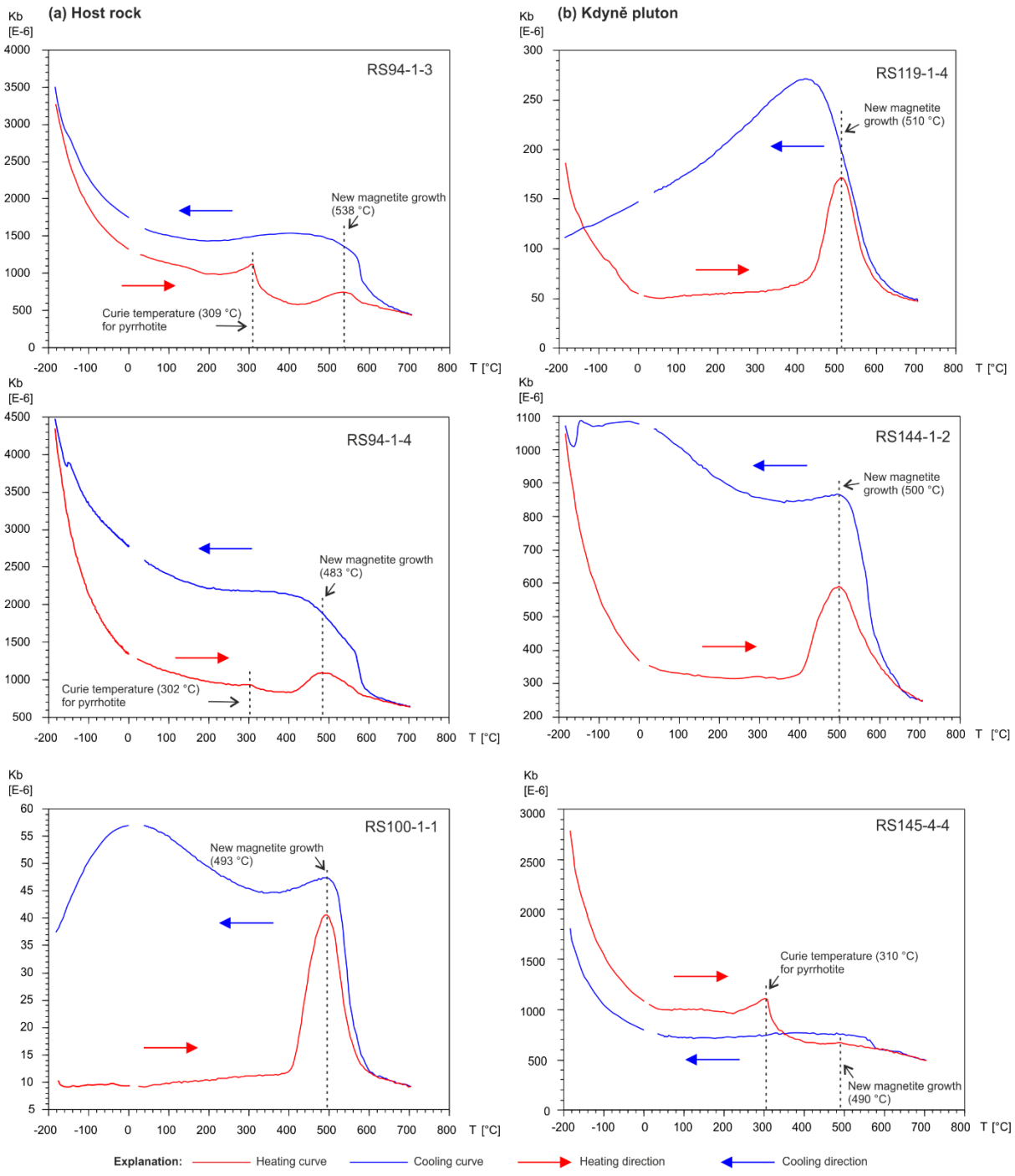


**Figure 12.** *Thermomagnetic curves (bulk magnetic susceptibility vs. temperature) for selected representative specimens taken in the Kdyně pluton and its host rocks.*

### *4.1.7. Diverse magnetic fabrics in the Kdyně pluton and its host rock*

The maximum ($k_1$) and minimum ($k_3$) principal susceptibilities are moderately to strongly clustered at individual sampling sites around their statistical mean values, except at a

few locations which are interpreted with caution (RS99, RS117, RS100). One station dominated by diamagnetic specimens (RS99) was excluded from further analysis. For the interpretation of the AMS directional data, it is essential to consider the measured orientation distribution and angular relationships of the principal susceptibilities with respect to the mesoscopic fabric measured on the outcrop and to the trend of intrusive contacts (plotted on stereonets from the map). We thus classify these relationships in both the pluton and its host rocks into three types (Fig. 13). Type 1 fabric is characterized by macroscopically indiscernible foliation (all stations in the pluton and three in the host rock), Type 2 fabric is marked by magnetic foliations at a small angle (between 15° and 25°) to the measured mesoscopic foliation (7 stations), and Type 3 is represented by a high angle (>30°) relationship between the mesoscale and magnetic foliations (3 stations).

#### *4.1.8. Fabric orientation in the host rock*

In the host rock, the Type 1 and 2 fabrics can be further classified according to whether they are subparallel or at a high angle to lithologic boundaries and pluton margin. The former case is observed in the northern and middle domains, where magnetic foliations dip steeply to moderately to the ~NW or ~SE and then seem to continuously wrap around the bend of the pluton into a ~NW–SE strike in the southern domain (Fig. 14a). The exceptions are stations RS126 and RS132 (Figs. 13 and 14a), which exhibit foliations dipping to the ~N, and station RS94 with foliations dipping to the ~SE, all at a high angle to the nearby intrusive contact.

Magnetic lineations are either down-dip or dip-oblique to magnetic foliations in most cases (Figs. 13 and 14b), except at three stations, where the lineations are subhorizontal, trending either ~NNE–SSW (RS138) or ~WNW–ESE (RS126).

Type 3 fabric is the most intriguing. The ~N–S magnetic foliations are steep to moderately dipping and are at a high angle to the mesoscopic foliation which exhibits a shallower dip (stations RS100, RS121A, RS136; Fig. 13). Magnetic lineations lay close to the

intersection of the magmatic and mesoscopic foliations ($k_1$ axes for RS100 are too scattered to define well a lineation).

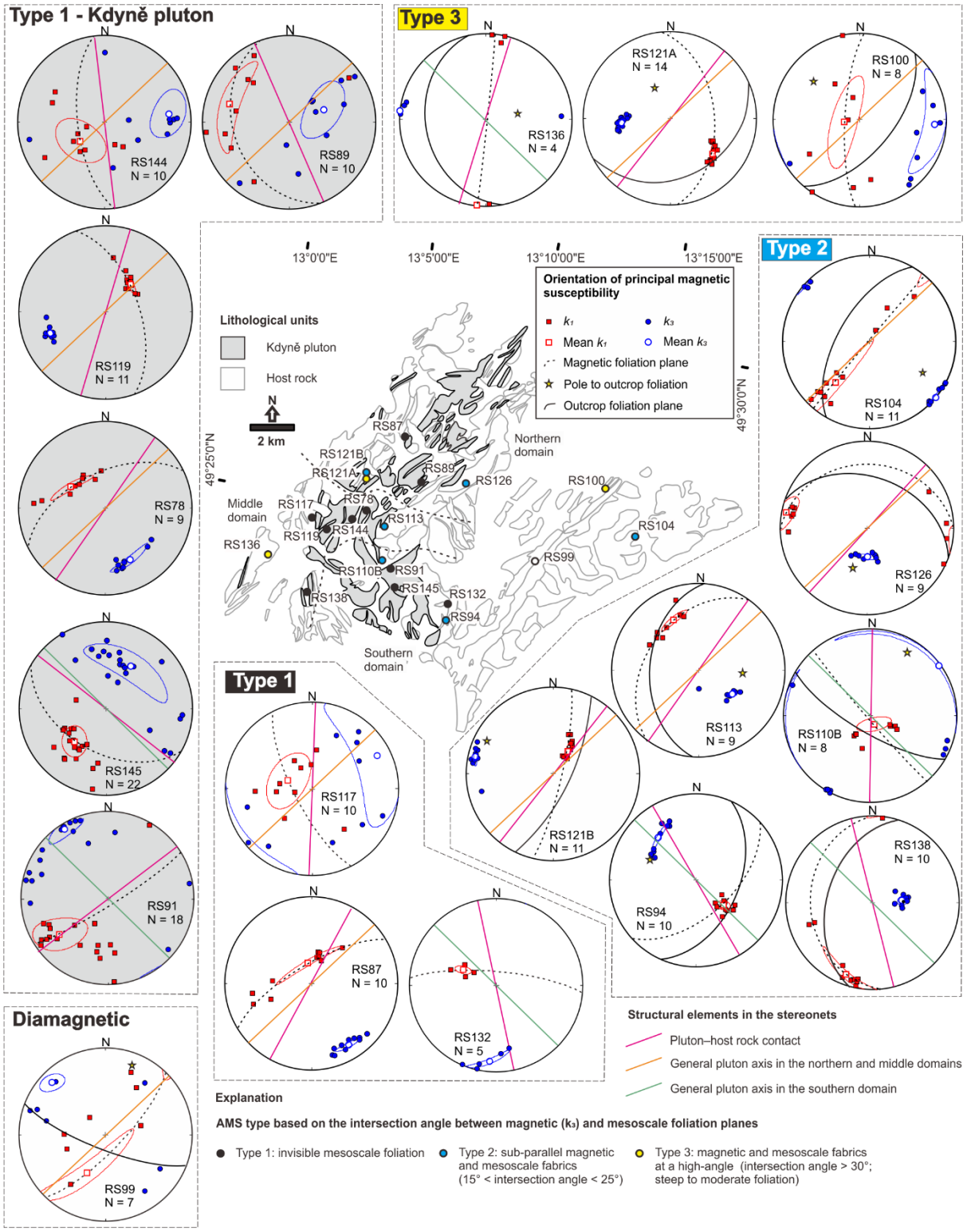


***Figure 13.*** *Orientation of the principal susceptibilities in the Kdyně pluton and its host rocks and their relation to other structural features (see text for details). Stereonets are equal area, lower hemisphere projection.*

### *4.1.9. Fabric orientation in the pluton*

Magnetic fabric differs in orientation along the pluton strike. In the northern and middle domains, foliations trend ~NNW–SSE and dip moderately to steeply to the WSW or ENE and thus are at a high angle to the pluton axis but, at the same time, are subparallel to a local segment of the intrusive contact (stations RS89, RS144, RS119; Figs. 13 and 14a). The associated magnetic lineations are almost down-dip (Fig. 13). At station RS78, magnetic foliations strike subparallel to both the pluton axis and local intrusive contact (~NE–SW) and dip moderately to NW, with down-dip lineation. A similar relationship is observed in the southern domain at station RS145 (magnetic foliations parallel to the axis and local contact, down-dip lineations), whereas at station RS91 foliations are almost pluton axis-perpendicular, parallel to a local ~NE–SW-trending step in pluton margin, and associated with subhorizontal lineations (Figs. 13 and 14).

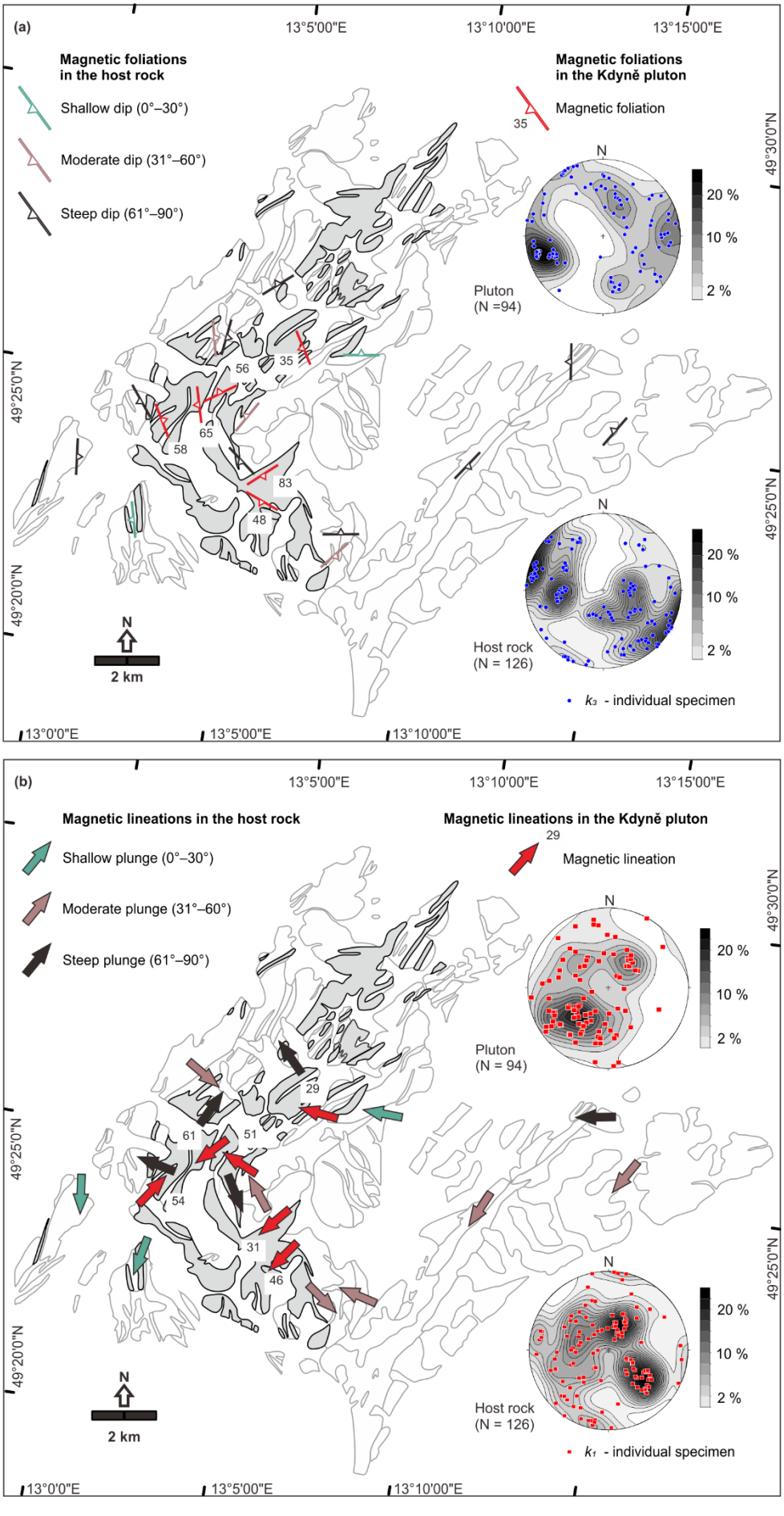


***Figure 14.*** *Maps of site-mean (a) magnetic foliations and (b) magnetic lineations in the Kdyně pluton and its host rocks. Stereonets are equal area, lower hemisphere projection.*

### 4.2. Cambrian sedimentary basins (Příbram–Jince)

At the present-day erosional level, the Příbram–Jince basin covers an area of about 400 $km^2$ along the southeastern margin of the Teplá–Barrandian unit, a large exposure of upper crust in the center of the Bohemian Massif (Fig. 4). The basin overlies Cadomian basement made up of a late Neoproterozoic to early Cambrian accretionary wedge, referred to as the Blovice complex (e.g., Hajná et al., 2017), with a regional angular unconformity and is, in turn, overlain by basal Lower Ordovician (Tremadocian) strata of the Prague basin, also with a slight angular unconformity. The southeastern end of the basin is truncated by a system of NW–SE-trending normal faults that juxtapose the basin against Cadomian basement in the footwall (Fig. 5). The basin axis trends ~NE–SW, which is roughly parallel to the lithotectonic belts in the underlying accretionary wedge, and aligned at an angle of approximately 20° to axis of the overlying Prague basin (Fig. 5). The basin interior is segmented into alternating, NE–SW-trending horsts and grabens (Fig. 15a), the fault-bounded basement blocks being overlain by fill of variable thickness and spatially changing depocenters (e.g., Havlíček, 1971; Kukal, 1971). Nevertheless, the basin fill thickness generally increases from older formations along its southeastern margin to the basin center and then continuously decreases towards younger formations in the northwest.

Correlative outliers comprising Cambrian siliciclastic deposits occur to the south and southeast of the basin as narrow, faulted and folded belts and in a roof pendant enclosed by a Variscan plutonic complex (Fig. 5), all strongly overprinted by Variscan shortening and contact metamorphism. Another graben-type basin, somewhat restricted in terms of its spatial extent, fill, and thickness, occurs about 20 km to the northwest (the Skryje–Týřovice basin; Fig. 5). Among these Cambrian basinal relicts, the Příbram–Jince basin is the largest, provides the most complete tectonostratigraphic record, and is the least affected by younger deformation (e.g., Fatka and Mergl, 2009; Geyer et al., 2008; Kukal, 1971).

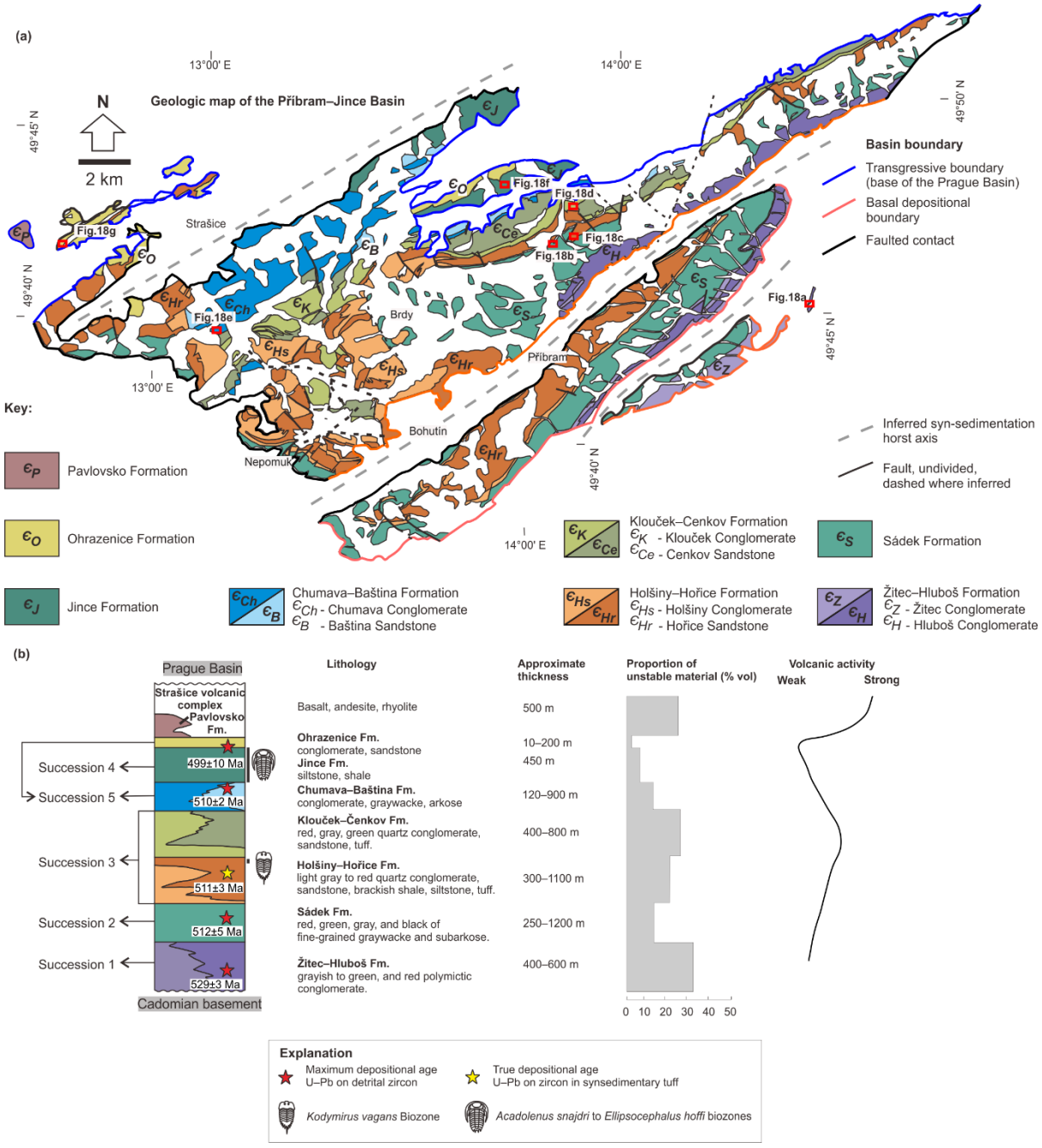


***Figure 15.*** *(a) Simplified geologic map of the Příbram–Jince basin compiled from Havlíček (1971) and geological map 1:25,000 scale from Czech Geological Survey. Inferred horst axis after Havlíček (1971). (b) Lithostratigraphic scheme of the Příbram–Jince basin and graphs showing variations in the proportion of unstable material and volcanic activity across stratigraphy (Kukal, 1971). U–Pb detrital zircon ages from Drost et al. (2004, 2011) and Hajná et al. (2018) are maximum depositional ages. U–Pb detrital zircon age in synsedimentary tuff from Hajná et al. (2018).*

### *4.2.1. Lithostratigraphy*

The Příbram–Jince basin is dominated by continental siliciclastic deposits interlayered with a marine horizon and capped by an intermediate to felsic volcanic complex (Strašice complex: Fig. 15; e.g., Havlíček, 1971; Kukal, 1971). The basin infill is subdivided into eight formations (Fig. 15). The contacts between adjacent formations are mostly gradational over a few meters in vertical section while lateral transitions and interdigitation are also observed, especially between the individual stratigraphic members. From bottom to top, the eight formations can be informally grouped into five different successions (Fig. 16). Their main characteristics are described below and depicted in a cross-section in Figure 17.

The Žitec–Hluboš Formation in the southeastern part of the basin is dominated by red and green polymictic conglomerates and sandstones. The clasts are up to 30 cm in size (boulders) and composed of quartz, Cadomian unstable material derived from a volcanic arc (granites, porphyritic plagiogranites, intermediate to felsic lavas, tuffs) and low- to medium-grade metamorphic basement (metagraywackes, phyllites, mica schists, and gneisses; Fig. 18a). Metamorphic clasts are absent at higher stratigraphic levels (Fig. 17) and have been interpreted as sourced from an unknown terrain to the southeast (present-day coordinates; Kettner, 1919, 1946). The clast size in conglomerates decreases significantly to the northwest where they are frequently overlain by a few centimeter to decimeter layers of sandstones.

The Sádek Formation in the southeastern part of the basin lacks conglomerates and is dominated by graywackes to sub-graywackes or even arkoses to subarkoses interbedded with siltstones and claystones (Fig. 18b). Grain size generally decreases in the western part of the basin down to siltstone (Kukal, 1971; Havlíček, 1971). Mudstone rip-up clasts, slump structures, and several centimeter-thick lenses of conglomerates may also occur within the sandstone beds (Kukal, 1971).

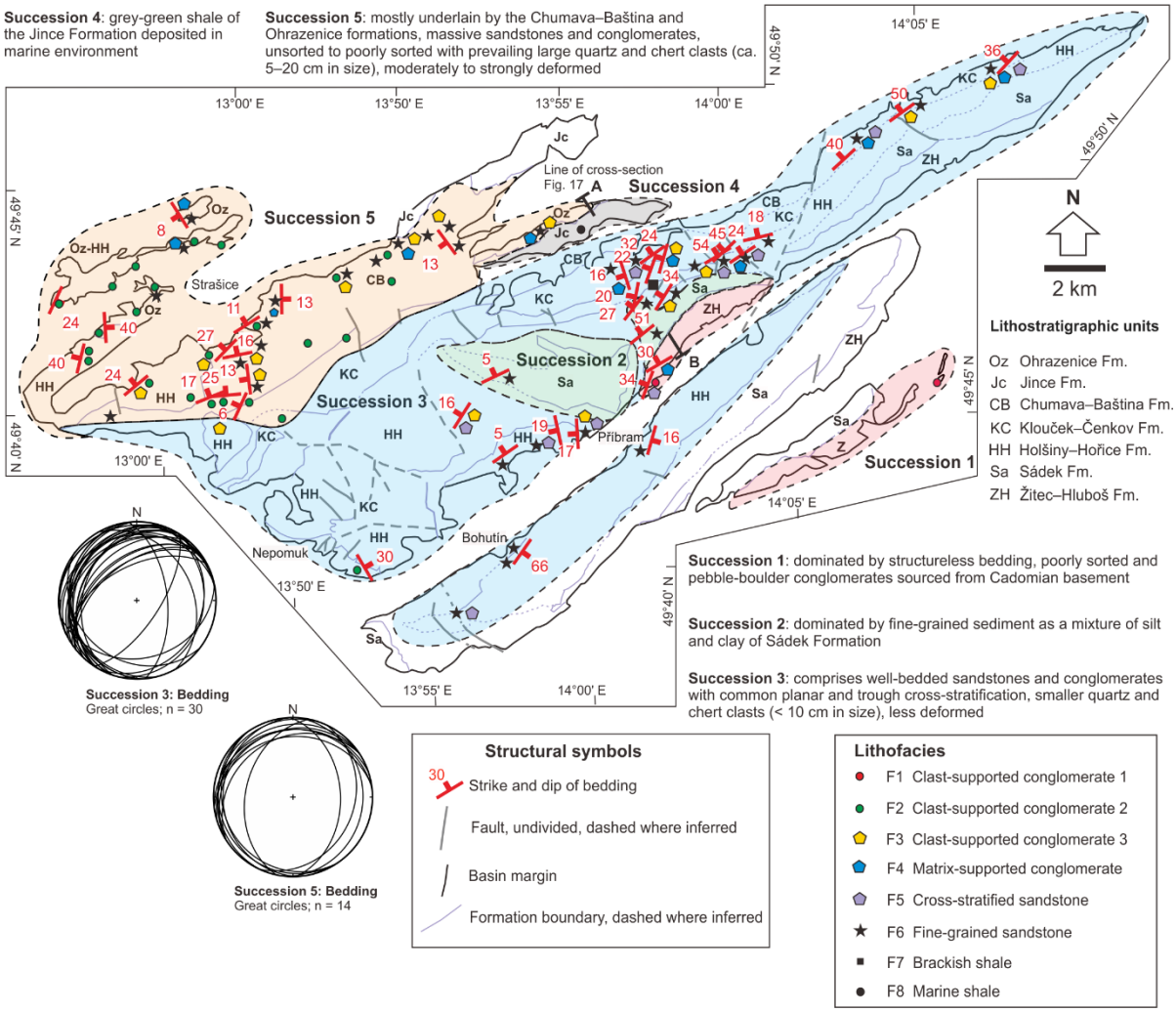


**Figure 16.** *Field measurements from the Příbram–Jince basin. The lithostratigraphy (color-coded) is divided into five successions, dominated by alluvial and fluvial depositional settings with a short-lived marine transgression (Jince Formation).*

---

The overlying succession, areally the most extensive and occupying the center of the basin, is composed of monomictic conglomerates and conglomeratic sandstones with a smaller clast size (typically 1–5 cm), but also includes restricted occurrences of brackish shales. This succession comprises, in stratigraphic order, the Holšiny–Hořice and Klouček–Čenkov formations and the Baština Sandstone. The conglomerates generally consist of quartz and chert clasts, but the chert proportion decreases significantly up-section (in the Klouček–Čenkov Formation). The overlying Holšiny–Hořice Formation is dominated by light gray to red

sandstones and monomictic conglomerates (Fig. 18c) with a significant marker horizon of silty shales (Paseky Shale) and minor felsic tuff intercalations within the sandstones. The tuffitic material also occurs as small fragments, becoming increasingly abundant in the Klouček–Čenkov Formation (Fig. 18d). The Baština Sandstone fills the north-central part of the basin and is characterized by a decreasing abundance of tuff fragments, marking the waning of volcanic activity towards the end of continental deposition.

The fourth succession, which occupies a limited area in the northern part of the basin, differs markedly from the successions above and below, and comprises finely laminated siltstones and shales of the Jince Formation, accompanied by centimeter-thick layers of sandstones (Fig. 18f). The succession's Lingullela, trilobite, and Agnostid Biofacies indicate sea-level rise (transgression) and deposition in a shallow to deep water marine environment (e.g., Babcock et al., 2015; Fatka and Szabad, 2014; Fatka and Mergl, 2009).

The Chumava Conglomerate was deposited at the same time as the Baština Sandstone, but shares similar lithologic characteristics with the Ohrazenice Formation in the northwestern part of the basin. The lithologies include monomictic conglomerates and lithic sandstones (Fig. 18e and 18g) with minor admixture of felsic tuffitic material in some places (Kukal, 1971). Clasts in the conglomerates range from 5 to 20 cm in size. The overlying Pavlovsko Formation contains sandstones with abundant unstable clasts and clay (Kukal, 1971), and was deposited during vigorous volcanic activity of the Strašice complex (Fig. 15).

| | Ohrazenice Fm. | Jince Fm. | Chumava–Baština Fm. | Klouček–Čenkov Fm. | Holšiny–Hořice Fm. | Sádek Fm. | Žitec–Hluboš Fm. |
|---|---|---|---|---|---|---|---|
| **Dominant lithology** | Monomictic conglomerate | Siltsone and shale | Monomictic conglomerate | Quartz sandstone conglomerate | Quartz sandstone conglomerate | Sandstone, siltstone, shale | Polymictic conglomerate |
| **Bedding** | Massive to thickly bedded | Massive bedded | Massive to thickly bedded | Thin to thickly bedded | Massive to thickly bedded | Massive to thinly bedded | Massive to thickly bedded |
| **Internal structures** | Poorly sorted, pebbles layer | Fine-scale lamination, bedding-parallel cleavage | Poor-moderately sorted, pebbles layer | Moderately sorted, pebbles layer, cross-stratification | Moderately sorted, cross-stratification | mud strips, cross-stratification | Chaotic, cross-stratification |
| **Dominant clast composition** | Quartz and chert | Silt and shale (sub/graywacke) | Quartz and chert (sub/graywacke) | Quartz and chert (sub/graywacke) | Quartz and chert (sub/graywacke) | Q:F:L = 80:5:15 (subarkose) | Quartz, chert, granite, rhyolite, plagio-granite |
| **Clast size** | Up to 5–20 cm | Silt and shale | Up to 10–20 cm | Up to 1–5 cm | Up to 1–10 cm | Fine-grained sand | Up to 20–30 cm |
| **Lithofacies** | F2, F4, F6 | F8 | F2, F3, F4, F6 | F3–F6 | F2–F6 | F6 | F1 |

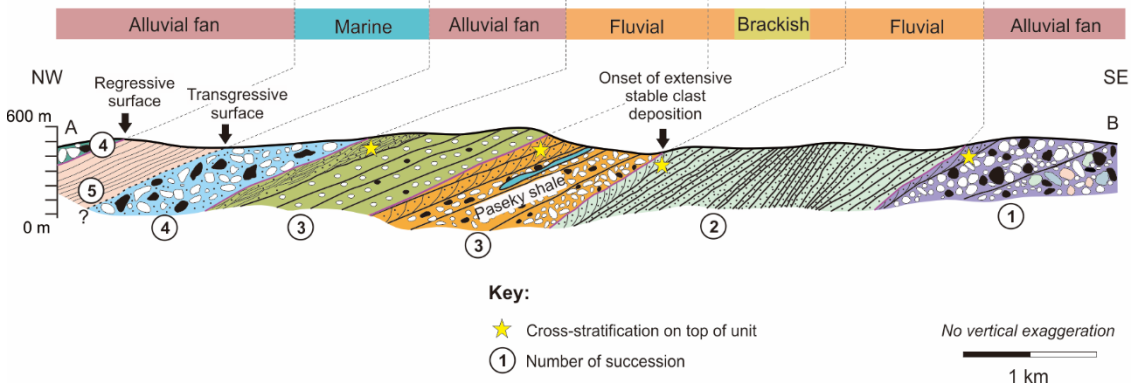


**Figure. 17.** *Cross-section of the Příbram–Jince basin along the Litavka River with descriptions of each rock formation.*

### *4.2.2. Temporal constraints on the evolution of the Příbram–Jince basin*

The exact timing of deposition in the Příbram–Jince basin, a key for inter-regional correlation and the interpretation of geodynamic processes, is only broadly constrained. Drost et al. (2011) reported a maximum depositional age of 529 ± 3 Ma from U–Pb detrital zircons in the lowermost Žitec–Hluboš Formation. However, significantly younger maximum depositional ages (512 ± 5 Ma) were reported by Hajná et al. (2018) from the directly overlying Sádek graywackes. The difference in age implies either a protracted time span of deposition of the basin's basal infill or that the maximum depositional age of 529 Ma is significantly older than the true depositional age. Further up-section, a U–Pb age from a silicified tuff constrains the true depositional age of the Holšiny–Hořice Formation to 511 ± 3 Ma (Hajná et al., 2018), while a maximum depositional age for the overlying Chumava–Baština Formation has been estimated at 510 ± 2 Ma (Drost et al., 2011). The trangressive marine shales of the Jince

Formation are dated paleontologically and were assigned to the Acadolenus snajdri to Ellipsocephalus hoffi biozones, corresponding to the time interval ca. 506–503 Ma (Fatka and Szabad, 2014). This is in agreement with the maximum depositional age of 499 ± 10 Ma determined for the uppermost levels of the Jince Formation (Drost et al., 2011). In summary, ca. 515 Ma and ca. 499 Ma may be considered the maximum and minimum time constraints for deposition within the Příbram–Jince basin (Fig. 15b).

#### *4.2.3. Structure of the Příbram–Jince basin*

Major NE–SW-trending faults divide the Příbram–Jince basin into three segments parallel to the basin axis (Fig. 15a). These faults were active during deposition as inferred from thickness variations reflecting differential subsidence in several depocenters (Havlíček, 1998, 1971). The most notable examples are the Žitec–Hluboš and Sádek formations, which pinch out northwestwards, and the younger formations, which are spatially restricted to the northwestern margin of the basin (Fig. 15a). Otherwise, the overall structure of the basin is simple, resulting from weak Variscan shortening. Bedding dips mostly to the NW and NNW at shallow to moderate angles (between 16° to 54°) in succession 3 as a result of Variscan tilting, whereas in the northwesterly succession 5 it dips gently (mostly less than 25°) in various directions (Fig. 3). Consequently, the formations within the basin are arranged from the oldest in the SE to the youngest in the NW (Fig. 16).

#### *4.2.4. Lithofacies*

In this study, we distinguish eight main lithofacies (F1–F8) based on clast composition, clast size and sedimentary structures; these facies are attributed to four depositional environments (for detailed characteristics see Tab. 3).

*4.2.4.1. Alluvial fan facies (F1–F3)*

The F1 lithofacies is represented by clast-supported, mostly non-bedded, poorly sorted polymictic conglomerates with subrounded to rounded clasts up to boulders, in places interbedded with thin sandstone beds bounded by irregular erosional contacts (Fig. 19a). Conversely, similar clast-supported conglomerates of lithofacies F2 are poorly sorted monomictic conglomerates composed of subrounded to rounded quartz pebbles to cobbles embedded in a light gray or red matrix (Fig. 19b).

The clast-supported monomictic conglomerates of lithofacies F3 comprise subrounded to rounded quartz and chert pebbles to cobbles embedded in a moderately sorted, fine- to medium-grained sandy matrix. This facies forms thin graded layers (0.1 and 1 m in thickness), each with a sharp erosional base (Fig. 19c).

**Table 3.** *Principal characteristics of lithofacies in the Příbram–Jince basin*

| **Lithofacies association (F)** | **Description (petrography, field relationships)** | **Interpretation of the depositional processes** | **Inferred depositional environment** | **Stratigraphic occurrence (formation)** |
|---|---|---|---|---|
| **Clast-supported conglomerates 1 (F1)** | Clasts are quartz, cherts, metasandstones, metapelites, volcanic and plutonic rocks (intermediate to felsic lavas, banded tuff fragments, granite), and metamorphic rocks (schist, gneiss). Red and green poorly sorted polymictic conglomerates with large clasts (up to 30 cm in size) mostly subrounded to rounded. Sandstone interbeds only a few centimeters to | Absence of dynamic sorting into different clast sizes creating poorly sorted conglomerates induced by debris flows. Grain shape indicates transport to moderate distance from the source, probably between proximal and medial fan. Low intensity erosion, absence of scour marks, and chaotic bedding indicate sedimentary materials | Alluvial fan | Žitec–Hluboš |

| | | | | |
|---|---|---|---|---|
| | decimeters thick. Most sandstone beds are ungraded and overlain by pebbly sandstone with irregular erosive base. | driven by laminar flow. Deposition presumably resulted from syn-sedimentary faulting. | | |
| **Clast-supported conglomerates 2 (F2)** | Similar to F1 but dominated by monomictic conglomerates composed of poorly-sorted quartz and chert pebbles (clasts may reach 20 cm) embedded in light gray or red sandstone matrix. Clasts subrounded to rounded. Irregular to sharp base. | Clast arrangement and sorting suggest deposition by debris flows at moderate distance from source area (presumably in medial to distal fan). Largest clasts found near edge of basin (northern and western part) with finer- grained material toward the NE. Syn-depositional fault controlled sedimentation. | Alluvial fan | Holšiny–Hořice, Chumava–Baština, Ohrazenice |
| **Clast-supported conglomerates 3 (F3)** | Monomictic quartz conglomerates. Some chert clasts of similar size. Quartz and cherts are subrounded to rounded with up to 20 cm in size, commonly formed a laminated pebble. Clasts moderately sorted. Sharp erosive base. Matrix medium- to coarse-grained sandstone. | Transport involved different process from F2, possibly due to traction setting. Erosive base, fining upward succession, and clasts nearly parallel to bedding suggest grains rolled on bed of river. Smaller size, rounded shape, and monotonous quartz clasts from fluvial setting or different area, possibly broader than F1. | Fine-grained component of sheetflood fan | Klouček–Čenkov, Chumava–Baština, Ohrazenice |
| **Matrix-supported conglomerates (F4)** | Quartz pebbles and cobbles (up to 10 cm) set in light gray or red, medium- to coarse-grained sandstone matrix. | Transition between sharp and gradational contact, subhorizontally stratified conglomerate, and moderate to poor | Bar in braided stream (middle to upper part of bar profile) | Holšiny–Hořice, Klouček–Čenkov Ohrazenice |

| | | | | |
|---|---|---|---|---|
| | Moderate to poorly sorted with sharp to gradational base. Massively stratified but sometimes fining upward. Layer thickness 0.1 to 1 m. Occasionally planar cross-stratified and imbricated. | sorting suggest deposition under high discharge levels during waning stage flow of fluvial current. Transported far away from apex, sandy matrix likely came from the same source as conglomerates, interpreted as disintegration of pre-Cambrian quartz. | | |
| **Cross-stratified sandstones (F5)** | Medium- to fine-grained sandstones sometimes with granules to pebbles aligned with cross-stratification. Stratification 5 to 30 cm. Planar (with either angular or tangential foresets) and trough cross-stratification. | Part of lithofacies F4. Angular and tangential cross-stratified unit indicating difference in velocity and sediment transport rate. Pebbly or gravelly cross-stratification from downstream migration of bar with coarser material presumably from traction current at base, while finer sand or silt indicate abandonment of bar deposit when the flow waning. | Bar in braided stream (middle part of bar profile) | Sádek, Holšiny–Hořice, Klouček–Čenkov |
| **Massive bedded fine- to coarse-grained sandstones (F6)** | Red or gray subgraywacke–graywacke to subarkose–arkose, dominated by mixture of silt and clay in various proportions. Sometime accompanied by dark-mud rip-ups (only in Sádek Formation). Volcanic fragments (e.g., tuff) | Fine grained sediment indicating dominantly low energy current and deeper river water depth or very distal part of fluvial system. | Flood plains or braid plains | Sádek, Hořice Sandstone, Čenkov Sandstone, Baština Sandstone |

| | | | | |
|---|---|---|---|---|
| | occur locally in upper part. | | | |
| **Brackish shales (F7)** | Single horizon of gray shale overlain by layer of fine-grained quartzose sandstone with sharp erosive boundary. Rare non-marine crustaceans (endemic). | Shale indicates sediments deposited in low energy environment such as lake, although geochemical data from Kukal (1995) suggest deposit neither marine nor freshwater. | Brackish embayment? | Holšiny–Hořice |
| **Marine shales (F8)** | Mainly gray to green silty shale and siltstone with abundant marine fossils, rare interbeds of massive graywacke and thin layers of monomictic conglomerate. Dominant structure is bedding-parallel cleavage. | Lack of coarser material in fine grained sediment, existence of marine fauna, and homogenous bedding suggest lithofacies originated in marine environment. | Shallow marine seaway (max. water column around 100 m) | Jince |

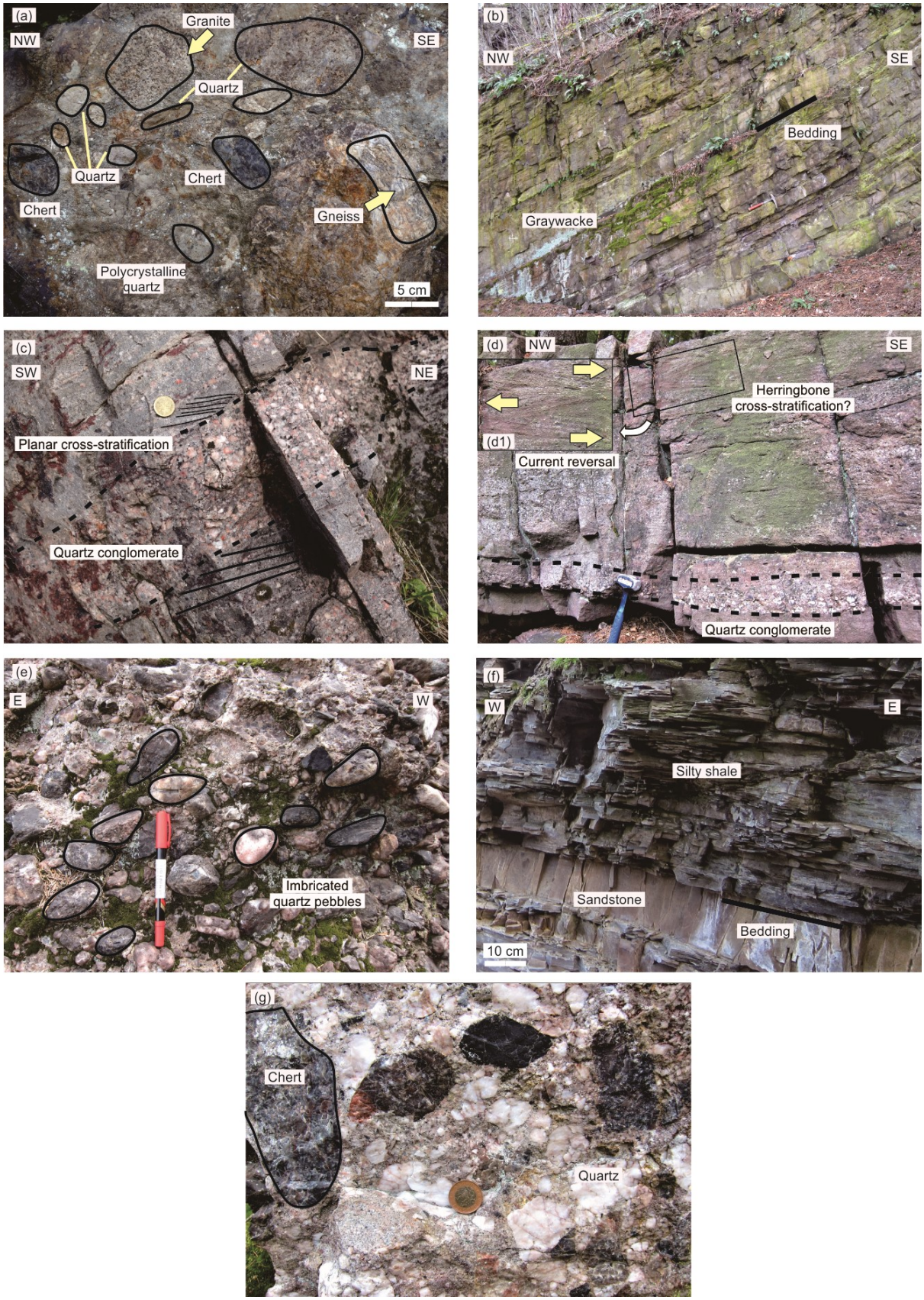


**Figure. 18.** *Field photographs of Cambrian outcrops in the Příbram–Jince basin, arranged from older to younger. (a) Polymictic conglomerate of the Žitec–Hluboš Formation. Clasts were derived from a volcanic arc and*

*metamorphic basement of the Cadomian; Tuškov [WGS84 coordinates: N49°44'26.394", E14°10'38.363"]. (b) Graywacke of Sádek Formation. Beds dip to the NW; Bratkovice [WGS84 coordinates: N49°45'4,530", E13°59'59,115"]. (c) Planar cross-stratification in the Holšiny–Hořice Formation with layer of quartz conglomerate interpreted as a fine-grained sheetflood fan (F3); near Hořice hill [WGS84 coordinates: N49°45'23.134", E14°1'1.627"]. (d) The Klouček–Čenkov Formation with herringbone (?) cross-stratification implying current reversal; Bílá huť [WGS84 coordinates: N49°46'12.495", E14°0'51.558"]. (e) Typical monomictic conglomerate with imbricated quartz pebbles in the Chumava–Baština Formation; Hlava [WGS84 coordinates: N49°43'22.272", E13°49'23.978"]. (f) Shale with thin intercalation of sandstone from the Jince Formation; Jince [WGS84 coordinates: N49°47'3.975", E13°59'24.791"]. (g) Ohrazenice Formation composed of quartz and cherts pebbles; Konesův vrch [WGS84 coordinates: N49°43'26.447", E13°40'51.05"]. Scale: pen = 14 cm; hammer = 26 cm; coin diameter = 2.5 cm.*

---

#### *4.2.4.2. Fluvial distributary system facies (F4–F6)*

Matrix-supported conglomerates of lithofacies F4 overlie the F3 facies with sharp to gradational basal contacts, forming a depositional couple. The F4 conglomerates are dominated by medium to coarse-grained, poorly to moderately sorted arkoses, subarkoses, and graywackes with scattered quartz pebbles to cobbles, fining upward (Fig. 19d).

Cross-stratified sandstones of lithofacies F5 show both planar and trough cross-stratification of low and high angle with bed thicknesses up to 30 cm (Fig. 19e). In some places, granules to pebbles of quartz are aligned within the cross-stratification.

Red or gray coarse to fine-grained sandstones of lithofacies F6 comprise bedded graywackes, subgraywackes, subarkoses, and arkoses. The sandstones show a significant compositional difference to the other facies and occur only in the Sádek Formation. The basal sandstones have a silty and clayey matrix whereas those in the upper stratigraphic levels are accompanied by thin tuffaceous layers (Fig. 19f).

#### *4.2.4.3. Brackish environment facies (F7)*

Brackish shales of lithofacies F7 were deposited in a spatially restricted area and forms a marker horizon about 10–15 m thick within the Holšiny–Hořice Formation. The base of the

shale horizon is an erosive boundary (Kukal, 1971). The lithofacies comprises dark-gray silty shale with reported rare endemic arthropod fossils (the Kodymirus association), representing the oldest macrofauna in the Bohemian Massif (e.g., Chlupáč and Havlíček, 1965; Chlupáč et al., 1995;) and perhaps indicating a brackish environment (Kukal, 1995).

*4.2.4.4. Marine facies (F8)*

The marine Jince Formation conformably overlies the continental deposits and is composed predominantly of siltstones and shales (lithofacies F8) with thin sandstone intercalations and, locally, with conglomerates (Kukal, 1971). The formation is world-famous for its rich fossil record, mostly brachiopods, trilobites, Agnostids, and an echinoderm-dominated association (Geyer et al., 2008; Fatka and Mergl, 2009; Fatka and Szabad, 2014).

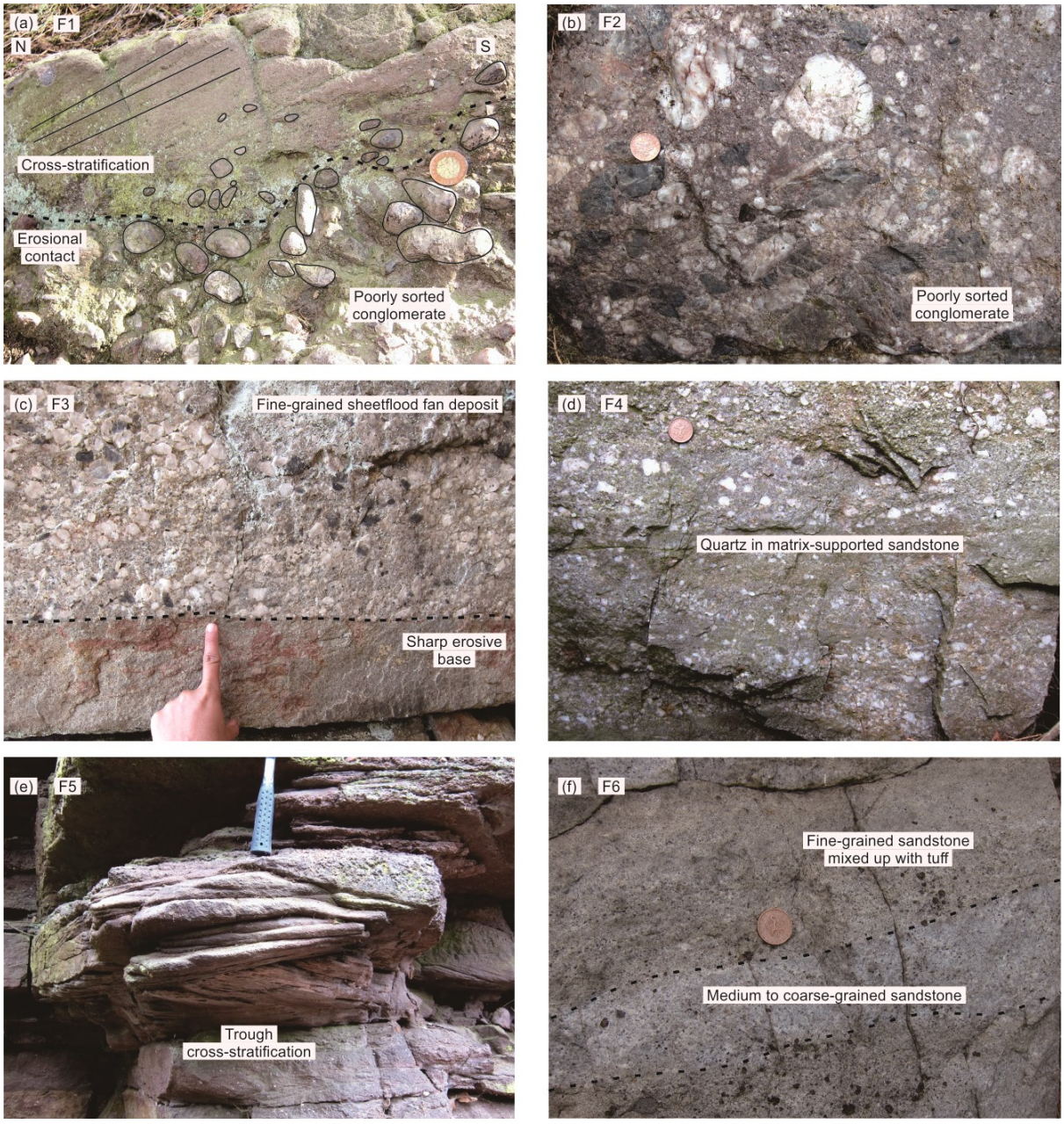


**Figure. 19.** *Field photographs of Cambrian lithofacies in the Příbram–Jince basin. (a-c) Alluvial fan deposit from a debris flow. (a) F1 Clast-supported conglomerate showing chaotic internal structure with an erosional contact; between Dratovna and Valcha [WGS84 coordinates: N49°43'23.459", E14°0'48.661"]. (b) Poorly-sorted F2 clast-supported conglomerate in a sandy matrix; Konesův vrch [WGS84 coordinates: 49°43'26.447", E13°40'51.05"]. (c) Clast-supported conglomerate interpreted as a fine-grained sheetflood fan (F3) with sharp erosive base; Stožec [WGS84 coordinates: N49°50'7.68", E14°8'13.311"]. (d-f) Fluvial distributary system. (d) Granule-pebble quartz in a matrix-supported sandstone (F4); Chocolatá skála [WGS84 coordinates: N49°41'44.99", E13°47'30.718"]. (e) Trough cross-stratification in sandstone, sometimes found together with granule-pebble quartz (F5); Slonovec [WGS84 coordinates: N49°45'42.900", E13°59'50.200"]. (f) Fine-grained sandstone (F6), sometimes associated with thin tuffaceous layers in the upper stratigraphic levels; Kazatelna [WGS84 coordinates: [N49°41'33.286", E13°56'35.607"]. Scale: hammer = 26 cm; coin diameter = 2.5 cm.*

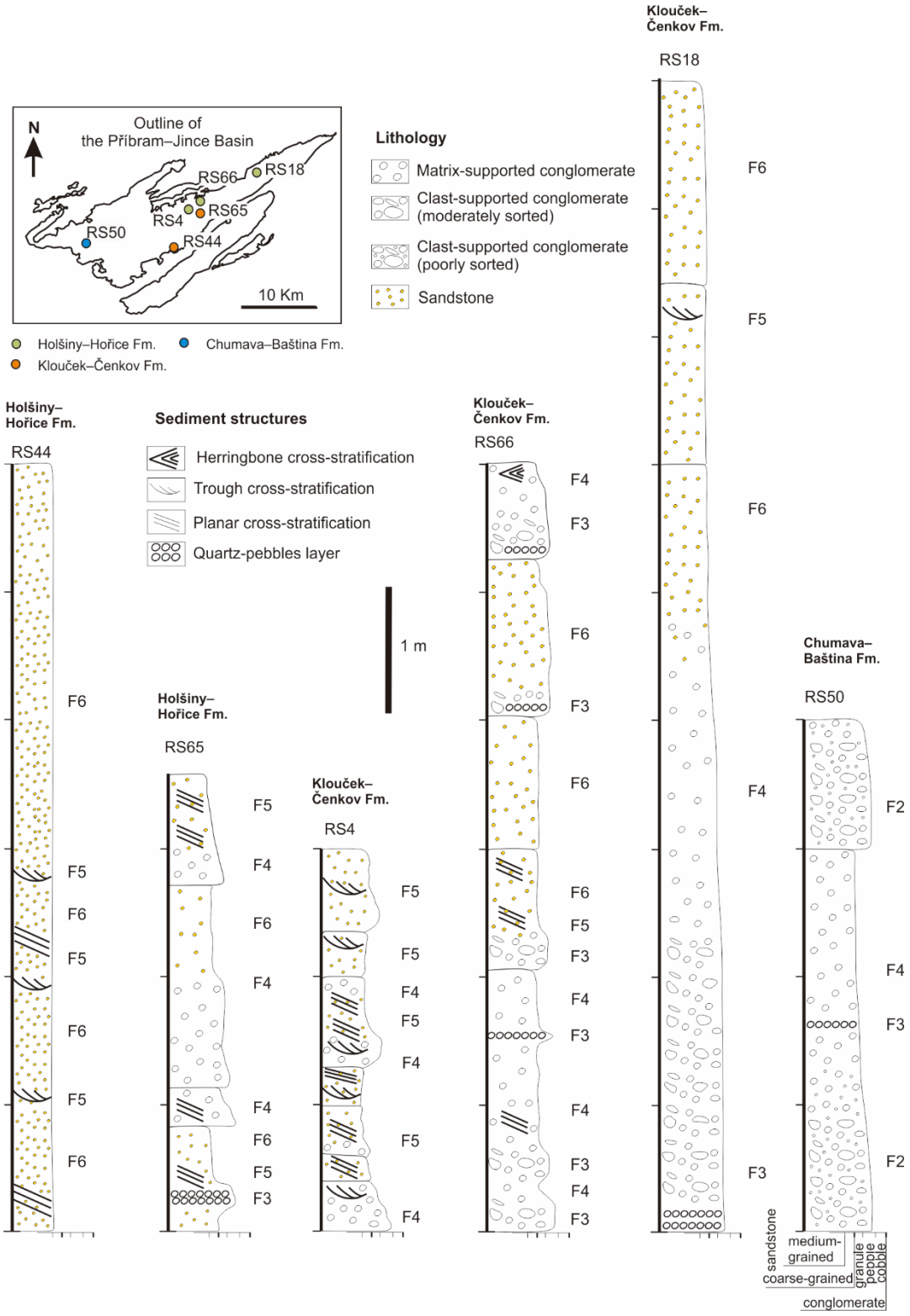


**Figure 20.** *Representative sedimentary logs of lithofacies of the fluvial distributary system and alluvial fans. A fining-upward pattern dominates the entire section, indicating waning of paleocurrents in the upper part.*

### *4.2.5. Spatial and stratigraphic distribution of lithofacies*

The alluvial fan deposits of lithofacies F1 are distributed near the southeastern edge of the basin, and are only developed in succession 1 (Žitec–Hluboš Formation). In the middle of the basin, which contains the most extensive part of succession 3, the alluvial fan was replaced by a mixture of the fine-grained sheetflood fan deposits of lithofacies F3 and the fluvial distributary system of lithofacies F4 and F5 (representing a set of bar packages in a braided stream), and F6. In detail, the lower part of the Holšiny–Hořice and Klouček–Čenkov formations is mostly dominated by lithofacies F3, changing upward to the finer grained lithofacies F4 to F6 (Fig. 20). Except for lithofacies F4, which is not present in the southwestern part of the basin, or the middle part near Příbram, the fluvial distributary system narrows from the central to the northeastern part of the basin (see Fig. 16).

In the NW part of the basin, the thickly bedded lithofacies F2 in succession 5 is frequently overlain by laminated pebbles of the F3 sheetflood fan, and conformably capped by sandstones of the F4 fluvial distributary system (see profile of Chumava–Baština Formation in Fig. 20).

The marine lithofacies F8 is limited to succession 4 and is mostly confined to the north-central part of the Příbram–Jince basin (Kukal, 1971).

### *4.2.6. Paleocurrent analysis*

#### *4.2.6.1. Method and description of paleocurrent indicators*

Paleocurrent analysis was carried out on 15 outcrops (out of 74 stations documented in total). These outcrops expose reliable paleocurrent indicators and are mostly distributed within a 2–3 km wide belt along the southeastern margin of the basin, ranging stratigraphically from the basal Žitec–Hluboš Formation up to the Klouček–Čenkov Formation (Fig. 21). All measured paleocurrent indicators were cross-stratification structures.

Cross-stratification was most commonly preserved in the fine- to medium-grained sandstones and, occasionally, in the quartz-pebble conglomerates of succession 3 at the middle and the upper levels of the Holšiny–Hořice and the Klouček–Čenkov formations. The structures include planar, trough, and rarely bi-directional subtypes.

Planar cross-stratification is the most abundant structure, commonly present in lithofacies F5, but sometimes appearing in lithofacies F4. Figure 21a–b shows examples of planar cross-stratification in angular and tangential foresets at high and low angles to the lower bounding surface, respectively (e.g. Blair, 2000; Herbert et al., 2020). A reactivation surface sometimes occurs within the planar cross-stratification (Fig. 21c), resulting from interaction between bedforms in unidirectional flow (e.g., Allen, 1973). The foresets have a thickness of up to 30 cm with a maximum width of 2 m, and the surface beneath and above each coset is non-erosional.

Trough cross-stratification is much less common, mostly occurring in lithofacies F5 in the Klouček–Čenkov and the Sádek formations, with coset thicknesses between 5 to 30 cm and widths from 50 to 60 cm. The foreset shape is tangential and bounded by a flat surface.

Bi-directional stratification occurs rarely in the Klouček–Čenkov and Holšiny–Hořice formations. This sedimentary structure is interpreted as herringbone cross-stratification, in which the upper and lower straight foresets have opposite dips, in Figure 18d to the ~NE (68°) and ~SE (151°), respectively.

The paleocurrent data were collected on outcrops as dip directions of planar cross-beds and treated as a vector of unit length (e.g., Potter and Pettijohn, 1977; Nichols, 2009). The paleocurrent direction was assumed to be down dip. To remove the effect of post-depositional tectonic deformation (bedding tilt), the paleocurrent vectors have been rotated to the horizontal about a rotation axis represented by the strike of the bedding through an angle equal to the

bedding dip. The rotated paleocurrent directions are presented in map view and as a rose diagram in Figure 21.

#### *4.2.6.2. Inferred paleocurrent directions and their distribution within the basin*

Statistically, the inferred paleocurrent directions scatter from ~NNW (332°) to ESE (104°) with a mean direction of 030° calculated using the method of Fisher et al. (1987). An intriguing pattern, however, emerges when the data are viewed in stratigraphic succession and with respect to their spatial distribution across the basin (note the bedding dips generally to the NW; Fig. 15). Going up-section (and from SE to NW), the basal Žitec–Hluboš Formation shows paleocurrents to the ~WNW, changing to ~N in the overlying the Sádek Formation, and to frequent ~ENE directions in the Holšiny–Hořice and Klouček–Čenkov formations. This suggests basin axis-oblique sediment transport in the early stages of basin evolution gave way to predominantly axis-parallel transport as the basin matured. Only two localities yielded paleocurrent directions opposite to this overall trend (Fig. 21).

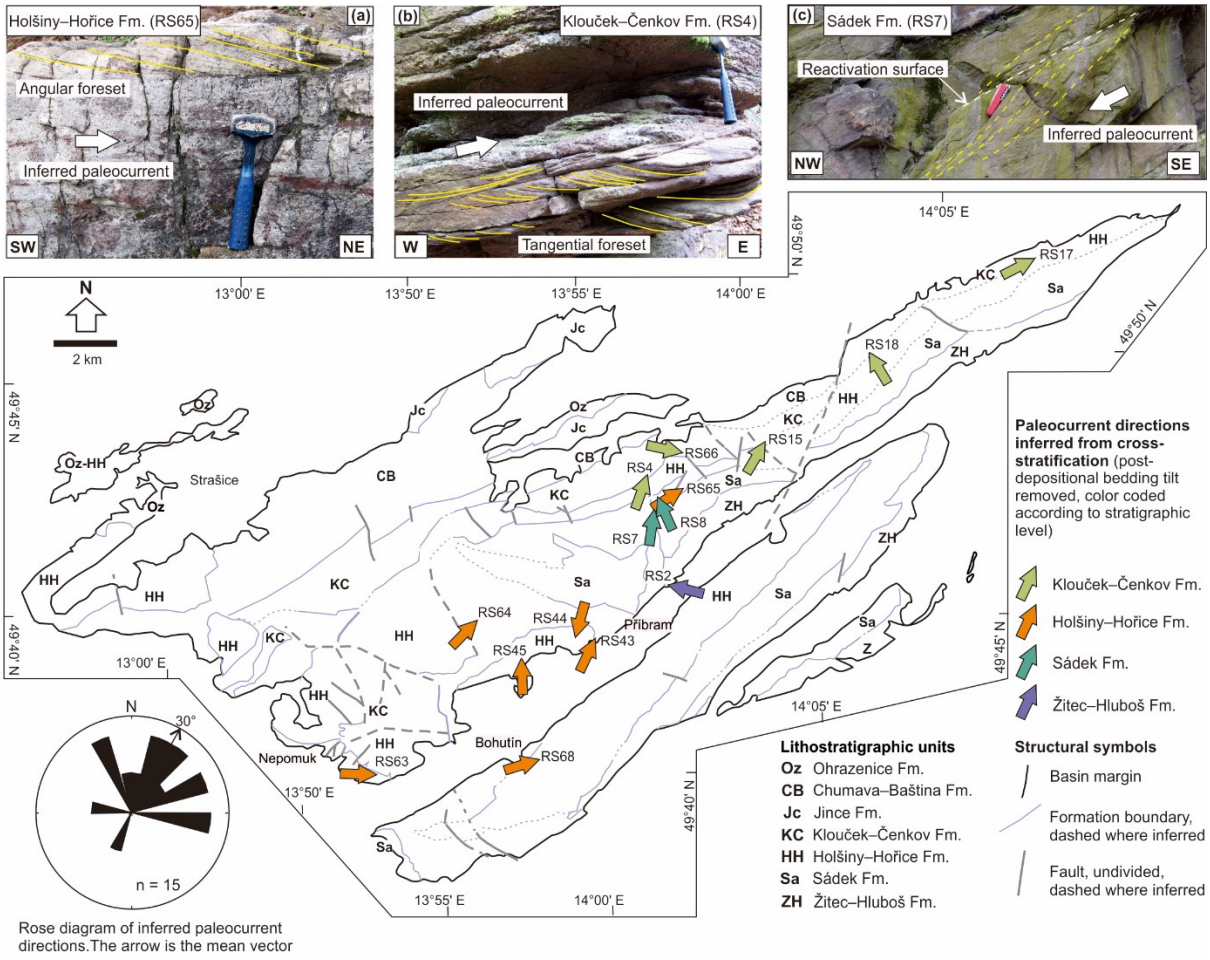


**Figure. 21.** *Inferred paleocurrents from cross-stratification measurements. Mean direction of presumed paleoflowed is ~30° NE, calculated using a method by Fisher et al. (1987). Effects of tilting have been removed. Field examples of (a) angular; near Hořice hill [WGS84 coordinates: N49°45'23.134", E14°1'1.627"] and (b) tangential foresets in planar cross-stratification; Slonovec [WGS84 coordinates: N49°45'42.900", E13°59'50.200"]. (c) Reactivation surface indicating uniform paleoflow to the ~NNW in the Sádek Formation; Bratkovice [WGS84 coordinates: N49°45'4.530", E13°59'59.115"]. Hammer = 26 cm; folded knife = 10 cm.*

### *4.2.7. Microstructures*

Microstructures were examined at 18 stations distributed across the basin in order to characterize the clast compositions and their relationships in the matrix, the presence or absence of volcanic admixture, and deformational features in quartz that could be used to infer the metamorphic grade of the source rocks and thus their provenance. Figure 8 shows representative examples of microstructures within the continental successions in stratigraphic order from the oldest to the youngest.

A conglomerate sample collected from the Žitec–Hluboš Formation (Fig. 22a) comprised subrounded to subangular clasts, typically 4–5 mm in size. Fragments of volcanic rocks (lava, tuff, and volcanic glass, mostly recrystallized) are particularly abundant, with about half of the thin section area made up of skeletal plagioclase. The volcanic fragments are highly variable in size, ranging from 0.1 to 1 mm. On the other hand, the quartz grains are mostly uniform in size (ca. 0.5–0.7 mm). Polycrystalline aggregates within a single clast exhibit undulose extinction and experienced low- to high-temperature dynamic recrystallization ranging from bulging through sub-grain rotation to grain boundary migration (e.g., Blenkinsop, 2000; Stipp et al., 2002; Xia and Platt, 2018). Clastic grains of chlorite are frequent along contacts between the quartz grains, occasionally accompanied by new growth of muscovite.

A fine-grained sandstone (sub-arkose) sample collected from the overlying Sádek Formation (Fig. 22b) is dominated by angular to sub-angular quartz grains (100–250 μm in size) that generally lack undulose extinction. The quartz grains are set in a clay-rich matrix, which also contains abundant clastic grains of chlorite. Volcanic material is absent, and plagioclase occurs only in minor proportions. New growth of muscovite is sparse and crudely aligned with grain contacts. Quartz microveins are common, showing undulose extinction in some cases but no evidence of dynamic recrystallization.

The matrix in a quartz-pebble conglomerate sample from the Holšiny–Hořice Formation (Fig. 22c) is fine to medium-grained and composed of sub-angular to sub-rounded quartz clasts (0.5–2 mm in size). Most of the quartz grains within the clasts exhibit undulose extinction and evidence of low- to high-temperature dynamic recrystallization. Lamellae and other internal features, such as grain–grain contacts, are truncated by the outer clast boundaries (Fig. 22c). Volcanic fragments, mostly composed of recrystallized tuff, are rare, amounting to ca. 5 % of the thin-section area. Clastic grains of chlorite occasionally delineate the clast boundaries.

Quartz-pebble conglomerate samples collected from the Klouček–Čenkov (Fig. 22d), Chumava–Baština (Fig. 22e) and Ohrazenice (Fig. 22f) formations are similar in terms of their microstructure. They exhibit a fine to coarse-grained matrix, and the quartz clasts are sub-angular to sub-rounded, 1–2 mm in size, and show undulose extinction. Most polycrystalline quartz aggregates show evidence of stretching and low- to high-temperature dynamic recrystallization (sub-grain rotation, bulging, and grain boundary migration in the smaller fragments). The modal proportion of volcanic material (mostly recrystallized tuff) increases to 10 % in the Klouček–Čenkov sample (Fig. 22d), but is lower in the Chumava–Baština and Ohrazenice samples (Fig. 22e and 22f). The size of volcanic clasts in the Ohrazenice sample is also generally larger than in the Klouček–Čenkov sample. Clastic grains of chlorite and new growth of muscovite (up to 3–5 % modal proportion) were also observed.

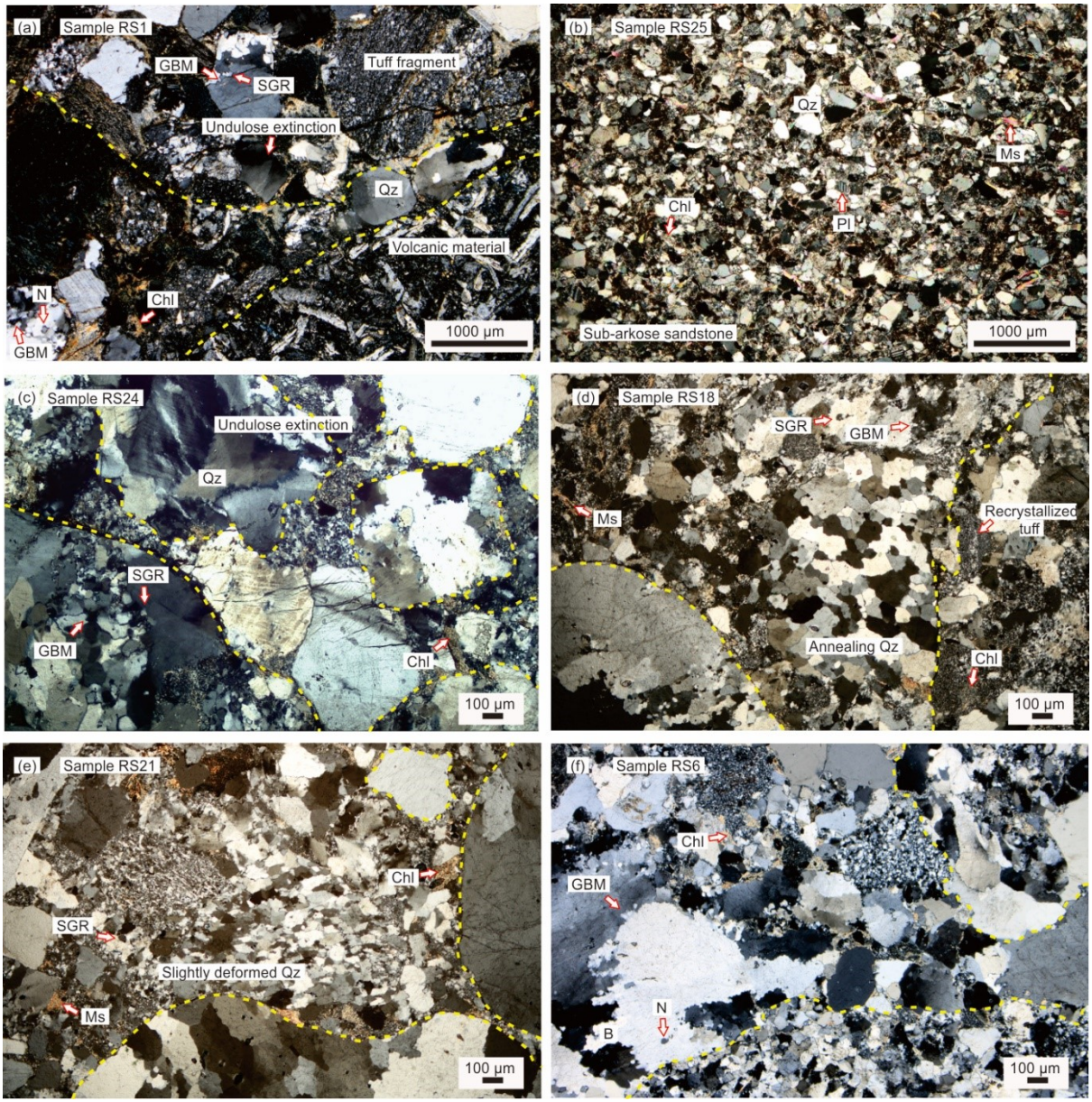


**Figure 22.** *Photomicrographs (cross polars) of conglomerates and sandstones in the Příbram–Jince basin. Yellow dashed lines outline clasts with multiple grains. Most quartz grains show undulose extinction and low- to high-temperature dynamic recrystallization. (a) Polymictic clasts with various volcanic and metamorphic grains in the Žitec–Hluboš Formation (see Fig. 5a for location). (b) Sub-arkose sandstone from the Sádek Formation with quartz embedded in a clay-rich matrix lacking undulose extinction; Bratkovice [WGS84 coordinates: N 49°44'29.404", E 14°0'26.471"]. (c) Conglomerate sample from the Holšiny–Hořice Formation. Quartz grains have lamellae and grain to grain contact; Jezevčí skála [WGS84 coordinates: N49°42'18.539", E13°41'55.344"]. (d–f) Polycrystalline quartz aggregates showing slight deformation. (d) Annealing resulting from grain boundary area reduction; Hradek [WGS84 coordinates: N49°48'46.26", E14°6'28.891"]. Recrystallized tuff most abundant in the Klouček–Čenkov Formation decreases significantly in the (e) Chumava–Baština; Srážka [WGS84 coordinates: N49°42'55.868", E13°46'50.242"] and (f) Ohrazenice formations; Koníček [WGS84 coordinates: N 49°46'33.100", E 13°56'51.800"]. New grain (N) formed by progressive subgrain rotation (SGR). Bulging (B)*

*resulting from grain boundary migration (GBM) that changed into a higher dislocation density. Chl = chlorite, Ms = muscovite, Pl = plagioclase, Qz = quartz.*

### *4.2.8. Material and sampling strategy of AMS*

The AMS samples were taken using a hand-held gasoline-powered drill at 18 stations distributed irregularly across the basin (a full list of samples is available in Table.4). At each station, up to 10 drill cores were taken from both cross-stratified and massive lithologies. Some larger and structurally diverse outcrops were sampled in several places. In that case, the drill cores were clustered in different positions so that, if necessary, each cluster could be treated in terms of statistics as a separate location. Orientation of bedding and cross-stratification were recorded near each cluster of drill cores. The cores were then cut into 285 standard cylindrical specimens (2.1 cm in height and 2.5 cm in diameter) in total.

**Table 4.** *Anisotropy of magnetic susceptibility (AMS) sample locations in the Příbram–Jince basin.*

| No. | Station | Degree, Minute, Second | | Lithology |
|---|---|---|---|---|
| | | Lattitude (Y) | Longitude (X) | |
| **1** | RS2 | 49°43'23.459" | 14°0'48.661" | Red greywacke and conglomerate |
| **2** | RS4 | 49°45'42,900" | 13°59'50,200" | Red quartz conglomerate |
| **3** | RS7 | 49°45'4.530" | 13°59'59.115" | Graywacke sandstone |
| **4** | RS8 | 49°45'17.243" | 14°0'5.154" | Graywacke sandstone |
| **5** | RS9 | 49°45'59.043" | 14°0'26.918" | Sandstone with conglomerate clast at the bottom |
| **6** | RS15 | 49°46'35,463" | 14°3'29,774" | Graywacke sandstone |
| **7** | RS18 | 49°48'46,26" | 14°6'28,891" | Graywacke sandstone |
| **8** | RS21 | 49°42'53,55" | 13°46'48,317" | Graywacke sandstone |
| **9** | RS25 | 49°44'29,404" | 14°0'26,471" | Silty shale |
| **10** | RS36 | 49°41'53,104" | 13°44'6,885" | Quartz conglomerate |
| **11** | RS44 | 49°42'8,526" | 13°58'16,801" | Graywacke sandstone |
| **12** | RS45 | 49°41'33,286" | 13°56'35,607" | Graywacke sandstone |
| **13** | RS50 | 49°41'44,99" | 13°47'30,718" | Quartz conglomerate |
| **14** | RS63 | 49°38'39,838" | 13°52'30,781" | Quartz conglomerate |
| **15** | RS65 | 49°45'23,134" | 14°1'1,627" | Graywacke sandstone |
| **16** | RS68 | 49°39'23.607" | 13°57'24.570" | Graywacke sandstone |
| **17** | RS72 | 49°46'22.002" | 14°0'9.679" | Graywacke sandstone |
| **18** | RS73 | 49°43'3.798" | 13°55'49.494" | Silty shale |

For each station, 7–39 specimens were taken. The specimens were measured in the Laboratory of Rock Magnetism, Institute of Geology and Paleontology, Charles University, Prague using an Agico MFK1-A Multi-function Kappabridge, which was supported by Safyr 7.0 instrument control software, and analyzed using Anisoft 5 software (written by M. Chadima, F. Hrouda, and V. Jelínek; www.agico.com). A full list of the measured AMS parameters is provided in Table 5.

**Table 5.** *AMS parameters in the Příbram–Jince basin.*

| Station | Specimen | *P* | *T* | $K_m$ | $K_1$-*Dec* | $K_1$-*Inc* | $K_3$-*Dec* | $K_3$-*Inc* |
|---|---|---|---|---|---|---|---|---|
| **RS2** | RS2/1/1 | 1.0242 | 0.8743 | 1.30E-04 | 331 | 30 | 124 | 57 |
| | RS2/1/2 | 1.0891 | -0.2544 | 1.44E-04 | 339 | 26 | 239 | 20 |
| | RS2/1/3 | 1.0134 | -0.2926 | 1.29E-04 | 32 | 19 | 124 | 8 |
| | RS2/1/4 | 1.0124 | -0.8813 | 1.18E-04 | 356 | 32 | 180 | 58 |
| | RS2/2/1 | 1.0164 | -0.2952 | 1.29E-04 | 20 | 14 | 127 | 49 |
| | RS2/2/2 | 1.0171 | -0.2304 | 1.29E-04 | 5 | 25 | 152 | 61 |
| | RS2/2/3 | 1.0106 | -0.5387 | 1.25E-04 | 23 | 25 | 153 | 54 |
| | RS2/2/4 | 1.0148 | -0.1938 | 1.15E-04 | 27 | 28 | 168 | 55 |
| | RS2/3/2 | 1.0167 | -0.3816 | 1.12E-04 | 344 | 20 | 106 | 56 |
| | RS2/3/4 | 1.0145 | -0.5522 | 1.12E-04 | 339 | 30 | 145 | 59 |
| | RS2/3/2 | 1.0165 | -0.3536 | 1.11E-04 | 10 | 15 | 140 | 68 |
| | RS2/3/4 | 1.0146 | -0.5409 | 1.12E-04 | 1 | 25 | 195 | 64 |
| | RS2/4/1 | 1.0129 | -0.2447 | 1.26E-04 | 353 | 19 | 111 | 54 |
| | RS2/4/2 | 1.0167 | -0.6907 | 1.34E-04 | 341 | 21 | 111 | 60 |
| | RS2/4/3 | 1.0393 | 0.199 | 1.30E-04 | 299 | 49 | 99 | 39 |
| | RS2/4/4 | 1.0155 | 0.6219 | 1.21E-04 | 335 | 10 | 240 | 24 |
| | RS2/4/5 | 1.0248 | -0.5044 | 1.28E-04 | 315 | 37 | 101 | 48 |
| | RS2/5/1 | 1.0161 | -0.2787 | 1.25E-04 | 73 | 29 | 343 | 1 |
| | RS2/5/2 | 1.0121 | -0.2061 | 1.24E-04 | 71 | 27 | 332 | 18 |
| | RS2/5/3 | 1.0158 | -0.2535 | 1.03E-04 | 43 | 23 | 192 | 64 |
| | RS2/6/1 | 1.0326 | 0.7568 | 1.30E-04 | 191 | 80 | 25 | 10 |
| | RS2/6/2 | 1.0159 | -0.5446 | 1.32E-04 | 23 | 11 | 157 | 74 |
| | RS2/6/3 | 1.0246 | -0.0549 | 1.15E-04 | 50 | 17 | 319 | 4 |
| | RS2/6/4 | 1.0115 | -0.4655 | 1.16E-04 | 17 | 24 | 229 | 63 |
| | RS2/7/1 | 1.0156 | -0.4702 | 1.14E-04 | 357 | 24 | 185 | 66 |
| | RS2/7/2 | 1.0148 | -0.7493 | 1.27E-04 | 358 | 20 | 224 | 63 |
| | RS2/7/3 | 1.0128 | 0.0651 | 1.13E-04 | 11 | 23 | 175 | 66 |

| | | | | | | | | |
|---|---|---|---|---|---|---|---|---|
| | RS2/8/1 | 1.059 | 0.1836 | 1.95E-04 | 1 | 18 | 95 | 13 |
| | RS2/8/2 | 1.0164 | -0.2328 | 1.35E-04 | 27 | 6 | 121 | 36 |
| | RS2/8/3 | 1.0142 | 0.3111 | 1.13E-04 | 19 | 48 | 204 | 42 |
| | RS2/8/4 | 1.038 | 0.3198 | 1.13E-04 | 28 | 18 | 121 | 7 |
| | RS2/8/5 | 1.0175 | -0.5975 | 8.28E-05 | 21 | 16 | 288 | 12 |
| | RS2/9/1 | 1.0255 | -0.0013 | 1.89E-04 | 182 | 2 | 272 | 1 |
| | RS2/9/2 | 1.1117 | 0.3765 | 1.31E-04 | 337 | 9 | 245 | 17 |
| | RS2/9/3 | 1.0179 | -0.0839 | 1.12E-04 | 35 | 16 | 132 | 22 |
| | RS2/10/1 | 1.0281 | 0.4506 | 1.13E-04 | 8 | 12 | 99 | 2 |
| | RS2/10/2 | 1.0417 | -0.0802 | 1.10E-04 | 8 | 55 | 172 | 34 |
| | RS2/10/3 | 1.0124 | -0.7051 | 1.13E-04 | 222 | 1 | 132 | 1 |
| | RS2/10/4 | 1.0343 | 0.6449 | 1.30E-04 | 223 | 7 | 130 | 22 |
| **RS4** | RS4/1/1 | 1.0146 | 0.2563 | 3.31E-05 | 66 | 16 | 322 | 40 |
| | RS4/1/2 | 1.0208 | 0.2616 | 2.87E-05 | 231 | 2 | 323 | 42 |
| | RS4/1/3 | 1.0276 | 0.0514 | 3.49E-05 | 65 | 6 | 330 | 42 |
| | RS4/1/4 | 1.0442 | 0.1473 | 2.76E-05 | 55 | 5 | 312 | 68 |
| | RS4/1/5 | 1.0324 | 0.4802 | 2.49E-05 | 63 | 19 | 310 | 49 |
| | RS4/2/1 | 1.0369 | 0.7026 | 3.18E-05 | 59 | 15 | 318 | 34 |
| | RS4/2/2 | 1.0276 | -0.0016 | 3.38E-05 | 68 | 22 | 320 | 38 |
| | RS4/2/3 | 1.0403 | -0.3574 | 3.23E-05 | 87 | 34 | 299 | 51 |
| | RS4/2/4 | 1.0291 | 0.4576 | 2.76E-05 | 66 | 16 | 324 | 36 |
| | RS4/2/5 | 1.0265 | 0.2716 | 2.95E-05 | 69 | 23 | 324 | 31 |
| | RS4/2/6 | 1.0255 | 0.5013 | 2.39E-05 | 63 | 12 | 326 | 32 |
| | RS4/3/1 | 1.019 | 0.4812 | 3.81E-05 | 78 | 51 | 302 | 30 |
| | RS4/3/2 | 1.0323 | 0.5116 | 4.39E-05 | 132 | 74 | 326 | 16 |
| | RS4/3/3 | 1.0269 | 0.1942 | 3.69E-05 | 197 | 24 | 307 | 37 |
| | RS4/3/4 | 1.0173 | 0.4672 | 3.73E-05 | 213 | 0 | 303 | 44 |
| | RS4/3/5 | 1.0175 | -0.0908 | 3.43E-05 | 205 | 9 | 307 | 52 |
| | RS4/3/6 | 1.0171 | 0.3706 | 3.23E-05 | 208 | 15 | 307 | 30 |
| | RS4/4/1 | 1.0181 | 0.1272 | 3.74E-05 | 33 | 10 | 294 | 43 |
| | RS4/4/2 | 1.023 | -0.0238 | 3.65E-05 | 208 | 13 | 306 | 31 |
| | RS4/4/3 | 1.0253 | 0.8357 | 2.27E-05 | 97 | 57 | 299 | 31 |
| | RS4/5/1 | 1.0258 | 0.486 | 2.25E-05 | 161 | 40 | 316 | 47 |
| | RS4/5/2 | 1.0192 | 0.8314 | 2.71E-05 | 82 | 16 | 334 | 48 |
| | RS4/5/3 | 1.0407 | 0.1771 | 3.18E-05 | 68 | 1 | 337 | 48 |
| | RS4/5/4 | 1.1416 | 0.1747 | 4.04E-05 | 175 | 4 | 288 | 79 |
| | RS4/5/5 | 1.0231 | -0.1802 | 3.48E-05 | 67 | 10 | 320 | 58 |
| | RS4/6/1 | 1.0718 | 0.4545 | 2.45E-05 | 62 | 6 | 328 | 36 |
| | RS4/6/2 | 1.034 | 0.7542 | 2.08E-05 | 77 | 22 | 327 | 39 |

| | | | | | | | | |
|---|---|---|---|---|---|---|---|---|
| | RS4/6/3 | 1.0449 | 0.4621 | 2.11E-05 | 59 | 10 | 322 | 35 |
| | RS4/6/4 | 1.0325 | 0.016 | 2.46E-05 | 52 | 3 | 320 | 44 |
| | RS4/6/5 | 1.0673 | 0.4696 | 2.86E-05 | 56 | 6 | 322 | 33 |
| | RS4/6/6 | 1.0423 | 0.1024 | 2.22E-05 | 62 | 5 | 328 | 35 |
| **RS7** | RS7/1/1 | 1.5459 | 0.9176 | 1.13E-04 | 322 | 55 | 133 | 35 |
| | RS7/1/2 | 2.0179 | 0.6163 | 1.91E-04 | 318 | 49 | 178 | 33 |
| | RS7/1/3 | 1.0639 | 0.6079 | 6.89E-05 | 44 | 79 | 219 | 11 |
| | RS7/1/4 | 1.299 | 0.6313 | 8.96E-05 | 331 | 46 | 99 | 30 |
| | RS7/1/5 | 1.1576 | 0.7933 | 8.48E-05 | 350 | 45 | 126 | 35 |
| | RS7/1/6 | 1.0112 | 0.2327 | 8.54E-05 | 53 | 22 | 201 | 65 |
| | RS7/1/7 | 1.015 | 0.4339 | 1.02E-04 | 34 | 14 | 160 | 67 |
| | RS7/1/8 | 1.0187 | 0.7607 | 1.24E-04 | 255 | 2 | 161 | 62 |
| | RS7/2/1 | 1.0965 | -0.2744 | 1.13E-04 | 311 | 47 | 58 | 15 |
| | RS7/2/2 | 1.1756 | 0.7035 | 1.04E-04 | 319 | 53 | 165 | 34 |
| | RS7/2/3 | 1.1979 | 0.7997 | 1.01E-04 | 312 | 53 | 127 | 37 |
| | RS7/2/4 | 1.0804 | 0.6471 | 8.38E-05 | 181 | 6 | 88 | 24 |
| | RS7/2/5 | 1.0662 | 0.4215 | 9.34E-05 | 351 | 7 | 84 | 25 |
| | RS7/2/6 | 1.0126 | -0.3613 | 7.77E-05 | 10 | 2 | 106 | 70 |
| | RS7/3/1 | 1.0239 | 0.0656 | 2.97E-04 | 319 | 29 | 120 | 60 |
| | RS7/3/2 | 1.0604 | 0.1046 | 2.99E-04 | 349 | 18 | 253 | 18 |
| | RS7/3/3 | 1.0494 | 0.1867 | 2.82E-04 | 315 | 37 | 210 | 19 |
| | RS7/3/4 | 1.0543 | -0.22 | 2.28E-04 | 7 | 50 | 247 | 23 |
| | RS7/3/5 | 1.0194 | 0.5063 | 2.04E-04 | 353 | 20 | 120 | 59 |
| | RS7/4/1 | 1.0177 | -0.0212 | 1.92E-04 | 3 | 12 | 196 | 78 |
| | RS7/4/3 | 1.0595 | 0.6788 | 2.36E-04 | 87 | 22 | 177 | 1 |
| | RS7/4/4 | 1.0168 | 0.2755 | 2.20E-04 | 73 | 7 | 188 | 75 |
| | RS7/4/5 | 1.0205 | 0.2959 | 2.58E-04 | 69 | 6 | 179 | 74 |
| | RS7/4/6 | 1.0189 | 0.328 | 2.40E-04 | 81 | 2 | 178 | 73 |
| | RS7/5/1 | 1.0207 | 0.6997 | 2.72E-04 | 287 | 23 | 77 | 64 |
| | RS7/5/3 | 1.2043 | 0.5328 | 2.17E-04 | 269 | 25 | 0 | 3 |
| | RS7/5/4 | 1.0179 | 0.497 | 1.92E-04 | 297 | 23 | 73 | 60 |
| | RS7/5/5 | 1.0181 | 0.5036 | 1.99E-04 | 306 | 20 | 78 | 61 |
| | RS7/5/6 | 1.0204 | 0.2998 | 2.16E-04 | 316 | 22 | 89 | 60 |
| **RS8** | RS8/1/1 | 2.3717 | 0.7527 | 4.45E-05 | 342 | 27 | 178 | 62 |
| | RS8/1/2 | 1.0317 | -0.2597 | 1.00E-05 | 304 | 29 | 52 | 30 |
| | RS8/1/3 | 1.0248 | -0.0577 | 8.37E-03 | 166 | 4 | 74 | 33 |
| | RS8/2/1 | 1.0679 | 0.909 | 1.27E-05 | 156 | 57 | 10 | 28 |
| | RS8/2/2 | 1.0736 | 0.7046 | 1.28E-05 | 233 | 57 | 16 | 28 |
| | RS8/2/3 | 1.364 | 0.4175 | 1.90E-05 | 155 | 57 | 24 | 23 |

| | | | | | | | | |
|---|---|---|---|---|---|---|---|---|
| | RS8/2/4 | 1.4471 | 0.7196 | 1.97E-05 | 132 | 39 | 23 | 22 |
| | RS8/2/5 | 1.0874 | 0.6617 | 9.33E-03 | 275 | 10 | 10 | 27 |
| **RS9** | RS9/1/1 | 1.2792 | 0.8186 | 8.17E-05 | 351 | 47 | 196 | 40 |
| | RS9/1/2 | 1.2619 | 0.4671 | 1.00E-04 | 355 | 48 | 191 | 41 |
| | RS9/1/3 | 1.0742 | 0.6929 | 7.24E-05 | 342 | 39 | 217 | 35 |
| | RS9/1/4 | 1.0182 | 0.2546 | 7.06E-05 | 284 | 2 | 15 | 46 |
| | RS9/1/5 | 1.0172 | 0.2899 | 6.70E-05 | 250 | 25 | 24 | 56 |
| | RS9/2/1 | 1.2563 | 0.7141 | 8.27E-05 | 6 | 46 | 125 | 25 |
| | RS9/2/2 | 1.1437 | 0.4976 | 9.73E-05 | 2 | 44 | 141 | 38 |
| | RS9/2/3 | 1.0587 | 0.2723 | 7.86E-05 | 55 | 14 | 162 | 49 |
| | RS9/2/4 | 1.0814 | 0.7677 | 7.66E-05 | 222 | 0 | 132 | 33 |
| | RS9/2/5 | 1.015 | 0.6029 | 6.78E-05 | 270 | 26 | 115 | 61 |
| **RS15** | RS15/1/1 | 2.218 | -0.5858 | -2.32E-03 | 138 | 13 | 258 | 66 |
| | RS15/1/2 | 1.3074 | -0.806 | -3.59E-03 | 149 | 9 | 261 | 67 |
| | RS15/1/3 | 1.145 | -0.8488 | -4.85E-03 | 133 | 15 | 260 | 67 |
| | RS15/1/4 | 1.0427 | 0.2702 | -5.19E-03 | 99 | 16 | 352 | 45 |
| | RS15/2/1 | 1.4939 | -0.7398 | -3.07E-03 | 103 | 18 | 308 | 70 |
| | RS15/2/2 | 1.1477 | -0.5402 | -4.07E-03 | 54 | 0 | 323 | 69 |
| | RS15/2/3 | 1.3769 | -0.7764 | -3.64E-03 | 149 | 19 | 326 | 71 |
| | RS15/2/4 | 3.907 | -0.4903 | -9.68E-07 | 173 | 17 | 299 | 62 |
| | RS15/2/5 | 1.9449 | -0.647 | -2.03E-03 | 181 | 15 | 310 | 67 |
| | RS15/3/1 | 1.1287 | 0.1728 | -3.58E-03 | 96 | 28 | 293 | 61 |
| | RS15/3/2 | 1.4094 | -0.5945 | -4.30E-03 | 117 | 22 | 268 | 65 |
| | RS15/3/3 | 1.2064 | -0.7603 | -5.17E-03 | 162 | 11 | 272 | 60 |
| | RS15/3/4 | 1.335 | -0.7771 | -5.21E-03 | 16 | 7 | 273 | 62 |
| | RS15/4/1 | 1.1156 | 0.6384 | 1.62E-05 | 314 | 55 | 170 | 30 |
| | RS15/4/2 | 1.0794 | 0.8655 | 2.52E-05 | 196 | 30 | 23 | 60 |
| **RS18** | RS18/1/1 | 1.0369 | -0.4882 | 1.12E-05 | 272 | 6 | 155 | 76 |
| | RS18/1/2 | 1.0377 | 0.2122 | 1.16E-05 | 62 | 4 | 161 | 62 |
| | RS18/1/3 | 1.0332 | 0.2471 | 1.00E-05 | 278 | 6 | 36 | 78 |
| | RS18/1/4 | 1.0275 | 0.4676 | 9.92E-03 | 10 | 6 | 270 | 59 |
| | RS18/1/5 | 1.0221 | -0.644 | 9.48E-03 | 255 | 13 | 6 | 56 |
| | RS18/1/6 | 1.0866 | 0.4124 | 8.53E-03 | 149 | 22 | 277 | 57 |
| | RS18/1/7 | 1.1172 | 0.1312 | 6.42E-03 | 294 | 11 | 41 | 55 |
| | RS18/2/1 | 1.0138 | -0.6157 | 1.11E-05 | 224 | 5 | 318 | 37 |
| | RS18/2/2 | 1.0271 | 0.1639 | 1.16E-05 | 276 | 35 | 140 | 47 |
| | RS18/2/3 | 1.054 | 0.2634 | 1.26E-05 | 74 | 12 | 235 | 78 |
| | RS18/2/4 | 1.0238 | 0.0597 | 1.16E-05 | 42 | 24 | 194 | 64 |
| | RS18/2/5 | 1.17 | 0.7793 | 1.36E-05 | 78 | 1 | 171 | 76 |

| | | | | | | | | |
|---|---|---|---|---|---|---|---|---|
| | RS18/2/6 | 1.0574 | 0.3082 | 1.07E-05 | 59 | 3 | 169 | 81 |
| **RS21** | RS21/1/1 | 1.1382 | -0.4292 | -5.65E-03 | 258 | 8 | 102 | 82 |
| | RS21/1/2 | 1.0566 | 0.0695 | -4.61E-03 | 282 | 8 | 154 | 77 |
| | RS21/1/3 | 1.0601 | -0.2647 | -5.29E-03 | 51 | 1 | 147 | 78 |
| | RS21/1/4 | 1.4249 | -0.6913 | -4.31E-03 | 237 | 2 | 125 | 85 |
| | RS21/1/5 | 1.5149 | -0.7065 | -5.40E-03 | 310 | 5 | 152 | 85 |
| | RS21/1/6 | 1.742 | -0.3482 | 2.95E-05 | 225 | 39 | 356 | 39 |
| | RS21/1/7 | 1.0311 | -0.6521 | -6.31E-03 | 97 | 53 | 191 | 4 |
| **RS25** | RS25/1/1 | 1.0055 | 0.4097 | 1.82E-04 | 275 | 13 | 176 | 31 |
| | RS25/1/2 | 1.0077 | 0.3061 | 1.83E-04 | 298 | 25 | 186 | 39 |
| | RS25/1/3 | 1.0142 | 0.6345 | 1.70E-04 | 31 | 19 | 133 | 30 |
| | RS25/1/4 | 1.0178 | 0.6724 | 1.64E-04 | 213 | 5 | 120 | 31 |
| | RS25/1/5 | 1.0178 | 0.4798 | 1.89E-04 | 216 | 7 | 122 | 33 |
| | RS25/1/6 | 1.0197 | 0.5692 | 1.98E-04 | 220 | 1 | 129 | 31 |
| | RS25/1/7 | 1.0176 | 0.2949 | 2.14E-04 | 345 | 71 | 163 | 19 |
| | RS25/2/1 | 1.0078 | 0.3841 | 1.61E-04 | 5 | 44 | 117 | 21 |
| | RS25/2/2 | 1.01 | 0.5174 | 1.74E-04 | 224 | 6 | 133 | 17 |
| | RS25/2/3 | 1.0126 | 0.5565 | 1.93E-04 | 222 | 0 | 132 | 17 |
| | RS25/2/4 | 1.0167 | 0.3889 | 1.95E-04 | 44 | 5 | 136 | 24 |
| | RS25/2/5 | 1.0164 | 0.3099 | 1.84E-04 | 219 | 1 | 129 | 15 |
| **RS36** | RS36/1/1 | 1.0654 | -0.5628 | -8.06E-03 | 62 | 28 | 173 | 34 |
| | RS36/1/3 | 1.0411 | 0.1685 | -6.58E-03 | 357 | 14 | 255 | 40 |
| | RS36/1/4 | 1.03 | -0.1725 | -9.31E-03 | 8 | 13 | 196 | 77 |
| | RS36/1/5 | 1.305 | -0.3518 | -5.88E-03 | 326 | 25 | 168 | 63 |
| | RS36/1/6 | 1.0793 | -0.8433 | -7.33E-03 | 47 | 1 | 141 | 80 |
| | RS36/2/1 | 1.0551 | -0.8079 | -8.40E-03 | 50 | 4 | 291 | 82 |
| | RS36/2/2 | 1.098 | -0.0406 | -7.41E-03 | 303 | 10 | 106 | 80 |
| | RS36/2/3 | 1.1283 | -0.0079 | -8.10E-03 | 130 | 8 | 10 | 75 |
| | RS36/2/4 | 1.0247 | -0.6458 | -8.96E-03 | 305 | 4 | 48 | 74 |
| | RS36/2/5 | 1.0357 | -0.2405 | -8.53E-03 | 346 | 17 | 178 | 73 |
| **RS44** | RS44/1/1 | 1.0245 | 0.118 | 5.88E-05 | 184 | 11 | 302 | 67 |
| | RS44/1/2 | 1.0212 | -0.1953 | 6.71E-05 | 179 | 16 | 6 | 74 |
| | RS44/1/3 | 1.0207 | 0.12 | 7.59E-05 | 193 | 8 | 35 | 81 |
| | RS44/1/4 | 1.0206 | 0.4342 | 8.52E-05 | 208 | 13 | 62 | 74 |
| | RS44/1/5 | 1.0244 | 0.4056 | 9.25E-05 | 202 | 3 | 33 | 87 |
| | RS44/1/6 | 1.0233 | 0.3273 | 9.20E-05 | 210 | 12 | 64 | 75 |
| | RS44/1/7 | 1.0269 | 0.3033 | 9.20E-05 | 204 | 0 | 296 | 78 |
| | RS44/2/1 | 1.0185 | -0.1354 | 5.76E-05 | 310 | 19 | 195 | 51 |
| **RS45** | RS45/1/1 | -2.9 | 0.9 | 1.41E-03 | 223 | 34 | 333 | 27 |

| | | | | | | | | |
|---|---|---|---|---|---|---|---|---|
| | RS45/1/2 | 2.2 | -0.5831 | -1.28E-03 | 101 | 50 | 337 | 25 |
| | RS45/1/3 | 2.9 | -0.1977 | -1.22E-03 | 78 | 21 | 337 | 28 |
| | RS45/1/4 | -0.2 | 0.9 | -2.16E-07 | 91 | 47 | 334 | 23 |
| | RS45/2/1 | -1.9 | 0.9 | 7.91E-07 | 243 | 12 | 336 | 15 |
| | RS45/2/2 | -1.3 | 0.9 | 7.95E-07 | 241 | 20 | 337 | 17 |
| | RS45/2/3 | -0.8 | 0.9 | 3.10E-07 | 70 | 5 | 338 | 21 |
| | RS45/2/4 | -7.5 | 0.9 | 1.69E-03 | 243 | 14 | 339 | 21 |
| | RS45/2/5 | 7.3 | 0.9394 | 3.35E-03 | 85 | 39 | 334 | 23 |
| **RS50** | RS50/1/1 | 1.0491 | -0.0795 | -6.22E-03 | 134 | 12 | 251 | 66 |
| | RS50/1/2 | 1.1026 | -0.7755 | -7.79E-03 | 36 | 27 | 259 | 55 |
| | RS50/2/1 | 1.0438 | -0.8402 | -5.67E-03 | 29 | 9 | 274 | 70 |
| | RS50/2/2 | 1.048 | -0.6287 | -6.11E-03 | 106 | 36 | 284 | 54 |
| | RS50/2/3 | 1.1611 | -0.2038 | -6.69E-03 | 33 | 16 | 289 | 39 |
| | RS50/2/4 | 1.1171 | -0.7829 | -5.41E-03 | 28 | 17 | 271 | 57 |
| | RS50/3/1 | 1.6987 | -0.7159 | -3.89E-03 | 351 | 22 | 240 | 40 |
| **RS63** | RS63/1/1 | 1.6138 | 0.638 | 5.99E-03 | 344 | 20 | 227 | 51 |
| | RS63/2/1 | 1.237 | 0.7113 | 3.59E-03 | 169 | 14 | 75 | 15 |
| | RS63/2/2 | 1.4268 | 0.0325 | 1.85E-03 | 340 | 5 | 248 | 12 |
| **RS65** | RS65/1/1 | 1.0746 | -0.8361 | 1.19E-05 | 240 | 16 | 139 | 32 |
| | RS65/1/2 | 1.3929 | 0.7001 | 1.36E-05 | 242 | 13 | 349 | 51 |
| | RS65/1/3 | 1.2071 | 0.578 | 1.96E-05 | 244 | 11 | 347 | 51 |
| | RS65/1/4 | 1.2011 | 0.6569 | 1.58E-05 | 104 | 19 | 350 | 50 |
| | RS65/1/5 | 1.1612 | 0.6645 | 1.19E-05 | 109 | 29 | 338 | 50 |
| | RS65/2/1 | 1.3861 | 0.7008 | 1.24E-05 | 235 | 17 | 348 | 52 |
| | RS65/2/2 | 1.4857 | 0.7784 | 1.24E-05 | 218 | 30 | 2 | 54 |
| | RS65/2/3 | 1.3917 | 0.8507 | 1.29E-05 | 231 | 26 | 4 | 55 |
| | RS65/2/4 | 1.6377 | 0.8556 | 1.59E-05 | 136 | 29 | 358 | 53 |
| | RS65/2/5 | 1.2603 | 0.9378 | 1.25E-05 | 196 | 34 | 351 | 53 |
| | RS65/2/6 | 1.0482 | 0.4113 | 8.85E-03 | 174 | 31 | 360 | 59 |
| | RS65/2/7 | 1.0755 | 0.5019 | 7.50E-03 | 228 | 28 | 8 | 55 |
| | RS65/3/1 | 1.5114 | -0.0766 | 2.12E-05 | 150 | 20 | 338 | 70 |
| | RS65/3/2 | 1.6438 | 0.559 | 3.00E-05 | 169 | 25 | 345 | 65 |
| | RS65/3/3 | 1.6699 | 0.6202 | 2.03E-05 | 187 | 22 | 341 | 66 |
| | RS65/3/4 | 1.5319 | 0.8518 | 1.64E-05 | 201 | 21 | 341 | 64 |
| | RS65/3/5 | 1.3431 | 0.9272 | 1.10E-05 | 217 | 14 | 344 | 67 |
| | RS65/3/6 | 1.5043 | 0.8678 | 1.61E-05 | 152 | 26 | 344 | 64 |
| | RS65/3/7 | 1.463 | 0.5695 | 1.46E-05 | 148 | 24 | 336 | 66 |
| | RS65/4/1 | 1.2353 | 0.6363 | 1.33E-05 | 142 | 26 | 353 | 60 |
| | RS65/4/2 | 1.5156 | 0.8276 | 1.67E-05 | 174 | 27 | 352 | 63 |

| | | | | | | | | |
|---|---|---|---|---|---|---|---|---|
| | RS65/4/3 | 1.3761 | 0.6049 | 1.43E-05 | 237 | 11 | 344 | 59 |
| | RS65/4/4 | 1.3364 | 0.8781 | 1.62E-05 | 175 | 26 | 340 | 64 |
| | RS65/4/5 | 1.5369 | 0.2925 | 2.38E-05 | 131 | 34 | 319 | 56 |
| | RS65/4/6 | 1.2839 | 0.4001 | 1.32E-05 | 161 | 31 | 335 | 59 |
| | RS65/4/7 | 1.2276 | 0.6539 | 1.25E-05 | 153 | 30 | 354 | 58 |
| | RS65/4/8 | 1.0636 | 0.81 | 1.04E-05 | 232 | 14 | 350 | 62 |
| | RS65/5/1 | 1.582 | 0.8844 | 1.29E-05 | 249 | 18 | 360 | 49 |
| | RS65/5/2 | 1.1701 | 0.5828 | 2.24E-05 | 163 | 21 | 28 | 61 |
| | RS65/5/3 | 1.3822 | 0.6473 | 5.55E-03 | 267 | 12 | 8 | 43 |
| | RS65/5/4 | 1.2549 | 0.8575 | 1.21E-05 | 227 | 28 | 4 | 54 |
| | RS65/5/5 | 1.304 | 0.9069 | 1.74E-05 | 259 | 15 | 5 | 47 |
| | RS65/5/6 | 1.618 | 0.6631 | 1.47E-05 | 193 | 41 | 359 | 48 |
| | RS65/5/7 | 1.4916 | 0.7842 | 1.12E-05 | 245 | 30 | 5 | 42 |
| | RS65/5/8 | 1.5542 | -0.2125 | 1.76E-05 | 218 | 30 | 29 | 60 |
| **RS68** | RS68/1/1 | 1.2128 | 0.0222 | 3.94E-02 | 20 | 11 | 289 | 4 |
| | RS68/1/2 | 1.1693 | -0.2472 | 4.00E-02 | 20 | 14 | 288 | 11 |
| | RS68/1/3 | 1.2006 | 0.0186 | 4.23E-02 | 24 | 31 | 291 | 4 |
| | RS68/1/4 | 1.2301 | 0.254 | 6.37E-02 | 19 | 24 | 110 | 1 |
| | RS68/1/5 | 1.247 | 0.5512 | 5.41E-02 | 16 | 9 | 107 | 5 |
| | RS68/1/6 | 1.1897 | -0.1417 | 3.93E-02 | 16 | 16 | 286 | 0 |
| | RS68/2/1 | 1.1925 | -0.0297 | 3.92E-02 | 30 | 17 | 300 | 1 |
| | RS68/2/2 | 1.1856 | -0.0538 | 3.92E-02 | 30 | 19 | 299 | 5 |
| | RS68/2/3 | 1.1978 | -0.1234 | 3.27E-02 | 30 | 17 | 297 | 9 |
| | RS68/2/4 | 1.2087 | -0.0657 | 3.17E-02 | 35 | 15 | 302 | 8 |
| | RS68/2/5 | 1.2009 | -0.1404 | 3.22E-02 | 31 | 15 | 300 | 2 |
| | RS68/2/6 | 1.2012 | -0.176 | 3.29E-02 | 30 | 16 | 297 | 9 |
| **RS72** | RS72/1/1 | 1.0077 | -0.5282 | 4.08E-05 | 251 | 17 | 53 | 72 |
| | RS72/1/2 | 1.3737 | 0.5756 | 4.22E-05 | 355 | 1 | 265 | 5 |
| | RS72/1/3 | 1.0335 | 0.5584 | 2.43E-05 | 244 | 9 | 95 | 80 |
| | RS72/1/4 | 1.0912 | 0.7417 | 1.24E-05 | 313 | 10 | 95 | 77 |
| | RS72/1/5 | 1.0764 | 0.8153 | 1.47E-05 | 250 | 14 | 71 | 76 |
| | RS72/1/6 | 1.0509 | 0.1837 | 6.53E-03 | 284 | 16 | 80 | 72 |
| | RS72/2/1 | 1.0289 | 0.8431 | 4.40E-05 | 205 | 4 | 101 | 74 |
| | RS72/2/2 | 1.0688 | 0.4923 | 1.97E-05 | 286 | 17 | 106 | 73 |
| | RS72/2/3 | 1.0904 | 0.9688 | 1.73E-05 | 315 | 16 | 104 | 71 |
| | RS72/2/4 | 1.0962 | 0.7502 | 1.52E-05 | 210 | 9 | 91 | 71 |
| | RS72/2/5 | 1.1159 | 0.7125 | 1.58E-05 | 265 | 16 | 99 | 74 |
| | RS72/2/6 | 1.0953 | 0.9966 | 1.28E-05 | 304 | 16 | 88 | 71 |
| | RS72/2/7 | 1.5466 | 0.7001 | 1.09E-05 | 304 | 21 | 96 | 67 |

| | | | | | | | | |
|---|---|---|---|---|---|---|---|---|
| | RS72/3/1 | 1.0193 | 0.5937 | 2.56E-05 | 229 | 8 | 116 | 70 |
| | RS72/3/2 | 1.0129 | -0.1076 | 3.41E-05 | 184 | 30 | 71 | 34 |
| | RS72/3/3 | 1.0236 | 0.4768 | 1.71E-05 | 214 | 2 | 108 | 83 |
| | RS72/4/1 | 1.035 | 0.2293 | 5.87E-05 | 349 | 7 | 258 | 7 |
| | RS72/4/2 | 1.3064 | 0.6498 | 6.82E-05 | 226 | 7 | 319 | 18 |
| | RS72/4/3 | 1.099 | 0.3151 | 1.69E-05 | 244 | 15 | 122 | 64 |
| | RS72/4/4 | 1.0725 | -0.7146 | 1.39E-05 | 14 | 8 | 283 | 4 |
| | RS72/4/5 | 1.0102 | 0.4691 | 3.04E-05 | 318 | 12 | 108 | 76 |
| | RS72/4/6 | 1.0816 | 0.3743 | 8.44E-03 | 249 | 9 | 125 | 74 |
| **RS73** | RS73/1/1 | 1.0084 | 0.4913 | 2.71E-04 | 326 | 5 | 64 | 56 |
| | RS73/1/2 | 1.0121 | 0.5282 | 2.66E-04 | 329 | 5 | 67 | 58 |
| | RS73/1/3 | 1.0077 | 0.3605 | 2.60E-04 | 327 | 1 | 59 | 71 |
| | RS73/1/4 | 1.0095 | 0.197 | 2.59E-04 | 316 | 21 | 101 | 66 |
| | RS73/1/5 | 1.0131 | 0.4552 | 2.51E-04 | 318 | 20 | 115 | 69 |
| | RS73/1/6 | 1.0154 | 0.6425 | 2.53E-04 | 343 | 17 | 143 | 72 |
| | RS73/1/7 | 1.0194 | 0.6028 | 2.27E-04 | 323 | 4 | 74 | 79 |
| | RS73/2/1 | 1.0118 | 0.1725 | 2.48E-04 | 333 | 5 | 66 | 37 |
| | RS73/2/2 | 1.0096 | 0.2132 | 2.43E-04 | 146 | 0 | 56 | 63 |
| | RS73/2/3 | 1.0124 | 0.452 | 2.67E-04 | 150 | 7 | 42 | 69 |
| | RS73/2/4 | 1.012 | 0.2241 | 2.45E-04 | 151 | 2 | 54 | 72 |
| | RS73/2/5 | 1.01 | -0.0117 | 2.53E-04 | 324 | 13 | 187 | 73 |
| | RS73/2/6 | 1.0128 | 0.4236 | 2.47E-04 | 324 | 5 | 102 | 83 |

#### *4.2.9. Magnetic mineralogy*

The mean (bulk) susceptibility ranges from $-10^{-3}$ to $10^{-2}$ (SI), with the highest frequency of values between $10^{-5}$ and $10^{-4}$ (Fig. 23a). About 15 % of the specimens have negative (less than $10^{-7}$) susceptibility (RS15, RS21, RS36, RS45, RS50), corresponding to diamagnetic minerals. Paramagnetic ($10^{-5} \leq k_m \leq 10^{-4}$) and ferromagnetic ($k_m = 10^{-2}$) minerals carry the AMS in 74 % and 2 % of the specimens, respectively (Fig. 10a). Bulk susceptibility at two stations (RS45 and RS63) indicates a mixture of paramagnetic and ferromagnetic minerals.

The AMS carriers can be identified more rigorously through measurement of susceptibility variations with temperature plotted on a temperature–bulk susceptibility ($T$– $k_m$) curve. These variations were measured on 7 representative specimens using CS-L Cryostat and

CS4 nonmagnetic furnace units plugged into an MFK1-A Kappabridge (Hrouda, 1994; Hrouda et al., 1997; Jelínek & Pokorný, 1997). The specimens were measured and monitored with the Cureval 8 program (www.agico.com; Hrouda et al., 1997) in three separate steps in a temperature range between –196 °C and 700 °C. The first step involved cooling to ca. –196 °C using liquid nitrogen, and subsequent heating back to room temperature of ca. 20 °C. The second step involved heating to ~700 °C, followed by immediately cooling to room temperature using argon (to prevent oxidation in minerals) at an approximate rate of 14 °C/min. The final step comprises cooling to the same temperature as the first step using liquid nitrogen.

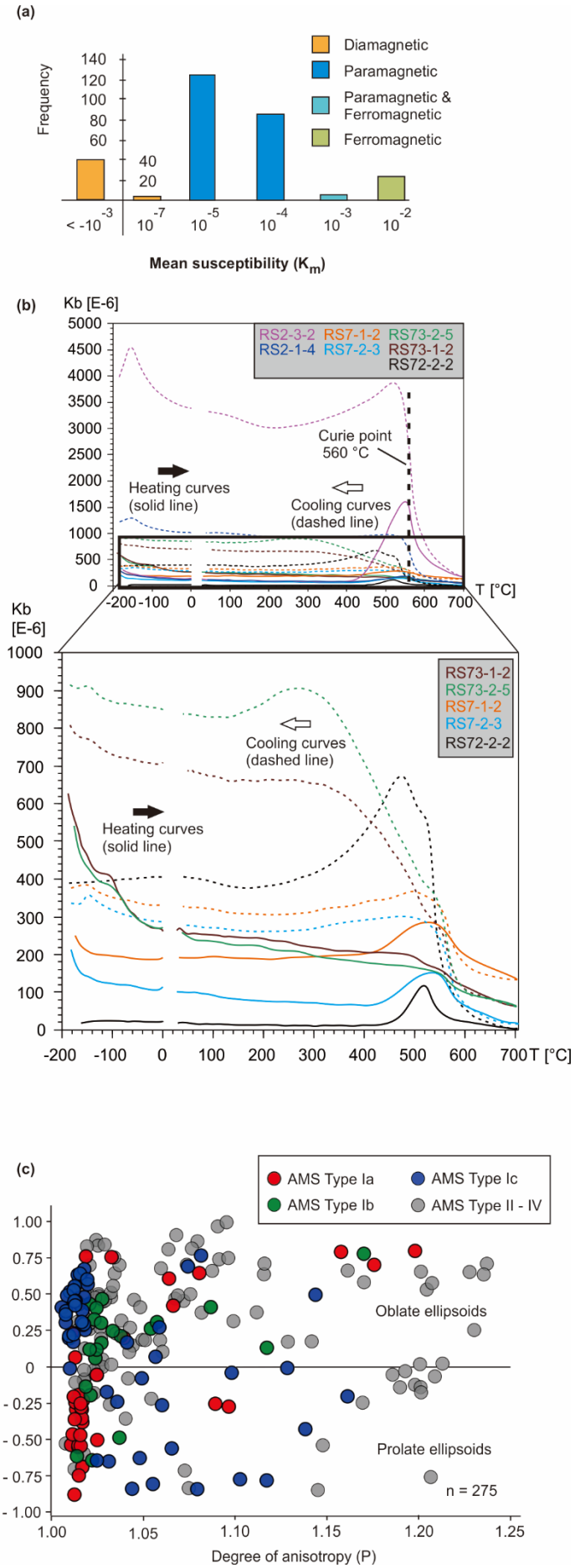


***Figure. 23.*** *(a) Histogram of mean (bulk) susceptibility from AMS specimens in the Příbram–Jince basin dominated with paramagnetic minerals. (b) Magnetic susceptibility variation under influence of cooling (dash lines) and heating (solid lines) in seven selected specimens. Higher magnetic susceptibility increases in the cooling processes suggest new growth of magnetite minerals (detail explanation in section 6.3. magnetic mineralogy). (c) Plot of shape parameter (T) versus degree of anisotropy (P) for all specimens. Highlighted colours represent the AMS Type I (depositional fabric).*

Specimens for thermomagnetic analysis were selected as follows. Specimens RS2-1-4, RS2-3-2, RS7-1-2, RS7-2-3, RS73-1-2, and RS73-2-5 represent the most common paramagnetic massive and cross-stratified sandstones and have a bulk susceptibility of $10^{-4}$. Specimens RS2-3-2, RS7-1-2, RS7-2-3, and RS72-2-2 ($k_m = 10^{-5}$) were selected because of their medium *P* and *T* values. In addition, any anomaly, such as an excessively high degree of anisotropy (RS7-1-2), intermediate *P* and slightly prolate (RS73-2-5), and

an extremely low shape parameter (RS2-1-4), becomes a key characteristic for conducting the analysis.

The $k_m$–$T$ curves generally follow a hyperbolic trend (Fig. 23b). In the low temperature range, cooling curves for specimens RS2-3-2 and RS2-1-4 indicate the Verwey transition of magnetite below -150 °C. Magnetic susceptibility in the high temperature range shows a gradual increase on both the heating and cooling curves as the Curie temperature of magnetite is approached (between 520 and 560 °C). This increase in bulk susceptibility is much higher during cooling than during heating, suggesting growth of new magnetite. Magnetic susceptibility increased significantly during cooling in specimens RS73-1-2 and RS73-2-5 at a temperature of ca. 300 °C, suggesting that some ferromagnetic minerals must have been present in the rock before heating. Altogether, the thermomagnetic analyses indicate that the susceptibility is carried by paramagnetic minerals with some ferromagnetic admixture in a few cases.

#### *4.2.10. Diverse magnetic fabrics in the Příbram–Jince basin*

The most unexpected outcome of our analysis is that several distinct magnetic fabric types can be distinguished in the Příbram–Jince basin and that more than one fabric type may occur in a single outcrop (e.g., stations RS2 and RS7). For the purpose of this study, we classify these diverse fabrics into four end-member types (numbered here as I–IV*)* on the basis of orientation distribution and angular relationships of the maximum ($k_1$) and minimum ($k_3$) principal susceptibilities to bedding and/or cross-stratification (Fig. 24).

Type I fabric is the most widespread in the basin. It is characterized by strongly clustered maximum ($k_1$) and minimum ($k_3$) principal susceptibilities, a $T$ parameter scattered across both the oblate and prolate fields, and a $P$ parameter mostly not exceeding 1.15 (Fig. 23c). The Type I fabric may be further subdivided into subtypes referred to as Ia, Ib, and Ic. At

two stations (RS2 and RS7), two subtypes were found in different parts of the same outcrop (distinguished as data groups).

Type Ia (data group 1 of station RS2, data group 1 of station RS7) is defined by magnetic foliations subparallel to bedding and magnetic lineations oriented down-dip or dip-oblique with respect to the cross-stratification plane (Fig. 11). This type is also characterized by a degree of anisotropy mostly less than 1.05 and by prolate AMS ellipsoids (Fig. 23c).

Type Ib (stations RS18, RS44) is represented by magnetic foliations subparallel to the bedding plane rather than the cross-stratification plane, and magnetic lineations showing a transition between clustered and girdle-like orientation distributions along the bedding/foliation plane (Fig. 24). Magnetic lineations thus tend to lie closer to the bedding plane than to the cross-stratification plane. Scalar fabric parameters indicate a transition from prolate to oblate shapes of the AMS ellipsoid ($-0.6 \leq T \leq 0.5$) and a low degree of anisotropy ($P$=1.02–1.17).

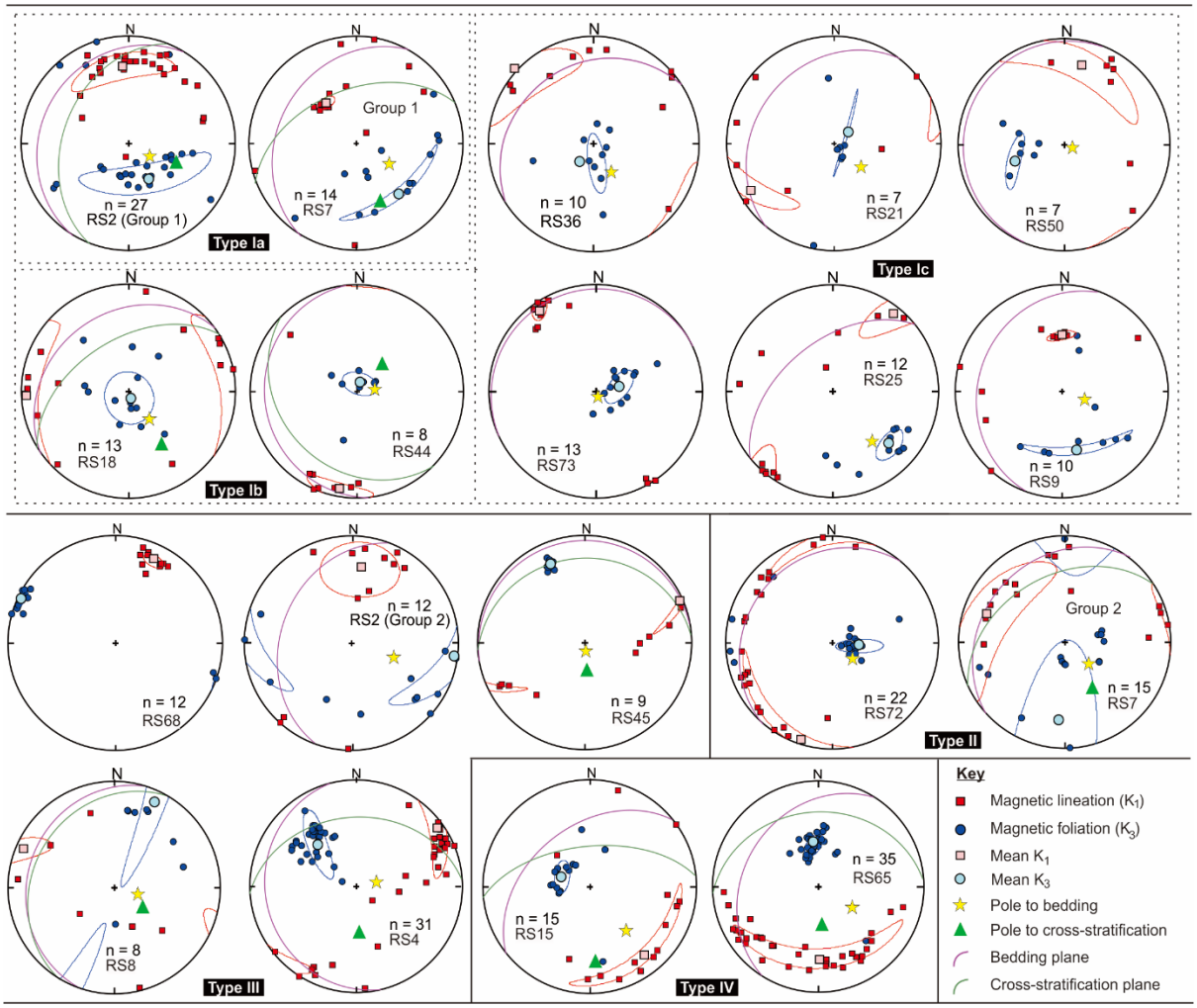


**Figure 24.** *Orientation of maximum (red squares) and minimum (blue circles) principal susceptibilities in sandstone of the Příbram–Jince basin, categorized into four different types (Type I, II, III, IV).*

When cross-stratification is absent (stations RS36, RS50, RS21, RS73, RS25, RS9), we distinguish Subtype Ic since it is impossible to evaluate the relationship of the magnetic fabric to the internal bed structure (Fig. 24). Nevertheless, magnetic foliations vary from bedding-parallel to slightly bedding-oblique, while magnetic lineations are likewise oriented parallel and oblique to the bedding plane. This subtype exhibits a wide range of fabric parameters, but it is dominated by oblate AMS ellipsoids and a low degree of anisotropy (less than 1.05).

The Type I fabric is considered a depositional fabric (e.g., Rees and Woodall, 1975; Tarling and Hrouda, 1993).

In the Type II fabric, magnetic foliations are still sub-parallel to bedding/cross-stratification, but magnetic lineations scatter widely within or close to the bedding/cross-stratification plane. On a stereonet, the foliation data points are clustered close to the pole of the bedding/cross-stratification plane, whereas the lineation data points show a girdle-like orientation distribution along the great circle for bedding/cross-stratification. Oblate ($0.06 < T < 0.9$) AMS ellipsoids and low to moderate degrees of anisotropy (P between 1.0 and 1.7) are associated with this fabric type. The Type II fabric likely records compaction strain (flattening) during burial (e.g., Hrouda et al., 2009).

The Type III fabric is characterized by steep, ~N–S to ~NE–SW-striking magnetic foliations that are at a high angle to the bedding and associated with subhorizontal magnetic lineations lying close to the bedding plane. On a stereonet, the data points for both foliations and lineations are strongly clustered. The *P* parameter ranges widely between 1.01 and 2.3 (station RS45), as does the shape parameter *T*, exhibiting both oblate and prolate AMS ellipsoids ($T$ = -0.7–0.9). These characteristics suggest that Type III is a tectonic fabric (Callot et al., 2010; Parés, 2015; Parés et al., 1999; Saint-Bezar et al., 2002), closely corresponding to the regional Variscan cleavage and stretching lineation in ductile deformed domains (Casas and Murphy, 2018; Stephan et al., 2016; Žák et al., 2013).

In the Type IV fabric, both magnetic foliations and lineations are clustered at a high angle to bedding, while the $k_1$ data points plot close to the pole to bedding and cross-stratification on a stereonet. Type IV fabric is associated with a high degree of anisotropy (P = 1.3–1.5) and both oblate (0.6; RS65) and prolate (-0.37; RS15) AMS ellipsoids, and is an example of inverse magnetic fabric (e.g., Černý et al., 2020; Chadima et al., 2009; Usui et al., 2019).

### *4.2.11. Paleocurrent directions inferred from magnetic fabric*

It is apparent from the analysis presented above that of the four magnetic fabric types found in the Příbram–Jince basin, only Type I can be used to infer paleocurrent directions. At each station where Type I fabric was detected, we applied the same approach used for the mesoscopic paleocurrent indicators. The mean magnetic lineations were rotated to horizontal about a rotation axis represented by the strike of the bedding through an angle equal to the dip of the bedding. The rotated paleocurrent directions derived from the AMS were then plotted in map view and presented as rose diagrams. The mesoscopic paleocurrent indicators are also shown for comparison (Fig. 25).

It should be noted that interpretation of the magnetic lineations is not as straightforward as that of mesoscopic paleocurrent indicators. First, in cases where lineations are subhorizontal and scattered more or less symmetrically about opposite trends, the calculated site-mean lineation, and thus the inferred paleocurrent direction, may be strongly affected by the statistical distribution of individual specimens and may easily flip by ~180°.

Second, fine-grained magnetic particles may align systematically either parallel or perpendicular to flow lines during deposition, depending on the velocity gradient and depositional mechanism (e.g., Rees, 1965, Rees and Woodall, 1975; Taira and Scholle, 1979; Stachowska et al., 2020 and references therein). Hence, the AMS-derived paleocurrent directions must be interpreted with caution.

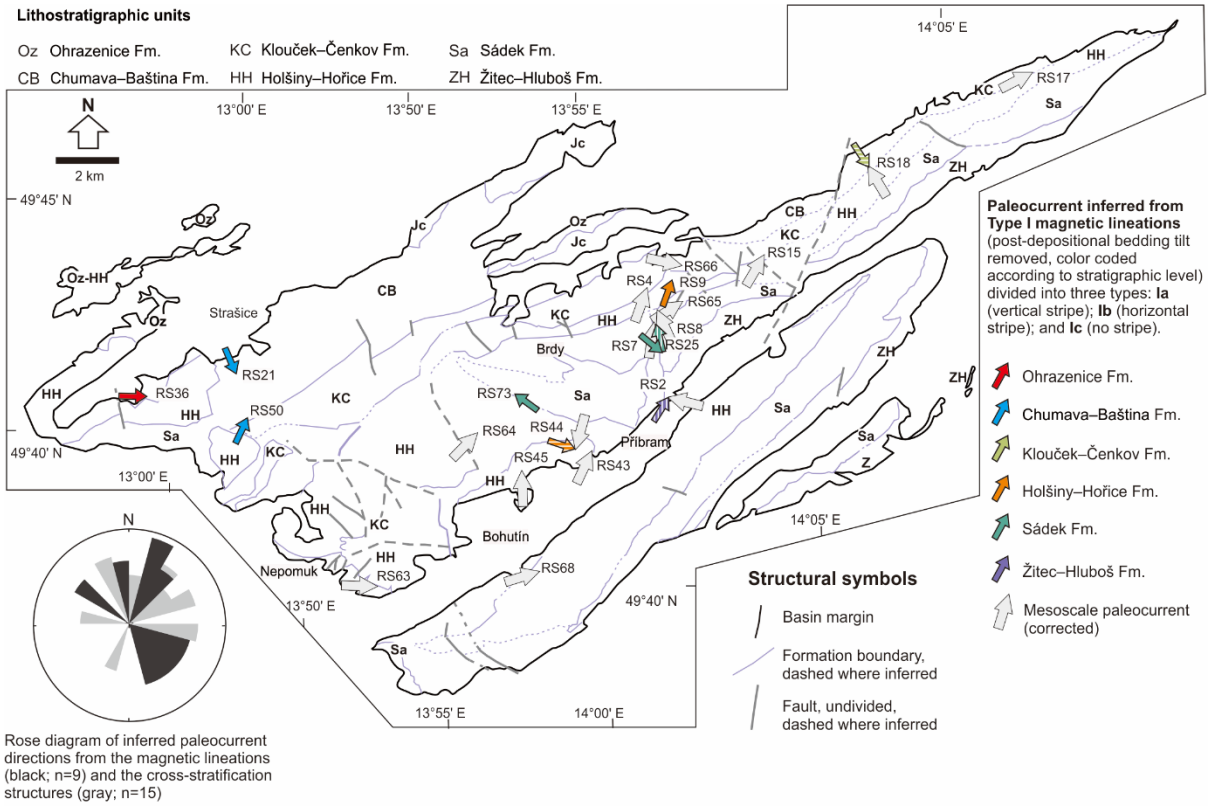


**Figure 25.** *Map of paleocurrents inferred from cross-stratification and magnetic lineations (Type I interpreted as depositional fabric).*

In the Příbram–Jince basin, the paleocurrent directions inferred from the magnetic lineations in most cases show a good match with those obtained from mesoscopic cross-stratification. In succession 1 (the Žitec–Hluboš Formation), the cross-stratification indicates a paleocurrent toward the ~NW, whereas the magnetic lineation points to the ~NE (station RS2; Figs. 24, 25). In the overlying succession 2 (the Sádek Formation), the mesoscopic paleocurrent directions point to the ~N to ~NNW in agreement with the magnetic lineations, which point to NNW to NW. An exception is the magnetic lineation at station RS25 (Fig. 25), which points to the SE (i.e., away from the basin) and may be a case of the statistical 'flip' effect mentioned above. In succession 3, the inferred paleocurrent directions are more varied, as are the magnetic lineations. At station RS44 (the Holšiny–Hořice Formation), the lineation is perpendicular to the cross-stratification, but both point in directions away from the basin. At station RS9 (same formation), the magnetic lineation points to the ~NE in agreement with the mesocopic

indicators, whereas in the Klouček–Čenkov Formation it points in exactly the opposite direction to the inferred paleocurrent (to the ~SE; Fig. 25). In succession 5 in the northwestern corner of the basin (stations RS21, RS36, RS50; Chumava–Baština and Ohrazenice formations), where mesoscopic paleocurrent indicators were absent, the magnetic lineations point in various directions (NE, E, SSE) but consistently into the basin (Fig. 25).

### 4.3. Moldanubian orthogneisses

The Moldanubian metagranites and orthogneisses (Figs. 26, 27, 28) may be classified into two main textural and compositional types with protolith compositions ranging from quartz diorite (Deštná type) to highly fractionated alkali feldspar granite (Blaník type). They are typically quartz-rich, sodic, and peraluminous, and are variably overprinted by Variscan deformation and metamorphism (e.g., Buriánek et al., 2020; Klomínský et al., 2010; René and Finger 2016). The Deštná type (Fig. 28c) is represented by the biotite to muscovite–biotite (± amphibole) orthogneisses of the Bechyně, Stráž, and Pacov bodies (Figs. 26, 27, 28a). These rocks are typically medium- to coarse-grained, sometimes leucocratic, and consist of quartz (~20–40 vol. %), plagioclase (~20–35 vol. %), K-feldspar (~25–30 vol.%), biotite (~8–10 vol. %), and muscovite (~5 vol. %). The Blaník type is represented by the leucocratic, two mica and muscovite–tourmaline orthogneisses of the Blaník, Choustník, Přibyslavice, Vlastějovice, Hluboká, and Radonice bodies (Figs. 26, 27, 28b, d). The Blaník type (Figs. 27c, 28d) is medium-grained (the muscovite–biotite variety) to medium- to coarse-grained (the muscovite–tourmaline variety), mostly dominated by K-feldspar (more than 50 vol. %), quartz (~20–35 vol. %), plagioclase (~20–30 vol. %), muscovite (~15 vol. %), biotite (~5 vol. %), and tourmaline (~5–15 vol. %), accompanied by garnet and sillimanite.

### *4.3.1. Existing radiometric ages*

The age of the metagranites and orthogneisses was previously largely unknown except for a few samples dated in the 1980s and early 1990s using the less reliable Rb–Sr whole rock and Pb–Pb methods (Klomínský et al., 2010; van Breemen et al., 1982 and references therein). Modern geochronologic studies have reported early to mid-Ordovician metagranites in the southwestern Moldanubian unit, dated at 486 ± 7 Ma and 480 ± 6 Ma (U–Pb on zircon; Teipel et al., 2004) and 456 ± 3 Ma (U–Pb on zircon; Friedl et al., 2004). Other ages of 494 ± 2 Ma and 485 ± 4 Ma come from orthogneisses in the central part of the Moldanubian unit (Pacov orthogneiss, U–Pb on zircon; Buriánek et al., 2020) and from units along its northeastern margin, ranging from 492 ± 4 to 484 ± 2 Ma (Kouřim nappe, U–Pb on zircon; Soejono et al., 2020) and 470 ± 30 Ma (Svratka metagranite, Pb–Pb on zircon; Schulmann et al. 2005).

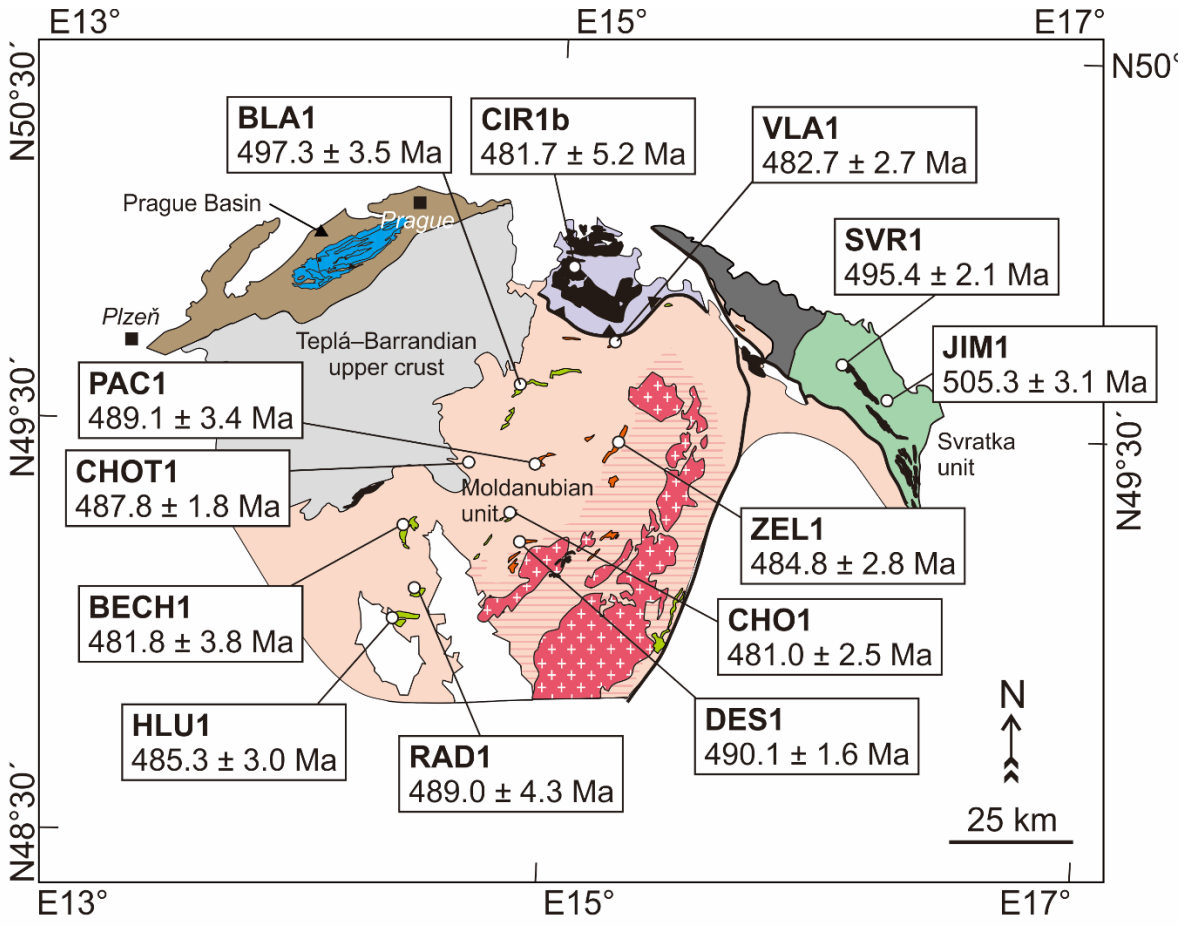

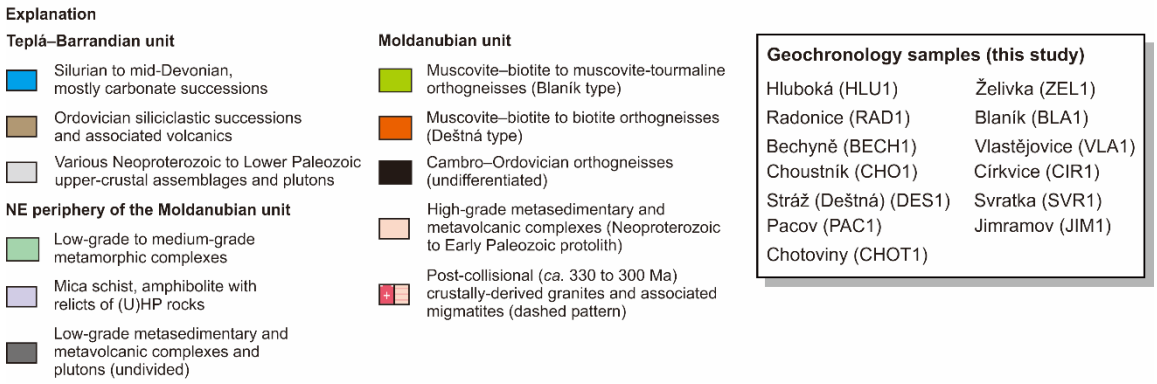


**Figure 26.** *Distribution of metagranites and orthogneisses in the Moldanubian unit. Geochronological data were derived from new U–Pb zircon analysis.*

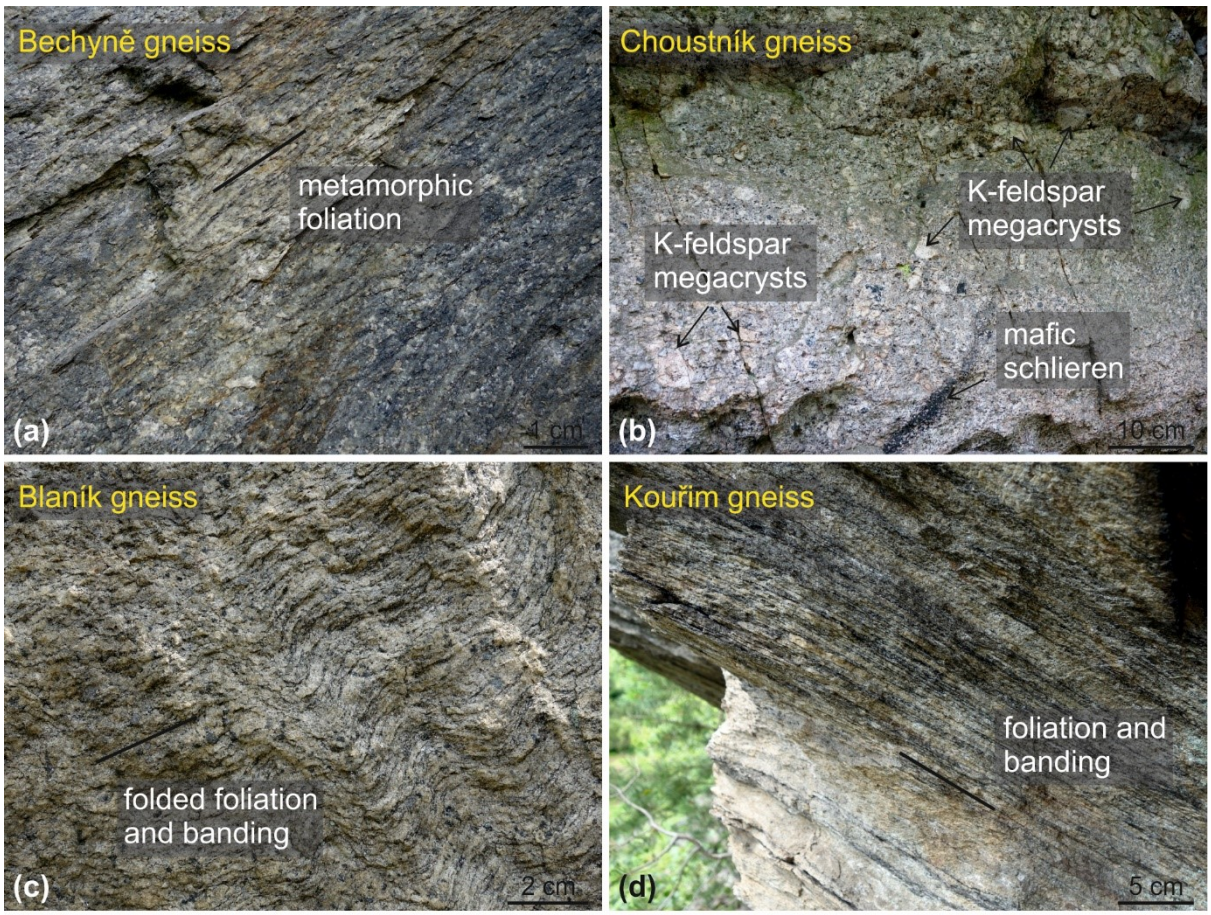


**Figure 27.** *Field examples of the sampled units: (a) Bechyně biotite–amphibole orthogneiss (sample BECH1; WGS84 coordinates: 49.300824°N, 14.459932°E), (b) Choustník muscovite–biotite orthogneiss (sample CHO1; WGS84 coordinates: 49.33719°N, 14.865706°E), (c) Blaník muscovite–biotite orthogneiss with compositional banding defined by alternating quartzofeldspathic and mica-rich bands(sample BLA1; WGS84 coordinates: 49.651813°N, 14.887816°E), and (d) Kouřim orthogneiss with compositional banding defined by alternating quartzofeldspathic and mafic bands (outcrop ca. 850 m northwest of sample CIR1b; WGS84 coordinates: 49.922935°N, 15.003162°E).*

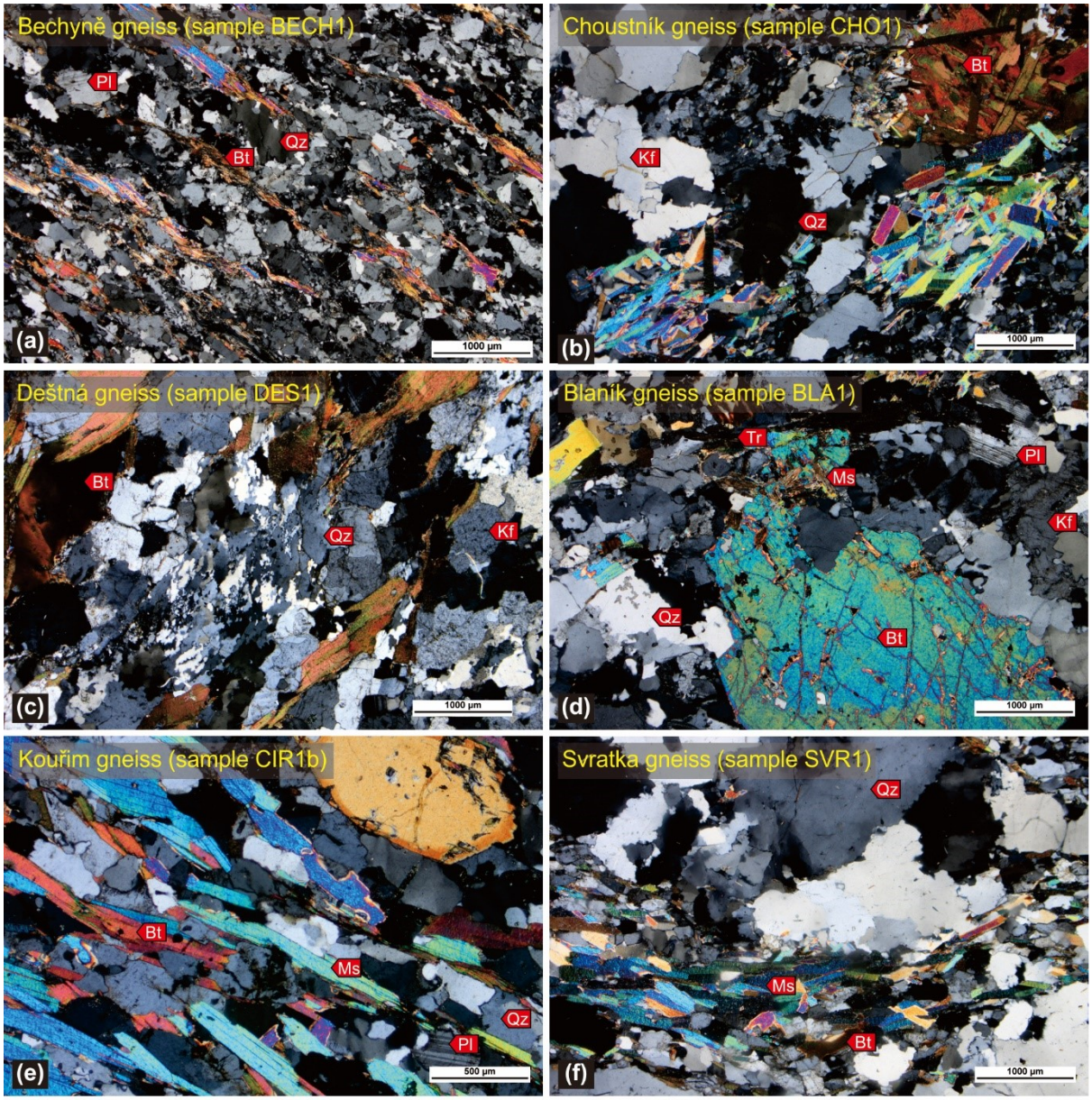


**Figure 28.** *Microphotographs of representative samples in crossed polars: (a) sample BECH1, (b) sample CHO1, (c) sample DES1, (d) sample BLA1, (e) sample CIR1b, and (f) sample SVR1 (see Fig. 1b for sample locations). Mineral abbreviations: Bt – biotite, Kf – K-feldspar, Ms – muscovite, Pl – plagioclase, Qz – quartz, Tr – tourmaline.*

### *4.3.2. Methods and analytical details of new U–Pb zircon geochronology*

The U–Pb zircon geochronology was pursued as external contract by Dr. J. Sláma of the Institute of Geology of the Czech Academy of Sciences. Thirteen samples, about 5–10 kg each, were taken in a systematic way from the metagranite/orthogneiss bodies scattered all over

the Moldanubian unit and in its northeastern periphery (see Fig. 26). Zircons were separated from the crushed samples by sieving and electromagnetic and heavy liquids separation in the laboratories of the Czech Geological Survey, Prague, hand-picked (with the goal to select the most euhedral and clear grains), and mounted in epoxy resin and polished for CL imaging prior to U–Pb measurements.

A Thermo Scientific Element 2 sector field ICP-MS (inductively coupled plasma mass spectrometry) with a 193 nm ArF excimer laser (Teledyne Cetac Analyte Excite laser) at the Institute of Geology of the Czech Academy of Sciences, Prague, Czech Republic, was used to measure the Pb/U and Pb isotopic ratios in zircons. The laser was fired at a repetition rate of 5 Hz and fluence of 3.17 J/cm$^2$ with 22–25 micron spot size, depending on the zircon grain size. Helium carrier gas was flushed through the two-volume ablation cell at a flow rate of 0.73 L/min and mixed with 0.84 L/min Ar and 0.004 L/min N prior to introduction into the ICP. The in-house glass signal homogenizer (design of Tunheng and Hirata, 2004) was used for mixing all the gases and aerosol resulting in smooth, spike-free signal. The signal was tuned for maximum sensitivity of Pb and U, Th/U ratio close to unity and low oxide level, commonly below 0.1 %. Typical acquisitions consisted of 15 second of blank measurement followed by measurement of U, Th and Pb signals from the ablated zircon for another 35 seconds. The total of 420 mass scans data were acquired in time resolved – peak jumping – pulse counting / analogue mode with 1 point measured per peak for masses $^{204}$Pb + Hg, $^{206}$Pb, $^{207}$Pb, $^{208}$Pb, $^{232}$Th, $^{235}$U, and $^{238}$U. Owing to a non-linear transition between the counting and analogue acquisition modes of the ICP instrument, the raw data were pre-processed using a purpose-made Microsoft Excel macro. As a result, the intensities of $^{238}$U were left unchanged if measured in a counting mode and recalculated from $^{235}$U intensities if the $^{238}$U was acquired in analogue mode. Data reduction was then carried out off-line using the Iolite data reduction package version 3.4 with VizualAge utility (Petrus and Kamber, 2012). Full details of the data

reduction methodology can be found in Paton et al., 2011). The data reduction included correction for gas blank, laser-induced elemental fractionation of Pb and U and instrument mass bias. For the data presented here, blank intensities and instrumental bias were interpolated using an automatic spline function while down-hole inter-element fractionation was corrected using an exponential function. No common Pb correction was applied to the data due to the high Hg contamination of the commercially available He carrier gas, which precludes accurate correction of the interfering $^{204}$Hg on the very small signal of $^{204}$Pb (common lead).

Residual elemental fractionation and instrumental mass bias were corrected by normalization to the natural zircon reference material Plešovice (Sláma et al., 2008b). Zircon reference materials GJ-1 (Jackson et al., 2004) and 91500 (Wiedenbeck et al., 1995) were periodically analysed during the measurement for quality control. The values obtained from analyses performed over three days (GJ-1: mean Concordia age of 608 ± 3 Ma (2σ), concordance MSWD: 0.053, probability: 0.82; 91500: mean Concordia age of 1058 ± 6 Ma (2σ), concordance MSWD: 1.3, probability: 0.25) correspond perfectly and are within less than 1% error of published reference values (GJ-1: $^{207}$Pb/$^{206}$Pb age of 608.53 ± 0.4 Ma; Jackson et al., 2004; 91500: $^{207}$Pb/$^{206}$Pb age of 1065.4 ± 0.3 Ma; Wiedenbeck et al., 1995). Following the recommendations of Horstwood et al. (2016), the excess variance (i.e. the reproducibility) of the primary reference zircon was calculated in Isoplot (Paton et al., 2010) and quadratically added to the measurement uncertainties of all unknowns as well as to all pooled ages (concordia age as called in Isoplot).

The measured U–Pb zircon data and cathodoluminescence (CL) images are presented in Figures 29–31. Zircon U–Pb ages are presented as concordia (pooled) age plots generated with the ISOPLOT program v. 4.16 (Ludwig, 2012).

### *4.3.3. U–Pb zircon ages*

The average Th/U ratios in analysed zircon grains from the orthogneiss samples is

above 0.1, varying from 0.11 in sample Cir-1B to 0.42 in sample Zel-1. Although the meaning of this ratio may be equivocal, it is considered here to indicate that the zircons formed originally by magmatic crystallization of the orthogneiss protoliths (e.g., Hoskin and Black, 2002; Hoskin and Schaltegger, 2003; Rubatto, 2017). Descriptions of dated samples and results according to their broad present-day locations from the south and southwest to the north and northeast are presented as follows (Fig. 26).

*4.3.3.1. Hluboká orthogneiss (sample HLU1)*

The homogenous population of short to long prismatic zircon crystals in this sample show variable textures on the CL images. Some crystals are textureless and bright with a thin to wide outer dark rim and faded, uneven oscillatory zonation. Others are completely dark, and a few crystals preserve a very bright inner core. One analysis of this bright core provided a discordant $^{207}Pb/^{206}Pb$ age of ca. 2370 Ma. All the other analysed grains gave ages below ca. 570 Ma. Ages from the bright unzoned zircon grains form a cluster with a Concordia age of 485 ± 3 Ma (Fig. 29). Most of the dark zircons provided discordant data either older or younger than the main age cluster. These latter analyses show on average higher contents of U, suggesting their U–Pb ratio was compromised by metamictization and partial lead loss. The data invoke the existence of two separate Pb-loss events, one corresponding to magma crystallization at ca. 485 Ma and the other recording a later Variscan event evidenced by a single analysis of ca. 340 Ma. This analysis came from dark zircon that rims bright zircon with a discordant age of ca. 490 Ma.

*4.3.3.2. Stráž orthogneiss (sample DES1)*

The zircon in this sample is uniform and forms usually long prismatic euhedral crystals with typical magmatic zonation in the CL images. The grain cores are often bright without any apparent texture, the CL intensity decreases towards the rims, and the crystals develop typical

oscillatory zonation. The ends of some long prismatic crystals are almost black, indicating progressive depletion in U in the magma reservoir during zircon crystallization. Almost all U–Pb data lie on a discordia with an upper intercept age of *ca.* 491 Ma. When only analyses with less than 1% discordance are taken into account (approximately two thirds of all analyses), they form a cluster with a Concordia age of 490 ± 2 Ma (Fig. 29). This age is interpreted as representing magma crystallization. No zircon xenocryst or inherited components were found in sample DES1.

#### *4.3.3.3. Bechyně orthogneiss (sample BECH1)*

The selected zircon grains from sample Bech1 show great variability in CL images. Some grains are long prismatic crystals with an unzoned bright inner part and an outer dark rim with oscillatory zonation. Other grains have a dark inner part, which truncates the originally bright zircon and thus leaves uneven rims with high CL intensities. The U–Pb analyses provided mixed data with one Paleoproterozoic grain and two separate age clusters between *ca.* 620–550 Ma and 515–470 Ma. The zircons of the older age group are characterised by higher CL intensities and short to long prismatic shapes. Generally long prismatic shapes with low CL intensities characterise zircon grains of the younger age group. Some of the latter grains have textureless inner zones with higher CL intensities, and most provide concordant U–Pb ages. A Concordia age was calculated from the youngest analyses with discordance generally lower than 1% at *ca.* 482 ± 4 Ma (Fig. 29). It is difficult to determine whether this is the age of new zircon crystallization or solid state recrystallization as most of the zircon grains are either older than *ca.* 482 Ma or show features typical of altered/recrystallized zircon.

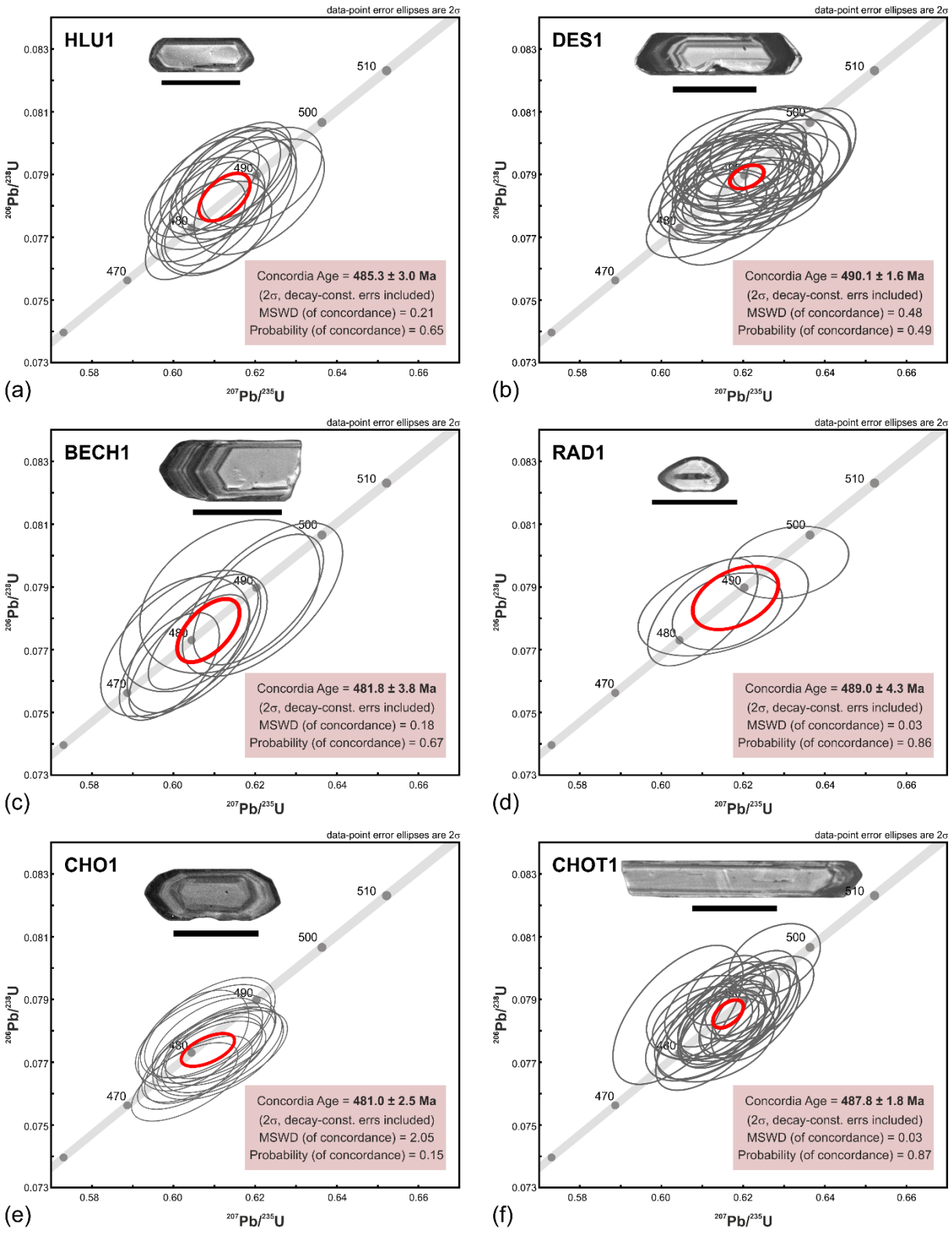


**Figure 29.** *Concordia diagrams with zircon weighted mean (concordia) Pb/U ages for samples (a) HLU1, (b) DES1, (c) BECH1, (d) RAD1, (e) CHO1, and (f) CHOT1. Insets are representative cathodoluminescence (CL) images of zircon, the bold line in each inset represents a length of 1 mm.*

*4.3.3.4. Radonice orthogneiss (sample RAD1)*

The CL images reveal the complex nature of the zircon grains in sample Rad1. Most of the grains are dark on the CL images or show features typical of altered zircon such as patchy zonation and local recrystallization. Other grains are almost black with only tiny remnants of core or rim and very low CL intensities. Accordingly, the U–Pb analyses yielded mostly discordant data. The near-concordant dates are spread between ca. 700 and 490 Ma. Of these, four analyses cluster at ca. 568 ± 5 Ma and a further four at ca. 489 ± 4 Ma (Fig. 29). All of these eight analyses come from complex zircon grains with a brighter inner part and dark rim, probably affected by metamictization, Pb-loss, or recrystallization. Hence, it is not possible to interpret the nature of these two thermal events. If the later ca. 489 Ma event was magmatic (melting), it most likely produced only limited growth of new zircon.

*4.3.3.5. Choustník orthogneiss (sample CHO1)*

Zircons in this sample show variable textures on the CL images, most with a preserved bright inner part and darker outer parts. Cores with preserved oscillatory zonation are xenocrysts truncated by later-formed zircon rims. Some of the grains show uneven zonation patterns with medium to high CL intensities. The four discordant analyses with $^{207}Pb/^{206}Pb$ ages older than 1 Ga come from the bright cores. The discordant to near-concordant analyses with $^{206}Pb/^{238}U$ age between ca. 620 and 500 Ma come from euhedral zircon crystals with medium to high CL intensities and oscillatory zonation. The zircons with low CL intensities and faded uneven (rarely oscillatory) zonation produced an array of concordant to discordant data with a mean $^{206}Pb/^{238}U$ age of ca. 481 Ma. The Concordia age calculated from analyses with discordance lower than 1% provide a crystallization age of 481 ± 3 Ma (Fig. 29). The abundance of older cores suggests that the protolith of the orthogneiss was an S-type granite. There is no evidence for later disturbance of the U–Pb system other than the ca. 481 Ma

magmatic event.

*4.3.3.6. Chotoviny orthogneiss (sample CHOT1)*

The zircons of sample Chot1 form long prismatic euhedral crystals with low to medium CL intensities. The internal textures are mostly irregular or homogenous, less often with oscillatory zonation. A few xenocrystic cores were identified in the CL images. The U–Pb analysis yielded ages in the range ca. 530 and 460 Ma with variable discordance. Other than a few analyses that yield ages older than ca. 500 Ma (an inherited component), the main concordant cluster yields a Concordia age of 488 ± 2 Ma (Fig. 29), which was considered to date the age of magmatic crystallization.

*4.3.3.7. Pacov orthogneiss (sample PAC1)*

Except for two zircon grains older than ca. 600 Ma, which are smaller in size, have short prismatic habits, and higher CL intensities with patchy and oscillatory zonation, most of the zircon grains from this sample are long prismatic crystals with low to medium CL intensities and ages between ca. 500 and 480 Ma. Out of this group, the selection of CL-bright grains and most concordant analyses yielded a Condordia age of 489 ± 3 Ma (Fig. 30). On average, these analyses have lower concentrations of U compared to more discordant analyses. We interpret the date of ca. 489 Ma as the age of magmatic crystallization of the orthogneiss protolith. The later disturbance of the U–Pb system mostly affected the U-rich zircon grains.

*4.3.3.8. Blaník orthogneiss (sample BLA1)*

The zircon in sample Bla1 is variable in shape as well as in the CL images. The habit varies from short stubby grains to long prismatic euhedral crystals. The CL images reveal complex textures commonly with CL-bright cores and dark rims; some grains have xenocrystic cores with high CL intensities passing irregularly into CL-dark rims with altered textures. The faded, patchy, and altered textures are the most common evidence of zircon alteration. This is

confirmed by the discordant age data of the U–Pb analysis. The stubby grains or those with apparent xenocrystic cores provide ages generally older than ca. 520 Ma. The prismatic grains yield an array of concordant to discordant data with ages ranging between ca. 500 and 200 Ma. Most of the discordant data come from zircons with low CL intensities and average U contents of ca. 1600 ppm. The most concordant cluster with a Concordia age of 497 ± 4 Ma was obtained from zircons with higher CL intensities and an average U content of ca. 600 ppm. The available data suggest that the orthogneiss protholith crystallized at ca. 497 Ma (Fig. 30) and experienced a later thermal disturbance that led to a partial Pb loss of metamict zircon.

#### *4.3.3.9. Želivka orthogneiss (sample ZEL1)*

Zircons in this sample forms long prismatic, occasionally short euhedral crystals with variable CL textures. Most grains have middle to low CL intensities with weakly developed oscillatory zonation. Some grains reveal more or less extensive inner parts that have higher CL intensities and often sector zonation. A few xenocrystic cores with irregular outer boundaries were identified in the CL images but not targeted during the U–Pb analysis. Other than a few analyses that are older than ca. 500 Ma and probably represent an inherited component, most data yield ages in the range ca. 500–400 Ma with variable degrees of discordance. The most concordant data from CL-bright zircons with an average U content of ca. 300 ppm form a cluster with a Concordia age of 485 ± 3 Ma (Fig. 30). The other data-points with higher degrees of discordance come from darker CL zones with an average U content of ca. 800 ppm. The 485 Ma age is considered to date magmatic crystallization, while the younger discordant ages record later alteration and lead loss in U-rich, metamict zircon.

#### *4.3.3.10. Vlastějovice orthogneiss (sample VLA1)*

The zircon in sample Vla1 is uniform in shape and CL textures. The grains form short to long prismatic euhedral crystals, mostly with very low CL intensities although some grains

preserve CL brighter inner parts. The dark rims show either faded oscillatory zonation or a convoluted texture. The brighter inner zones are either textureless or convolutely zoned and show irregular boundaries with the dark zircon of the rim. The U–Pb analysis reveals an array of age data ranging from ca. 540 to 340 Ma. Most of the data form a cluster with a Concordia age of 483 ± 3 Ma, while a few younger concordant data-points provide a Concordia age of 342 ± 2 Ma. These ages correspond well with the CL images and chemistry. The CL-bright inner parts of the grains form the ca. 483 Ma cluster and their average concentration of U is about 850 ppm. The analyses of the medium to dark CL zones with average U concentrations of about 1320 ppm show discordant ages younger than 480 Ma. The three most concordant analyses at ca. 342 Ma have the highest average U concentration of ca. 3430 ppm and come from completely dark grains with no remnant of a CL bright zone. The data indicate that the zircon crystallized at ca. 483 Ma (Fig. 30), which corresponds to the magmatic crystallization age. A later Variscan event at ca. 342 Ma caused the Pb loss in metamictized zircon. This resetting of U–Pb was proportional to the degree of radiation damage of the zircon; hence, zircons with the highest U contents suffered complete Pb loss and recorded the later thermal event (probably the metamorphism of the granitic precursor that formed the orthogneiss).

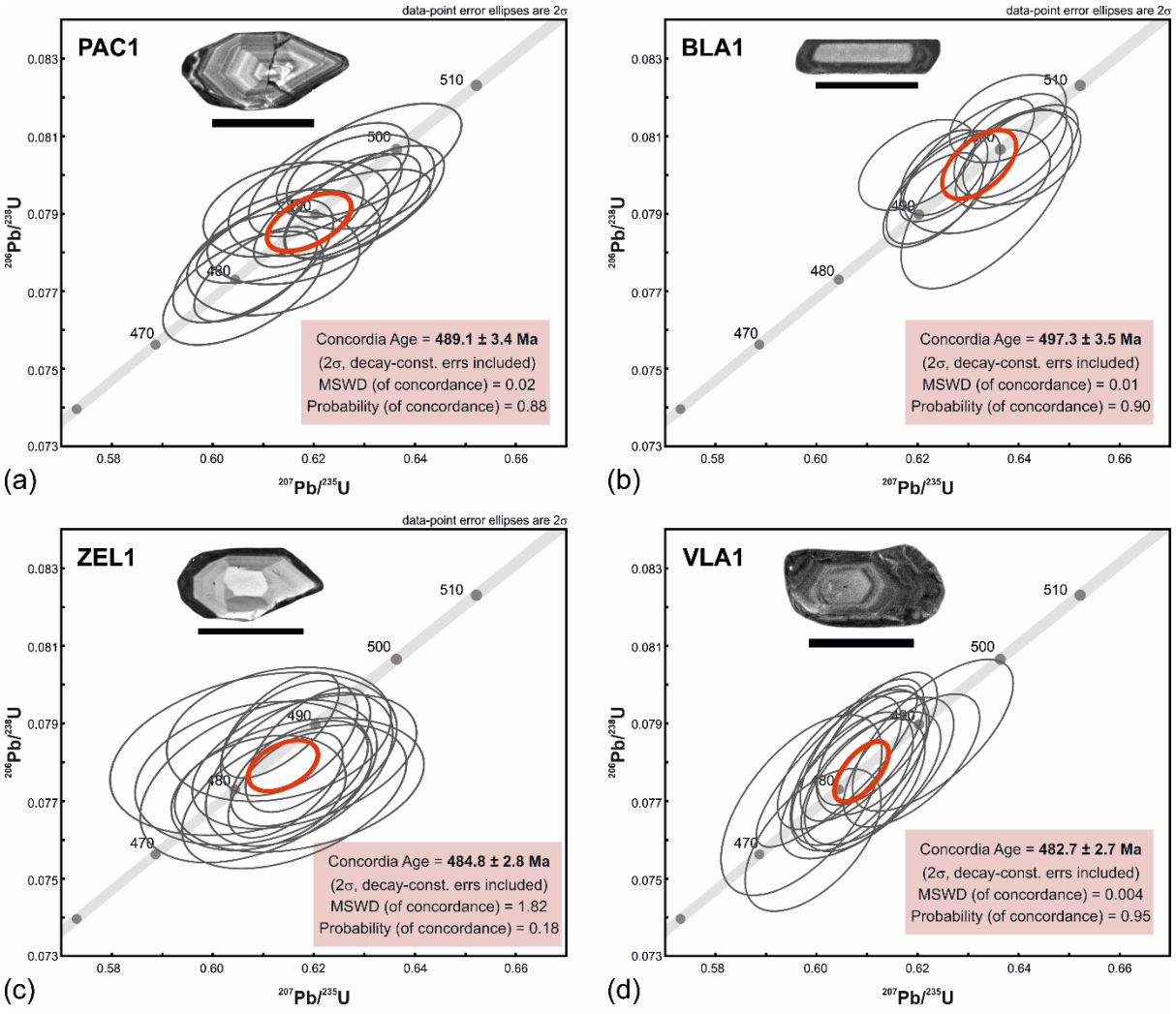


**Figure 30.** *Concordia diagrams with zircon weighted mean (concordia) Pb/U ages for samples (a) PAC1, (b) BLA1, (c) ZEL1, and (d) VLA1. Insets are representative cathodoluminescence (CL) images of zircon, the bold line in each inset represents a length of 1 mm.*

#### *4.3.3.11. Církvice orthogneiss (sample CIR1b)*

The zircon in this sample is variable in CL images, forming almost isometric to long prismatic grains with complex CL patterns ranging from oscillatory to patchy and convolute zonation,and exhibiting low to high CL intensities as well as xenocrystic cores and bright reaction zones indicating zircon alteration. Accordingly, the U–Pb ages vary significantly and most analyses are slightly to significantly discordant with ages ranging between ca. 560 and 480 Ma. Analyses that are less than 1% discordant selected from the youngest age cluster yield a Concordia age of 482 ± 5 Ma (Fig. 31). These analyses come from mostly textureless CL-

dark zircon grains with rather high U contents. Based on the CL images and chemistry, the ca. 482 Ma age dates zircon alteration rather than zircon growth. Most zircon grains are older and may represent a detrital component inherited from the magma source. We consider the zircon alteration to record a significant thermal event that mostly affected the U-rich (metamict) zircon grains which were most prone to U–Pb resetting.

#### *4.3.3.12. Jimramov orthogneiss (sample JIM1)*

The analyzed zircon grains in sample Jim1 are similar in CL imaging with long prismatic shapes, oscillatory zonation, and occasionally preserved older cores. U–Pb analysis of visually similar zircons reveals variable ages, mostly ranging from ca. 550 to 490 Ma, and variable discordance from near-concordant to strongly discordant ages. The two oldest detected ages of ca. 2017 Ma and 686 Ma represent zircon cores. Most of the analyses concentrate in a cluster that gives a Concordia age of 505 ± 3 Ma (Fig. 31). This cluster comprises long prismatic grains with higher CL intensities and oscillatory zonation, sometimes with parts that have faded or have no visible zonation patterns. Other grains that are visually similar to these ca. 505 Ma zircons, or those that have lower CL intensities, are either older or discordant. One such grain with low CL intensity gave a single age of ca. 490 Ma. The age of ca. 505 Ma is considered to date the thermal event, but the nature of the investigated zircon does not determined whether this was a period of magmatic growth or recrystallization of older zircon.

#### *4.3.3.13. Svratka metagranite (sample SVR1)*

The zircons in this sample are homogenous under the microscope with long prismatic crystal shapes. In the CL images, textures vary with prevailing diffuse, patchy and irregular zonation and remnants of oscillatory textures in some grains. The CL intensity also varies from very low to high. A few grains, notably those with shorter, stubby habits or with darker cores, provided U–Pb ages older than ca. 500 Ma (ca. 700–520 Ma). The majority of grains have

variable $^{206}Pb/^{238}U$ ages between ca. 500–490 Ma (Fig. 31), so that the data form an array parallel to the $^{207}Pb/^{235}U$ axis in the Concordia plot. Such data dispersal may indicate an intermediate daughter product ($^{231}Pa$ from decaying $^{235}U$) disequilibrium during initial zircon crystallization (e.g., Anczkiewicz et al., 2001). This data array intercepts the Concordia at ca. 495 ± 1 Ma, which is consistent with the Concordia age of 495 ± 2 Ma calculated from the most concordant data. This age is interpreted to date magmatic crystallization.

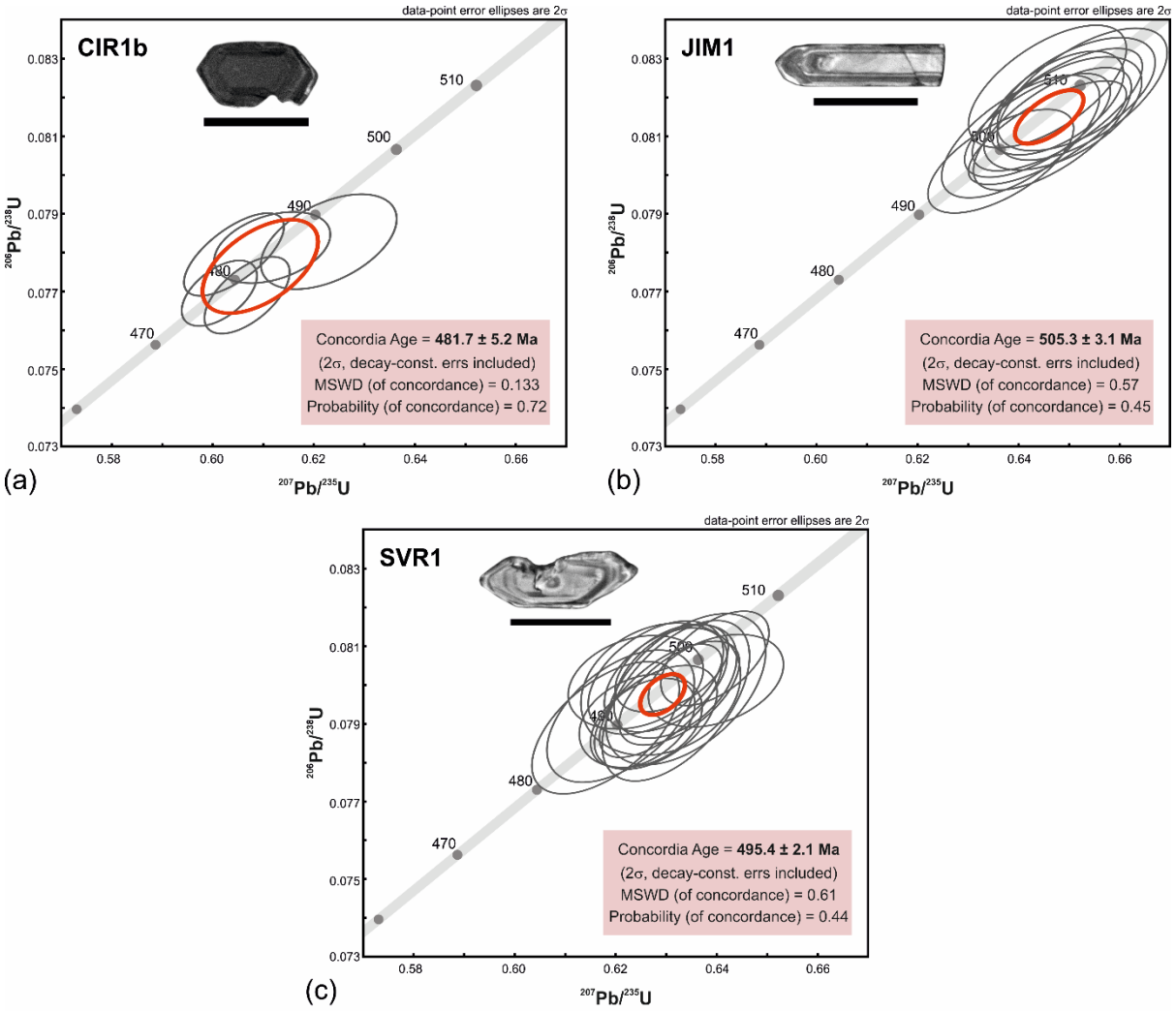


**Figure 31.** *Concordia diagrams with zircon weighted mean (concordia) Pb/U ages for samples (a) CIR1b, (b) JIM1, and (c) SVR1. Insets are representative cathodoluminescence (CL) images of zircon, the bold line in each inset represents a length of 1 mm.*

# 5. DISCUSSION

## 5.1. Emplacement of Cambrian Kdyně pluton

The crescent shape of the Kdyně pluton is highly unusual, as most plutons in the upper crust are either circular/elliptical or elongated in plan view (e.g., Buddington, 1959; Cruden et al., 2017; Cruden and McCaffrey, 2001; Miller and Paterson, 1999, 2001; Paterson et al., 1989; Paterson and Vernon, 1995). Though overlapping within errors, the ages of smaller intrusions within the pluton (Všepadly and Smržovice granodiorites; Fig. 7a) dated at 524 ± 3 Ma and 523 ± 3 Ma, respectively (Dörr et al., 2002) may indicate that the northern domain is slightly older than the southern domain. The possible age progression is further indicated by differences in the pluton–host rock relationships, the abundance of host rock screens and blocks, and the orientation of structural features and magnetic fabrics, including magnetic mineralogy, in both pluton segments (see Figs. 7a and 14a). The northern and southern domains may thus imply different and temporally evolving emplacement mechanisms during the assembly of the Kdyně pluton.

The pluton assembly started in the northern domain via multiple sheet-like magma batches with the composition varying from diorite through diorite–gabbro to granodiorite. These discordant (Fig. 7c), and in some places irregular (Fig. 14), magmatic sheets intruded presumably by a magma wedging mechanism (e.g., Hutton, 1992; Ingram and Hutton, 1994; Miller and Paterson, 2001; Tomek et al., 2015; Weinberg, 1999), likely facilitated by a component of WNW–ESE extension (Fig. 32). These sheets were emplaced into the pre-existing, generally flat-lying fabric of the host rock resulting from late Cadomian (latest Neoproterozoic to early Cambrian) regional deformation and metamorphism and modified by crustal tilting (e.g., Bues et al., 2002; Zulauf et al., 1997). In turn, the pre-emplacement fabric in the northern domain was progressively replaced by the high-T syn-emplacement hornfelsic

fabric in the middle domain. This change may have been caused by the gradual heating of the host rock and its thermal weakening as more magma was added at the emplacement level. As a result, the wall rock was pushed aside and heterogeneously shortened, forming the narrow, margin-parallel belts of steep foliation and upright folds (Fig. 7c). Before final magma solidification, local stoping may have occurred, producing sharp, irregular, or stepped, and discordant intrusive contacts and xenolith accumulations (Fig. 8h).

The AMS analyses indicate that the AMS carriers in the host rock involve some admixture between paramagnetic, ferromagnetic, and diamagnetic minerals, while the Kdyně pluton is influenced by paramagnetic and ferromagnetic phases (Figs. 11, 12). The AMS data thus fit well the observed microstructures (Fig. 9). The magnetic fabric in the pluton then represents the alignment of paramagnetic and ferromagnetic mineral grains acquired during the magmatic to submagmatic stage, i.e., in the presence of melt (Fig. 9e). It has been known that hydrothermal alteration may lower the bulk susceptibility and the degree of anisotropy (e.g., Just et al., 2004; Just and Kontny, 2012; Krása and Herero-Bervera, 2002; Lapointe et al., 1986). However, these both parameters are increasing in our samples (Fig. 11b and specimen RS94 in Fig. 12), proving that alteration (pinitization) occurred only locally and has a negligible effect on the magnetic properties.

Importantly, the magnetic fabric in the pluton is decoupled from the regional host rock structures, but instead, it tends to follow the local pluton–host rock contacts (Figs. 13 and 14a). This results in two dominant orientations of the magnetic foliations and lineations, either subparallel or at a high angle to the map-scale pluton axis (Figs. 7b and 14b). A fabric pattern is interpreted as a result of magma flow and emplacement, where mineral grains aligned parallel to the local pluton–host contacts. In turn, the two distinct magmatic fabrics may indicate that the pluton emplacement was controlled by two sets of orthogonal extensional fractures oriented ~NNE–SSW and ~WNW–ESE. The presence of orthogonal fracture sets is

also indicated by the late-stage quartz veins (Fig. 7b).

Similar processes likely operated also in the southern domain, however, its elongation suggests the dominant control of WNW–ESE fractures during emplacement. It seems that the steep NNE–SSW-trending foliations (both mesoscopic and magnetic), which were interpreted above as formed due to lateral expansion of the northern pluton segment, are truncated at the northeastern margin of the southern pluton segment. This would fit well with a younger age of the latter. In contrast, magnetic foliations as well as lithological boundaries seem to be deflected parallel to the southwestern pluton margin, indicating a minor ductile expansion (Fig. 32).

The above interpretations suggest that the emplacement of the Kdyně pluton was largely driven by internal buoyancy forces, less so by regional tectonic deformation, and controlled by brittle processes at the present-day level of erosion. In our view, the pluton represents an apical part of a high-temperature dome, where the peculiar crescent shape and a complex fracture network developed, record two orthogonal principal extension directions (WNW–ESE, and NNE–SSW; Fig. 32a) during doming. In detail, the orientation of the northern domain may have been significantly predetermined by tectonic inheritance, i.e., by the overall ~NE–SW structural grain of the underlying Blovice accretionary complex. Furthermore, a coeval NNE–SSW-trending dextral transtensional shear zone was described by Zulauf et al. (1997) and Zulauf and Helferich (1997) as affecting the Mračnice trondhjemite some 15 km to the northwest of the Kdyně pluton (Fig. 32c). The pluton thus occupies a footwall of the transtensional shear zone, which may have acted as the main detachment. Yet, another transtensional shear zones may occur also to the east of the pluton (inferred from Bues et al., 2002, Figs. 32b and 32c, reactivated during the Variscan orogeny), allowing an interpretation of the southern domain as an extensional stepover (e.g., Johnson, 2006; Lacroix et al., 1998; Miller, 1994; Oldow et al., 2008; Figs. 32b and 32c). This stepover was probably the initial

stage that triggered the bigger and longer fault with similar orientation in the central and eastern part of the Teplá–Barrandian unit (Fig. 32c). The above inferences thus also suggest that the deformation during pluton emplacement was strongly partitioned into simple shear-dominate zones that delimited pure shear-dominated belts (Fig. 32).

A late stage of the doming process, post-dating emplacement of the pluton, may then be represented by the normal shear bands and asymmetric cascading folds that overprint the syn-emplacement steep foliation (Fig. 32a).

In summary, the whole structure of the Kdyně pluton geometrically resembles a combination of the "b-type" and "a-type" domes described in metamorphic core complexes in the Aegean Sea and Alaska with two orthogonal principal extension directions and normal low-angle detachments accommodating exhumation of the hot, magma-bearing domains in the footwall (e.g., Amato et al., 2002; Jolivet et al., 2004).

### 5.2. What terminated the Cadomian active-margin processes?

The model developed above demonstrates that the emplacement of the Kdyně pluton post-dates the deposition, accretion, and shortening of the turbidite sequences of the Blovice accretionary complex and thus represents the upper age bracket for the Cadomian orogeny in the Teplá–Barrandian unit. One of the most intriguing aspects is the rather short time span between the end of accretion at around 527 Ma as inferred from the detrital zircon ages (e.g., Ackerman et al., 2019, 2022; Hajná et al., 2017; Žák et al., 2020) and the onset of plutonism and transtension at around 524 Ma (e.g., Dörr et al., 2002, Zulauf et al., 1997; Zulauf and Helferich, 1997, this study), implying a significant rapid heat input into an otherwise cold accretionary/forearc setting. The data presented in this paper do not allow for rigorous discrimination between several possibilities, but are at least consistent with the previously proposed ridge subduction and/or interference of a mantle plume with the active margin, followed by slab break-off (e.g., Ackerman et al., 2019; Dörr et al., 2002; Linnemann et al.,

2008; Sláma et al. 2008; Vítková Kachlík, 2001; Zulauf et al., 1997). The slab break-off model is also consistent with the northward migration of Cambrian plutonism over the Teplá–Barrandian unit (Fig. 5), perhaps reflecting opening slab tear in this direction and triggering an incipient lithospheric extension of the former fore-arc region (e.g., Zurbriggen, 2015).

Furthermore, the heat pulse anomaly during slab break-off is time-space limited giving rise to small-volume melts emplaced as multiple granitoid plutons over a short period of several millions of years (e.g., Atherton and Ghani, 2002; Cooper et al., 2013; Davies and von Blanckenburg, 1995; Ghani and Atherton, 2008; Murphy et al., 2019; Neilson et al., 2009). Zurbriggen (2015) also suggested that the heat in such a cold supra-subduction setting comes first from mantle-derived mafic magmas (with a temperature reaching more than 1000 °C), subsequently underplated below an accretionary wedge and triggering crustal melting and generation of hybrid magmas. These models thus explain well not only the short time of emplacement but also the observed compositional variations in the Kdyně pluton (gabbro diorite, trondhjemite, tonalite).

The rapid change in the tectonic regime may thus be viewed as the very first sign of the protracted transition from subduction–accretion processes to an extensional, passive-margin setting in the Teplá–Barrandian unit, which likely spanned the whole Cambrian period as recorded not only by the ca. 524–505 Ma plutons, but also ca. 515–503 Ma transtensional basins, and ca. 500–485 intermediate to felsic dike swarms and volcanic complexes (Fig. 5; e.g., Dörr et al., 2002; Drost et al., 2011; Hajná et al., 2018; Sláma et al., 2008a; Vítková and Kachlík, 2001; Zulauf et al., 1997, 1999; Žák et al., 2013). The geodynamic causes of this transition have been extensively debated for the whole Avalonian–Cadomian belt, but with no conclusive model (e.g., Arenas et al., 2007; Crowley et al., 2000; Díez Fernández et al. 2012; Floyd et al., 2000; Hajná et al., 2018; Linnemann et al., 2008, 2010; Nance et al., 2002; Sánchez-García et al., 2003; Winchester et al., 2006). The data from the Kdyně pluton highlight

the importance of magmatic activity as a driving force and suggest an active rifting mode (e.g., rifting in Ossa Morena: Sánchez-Garcia et al., 2010; Saxothuringia: Linnemann et al., 2008) at least during the very initial stages of the post-Cadomian evolution. In turn, the active rifting mode may have been replaced by a passive rifting mode due to the onset of Iapetus Ocean subduction beneath Laurentia and thus slab-pull force exerted on the northern Gondwanan margin from ca. 510 Ma onwards (e.g., Nance et al., 2010). If so, the end of the Cadomian orogeny and the transition to passive margin during the Cambrian was not only a multi-stage process, but was also caused by a superposition of different geodynamic causes.

**a) A model of Cambrian peri-Gondwana forearc magmatism, deformation partitioning, and emplacement of the Kdyně pluton**

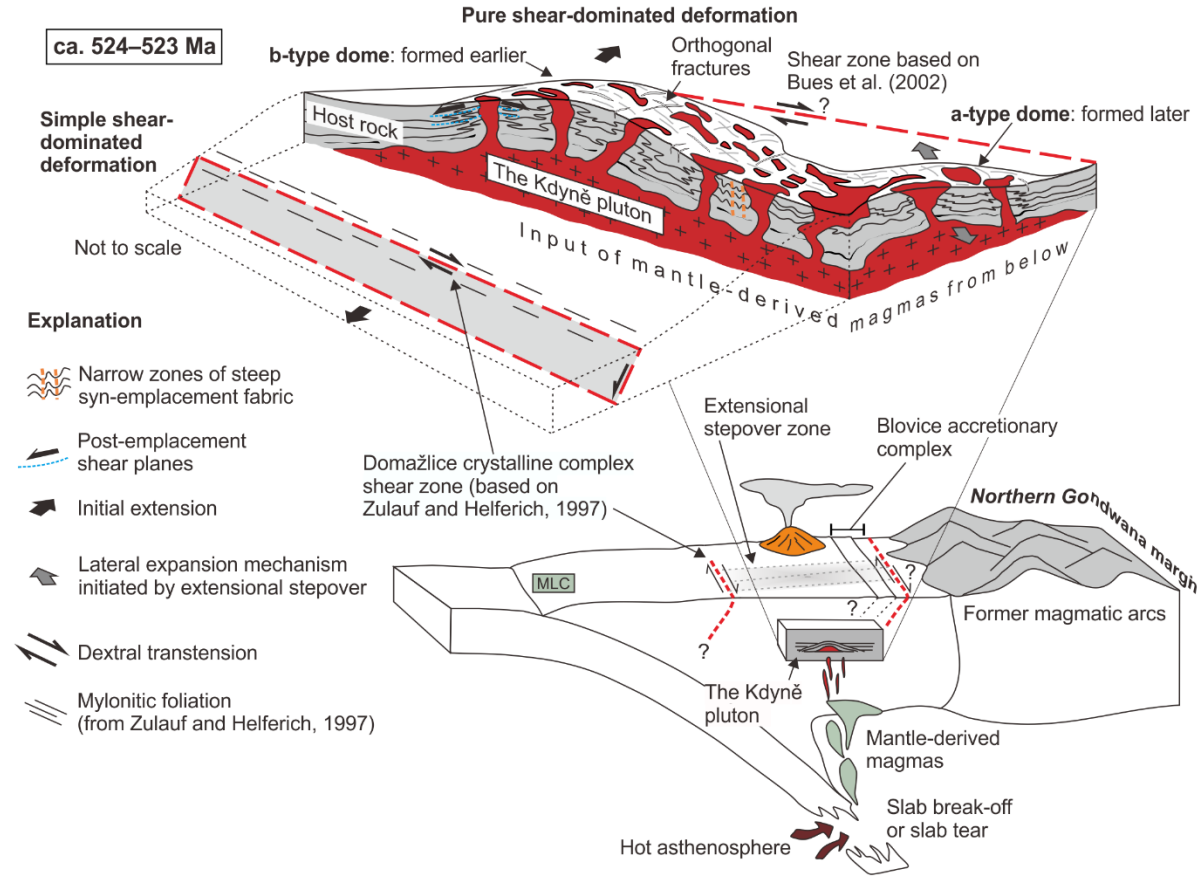


**b) Early Cambrian magmatism with extensional stepovers in the Teplá–Barrandian unit**

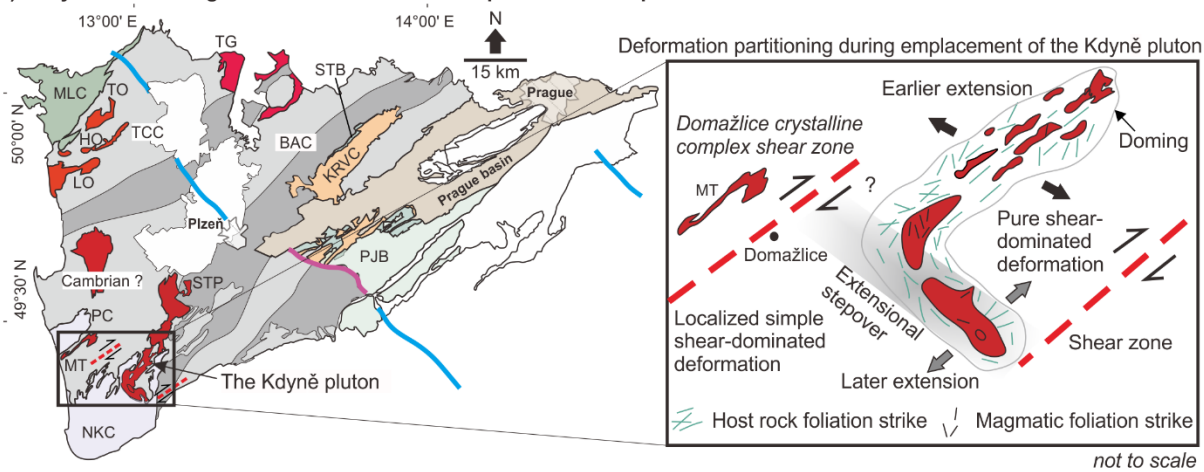


**Lithology**

Cambrian plutonic rocks (granite, granodiorite)

> 520 Ma | 520–510 Ma | < 510 Ma

Late Cambrian volcanic rocks (basalt, andesite, dacite, rhyolite)

Middle to late Cambrian marine siliciclastic rocks (shale, siltstone, sandstone, conglomerate)

Middle Cambrian continental siliciclastic rocks (graywacke, sandstone, conglomerate)

Ordovician marine siliciclastic and basic volcanic rocks (shale, siltstone, sandstone, tuff, tuffite, basalt)

Ediacaran to early Cambrian relict ophiolite

Neukirchen–Kdyně complex (NKC; greenschist, amphibolite, hornfels) and Poběžovice complex (PC; amphibolite, gabbro, meta-gabbro, serpentinite, diorite, metadiorite)

Alternating belts of Blovice accretionary complex (BAC)

**Explanation**

Syn-sedimentary fault (Cambrian), multiply reactivated (after Syahputra et al., 2022)

Large-scale basement faults of unknown age that may have been initiated during the early Cambrian and were then multiply reactivated

***Figure 32.*** *(a) Emplacement of the Kdyně pluton into the Neoproterozoic forearc region (Blovice accretionary complex) during the early Cambrian (ca. 524–523 Ma) controlled by slab break-off. Two dextral transtensional zones based on Zulauf and Helferich, 1997 and Bues et al., 2002 acted as detachments and generated the extensional stepover inbetween. The Kdyně pluton was emplaced into a pure shear-dominated segment. (b) Distribution of Cambrian plutons and volcanic complexes in the Teplá–Barrandian unit. Note that the Cambrian plutons are getting younger toward the northern part. The Cambrian Příbram–Jince basin (PJB) was bounded from southwest by a multiply reactivated fault (after Syahputra et al., 2022), which resembles the inferred extensional stepover of the Kdyně pluton. Other undefined faults with similar orientation also occur throughout the Teplá–Barrandian unit (left panel). Fabric and structural evolution of deformation partitioning during the emplacement of the Kdyně pluton is shown in the right panel. Geochronological data are taken from Fig. 1c. Abbreviations: Cadomian units: BAC Blovice accretionary complex, MLC Mariánské Lázně complex; Cambrian plutons and volcanics: KRVC Křivoklát–Rokycany volcanic complex; MT Mračnice trondhjemite, NKC Neukirchen–Kdyně complex; TCC Teplá crystalline complex comprises HO Hanov orthogneiss, LO Lestkov orthogneiss, TO Teplá orthogneiss; STP Stod pluton, TG Tis pluton; Lower Paleozoic basins: PB Prague Basin, PJB Příbram–Jince Basin, STB Skryje–Týřovice Basin.*

---

### 5.3. Cambrian sedimentary sources in the Příbram–Jince basin

As documented by clast compositions, the sediment sources in the middle Cambrian Žitec–Hluboš Formation (ca. 515 Ma) came from a volcanic arc and metamorphic basement (Fig. 17), with the source area presumably located to the ~ESE of the basin as inferred from the paleocurrent and AMS data (Figs. 21 and 25). The metamorphic sources were also reflected in the clast microstructures, with prevailing low- to high-temperature dynamic recrystallization (Fig. 22). Moreover, the published detrital zircon ages reveal that the Žitec–Hluboš Formation involved Paleoproterozoic, Neoproterozoic, and Cambrian detritus (Drost et al., 2011). The eroded material was transferred to the Příbram–Jince basin by debris flows to form alluvial fans in succession 1 that filled in the isolated depocenters in the southeastern part of the basin. The clast size indicates that they had traveled a short distance. The distal part of the alluvial fans, however, reached the main basin area (see Fig. 16), towards which the clasts become progressively smaller in size.

Subsequently (at 512 ± 5 Ma), medium- to fine-grained sediments were deposited in flood plains or braid plains (Sádek Formation), sourced from the ~SSE (transport to the ~NNW; Fig. 21). These sediments were presumably derived from a local source as shown by their sub-arkose dominated composition (Fig. 22b) and by detrital zircon ages that increasingly indicate Neoproterozoic detritus (Hajná et al., 2018). Based on the sediment distribution, the basin was almost entirely inundated by rivers except its northern part.

The deposition in succession 3, especially of the Holšiny–Hořice Formation (ca. 511 ± 3 Ma), is marked by a major change in the sedimentary source. The distribution of sediments in succession 3 was dominated by a fluvial distributary system (e.g., Nichols and Fisher, 2007) as axial channel belts (e.g., Gawthorpe and Leeder, 2000), interrupted by a local and short-lived brackish environment (represented by the Paseky shales). This river system, however, flowed obliquely to the underlying alluvial fan axes. A different source is indicated by a change in clast composition from unstable volcanic arc material to stable material entirely dominated by quartz and chert in the upper part of the succession (cross-section in Fig. 4 and microstructures in Fig. 22). The fluvial lithofacies in succession 3 were frequently disturbed by the fine-grained sheetflood fans (F3). The dominant paleocurrent, interpreted from mesoscale features and AMS, flowed from the western part of the basin towards the basin axis (Fig. 25), with the clasts becoming smaller to the ~NE. This re-adjustment of paleocurrent direction provides an independent argument for a change of the source area from that in the ~SE to a new one in the ~SW and ~W. This change is also demonstrated by the increasing proportion of Cambrian detrital zircon ages, which is twice that in the underlying succession (Hajná et al., 2018), perhaps as a result of faulting and recycling of some older parts of Cambrian volcano-sedimentary successions.

The Sádek and Holšiny–Hořice formations are the thickest and most areally extensive within the basin, following which the thickness of the basin fill gradually decreased (between

511 ± 3 and 510 ± 2 Ma; Hajná et al., 2018). Conversely, volcanic activity was at its peak during deposition of the overlying Klouček–Čenkov Formation, as shown by numerous recrystallized tuff grains (Figs. 15b and 22). This suggests that subsidence gradually decelerated and that the volcanic activity only occurred over a short time interval.

The conglomerates in succession 5 (Chumava–Baština and Ohrazenice formations) are again the product of alluvial fan deposition that were sourced from the ~W and ~NW. These conglomerates were interrupted periodically by sheetflood fans and, in part, were mixed with fluvial sandstones (see lithofacies distribution in Fig. 3). Interestingly, in the Chumava–Baština Formation, Neoproterozoic detrital zircon overwhelms the Cambrian detritus with a minor contribution from the Archean and Paleoproterozoic (Drost et al., 2011). Subsequently, the portion of the Cambrian detritus increased almost twofold in the overlying Ohrazenice Formation (499 ± 10 Ma; Drost et al., 2011). The sediment (and detrital zircon) transport was from the ~NW and ~SW toward the basin interior (Fig. 25).

Marine transgression occurred in succession 4 (ca. 506–503 Ma) and presumably flooded the basin above the Klouček–Čenkov Formation as depicted by the bi-directional cross-stratification (Fig. 18d).

The last volcanic activity in Cambrian was represented by the Strašice volcanic complex, which covered the NW part of the basin with subaerial, mostly andesitic lavas at ca. 500–485 Ma. The volcanism was presumably as a result of more intense rifting as shown by its alkaline composition (Štorch et al., 1993).

### 5.4. Tectonic evolution of the Příbram–Jince basin

The above-described changes in provenance and depositional settings record changes in the tectonic regime during deposition. The tectonic regime also likely controlled the basin fill thickness and syn-depositional volcanic activity. The basin is interpreted to have evolved kinematically in two main phases.

The first phase (at around 515 Ma) involved gravel accumulation in the SE with the basin fill younging toward the NW. We envision that small SE-side-up displacements along unconnected NE–SW-trending normal faults initially created fault scarps with river incision and thus several alluvial-fan depocenters. These faults propagated laterally and linked to form a master fault rimming the southeastern margin of the basin, now largely obscured by the Central Bohemian Plutonic Complex (Fig. 5). Based on parallelism of the basin axis with lithotectonic belts in the underlying Cadomian basement (Fig. 5), the initial normal faults and the master fault likely reactivated pre-existing tectonic boundaries and were active from ca. 515 Ma onwards (Fig. 33).

This first phase is interpreted to have been followed by a short period of tectonic quiescence (at around 512 Ma) as indicated by the abrupt change from gravel to the fine-grained basin fill represented by the areally extensive Sádek Formation (Fig. 33). Subsequently, faulting became active again and created a northwesterly facing half-graben system. The geometry of the basin fill and the location of depocentres suggest that the first stage of basin evolution was mainly controlled by NW–SE extension, roughly perpendicular to the basin axis (Fig. 33a and 33b; low obliquity rifting of Duclaux et al., 2020).

The major change in source area and in sediment transport from basin-axis-oblique (from the SE) to basin-axis-parallel (from SW or W) marks a major switch in the tectonic regime that controlled the basin evolution from ca. 511 Ma onwards (Fig. 33c). Together, the dominance of large quartz and chert pebbles at higher stratigraphic levels, the renewed alluvial fan deposition, and the inferred paleocurrent directions imply significiant uplift of the local Cadomian basement to the SW and W of the basin (Fig. 33c). Hence, the basin-axis-oblique, NW–SE-trending series of syn-sedimentary normal faults now bounding the southwestern end of the basin (Fig. 5) were initiated and became a major feature during this second phase of basin development (Fig. 33c), although they were likely multiply reactivated in post-Cambrian

times.

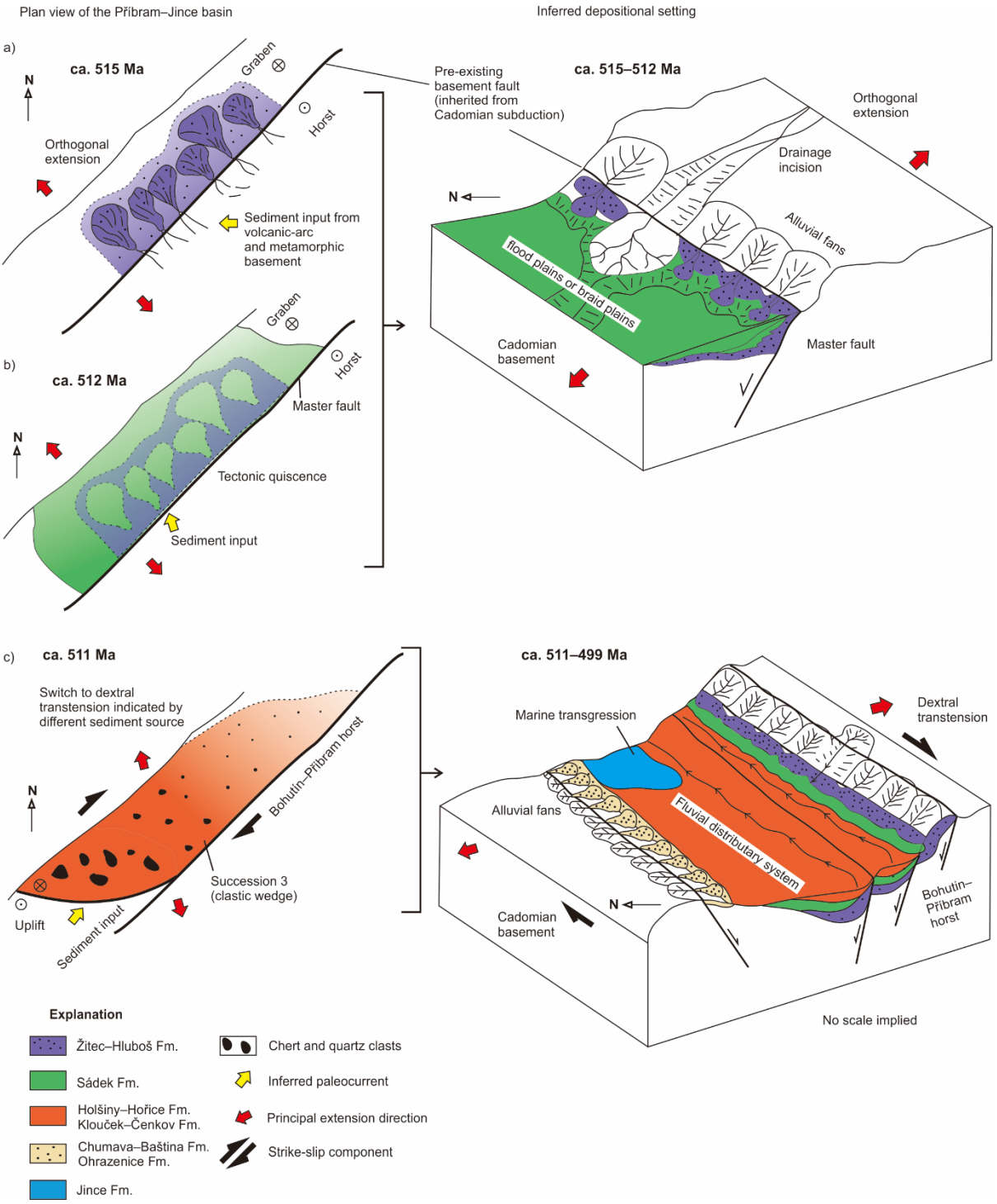


**Figure. 33.** *A model of tectono-sedimentary evolution of the Příbram–Jince basin. (a) Map view showing changes in source areas, basin infill, and fault kinematics from orthogonal extension to dextral transtension. (b) Interpretation of depositional environment controlled by normal faulting.*

At the same time, the net displacement along the southeasterly master fault is

interpreted to be increased, leaving behind the Bohutín–Příbram zone as a NE–SW-trending horst (Havlíček, 1971; Figs. 15 and 33). The horst controlled deposition of succession 3, interpreted as deposited by an axial river, which frequently changed its course by avulsion as reflected by cross-stratifications developed during lateral accretion (see log profile; Fig. 20). The axial river produced a clastic wedge fining and pinching out toward the NE (Fig. 33c). We therefore assume that the fault bounding the Bohutin–Příbram zone had an oblique dip-slip or scissor-like displacement, increasing to the SW.

Finally, a minor normal fault in the NW controlled deposition of the alluvial fan conglomerates and sandstones in the Chumava–Baština Formation at around 510 ± 2 Ma. During this period, the basin continued to subside until a short-lived marine transgression (the Jince Formation) occurred at ca. 506–503 Ma. Subsequently, an uplifted highland probably sourced the Ohrazenice Formation in the NW of the basin.

Taken together, the geometry of the basin fill and the inferred fault geometry and kinematics suggest that the Příbram–Jince basin developed as a dextral transtensional pull-apart basin with multiple depocenters and increasing obliquity of rifting (Fig. 33; e.g., Wu et al., 2009, Duclaux et al., 2020, Autin et al., 2013, Brune et al., 2018, Farangitakis et al., 2021).

### 5.5. Cambrian sedimentary basins as precursors for opening the Rheic Ocean

The above-developed model for the Příbram–Jince basin provides a background for comparison with other Cambrian basins along the former Avalonian–Cadomian belt. These basins represent a prelude to the opening the Rheic Ocean in the early Ordovician by the rift–drift transition of Avalonia (e.g., Cocks et al., 1997, Prigmore et al., 1997, Pollock et al., 2009, Nance et al., 1991, Murphy et al., 1999a), and are thus key features to understand the Early Paleozoic paleogeography of Gondwana and the development of its northern passive margin. The crucial issue is whether the evolution of these basins was similar or different in the western and eastern parts of the belt, since these two regions likely experienced different amounts of

separation from Gondwana during the Ordovician (e.g., Robardet, 2003; Servais and Sintubin, 2009; Romer and Kroner, 2019; Stephan et al., 2019a, b).

For this comparison, two lithotectonic units (often referred to as terranes) are selected as the best documented and well understood: Avalonia and the Teplá–Barrandian unit (part of Cadomia or Armorican Terrane Assemblage in some models; Tait et al., 2000). From their lithostratigraphy, tectonic setting and magmatism (Fig. 34), it can be seen that Avalonia and Cadomia differ significantly in their Cambrian evolution. Following the termination of subduction at around 540 Ma, Avalonia was overlain by a Cambrian marine platform sequence, only the basal part of which (ca. 540–530 Ma) comprises fluvial deposits (Fig. 34). In contrast, the Teplá–Barrandian unit recorded Cadomian subduction until ca. 527–524 Ma (Hajná et al., 2018). After a pulse of granitic plutonism, perhaps due to slab-breakoff, the Příbram–Jince basin was initiated at ca. 515 Ma and was filled with a thick package of alluvial and fluvial deposits (Fig. 34). Furthermore, bimodal volcanic

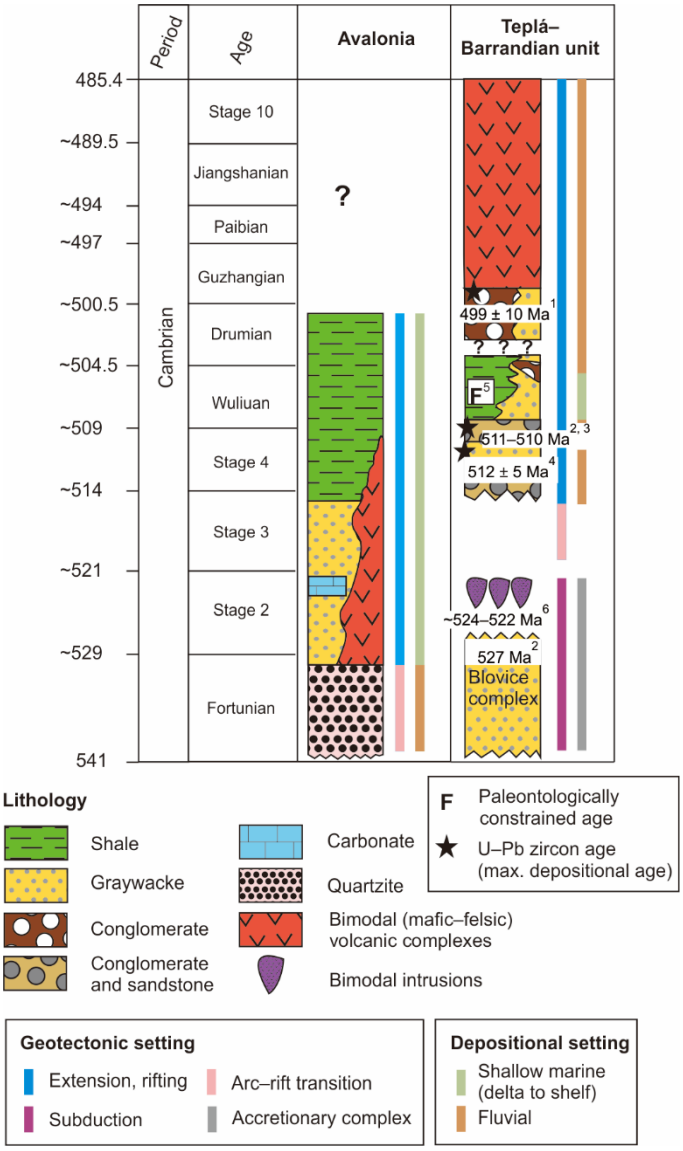


**Figure 34.** *(a) Tectono-stratigraphy of Avalonia (Nance et al., 2002, 2008) and Teplá–Barrandian unit during the Cambrian. Note difference in volcanic deposits and marine deposits indicating diachronous rifting in both terranes. Ages compiled from (1) Drost et al. (2004), (2) Drost et al. (2011), (3) Hajná et al. (2017), (4) Hajná et al. (2018), (5) Fatka and Szabad (2014), (6) Zulauf et al. (1997).*

activity was recorded in Avalonia throughout the Cambrian, whereas in the Teplá–Barrandian unit it was delayed and short-lived, lasting only from ca. 500 Ma to 485 Ma (Fig. 34).

The major differences between the Avalonian and Cadomian terranes in their Cambrian evolution were attributed by Mallard and Rogers (1997) and Murphy et al. (2006) to different tectonic inheritance, westerly Avalonia being rifted off from the previously accreted ca. 1.3–1.0 Ga juvenile crust, whereas easterly Cadomia was in contact with older, Paleoproterozoic (ca. 2.2–2.0 Ga) West African cratonic basement. In the former case, the presumed Neoproterozoic suture represented significant rheological weakness and facilitated complete separation of Avalonia from the Amazonian craton. Conversely, a similar paleosuture was absent in Cadomia and thus the rifting likely failed to form a (hyper-) extended continental shelf (Fig. 35; e.g., Romer and Kroner, 2019; Žák and Sláma, 2018).

The above inferences corroborate that the Rheic Ocean opened from west to east in a scissor-like manner by oblique rifting (e.g., Linnemann et al., 2008). However, the kinematics of this major rifting event still remains poorly understood, largely because extrapolating kinematics from local to plate scale is often not straightforward. For instance, kinematic data from Avalonia (Nova Scotia) suggest that both sinistral (Nance and Murphy, 1990) and dextral (Murphy and Hynes, 1990) strike slip were operative locally. However, on a large scale, Keppie et al. (2003) suggest the kinematics required to move Avalonia from Amazonia to Laurentia mandate a component of sinistral displacement during and following the rift–drift phase that opened the Rheic Ocean (see also Nance et al., 2008 and their fig. 13). In contrast, Linnemann et al. (2008) inferred dextral transtension for the Saxothuringian and Ossa Morena zones. Moreover, Zulauf and Helferich (1997) and Zulauf et al. (1997) also described dextral movements in a middle to upper continental crust of Teplá–Barrandian unit. This is being in agreement with our present study on the Příbram–Jince basin, which must have been located near the easterly tip/hinge of the opening rift.

The potentially opposing kinematics of the westerly and easterly segments of the Avalonian–Cadomian belt are difficult to reconcile with a simple, all-embrasive model for the opening of the Rheic Ocean. Yet, this conundrum may be overcome by incorporating and refining the model. For instance, Nance et al. (2002), Keppie et al. (2003, 2008), and Sánchez-García et al. (2008) postulated ridge–transform–trench interaction to explain the end of Cadomian subduction and its conversion to a passive margin during the Cambrian (see also Hajná et al., 2018). Adopting this model (Fig. 35), the mid-ocean ridge may have intersected Gondwana's northern margin at an angle and separated the contrasting segments. In this scenario, as spreading continued, the Avalonian part of the belt would experience sinistral kinematics while the Cadomian part underwent dextral movement. Furthermore, the oblique angle between the spreading ridge axis and the Avalonian continental margin would facilitate a larger magnitude of extension whereas the angle with Cadomia is more compatible with prevailing strike-slip and limited continental separation (Fig. 35). If, however, displacement during and following the rift–drift transition in Avalonia had a dextral component, as implied by Nance et al. (2002) and, more recently, by the plate reconstructions of van Staal et al. (2021), no intervening ridge would be required and a simpler, dextral model would account for the opening of the Rheic Ocean in which the kinematics of Cadomia continued westward into Avalonia with regional variations likely linked to the curvature of the margin.

If either of these inferences is correct, however, the presence of both an inherited paleosuture and a suitably oriented subducted ridge may have controlled the opening of the Rheic Ocean, leading to a rift–drift transition in Avalonia, but only to failed rifting in the eastern Cadomian segment during the late Cambrian to early Ordovician.

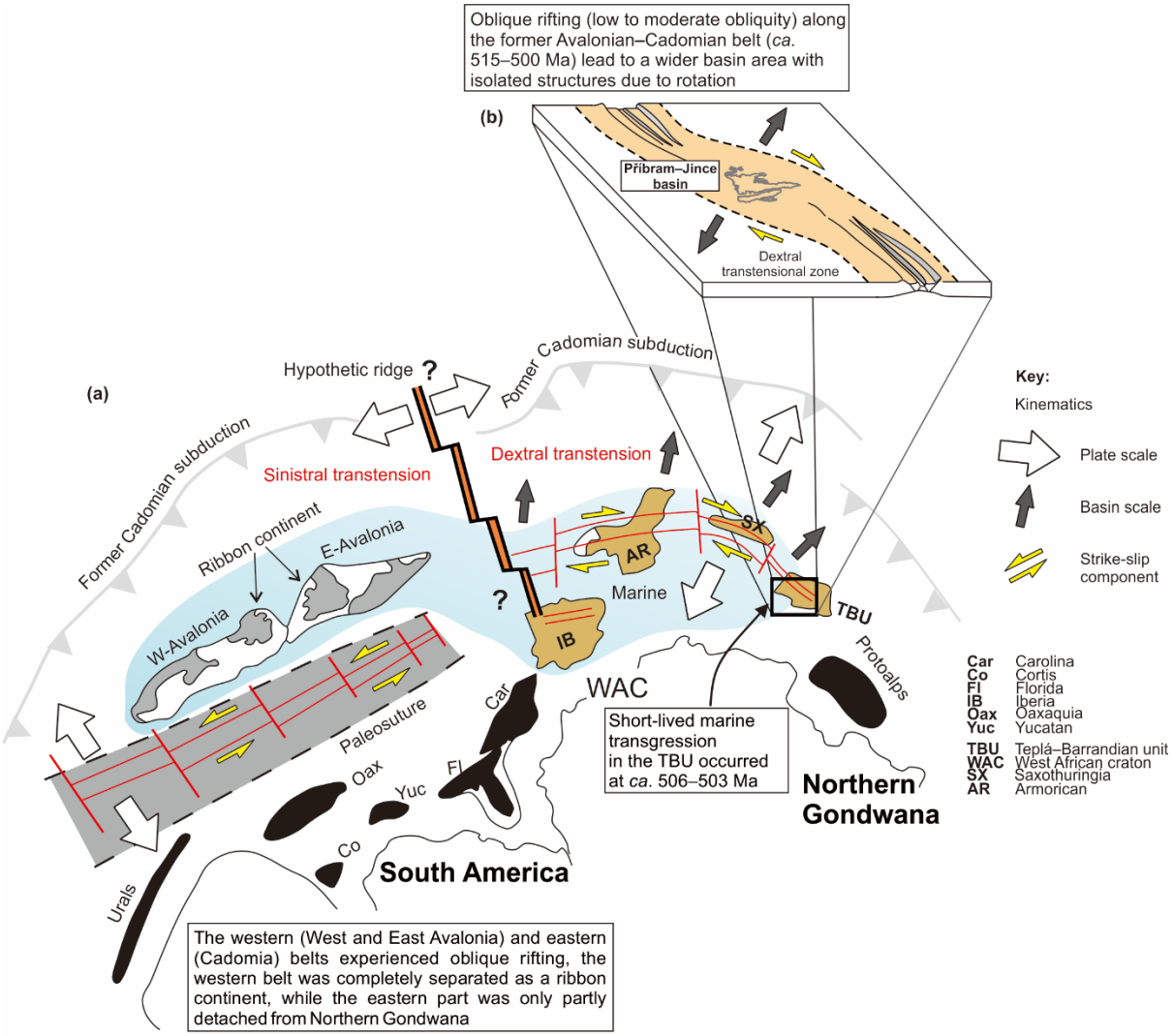


***Figure 35.*** *(a) A tentative plate-tectonic reconstruction of the peri-Gondwana terranes during the Cambrian (ca. 515–500 Ma; modified from Keppie et al., 2003; Murphy and Nance, 1989; Murphy et al., 1999; Gutiérrez-Alonso et al., 2003, Nance et al., 2008; and Linnemann et al., 2008, 2014). Inherited Neoproterozoic suture (after Murphy et al., 2006) is thought to have facilitated complete rifting in Avalonia. Lacking a paleosuture, the extended Cadomian terranes remained attached to the northern Gondwana margin. The kinematics of Avalonia separation has been debated. Here we examine a more complex scenario for opposing kinematics along the western and eastern segments of the former Avalonian–Cadomian belt separated by a hypothetic ridge (after Nance et al., 2002; Keppie et al., 2003, 2008; Sánchez-García et al., 2008). (b) Dextral transtension led to incipient rifting and development of a wide peri-Gondwanan shelf in the paleo-east (adopted from Duclaux et al., 2020). Except for the Teplá–Barrandian unit, which experienced only a short-lived marine transgression between ca. 506–503 Ma, a marine platform had already covered the other Cambrian basins.*

### 5.6. A case for non-uniform extension of the northern Gondwana margin

Despite their significantly different metamorphic grade, resulting from differential burial during the Late Devonian to early Carboniferous Variscan orogeny, the Teplá–Barrandian and Moldanubian units were arguably once formed a single, interconnected basinal system at the northern Gondwana periphery, presumably sourced from the Trans-Saharan belt and Saharan metacraton. The argument supporting this interpretation includes lithologic similarities (thick siliciclastic successions form the bulk of both units with younger carbonate deposition and intra-plate basaltic volcanism) and almost identical detrital zircon U–Pb age spectra suggesting that both units were sourced from the same area (e.g., Drost et al., 2011; Hajná et al., 2017; Hajná et al., 2018; Stephan et al., 2019a; Stephan et al., 2019b; Žák and Sláma, 2018; Žák et al., 2022). The present-day Teplá–Barrandian/Moldanubian boundary records a complex Variscan evolution and is extensively intruded by granodioritic plutons (e.g., Holub et al., 1997a; Holub et al., 1997b; Janoušek et al., 2000; Janoušek et al., 2010). But ophiolites that might indicate a spreading ridge and significant separation of the two units by a large tract of oceanic lithosphere (e.g., Franke, 2006; Franke et al. 2017) are absent. Hence, the Teplá–Barrandian and Moldanubian units, based on provided data, maybe viewed as exposures of two different crustal levels of the same Gondwanan passive margin; the Teplá–Barrandian unit having been little eroded whereas the Moldanubian metasedimentary host rocks to the orthogneisses (this study) were exhumed from mid-crustal levels at ca. 346–320 Ma (e.g., Žák et al., 2012). If this is the case, these two units may provide important information on the mechanism of rifting during the Cambrian and early Ordovician.

Cambro–Ordovician extension affected the entire northern Gondwana margin, which had previously been an accretionary orogenic belt, leading to the opening of the Rheic Ocean – a geodynamic process that has been studied extensively (e.g., Nance et al., 2010; Nance et al., 2012; Nance and Linnemann, 2008). Three general hypotheses have been proposed to

explain the geodynamic cause of this extension: (1) far-field slab pull due to subduction of the outboard Iapetus Ocean beneath Laurentia or Avalonia (e.g., Nance et al., 2010), (2) retreat of an oceanic plate subducting steeply beneath northern Gondwana (e.g., Arenas et al., 2007; Díez Fernández et al., 2012), and (3) impingement of the continental margin by a mantle plume (e.g., Crowley et al., 2000; Keppie et al., 2006). While most previous work has focused on the timing and petrogenesis of the associated magmatism, we combine precise age constraints with information on basin subsidence and changes in magma composition through time to characterize the detailed mechanism of lithospheric extension at different structural levels.

The Moldanubian orthogneisses dated in this thesis play an important role in completing this picture: they represent the only element that can provide temporal constraints since no fossils are preserved in the metaclastic successions, and sedimentary and amphibolite protoliths are difficult to date precisely. The orthogneiss protoliths are interpreted to have been variably evolved crustally derived granites produced by dehydration melting of muscovite-bearing metapelites (the Blaník type) or fluid-present melting of immature crustal sources (the Deštná type; Buriánek et al., 2020), likely the Cadomian arc-derived graywackes. Compositionally similar and coeval peraluminous granites emplaced in the same tectonic setting in Iberia were interpreted by Bea et al., 2007) as recording a short-lived magmatic event characterized by rapid magma generation and emplacement rates. This is agreement with our new U–Pb zircon ages, which define a restricted time span for protolith crystallization for most of the Moldanubian orthogneisses between 489 ± 3 Ma

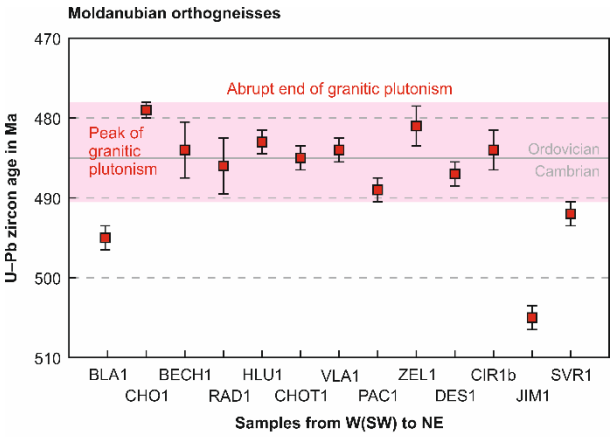


**Figure 36.** *Summary diagram showing all U–Pb ages (with error bars) of the Moldanubian orthogneisses sampled, implying a narrow time span of their emplacement and crystallization (highlighted as pink background).*

(sample PAC1; Figs. 30, 36) and 481 ± 3 Ma (sample CHO1; Figs. 29, 36). Based on an analysis of Huppert and Sparks (1988) and Bea et al. (2007), such rapid intracrustal melting is best explained by mafic magma underplating in an extensional, rift-related setting.

Consequently, the geologic record at the surface and in the upper crust of both the Teplá–Barrandian and Moldanubian units can be interpreted as reflecting processes occurring in the lower crust and subcrustal mantle (Fig. 37). To provide a broader context, Figure 37a shows a compilation of the available information on the timing of basin development, volcanism, and plutonism (including the dated orthogneisses) between the termination of the Cadomian accretionary processes at ca. 527 Ma (e.g., Hajná et al., 2017) and the mid-Ordovician passive margin stage at ca. 450 Ma (e.g., Drost, 2008; Drost et al., 2011; Patočka and Štorch, 2004; Štorch, 2006). The chronology of events during this period indicates three phases of Cambro–Ordovician extension at the lithospheric scale.

The first phase commenced with widespread ca. 524–522 Ma gabbro–trondhjemite–granodiorite–granite plutonism (Dörr et al., 1998; Zulauf et al., 1997; Zulauf and Helferich, 1997) that followed the termination of Cadomian accretion by only several millions of years (the youngest accreted units are ca. 527 Ma, Fig. 37a). This thermal event took place within an overall cold forearc setting and is interpreted as resulting from slab break-off, which terminated Cadomian subduction beneath the Teplá–Barrandian unit and input heat into the base of the graywacke-dominated crust. This phase was associated with transtensional tectonics followed by weak E–W upper-crustal extension and lasted until the early Ordovician.

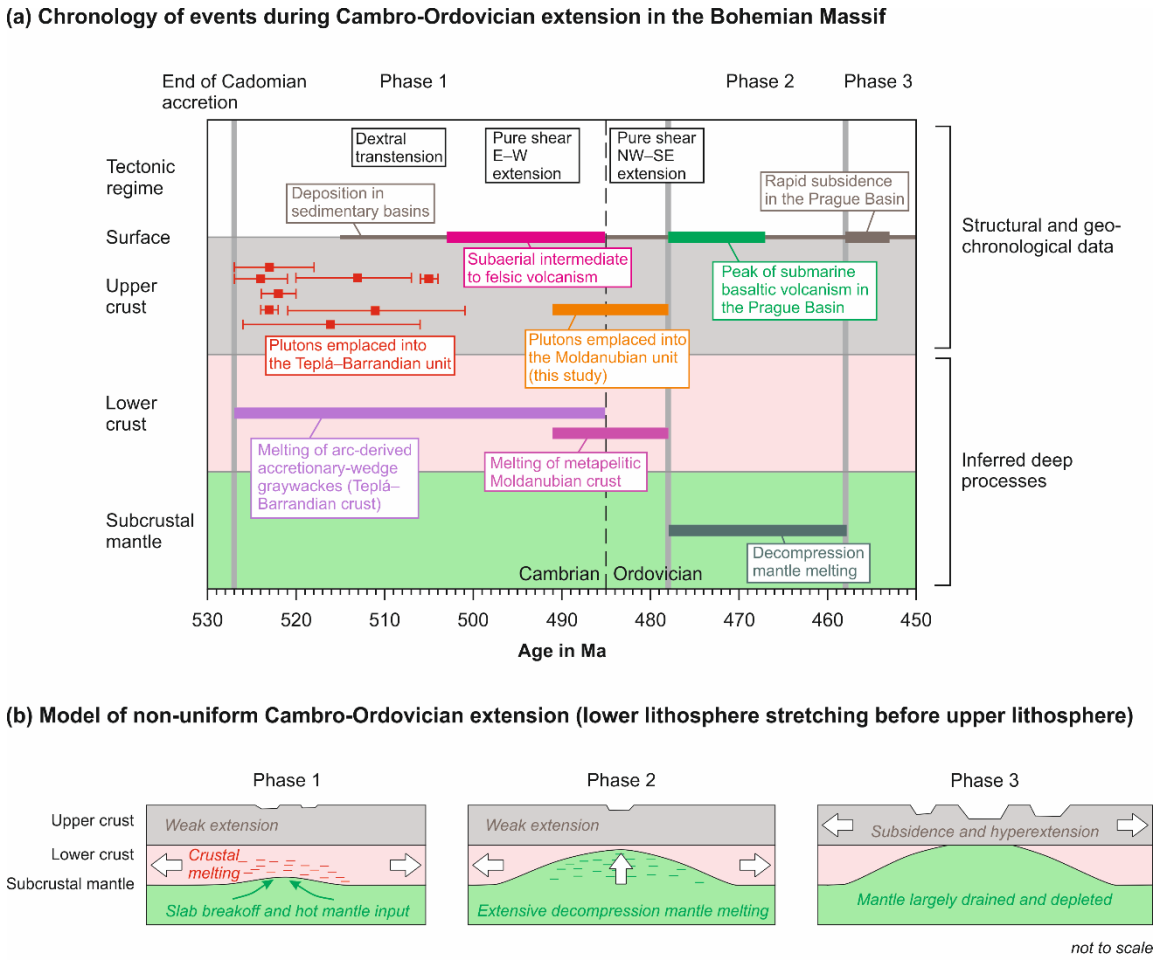


**Figure 37.** *(a) Synthetic chart showing both radioisotopically constrained and inferred temporal succession of tectonomagmatic events at different structural levels during the Cambrian as inferred from U–Pb ages and the rock record in the Teplá–Barrandian and Moldanubian units. (b) Model of three-stage non-uniform extension in the Bohemian Massif inferred from structural and geochronological data summarized in (a). See text for discussion and citations.*

The orthogneisses examined here appear to mark the end of the first phase and set the stage for the second; perhaps indicating basaltic underplating below an extending crust (Fig. 37a). Additionally, the emplacement of the Moldanubian orthogneisses is coeval with the rift–drift transition of Avalonia from Gondwana and the opening of the Rheic Ocean to the west (at ca. 485 Ma; e.g., Pollock et al., 2009; Prigmore et al., 1997; Thompson et al., 2010). The second phase is defined by an abrupt change in magma composition from felsic to mafic and culminated in a peak in the voluminous submarine basaltic volcanism in the Prague Basin at ca. 470 Ma (Fig. 37a), interpreted as recording decompression mantle melting. By contrast, the

third phase is defined by quiescence in the submarine volcanic activity and by rapid subsidence on the order of several kilometers at ca. 458–452 Ma (Fig. 37a).

This three-phase transition from Cadomian active plate margin to a rift/passive margin setting indicates non-uniform, depth-dependent lithospheric extension as discussed in detail by Huismans and Beaumont (2014). The chronology of events is compatible with a strong upper-crustal layer affected by only weak, distributed stretching and heated from below (phase 1; Fig. 37b), followed by necking of decoupled subcrustal mantle allowing for extensive decompression melting (phase 2; Fig. 37b), with basalt extraction from the mantle replaced by thinning of the upper crust (phase 3; Fig. 37b). The timing of events also suggests break-up of the lower lithosphere before the upper lithosphere (Type III extension of Huismans and Beaumont, 2014), which should produce an ultra-wide, hyper-extended passive margin. If these inferences are correct, they have important implications for interpreting the paleogeography of the Cambro–Ordovician extension of northern Gondwana and for the birth of the Rheic Ocean.

### 5.7. A rheological control on contrasting styles of opening of the Rheic Ocean?

Interpretations of the mechanism of Rheic Ocean opening have evolved considerably over the past two decades. For example, Nance et al. (2002) suggested that the Cadomian orogeny was terminated by ridge–trench collision, with diachronous termination of subduction and the generation of a continental transform fault. The subsequent, ca. 510–480 Ma continental rifting and separation of Avalonia and Carolinia from Gondwana followed a shift of the transform inboard and the transfer of these two terranes to the oceanic plate. Expanding on this model, Murphy et al. (2006) emphasized that the western and eastern portions of northern Gondwana had remarkably different pre-break-up histories. The westerly Avalonian-type terranes were built on previously accreted ‘proto-Avalonia’ (1.1–0.75 Ga TDM model ages) and rifted off along a pre-existing suture, whereas the easterly Cadomian-type terranes

were built on or adjacent to Eburnean (2.1–2.0 Ga) cratonic basement and remained attached to Gondwana (see also Linnemann et al., 2004; Linnemann et al., 2008; Žák and Sláma, 2018). Syahputra et al. (2022) further noted contrasting transtensional kinematics (sinistral in the western and dextral in the eastern terranes) during the middle to late Cambrian, supporting the presence of a subducting ridge or some sort of a transfer zone between the two domains (Fig. 35a).

Taken together with the rheological considerations developed above, it may be speculated that the western and eastern segments of the northern Gondwana margin were also characterized by contrasting rheological structure of the lithosphere, the former having a strong lower lithosphere ('proto-Avalonia') and the latter a strong upper lithosphere (cold accretionary wedges; the orthogneisses study). A strong lower lithosphere, together with the presence of a presumed inherited suture (Murphy et al., 2006), favored break-up along a narrow zone to the west, whereas a strong upper lithosphere favored a wide, hyper-extended margin break-up mode to the east (Fig. 35a; Huismans and Beaumont, 2014). In turn, the narrow-rift mode fostered the complete separation and drift of Avalonian-type terranes from Gondwana, whereas the wide-margin mode accommodated distributed extension that likely produced an extensive shelf consisting of multiple crustal fragments separated by thinned domains (e.g., Kroner and Romer, 2013; Stephan et al., 2019a; Žák and Sláma, 2018). Such thinned domains between crustal boudins do not imply seafloor spreading since stretching is accommodated by shallowly dipping detachments (e.g., Manatschal, 2004; Péron-Pinvidic and Manatschal, 2019). However, they may have formed complex tectonic boundaries during Variscan convergence, that could easily be misinterpreted as oceanic suture zones (e.g., the Teplá–Barrandian/Moldanubian boundary).

# 6. CONCLUSIONS AND EXECUTIVE SUMMARY

## 6.1. The incipient formation of the Cadomian ribbon terranes of the Bohemian Massif

Geodynamic changeover from the Cadomian active (subduction-accretion) to Cambro–Ordovician passive (extension) margin setting in the Teplá–Barrandian unit and Moldanubian zone of the Bohemian Massif was a protracted transition that can be divided into three major phases:

(1) The end of Cadomian orogeny in the Teplá–Barrandian unit was represented by the subduction and accretion of the turbidite sequences of the Blovice accretionary complex. This orogen ceased to develop at ca. 527 Ma and was followed emplacement of hot and buoyant magma of the Kdyně pluton into a cold forearc setting within a few millions of years (at ca. 524–523 Ma). The emplacement of the Kdyně pluton was primarily controlled by multiple emplacement styles (magma wedging in the northern and middle domains and lateral expansion in the southern domain with minor stoping mechanisms) rather than regional tectonic deformation. This interpretation was made based on the internal pluton fabric which is parallel to local pluton–host rock contacts and follows the orthogonal extensional fractures (~NNE–SSW and ~WNW–ESE), thus, affecting the pre- and post-plutonic structures in the host rock to be folded and sheared.

The pluton is interpreted as representing an apical part of a domal structure in the upper crust, presumably situated between two dextral transtensional shear zones that acted as detachments and generating an extensional stepover in the pluton southern domain. In terms of tectonic setting during emplacement, the pluton thus resembles metamorphic core complexes. The deformation during the pluton emplacement was partitioned into simple shear-dominated zones that delimited pure shear-dominated belts. A rapid turnover from compressional to extensional regimes may thus be viewed as the initial sign of the active-passive margin

protracted transition in the Teplá–Barrandian unit. Furthermore, younger Cambrian intrusion (ca. 511–480 Ma) migrated northward over the Teplá–Barrandian unit with an oblique pattern to the Cadomian accretionary belts, perhaps reflecting the opening slab tear/break-off in this direction and triggering an incipient lithospheric extension of the Rheic Ocean.

(2) The Cambrian pluton emplacement was partly overlapped with the sedimentary basin development. The Příbram–Jince basin represented the complete and well-preserved Cambrian stratigraphy. Continental conglomerates, coarse-grained sandstones, and thin tuffaceous layers dominate this basin with their depositional environment ranging from the alluvial fans, flood plains, and axial river channel. The tectonic setting in this basin controlled the sedimentary source evolving from pure shear dominated graben with its provenance mainly coming from the pre-Cambrian terranes (Gondwana mainland?) to a pull-apart dextral transtensional structure sourced from local material coming from the underlying Blovice accretionary complex at ca. 511 Ma (based on microstructural and existing geochronological data).

The tectonics and sedimentation in the Příbram–Jince basin suggest that strike-slip movements along the former Avalonian–Cadomian belt initiated the opening of the Rheic Ocean during ca. 515–500 Ma, placing this basin (and Teplá–Barrandian unit) at the rift-tip. This event also indicated a successful and abortive break-up of the ribbon continent in the peri-Gondwana terranes that was primarily influenced by an inherited suture in the Avalonian ribbon terrane while the Cadomian terranes remained partly attached to Gondwana. The sedimentation in the Příbram–Jince basin was accompanied by depocenter changes, rapid subsidence, a short-lived marine transgression at ca. 506–503 Ma, and bimodal volcanic activity that happened ca. 15 m.y. (delayed ca. 5 m.y. from volcanic activity in the Avalonian rifting).

(3) The slab break-off was coeval with dextral transtension in the surface of the Teplá–Barrandian unit and generated the emplacement of granitic magma at ca. 490–480 Ma in the Moldanubian zone (now the Moldanubian orthogneisses) due to the basaltic underplating in an extending crust. This process was coeval with Avalonia's rift–drift transition from Gondwana and the opening of the Rheic Ocean (at ca. 485 Ma). Subsequently, the magmatic composition changed from felsic to mafic and started to accumulate numerous submarine volcanic basalt at ca. 470 Ma due to decompression mantle melting, which was then followed by rapid subsidence in Prague Basin between 458 and 452 Ma.

### 6.2. General implication for ribbon continent formation

All the processes mentioned above are considered as a transition from Cadomian active plate margin to a rift/passive margin setting. The transition started with the slab break-off, which induced a rapid changeover from compressional to extensional regimes. It was demonstrated that the transition represented a non-uniform, depth-dependent lithospheric extension with a strong upper-crustal layer affected by only weak, distributed stretching and heated from below, followed by necking of decoupled subcrustal mantle allowing for decompression melting and basalt magma extraction, and finally by thinning of the upper crust.

(1) The series of above-inferred events are compatible with the Type III-A/C extension of Huismans and Beaumont (2014), where the ribbon continent formation involves weakening the lower crust first due to the slab break-off and subsequently by stretching of the upper crust. Thus, the lower lithosphere broke up before the upper lithosphere, likely resulting in a hyper-extended passive margin.

(2) These rheological considerations from the easterly Cadomian-type terranes together with the available data from the westerly Avalonian-type terranes suggest that the northern Gondwanan margin was characterized by contrasting mode of break-up of and ribbon continent formation. This break-up was controlled by rheological structure of the lithosphere, the

Cadomian-type terranes having a strong upper lithosphere (cold accretionary wedges) whereas the Avalonian-type terranes had a strong lower lithosphere (‘proto-Avalonia’) and contained a presumed inherited suture.

Altogether, the Avalonian-type terranes favored to break-up along a narrow zone and completely separated and drifted from Gondwana, whereas the strong upper lithosphere favored a wide-margin mode of break-up with distributed extension that likely produced an extensive shelf consisting of multiple crustal fragments separated by thinned domains. These inferences imply a key role of tectonic inheritance and the presence of lithospheric-scale weaknesses or discontinuities to generate ribbon microplate.

**Bibliography**

Ackerman, L., Hajná, J., Žák, J., Erban, V., Sláma, J., Polák, L., Kachlík, V., Strnad, L., Trubač, J., 2019. Architecture and composition of ocean floor subducted beneath northern Gondwana during Neoproterozoic to Cambrian: A palinspastic reconstruction based on Ocean Plate Stratigraphy (OPS). Gondwana Res. 76, 77–97.

Ackerman, L., Žák, J., Kachlík, V., Svojtka, M., Tomek, F., Santolik, V., Sláma, J., Trubač, J., Strnad, L., Vacek, F., 2022. The diversity of sources of late Archean granites reflects a transition from plume-dominated to plate tectonics in the Superior Province, Canada. Precambr. Res. 370, 20.

Agard, P., Yamato, P., Jolivet, L., Burov, E., 2009. Exhumation of oceanic blueschists and eclogites in subduction zones: Timing and mechanisms. Earth Sci. Rev. 92, 53–79.

Allen, J.R.L., 1973. Features of cross-stratified units due to random and other changes in bed forms. Sedimentology 20, 189–202.

Amato, J.M., Miller, E.L., Hannula, K.A., 2002. Orthogonal flow directions in extending continental crust: an example from the Kigluaik gneiss dome, Seward Peninsula, Alaska, In: Miller, E.L., Grantz, A., Klemperer, S.L. (Eds.), Tectonic evolution of the Bering shelf–Chukchi Sea–Arctic margin and adjacent landmasses. Geol. Soc. Am. Special Paper, 133–146.

Anczkiewicz, R., Oberli, F., Burg, J. P., Villa, I. M., Günther, D., and Meier, M., 2001, Timing of normal faulting along the Indus Suture in Pakistan Himalaya and a case of major $^{231}Pa/^{235}U$ initial disequilibrium in zircon. Earth Planet. Sci. Lett. 191, 101–114.

Arenas, R., Martínez Catalan, J.R., Martinez, S.S., Fernandez-Suarez, J., Andonaegui, P., Pearce, J.A., Corfu, F., 2007. The Vila de Cruces ophiolite: A remnant of the early Rheic Ocean in the Variscan suture of Galicia (northwest Iberian Massif). J. Geol. 115, 129–148.

Arenas, R., Sánchez Martínez, S., Albert, R., Haissen, F., Fernández-Suárez, J., Pujol-Solà, N., Andonaegui, P., Díez Fernández, R., Proenza, J.A., Garcia-Casco, A. and Gerdes, A., 2021. 100 myr cycles of oceanic lithosphere generation in peri-Gondwana: Neoproterozoic–Devonian ophiolites from the NW African–Iberian margin of Gondwana and the Variscan Orogen. Geol. Soc. London, Special Publications, 503, 169–184.

Atherton, M.P., Ghani, A.A., 2002. Slab breakoff: a model for Caledonian, Late Granite syn-collisional magmatism in the orthotectonic (metamorphic) zone of Scotland and Donegal, Ireland. Lithos 62, 65–85.

Autin, J., Bellahsen, N., Leroy, S., Husson, L., Beslier, M.O., d'Acremont, E., 2013. The role of structural inheritance in oblique rifting: Insights from analogue models and application to the Gulf of Aden. Tectonophysics 607, 51–64.

Babcock, L.E., Peng, S.C., Brett, C.E., Zhu, M.Y., Ahlberg, P., Bevis, M., Robison, R.A., 2015. Global climate, sea level cycles, and biotic events in the Cambrian Period. Palaeoworld 24, 5–15.

Bábek, O., Faměra, M., Hladil, J., Kapusta, J., Weinerová, H., Šimíček, D., Slavík, L., and Ďurišová, J., 2018a, Origin of red pelagic carbonates as an interplay of global climate and local basin factors: insight from the Lower Devonian of the Prague Basin, Czech Republic. Sediment. Geol. 364, 71–88.

Bábek, O., Faměra, M., Šimíček, D., Weinerová, H., Hladil, J., and Kalvoda, J., 2018b, Sea-level changes vs. organic productivity as controls on Early and Middle Devonian bioevents: facies- and gamma-ray based sequence-stratigraphic correlation of the Prague Basin, Czech Republic. Global and Planetary Change, 160, 75–95.

Ballèvre, M., Fourcade, S., Capdevila, R., Peucat, J.J., Cocherie, A., Fanning, C.M., 2012. Geochronology and geochemistry of Ordovician felsic volcanism in the Southern Armorican Massif (Variscan belt, France): implications for the breakup of Gondwana. Gondwana Res. 21, 1019–1036.

Ballévre, M., Goff, E.L., Hebert, R., 2001. The tectonothermal evolution of the Cadomian belt of northern Brittany, France: a Neoproterozoic volcanic arc. Tectonophysics 331, 19–43.

Bea, F., Montero, P., González-Lodeiro, F., and Talavera, C., 2007. Zircon inheritance reveals exceptionally fast crustal magma generation processes in Central Iberia during the Cambro-Ordovician. J. Petrology, 48, 2327–2339.

Blair, T.C., 2000. Sedimentology and progressive tectonic unconformities of the sheetflood-dominated Hell's Gate alluvial fan, Death Valley, California. Sed. Geol. 132, 233–262.

Blenkinsop, T., 2000. Deformation microstructures and mechanisms in minerals and rocks. Kluwer Academic Publishers, Dordrecht.

Blížkoský, M., Fusán, O., Ibrmajer, J., Plančár, J. and Suk, M., 1986. Geophysical phenomena of the deep structure in Czechoslovakia. J. Geodyn., 5, 165–178.

Borissova, I., Coffin, M.F., Charvis, P., Operto, S., 2002. Structure and development of a microcontinent: Elan bank in the southern Indian Ocean. Geochem. Geophys. Geosyst. 4.

Borradaile, G. J., Jackson, M., 2004. Anisotropy of magnetic susceptibility (AMS)venera: magnetic petrofabrics of deformed rocks. Geol. Soc. London, Special Publications 238, 299–360.

Borradaile, G., Henry, B., 1997. Tectonic applications of magnetic susceptibility and its anisotropy. Earth Sci. Rev. 42, 49–93.

Borradaile, G.J., Jackson, M., 2004. Anisotropy of magnetic susceptibility (AMS): magnetic petrofabrics of deformed rocks. Geol. Soc. London, Special Publications 238, 299–360.

Borradaile, G.J., Jackson, M., 2010. Structural geology, petrofabrics and magnetic fabrics (AMS, AARM, AIRM). J. Struct. Geol. 32, 1519–1551.

Bouchez, J.L., 1997. Granite is never isotropic: an introduction to AMS studies of granitic rocks, In: Bouchez, J.L., Hutton, D.H.W., Stephens, W.E. (Eds.), Granite: From segregation of melt to emplacement fabrics. Kluwer Academic Publishers, pp. 95–112.

Brenchley, P. J., Štorch, P., 1989, Environmental changes in the Hirnantian (upper Ordovician) of the Prague Basin, Czechoslovakia. Geol. J. 24, 165–181.

Brovarone, A.V., Beyssac, O., Malavieille, J., Molli, G., Beltrando, M., Compagnoni, R., 2013. Stacking and metamorphism of continuous segments of subducted lithosphere in a high-pressure wedge: The example of Alpine Corsica (France). Earth Sci. Rev. 116, 35–56.

Brown, H. C., Khan, M. A., Stacey, F. D., 1964. A search for flow structure in columnar basalt using magnetic anisotropy of rocks. Pure. Apl. Geophys. 57, 61–5.

Brune, S., Corti, G., Ranalli, G., 2017. Controls of inherited lithospheric heterogeneity on rift linkage: Numerical and analog models of interaction between the Kenyan and Ethiopian rifts across the Turkana depression. Tectonics 36, 1767–1786.

Brune, S., Williams, S.E., Müller, R.D., 2018. Oblique rifting: the rule, not the exception. Solid Earth 9, 1187–1206.

Buddington, A.F., 1959. Granite emplacement with special reference to North America. Geol. Soc. Am. Bull., 70: 671–747.

Bues, C., Dörr, W., Fiala, J., Vejnar, Z., Zulauf, G., 2002. Emplacement depths and radiometric ages of Paleozoic plutons of the Neukirchen–Kdyne massif: differential uplift and exhumation of Cadomian basement due to Carboniferous orogenic collapse Bohemian Massif). Tectonophysics 352, 225–243.

Buriánek, D., Buřivalová, L., Houzar, S., Losos, Z., and Míková, J., 2020, Geochronology and petrogenesis of orthogneisses from the Pacov body: implications for the subdivision of the Cambro–Ordovician peraluminous magmatism and related mineralizations in the Monotonous and Varied units of the Moldanubian Zone (Bohemian Massif). Mineralogy and Petrology, 114, 175–197.

Burton-Johnson, A., Macpherson, C.G., Muraszko, J.R., Harrison, R.J. and Jordan, T.A., 2019. Tectonic strain recorded by magnetic fabrics (AMS) in plutons, including Mt Kinabalu, Borneo: A tool to explore past tectonic regimes and syn-magmatic deformation. J. Struct. Geol. 119, 50–60.

Callot, J.P., Robion, P., Sassi, W., Guiton, M.L.E., Faure, J.L., Daniel, J.M., Mengus, J.M., Schmitz, J., 2010. Magnetic characterisation of folded aeolian sandstones: Interpretation of magnetic fabrics in diamagnetic rocks. Tectonophysics 495, 230–245.

Cappelletti, A., Tsikalas, F., Nestola, Y., Cavozzi, C., Argnani, A., Meda, M., Salvi, F., 2013. Impact of lithospheric heterogeneities on continental rifting evolution: Constraints from analogue modelling on South Atlantic margins. Tectonophysics 608, 30–50.

Casas, J.M., Murphy, J.B., 2018. Unfolding the arc: The use of pre-orogenic constraints to assess the evolution of the Variscan belt in Western Europe. Tectonophysics 736, 47–61.

Cawood, P.A., 2005. Terra Australis Orogen: Rodinia breakup and development of the Pacific and Iapetus margins of Gondwana during the Neoproterozoic and Paleozoic. Earth Sci. Rev. 69, 249–279.

Cawood, P.A., McCausland, P.J.A., Dunning, G.R., 2001. Opening Iapetus: Constraints from the Laurentian margin in Newfoundland. Geol. Soc. Am. Bull. 113, 443–453.

Černý, J., Melichar, R., Všianský, D., Drahokoupil, J., 2020. Magnetic anisotropy of rocks: A new classification of inverse magnetic fabrics to help geological interpretations. J. Geophys. Res. Solid Earth 125, e2020JB020426.

Cháb, J., Stráník, Z., and Eliáš, M., 2007. Geological map of the Czech Republic 1:500,000: Czech Geological Survey.

Chadima, M., Cajz, V., Týcová, P., 2009. On the interpretation of normal and inverse magnetic fabric in dikes: examples from the Eger Graben, NW Bohemian Massif. Tectonophysics 466, 47–63.

Chadima, M., Jelínek, V., 2008. Anisoft 4.2. – anisotropy data browser. Contrib. Geophys. Geod. 38, 41.

Chantraine, J., Egal, E., Thieblemont, D., Le Goff, E., Guerrot, C., Ballevre, M., Guennoc, P., 2001. The Cadomian active margin (North Armorican Massif, France): a segment of the North Atlantic Panafrican belt. Tectonophysics 331, 1–18.

Chlupáč, I., 1988. Possible global events and the stratigraphy of the Palaeozoic of the Barrandian (Cambrian–Middle Devonian, Czechoslovakia). Journal of Geological Sciences, Geology, 43, 83–146.

Chlupáč, I., 2003. Comments on facies development and stratigraphy of the Devonian, Barrandian area, Czech Republic. Bull. Geosci. 78, 299–312.

Chlupáč, I., Havlíček, V., 1965. Kodymirus n. g. a new aglaspid merostome of the Cambrian of Bohemia. J. Geol. Sci. Paleont. 6: 7–20.

Chlupáč, I., Havlíček, V., Kříž, J., Kukal, Z., Štorch, P., 1998. Palaeozoic of the Barrandian, Prague, Czech Geological Survey.

Chlupáč, I., Kraft, J., Kraft, P., 1995. Geology of fossil sites with the oldest Bohemian fauna (Lower Cambrian, Barrandian area). J. Czech Geol. Soc. 40, 1–8.

Cocks, L.R.M., McKerrow, W.S., van Staal, C.R., 1997. The margins of Avalonia. Geol. Mag. 134, 627–636.

Collins, W.J., 2002. Hot orogens, tectonic switching, and creation of continental crust. Geology 30, 535–538.

Cooke, R. A., and O´Brien, P. J., 2001, Resolving the relationship between high P–T rocks and gneisses in collisional terranes: an example from the Gföhl gneiss–granulite association in the Moldanubian Zone, Austria. Lithos, 58, 33–54.

Cooper, M.R., Crowley, Q.G., Hollis, S.P., Noble, S.R., Henney, P.J., 2013. A U–Pb age for the Late Caledonian Sperrin Mountains minor intrusions suite in the north of Ireland: timing of slab break-off in the Grampian terrane and the significance of deep-seated, crustal lineaments. J. Geol. Soc. 170, 603–614.

Crowley, Q.G., Floyd, P.A., Winchester, J.A., Franke, W., Holland, J.G., 2000. Early Palaeozoic rift-related magmatism in Variscan Europe: fragmentation of the Armorican Terrane Assemblage. Terra Nova 12, 171–180.

Cruden, A.R. and McCaffrey, K.J.W., 2001. Growth of plutons by floor subsidence: implications for rates of emplacement, intrusion spacing and melt-extraction mechanisms. Phys. Chem Earth 26, 303–315.

Cruden, A.R., McCaffrey, K.J.W. and Bunger, A.P., 2017. Geometric scaling of tabular igneous intrusions: implications for emplacement and growth. In: Physical Geology of Shallow Magmatic Systems. 11–38.

Dalziel, I.W.D., 1997. Neoproterozoic–Paleozoic geography and tectonics: Review, hypothesis, environmental speculation. Geol. Soc. Am. Bull. 109, 16–42.

Davies, J.H., von Blanckenburg, F., 1995. Slab breakoff: a model of lithosphere detachment and its test in the magmatism and deformation of collisional orogens. Earth Planet. Sci. Lett. 129, 85–102.

Davy, B., Hoernle, K., Werner, R., 2008. Hikurangi Plateau: Crustal structure, rifted formation, and Gondwana subduction history. Geochem. Geophys. 9, Q07004.

Díez Fernández, R., Castiñeiras, P., Gómez Barreiro, J., 2012. Age constraints on Lower Paleozoic convection system: Magmatic events in the NW Iberian Gondwana margin. Gondwana Res. 21, 1066-1079.

Dörr, W., Fiala, J., Vejnar, Z., Zulauf, G., 1998. U–Pb zircon ages and structural development of metagranitoids of the Teplá crystalline complex: evidence for pervasive Cambrian plutonism within the Bohemian massif (Czech Republic). Geol. Rundsch. 87, 135–149.

Dörr, W., Zulauf, G., 2010. Elevator tectonics and orogenic collapse of a Tibetan-style plateau in the European Variscides: the role of the Bohemian shear zone. Int. J. Earth Sci. 99, 299–325.

Dörr, W., Zulauf, G., Fiala, J., Franke, W., Vejnar, Z., 2002. Neoproterozoic to Early Cambrian history of an active plate margin in the Teplá–Barrandian unit - a correlation of U–Pb isotopic-dilution-TIMS ages (Bohemia, Czech Republic). Tectonophysics 352, 65–85.

Drost, K., Gerdes, A., Jeffries, T., Linnemann, U., Storey, C., 2011. Provenance of Neoproterozoic and early Paleozoic siliciclastic rocks of the Teplá–Barrandian unit (Bohemian Massif): evidence from U–Pb detrital zircon ages. Gondwana Res. 19, 213–231.

Drost, K., Linnemann, U., McNaughton, N., Fatka, O., Kraft, P., Gehmlich, M., Tonk, C., Marek, J., 2004. New data on the Neoproterozoic - Cambrian geotectonic setting of the Tepla–Barrandian volcano-sedimentary successions: geochemistry, U–Pb zircon ages, and provenance (Bohemian Massif, Czech Republic). Int. J. Earth Sci. 93, 742–757.

Drost, K., Linnemann, U., McNaughton, N., Fatka, O., Kraft, P., Gehmlich, M., Tonk, C., Marek, J., 2004. New data on the Neoproterozoic–Cambrian geotectonic setting of the Teplá–

Barrandian volcano-sedimentary successions: geochemistry, U–Pb zircon ages, and provenance (Bohemian Massif, Czech Republic). Int. J. Earth Sci. 93, 742–757.

Duclaux, G., Huismans, R.S., May, D.A., 2020. Rotation, narrowing, and preferential reactivation of brittle structures during oblique rifting. Earth Planet. Sci. Lett. 531, 12.

Duretz, T., Petri, B., Mohn, G., Schmalholz, S.M., Schenker, F.L., Muntener, O., 2016. The importance of structural softening for the evolution and architecture of passive margins. Scientific Reports 6, 7.

Dvořák, J., Hrouda. F., 1975. The reflection of the deeper structure of the Artmanov-Osoblaha block (Nízký Jeseník Mountains, Czechoslovakia) in the magnetic anisotropy and deformation history of overlying Palaeozoic sediments. Vest. Ustred. ust. geol. 50, 285–96.

Edel, J. B., Weber, K., 1995. Cadomian terranes, wrench faulting and thrusting in the central Europe Variscides: geophysical and geological evidence. Geol. Rundsch., 84, 412–432.

Ellwood, B. B., Wenner, D. B., 1981. Correlation of magnetic susceptibility with 18O:16O data in late orogenic granites of the southern Appalachian Piedmont. Earth Planet. Sci. Lett. 54, 200–2.

Epin, M.E., Manatschal, G., Amann, M., 2017. Defining diagnostic criteria to describe the role of rift inheritance in collisional orogens: the case of the Err-Platta nappes (Switzerland). Swiss J. Geosci. 110, 419–438.

Etxebarria, M., Chalot-Prat, F., Apraiz, A., Eguíluz, L., 2006. Birth of a volcanic passive margin in Cambrian time: rift paleogeography of the Ossa-Morena Zone, SW Spain. Precambr. Res. 147, 366–386.

Farangitakis, G.P., McCaffrey, K.J.W., Willingshofer, E., Allen, M.B., Kalnins, L.M., van Hunen, J., Persaud, P., Sokoutis, D., 2021. The structural evolution of pull-apart basins in response to changes in plate motion. Basin Res. 33, 1603–1625.

Faryad, S. W., Cuthbert, S. J., 2020. High-temperature overprint in (U)HPM rocks exhumed from subduction zones; A product of isothermal decompression or a consequence of slab break-off (slab rollback)? Earth Sci. Rev. 202, 103108.

Faryad, S. W., Kachlík, V., 2013. New evidence of blueschist facies rocks and their geotectonic implication for Variscan suture(s) in the Bohemian Massif. J. Metamorphic Geol., 31, 63–82.

Faryad, S. W., Kachlík, V., Sláma, J., Hoinkes, G., 2015. Implication of corona formation in a metatroctolite to the granulite facies overprint of HP–UHP rocks in the Moldanubian Zone (Bohemian Massif). J. Metamorphic Geol. 33, 295–310.

Fatka, O., Mergl, M., 2009. The 'microcontinent' Perunica: status and story 15 years after conception. Geological Society, London, Special Publications 325, 65–101.

Fatka, O., Szabad, M., 2014. Cambrian biostratigraphy in the Příbram-Jince Basin (Barrandian area, Czech Republic). Bull. Geosci. 89, 413–429.

Felletti, F., Dall'Olio, E., Muttoni, G., 2016. Determining flow directions in turbidites: An integrated sedimentological and magnetic fabric study of the Miocene Marnoso Arenacea Formation (northern Apennines, Italy). Sediment. Geol. 335, 197–215.

Festa, A., Balestro, G., Borghi, A., De Caroli, S., Succo, A., 2020. The role of structural inheritance in continental break-up and exhumation of Alpine Tethyan mantle (Canavese Zone, Western Alps). Geosci. Frontiers 11, 167–188.

Finger, F., Gerdes, A., Janoušek, V., René, M., Riegler, G., 2007. Resolving the Variscan evolution of the Moldanubian sector of the Bohemian Massif: the significance of the Bavarian and the Moravo–Moldanubian tectonometamorphic phases. J. Geosci. 52, 9–28.

Fisher, N. I., Lewis, T. L., Embleton, B. J., 1987. Statistical analysis of spherical data: Cambridge University Press, Cambridge.

Floyd, P.A., Winchester, J.A., Seston, R., Kryza, R. and Crowley, Q.G., 2000. Review of geochemical variation in Lower Palaeozoic metabasites from the NE Bohemian Massif: intracratonic rifting and plume-ridge interaction. Geol. Soc. London, Special Publications, 179, 155–174.

Franěk, J., Schulmann, K., Lexa, O., Tomek, C., Edel, J. B., 2011. Model of syn-convergent extrusion of orogenic lower crust in the core of the Variscan belt: implications for exhumation of high-pressure rocks in large hot orogens. J. Metamorphic Geol., 29, 53–78.

Franke, W., 2006. The Variscan orogen in Central Europe: construction and collapse. Geol. Soc. London. Memoirs 32, 333–343.

Franke, W., Cocks, L. R. M., Torsvik, T. H., 2017. The Palaeozoic Variscan oceans revisited. Gondwana Res. 48, 257–284.

Frey, F.A., Coffin, M.F., Wallace, P.J., Weis, D., Zhao, X., Wise, S.W., Wahnert, V., Teagle, D.A., Saccocia, P.J., Reusch, D.N., et al., 2000. Origin and evolution of a submarine large igneous province: the Kerguelen Plateau and Broken Ridge, southern Indian Ocean. Earth Planet. Sci. Lett. 176, 73–89.

Friedl, G., Finger, F., McNaughton, M.J., Fletcher, I.R., 2000. Deducing the ancestry of terranes: SHRIMP evidence for South America-derived Gondwana fragments in central Europe. Geology 28, 1035–1038.

Friedl, G., Finger, F., Paquette, J.-L., von Quadt, A., McNaughton, N.J., Fletcher, I.R., 2004. Pre-Variscan geological events in the Austrian part of the Bohemian Massif deduced from U–Pb zircon ages. Int. J. Earth Sci. 93, 802–823.

Garcia-Arias, M., Díez-Montes, A., Villaseca, C., Blanco-Quintero, I.F., 2018. The Cambro-Ordovician Ollo de Sapo magmatism in the Iberian Massif and its Variscan evolution: A review. Earth Sci. Rev. 176, 345-372.

Gawthorpe, R.L., Leeder, M.R., 2000. Tectono-sedimentary evolution of active extensional basins. Basin Res. 12, 195–218.

Gebauer, D. 1993. Geochronologische Übersicht. In : Bauberger W (ed) Geologische Karte von Bayern 1 : 25 000, Erläuterungen zum Blatt Nr. 6439 Tännesberg. Bayer. Geol. L.-Amt, München, 10–22

Geyer, G., Elicki, O., Fatka, O., Żylińska, A., 2008. Cambrian. In: McCann T (Ed), The geology of Central Europe. Precambrian and Palaeozoic, vol 1. Geological Society, London, 155–202.

Ghani, A.A., Atherton, M.P., 2006. The chemical character of the Late Caledonian Donegal granites, Ireland, with comments on their genesis. Earth Environ. Sci. Trans. R. Soc. Edinb. 97, 437–454.

Gutiérrez-Alonso, G., Fernández-Suárez, J., Jeffries, T.E., Jenner, G.A., Tubrett, M.N., Cox, R., Jackson, S.E., 2003. Terrane accretion and dispersal in the northern Gondwana margin. An Early Paleozoic analogue of a long-lived active margin. Tectonophysics 365, 221–232.

Gutiérrez-Alonso, G., Fernández-Suárez, J., Weil, A.B., Murphy, J.B., Nance, R.D., Corfu, F., Johnston, S.T., 2008. Self-subduction of the Pangaean global plate. Nature Geosci. 1, 549–563.

Hajna, J., Zak, J., Doerr, W., 2017. Time scales and mechanisms of growth of active margins of Gondwana: A model based on detrital zircon ages from the Neoproterozoic to Cambrian Blovice accretionary complex, Bohemian Massif. Gondwana Res. 42, 63–83.

Hajná, J., Žák, J., Dörr, W., Kachlík, V., Sláma, J., 2018. New constraints from detrital zircon ages on prolonged, multiphase transition from the Cadomian accretionary orogen to a passive margin of Gondwana. Precambr. Res. 317, 159–178.

Hajna, J., Zak, J., Kachlik, V., 2014. Growth of accretionary wedges and pulsed ophiolitic melange formation by successive subduction of trench-parallel volcanic elevations. Terra Nova 26, 322–329.

Hajná, J., Žák, J., Kachlík, V., Dörr, W., Gerdes, A., 2013. Neoproterozoic to early Cambrian Franciscan-type mélanges in the Teplá–Barrandian unit, Bohemian Massif: evidence of modern-style accretionary processes along the Cadomian active margin of Gondwana? Precam. Res. 224, 653–670.

Havlíček, J., 1981. Development of a linear sedimentary depression exemplified by the Prague Basin (Ordovician–Middle Devonian; Barrandian area – central Bohemia). J. Geol/ Sci. Geol. 35, 7–48.

Havlíček, V., 1971. Stratigraphy of the Cambrian of Central Bohemia. J. Geol. Sci. Geol. 20, 7–52.

Havlíček, V., 1998. Příbram–Jince Basin. In: Chlupáč, I., Havlíček V., Kříž, J., Kukal., Z., Štorch, P., Palaeozoic of the Barrandian (Cambrian–Devonian). Czech Geological Survey, Prague, 19–38.

Heilbronner, R., Tullis, J., 2002. The effect of static annealing on microstructures and crystallographic preferred orientations of quartzites experimentally deformed in axial compression and shear. Geol. Soc. London, Special publication 200, 191–218.

Herbert, C.M., Alexander, J., Amos, K.J., Fielding, C.R., 2020. Unit bar architecture in a highly-variable fluvial discharge regime: Examples from the Burdekin River, Australia. Sedimentology 67, 576–605.

Hibbard, J.P., Stoddard, E.F., Secor, D.T., Dennis, A.J., 2002. The Carolina Zone: overview of Neoproterozoic to Early Paleozoic peri-Gondwanan terranes along the eastern flank of the southern Appalachians. Earth Sci. Rev. 57, 299–339.

Hildebrand, R.S., Wahlen, J.B., 2014. Arc and slab-failure magmatism in Cordilleran Batholiths II – the Cretaceous Peninsular Ranges Batholith of Southern and Baja California. Geosci. Canada 44, 399–458.

Holub, F. V., Cocherie, A., Rossi, P., 1997a. Radiometric dating of granitic rocks from the Central Bohemian Plutonic Complex: constraints on the chronology of thermal and tectonic events along the Barrandian–Moldanubian boundary. Comptes Rendus de L'Academie des Sciences, Series IIA, Earth Planet. Sci. 325, 19–26.

Holub, F. V., Machart, J., and Manová, M., 1997b. The Central Bohemian Plutonic Complex: geology, chemical composition and genetic interpretation. J. Geol. Sci. Economic Geol. Mineralogy. 31, 27–50.

Horstwood, M. S. A., Košler, J., Gehrels, G., Jackson, S. E., McLean, N. M., Paton, C., Pearson, N. J., Sircombe, K., Sylvester, P., Vermeesch, P., Bowring, J. F., Condon, D. J., Schoene, B., 2016. Community-derived standards for LA-ICP-MS U–(Th–)Pb geochronology: uncertainty Propagation, age interpretation and data reporting. Geostandards and Geoanalytical Res. 40, 311–332.

Hoskin, P. W. O., Black, L. P., 2002. Metamorphic zircon formation by solid-state recrystallization of protolith igneous zircon. J. Metamorphic Geol. 18, 423–439.

Hoskin, P. W. O., Schaltegger, U., 2003. The composition of zircon and igneous and metamorphic petrogenesis. Rev. Mineral. Geochem. 53, 27–62.

Hrouda, F., 1982. Magnetic anisotropy of rocks and its application in geology and geophysics. Geophys. Surveys 5, 37–82.

Hrouda, F., 1994. A technique for the measurement of thermal changes of magnetic susceptibility of weakly magnetic rocks by the CS-2 apparatus and KLY-2 Kappabridge. Geophys. J. Int. 118, 604–612.

Hrouda, F., Jelínek, V., Hrušková, L., 1990. A package of programs for statistical eva- luation of magnetic data using IBM-PC computers. Eos Trans. AGU 71, 1289.

Hrouda, F., Jelínek, V., Zapletal, K., 1997. Refined technique for susceptibility resolution into ferromagnetic and paramagnetic components based on susceptibility temperature-variation measurement. Geophys. J. Int. 129, 715–719.

Hrouda, F., Kahan, Š., 1991. The magnetic fabric relationship between sedimentary and basement nappes in the High Tatra Mountains, N. Slovakia. J. Struct. Geol. 13 (4), 431–442.

Hrouda, F., Krejči, O., Potfaj, M., Stráník, Z., 2009. Magnetic fabric and weak deformation in sandstones of accretionary prisms of the Flysch and Klippen Belts of the Western Carpathians: Mostly offscraping indicated. Tectonophysics 479, 254–270.

Hrouda, F., Schulmann, K., Suppes, M., Ullemayer, K., de Wall, H., Weber, K., 1997. Quantitave relationship between low-field AMS and phyllosilicate fabric: a review. Phys. Chem. Earth 22, 153–156.

Huismans, R.S., Beaumont, C., 2014. Rifted continental margins: The case for depth-dependent extension. Earth Planet. Sci. Lett. 407, 148–162.

Huppert, H. E., Sparks, R. S. J., 1988. The generation of granitic magmas by intrusion of basalt into continental crust. J. Petrology. 29, 599–624.

Hutton, D.H.W., 1992. Granite sheeted complexes: evidence for the dyking ascent mechanism. Trans. R. Soc. Edin. Earth Sci. 83, 377–382.

Ingram, G.M., Hutton, D.H.W., 1994. The Great Tonalite Sill: emplacement into a contractional shear zone and implications for Late Cretaceous to early Eocene tectonics in southeastern Alaska and British Columbia. Geol. Soc. Am. Bull. 106, 715–728.

Ishihara, S., 1977. The magnetite-series and ilmenite-series granitic rocks. Mining Geology 27, 293–305.

Ishihara, S., Robb, L.J., Anhaeusser, C.R., Imai, A., 2002. Granitoid series in terms of magnetic susceptibility: a case study from the Barberton region, South Africa. Gondwana Res 5, 581–589.

Jackson, S. E., Pearson, N. J., Griffin, W. L., Belousova, E. A., 2004, The application of laser ablation-inductively coupled plasma-mass spectrometry to in situ U–Pb zircon geochronology. Chem. Geol. 211, 47–69.

Jakob, J., Andersen, T. B., Kjoll, H. J., 2019. A review and reinterpretation of the architecture of the South and South-Central Scandinavian Caledonides-A magma-poor to magma-rich transition and the significance of the reactivation of rift inherited structures. Earth Sci. Rev. 192, 513–528.

Janák, F. 1965. Determination of anisotropy of magnetic susceptibility of rocks. Stud. Geophys. Geod. 9, 290–301.

Janoušek, V., Bowes, D. R., Rogers, G., Farrow, C. M., Jelínek, E., 2000. Modelling diverse processes in the petrogenesis of a composite batholith: the Central Bohemian Pluton, Central European Hercynides. J. Petrology. 41, 511–543.

Janoušek, V., Holub, F., 2007. The causal link between HP–HT metamorphism and ultrapotassic magmatism in collisional orogens: case study from the Moldanubian Zone of the Bohemian Massif. Proceedings of the Geologists´ Association. 118, 75–86.

Janoušek, V., Wiegand, B. A., Žák, J., 2010. Dating the onset of Variscan crustal exhumation in the core of the Bohemian Massif: new U–Pb single zircon ages from the high-K calc-alkaline

granodiorites of the Blatná suite, Central Bohemian Plutonic Complex. J. Geol. Soc. London. 167, 347–360.

Jelinek, V. 1981. Characterization of the magnetic fabric or rocks. Tectonophysics 79, 63–7.

Jelínek, V., 1978. Statistical processing of anisotropy of magnetic susceptibility measured on groups of specimens. Stud. Geophys. Geod. 22, 50–62.

Jelínek, V., Pokorný, J., 1997. Some new concepts in technology of transformer bridges for measuring susceptibility anisotropy of rocks. Phys. Chem. Earth 22, 179–181.

Johnson, B.J., 2006. Extensional shear zones, granitic melts, and linkage of overstepping normal faults bounding the Shuswap metamorphic core complex, British Columbia. Geol. Soc. Am. Bull. 118, 366–382.

Johnson, S.E., Fletcher, J.M., Fanning, C.M., Vernon, R.H., Paterson, S.R., Tate, M.C., 2003. Structure, emplacement and lateral expansion of the San Jose tonalite pluton, Peninsular Ranges batholith, Baja California, Mexico. J. Struct. Geol. 25, 1933–1957.

Johnston, S. T., 2001. The great Alaskan terrane wreck: reconciliation of paleomagnetic and geological data in the northern Cordillera. Earth Planet. Sci. Lett. 193, 259–272.

Johnston, S.T., 2004. The New Caledonia-D'Entrecasteaux orocline and its role in clockwise rotation of the Vanuatu-New Hebrides Arc and formation of the North Fiji Basin. In: Sussman, A.J., Weil, A.B. (Eds.), Orogenic Curvature: Integrating Paleomagnetic and Structural Analyses. Geol. Soc. Am. Special Paper 383, 225–236.

Johnston, S.T., 2008. The Cordilleran ribbon continent of North America. Ann. Rev. Earth Planet Sci. 36, 495–530.

Johnston, S.T., Weil, A.B., Gutiérrez-Alonso, G., 2013. Oroclines: thick and thin. Geol. Soc. Am. Bull. 125, 643–663.

Jolivet, L., Famin, V., Mehl, C., Parra, T., Aubourg, C., Hébert, R., Philippot, P., Whitney, D.L. and Teyssier, C., 2004. Strain localization during crustal-scale boudinage to form extensional metamorphic domes in the Aegean Sea. GSA. Special papers 380, 185–210.

Just, J. and Kontny, A., 2012. Thermally induced alterations of minerals during measurements of the temperature dependence of magnetic susceptibility: a case study from the hydrothermally altered Soultz-sous-Forêts granite, France. Int. J. Earth Sci. 101, 819–839.

Just, J., Kontny, A., De Wall, H., Hirt, A.M. and Martín-Hernández, F., 2004. Development of magnetic fabrics during hydrothermal alteration in the Soultz-sous-Forets granite from the EPS-1 borehole, Upper Rhine Graben. Geol. Soc., London, Special Publications, 238, 509–526.

Karsli, O., Şengün, F., Dokuz, A., Aydin, F., Kandemir, R., Kristoffersen, M., Santos, J.F., Hofmann, M., Duygu, L., 2022. Early Cambrian S-type granites in the Sakarya Zone, NE Turkey: A record for transition from subduction to post-collisional extension deduced from U–Pb zircon age and Nd–Hf isotopes. Lithos 428, 16.

Kemnitz, H., Romer, R.L., Oncken, O., 2002. Gondwana break-up and the northern margin of the Saxothuringian belt (Variscides of Central Europe). Int. J. Earth Sci. 91, 246–259.

Keppie, J. D., Dostal, J., Nance, R. D., Miller, B. V., Ortega-Rivera, A., Lee, J. K. W., 2006. Circa 546 Ma plume-related dykes in the ~1Ga Novillo Gneiss (east-central Mexico): evidence for the initial separation of Avalonia. Precambr. Res. 147, 342–353.

Keppie, J. D., Nance, R. D., Murphy, J. B., Dostal, J., Braid, J. A., 2010. The high-pressure Iberian–Czech belt in the Variscan orogen: Extrusion into the upper (Gondwanan) plate? Gondwana Res., 17, 306–316.

Keppie, J.D., Dostal, J., Murphy, J.B., Nance, R.D., 2008. Synthesis and tectonic interpretation of the westernmost Paleozoic Variscan orogen in southern Mexico: From rifted Rheic margin to active Pacific margin. Tectonophysics 461, 277–290.

Keppie, J.D., Nance, R.D., Murphy, J.B., Dostal, J., 2003. Tethyan, Mediterranean, and Pacific analogues for the Neoproterozoic–Paleozoic birth and development of peri-Gondwanan terranes and their transfer to Laurentia and Laurussia. Tectonophysics 365, 195–219.

Kettner, R., 1919. On the Precambrian granites in Bohemia. Trans. Czechoslovak Acad. Sci. Art II 27, 1–13.

Kettner, R., 1946. Některé problémy českého algonkia a kambria. J. Czech Geol. Soc. 13, 41–67.

Klingelhoefer, F., Lafoy, Y., Collot, J., Cosquer, E., Geli, L., Nouze, H., Vially, R., 2007. Crustal structure of the basin and range system of New Caledonia (Southwest Pacific) from wide-angle and reflection seismic data. J. Geophys. Res. 112, 1–18.

Klomínský, J., Jarchovský, P., and Rajpoot, G. S., 2010. Atlas of plutonic rocks and orthogneisses in the Bohemian Massif: RAWRA Technical report, v. TR-1-2010, 1–638.

Kodama, K., Byrne, T., Lewis, J.C., Hibbard, J.P., Sato, M. and Koyano, T., 2018. Emplacement of a layered mafic intrusion in the Shimanto accretionary complex of southwest Japan: Evidence from paleomagnetic and magnetic fabric analysis. GSA, Special Paper, 534, 129–140.

Košler, J., Konopásek, J., Sláma, J., Vrána, S., 2014. U–Pb zircon provenance of Moldanubian metasediments in the Bohemian Massif. Geol. Soc., London, 171, 83–95.

Krása, D., Herrero-Bervera, E., 2005. Alteration induced changes of magnetic fabric as exemplified by dykes of the Koolau volcanic range. Earth Planet. Sci. Lett. 240, 445–453.

Kříž, J., 1992, Silurian field exkursions: Prague Basin (Barrandian), Bohemia. National Museum of Wales, Geological Notes, 13, 1–111.

Kroner, U., and Romer, R. L., 2013. Two plates – many subduction zones: the Variscan orogeny reconsidered. Gondwana Res. 24, 298–329.

Kukal, Z., 1971. Sedimentology of Cambrian deposits of the Barrandian area (Central Bohemia). J. Geol. Sci., Geol. 20, 53–100.

Kukal, Z., 1995. The lower Cambrian Paseky Shale: Sedimentology. J. Czech Geol. Soc. 40, 4, 67–78.

Lacroix, S., Sawyer, E.W. and Chown, E.H., 1998. Pluton emplacement within an extensional transfer zone during dextral strike-slip faulting: an example from the late Archaean Abitibi Greenstone Belt. J. Struct. Geol, 20, 43–59.

Lapointe, P., Morris, W.A. and Harding, K.L., 1986. Interpretation of magnetic susceptibility: a new approach to geophysical evaluation of the degree of rock alteration. Can. J.Earth Sci., 23, 393–401.

Lardeaux, J. M., Schulmann, K., Faure, M., Janoušek, V., Lexa, O., Skrzypek, E., Edel, J. B., Štípská, P., 2014, The Moldanubian Zone in the French Massif Central, Vosges/Schwarzwald and Bohemian Massif revisited: differences and similarities. Geol. Soc., London, Special Publications, 405, 7–44.

Lehnert, O., Frýda, J., Buggisch, W., Munnecke, A., Nützel, A., Kříž, J., Manda, Š., 2007, δ13C records across the late Silurian Lau event: new data from middle palaeo-latitudes of northern peri-Gondwana (Prague Basin, Czech Republic). Palaeogeography, Palaeoclimatology, Palaeoecology, 245, 227–244.

Linnemann, U. and Romer, R., 2010. Pre-Mesozoic Geology of Saxo-Thuringia: From the Cadomian Active Margin to the Variscan Orogen. Schweizerbart Science Publisher, Germany.

Linnemann, U., Gerdes, A., Hofmann, M., Marko, L., 2014. The Cadomian Orogen: Neoproterozoic to Early Cambrian crustal growth and orogenic zoning along the periphery of the West African Craton – constraints from U–Pb zircon ages and Hf isotopes (Schwarzburg Antiform, Germany). Precambr. Res. 244, 236–278.

Linnemann, U., McNaughton, N.J., Romer, R.L., Gehmlich, M., Drost, K., Tonk, C., 2004. West African provenance for Saxo-Thuringia (Bohemian Massif): did Armorica ever leave pre-Pangean Gondwana?– U/Pb-SHRIMP zircon evidence and the Nd-isotopic record. Int. J. Earth Sci. 93, 683–705.

Linnemann, U., Pereira, F., Jeffries, T.E., Drost, K., Gerdes, A., 2008. The Cadomian Orogeny and the opening of the Rheic Ocean: the diacrony of geotectonic processes constrained by LA-ICP-MS U–Pb zircon dating (Ossa-Morena and Saxo-Thuringian Zones, Iberian and Bohemian Massifs). Tectonophysics 461, 21–43.

Linnemann, U., Romer, R.L., 2002. The Cadomian Orogeny in Saxo-Thuringia, Germany: geochemical and Nd–Sr–Pb isotopic characterization of marginal basins with constraints to geotectonic setting and provenance. Tectonophysics 352, 33–64.

Lister, G.S., Etheridge, M. A., Symonds, P. A., 1986. Detachment Faulting and the Evolution of Passive Continental Margins. Geology,14, 246–250.

Ludwig, K. R., 2012. User´s manual for Isoplot 3.75. A geochronological toolkit for Microsoft Excel. Berkeley Geochronology Center Special Publication, 5, 1-75.

Macpherson, C.G., Hall, R., 2001. Tectonic setting of Eocene boninite magmatism in the Izu-Bonin-Mariana forearc. Earth Planet. Sci. Lett. 186, 215–230.

Mallard, L.D., Rogers, J.J.W., 1997. Relationship of Avalonian and Cadomian terranes to Grenville and Panafrican events. J. Geod. 23, 197–221.

Mallard, L.D., Rogers, J.J.W., 1997. Relationship of Avalonian and Cadomian terranes to Grenville and Panafrican events. J. Geodyn. 23, 197–221.

Manatschal, G., 2004. New models for evolution of magma-poor rifted margins based on a review of data and concepts from West Iberia and the Alps. Int. J. Earth Sci. 93, 432–466.

Martínez Catalán, J.R., 2011. Are the oroclines of the Variscan belt related to late Variscan strike-slip tectonics? Terra Nova 23, 241–247.

Martínez Catalan, J.R., Arenas, R., Abati, J., Martínez, S.S., García, F.D., Suárez, J.F., Cuadra, P.G., Castiñeiras, P., Barreiro, J.G., Montes, A.D., Clavijo, E.G., Pascual, F.J.R., Andonaegui, P., Jeffries, T.E., Alcock, J.E., Fernández, R.D., Carmona, A.L., 2009. A rootless suture and the loss of the roots of a mountain chain: The Variscan belt of NW Iberia. C. R. Geosci. 341, 114–126.

Martín-Hernández, F., Dekkers, M.J., Bominaar-Silkens, I.M.A., Maan, J.C., 2008. Magnetic anisotropy behaviour of pyrrhotite as determined by low- and high-field experiments. Geophys. J. Int. 174, 42–54.

McKenzie, D. 1978. Some remarks on the development of sedimentary basins Earth Planet. Sci. Lett. 40, 25–32

Medaris, G., Wang, H., Jelínek, E., Mihaljevič, M., and Jakeš, P., 2005, Characteristics and origins of diverse Variscan peridotites in the Gföhl Nappe, Bohemian Massif, Czech Republic: Lithos, 82, 1–23.

Metcalfe, I., 1984. Stratigraphy, palaeontology and palaeogeography of the Carboniferous of Southeast Asia. Mémoires. Soc. Géologique de France 147, 107–118.

Metcalfe, I., 2013. Gondwana dispersion and Asian accretion: Tectonic and palaeogeographic evolution of eastern Tethys. J. Asian Earth Sci. 66, 1–33.

Miller, R. B., 1994. A mid-crustal contractional stepover zone in a major strike-slip system, North Cascades, Washington. J. Struct. Geol. 16, 47–60.

Miller, R.B. and Paterson, S.R., 1999. In defense of magmatic diapirs. J. Struct. Geol, 21: 1161–1173.

Miller, R.B. and Paterson, S.R., 2001. Construction of mid-crustal sheeted plutons: Examples from the north Cascades, Washington. Geol. Soc. Am. Bull. 113, 1423–1442.

Mohn, G., Manatschal, G., Beltrando, M., Haupert, I., 2014. The role of rift-inherited hyper-extension in Alpine-type orogens. Terra Nova 26, 347–353.

Mohn, G., Manatschal, G., Masini, E., Muntener, O., 2011. Rift-related inheritance in orogens: a case study from the Austroalpine nappes in Central Alps (SE-Switzerland and N-Italy). Int. J. Earth Sci. 100, 937–961.

Mohriak, W. U., Danforth, A., Post, P. J., Brown, D. E., Tari, G. C., Nemčok, M., Sinha, S. T., 2013. Conjugate divergent margins: an introduction. Geol. Soc. London, Special Publication, 369, 1–10.

Molnar, N.E., Cruden, A.R., Betts, P.G., 2018. Unzipping continents and the birth of microcontinents. Geology 46, 451–454.

Monger, J. W. H., 1989. Overview of Cordilleran geology. Western Canada Sedimentary Basin: A Case History, Part I: Basin Framework, 9–32.

Morley, C.K., 2018. Understanding Sibumasu in the context of ribbon continents. Gondwana Res. 64, 184–215.

Müller, R.D., Gaina, C., Roest, W.R., Hansen, D.L., 2001. A recipe for microcontinent formation. Geology 29, 203–206.

Murphy, J.B., Cameron, K., Dostal, J., Keppie, J.D., Hynes, A.J., 1985. Cambrian volcanism in Nova Scotia, Canada. Can. J. Earth Sci. 22, 599–606.

Murphy, J.B., Eguiluz, L., Zulauf, G., 2002. Cadomian Orogens, peri-Gondwanan correlatives and Laurentia–Baltica connections. Tectonophysics 352, 1–9.

Murphy, J.B., Eguiluz, L., Zulauf, G., 2002. Cadomian Orogens, peri-Gondwanan correlatives and Laurentia–Baltica connections. Tectonophysics 352, 1–9.

Murphy, J.B., Gutiérrez-Alonso, G., Nance, R.D., Fernández-Suárez, J., Keppie, J.D., Quesada, C., Strachan, R.A., Dostal, J., 2006. Origin of the Rheic Ocean: rifting along a Neoproterozoic suture? Geology 34, 325–328.

Murphy, J.B., Hynes, A.J., 1990. Tectonic control on the origin and orientation of igneous layering: an example from the Greendale Complex, Antigonish Highlands, Nova Scotia, Canada. Geology 18, 403–406.

Murphy, J.B., Keppie, J.D., Dostal, J., Nance, R.D. 1999a. The Neoproterozoic–early Paleozoic evolution of Avalonia. Geological Society of America Special Paper 336: 253–266.

Murphy, J.B., Keppie, J.D., Nance, R.D., 1999b. Fault reactivation within Avalonia: plate margin to continental interior deformation. Tectonophysics 305, 183–204.

Murphy, J.B., Nance, R.D., 1989. Model for the evolution of the Avalonian–Cadomian Belt. Geology 17, 735–738.

Murphy, J.B., Nance, R.D., Gabler, L.B., Martell, A., Archibald, D.A., 2019. Age, Geochemistry and Origin of the Ardara Appinite Plutons, Northwest Donegal, Ireland. Geosci. Can. 46, 31–48.

Murphy, J.B., Strachan, R.A. and Quesada, C., 2021. Pannotia to Pangaea: Neoproterozoic and Paleozoic orogenic cycles in the Circum-Atlantic Region. Geological Society, London, Special Publications 503, 1–11.

Murphy, J.B., Strachan, R.A., Nance, R.D., Parker, K.D., Fowler, M.B., 2000. Proto-Avalonia: A 1.2–1.0 Ga tectonothermal event and constraints for the evolution of Rodinia. Geology 28, 1071–1074.

Nagata, T., 1961. Rock Magnetism. Maruzen, Tokyo, 350.

Nahodilová, R., Štípská, P., Powell, R., Košler, J., and Racek, M., 2014, High-Ti muscovite as a prograde relict in high pressure granulites with metamorphic Devonian zircon ages (Běstvina granulite body, Bohemian Massif): Consequences for the relamination model of subducted crust: Gondwana Res. 25, 630–648.

Nance, R. D., Gutierréz-Alonso, G., Keppie, J. D., Linnemann, U., Murphy, J. B., Quesada, C., Strachan, R. A., Woodcock, N. H., 2010. Evolution of the Rheic Ocean. Gondwana Res. 17, 194–222.

Nance, R. D., Gutiérrez-Alonso, G., Keppie, J. D., Linnemann, U., Murphy, J. B., Quesada, C., Strachan, R. A., Woodcock, N. H., 2012. A brief history of the Rheic Ocean. Geosci. Frontiers, 3, 125–135.

Nance, R.D., Linnemann, U., 2008. The Rheic Ocean: origin, evolution, and significance. GSA Today 18, 4–12.

Nance, R.D., Murphy, J.B., 1990. Kinematic history of the Bass River Complex, Nova Scotia - Cadomian tectonostratigraphic relations in the Avalon terrane of the Canadian Appalachians. Geological Society, London, Special Publications 51, 395–406.

Nance, R.D., Murphy, J.B., 1994. Contrasting basement isotopic signatures and the palinspastic restoration of peripheral orogens: example from the Neoproterozoic Avalonian–Cadomian belt. Geology 22, 617–620.

Nance, R.D., Murphy, J.B., 2019. Supercontinents and the case for Pannotia. Geological Society, London, Special Publications 470, 65–86.

Nance, R.D., Murphy, J.B., Keppie, J.D., 2002. A Cordilleran model for the evolution of Avalonia. Tectonophysics 352, 11–31.

Nance, R.D., Murphy, J.B., Strachan, R.A., D'Lemos, R.S., Taylor, G.K., 1991. Late Proterozoic tectonostratigraphic evolution of the Avalonian and Cadomian terranes. Precambr. Res. 53, 41–78.

Nance, R.D., Murphy, J.B., Strachan, R.A., Keppie, J.D., Gutiérrez-Alonso, G., Fernández-Suarez, J., Quesada, C., Linnemann, U., D´Lemos, R., Pisarevsky, S.A., 2008. Neoproterozoic–early Palaeozoic tectonostratigraphy and palaeogeography of the peri-Gondwanan terranes: Amazonian v. West African connections. Geological Society, London, Special Publications 297, 345–383.

Neilson, J.C., Kokelaar, B.P., Crowley, Q.G., 2009. Timing, relations and cause of plutonic and volcanic activity of the Siluro-Devonian post-collision magmatic episode in the Grampian Terrane, Scotland. J. Geol. Soc. 166, 545–561.

Nichols, G., 2009. Sedimentology and stratigraphy, 2nd ed. Wiley-Blackwell, West Sussex, UK.

Nichols, G.J., Fisher, J.A., 2007. Processes, facies and architecture of fluvial distributary system deposits. Sed. Geol. 195, 75–90.

Nixon, G.T., Scheel, J.E., Scoates, J.S., Friedman, R.M., Wall, C.J., Gabites, J., Jackson-Brown, S., 2020. Syn-accretionary multistage assembly of an Early Jurassic Alaskan-type intrusion in the Canadian Cordillera: U–Pb and 40Ar/39Ar geochronology of the Turnagain ultramafic-mafic intrusive complex, Yukon-Tanana terrane. Can. J. Earth Sci. 57, 575–600.

O´Brien, P.J., 2001. Subduction followed by collision: Alpine and Himalayan examples. Phys. Earth Planet Inter. 127, 277–291.

O'brien, P.J., Zotov, N., Law, R., Khan, M.A., Jan, M.Q., 2001. Coesite in Himalayan eclogite and implications for models of India-Asia collision. Geology, 29, 435-438.

Ogawa, Y., Mori, R., Tsunogae, T., Dilek, Y., Harris, R., 2015. New interpretation of the Franciscan melange at San Simeon coast, California: tectonic intrusion into an accretionary prism. Int. Geol. Rev. 57, 824–842.

Oldow, J.S., Geissman, J.W. and Stockli, D.F., 2008. Evolution and strain reorganization within late Neogene structural stepovers linking the central Walker Lane and northern Eastern California shear zone, western Great Basin. Int. Geol. Rev 50, 270–290.

Oriolo, S., Schulz, B., Geuna, S., González, P.D., Otamendi, J.E., Sláma, J., Druguet, E., Siegesmund, S., 2021. Early Paleozoic accretionary orogens along the Western Gondwana margin. Geosci. Front. 12, 109–130.

Ota, T., Kaneko, Y., 2010. Blueschists, eclogites, and subduction zone tectonics: Insights from a review of Late Miocene blueschists and eclogites, and related young high-pressure metamorphic rocks. Gondwana Res. 18, 167–188.

Parés, J.M., 2015. Sixty years of anisotropy of magnetic susceptibility in deformed sedimentary rocks. Front. Earth Sci. 3, 1–13.

Parés, J.M., van der Pluijm, B.A., Dinarés-Turell, J., 1999. Evolution of magnetic fabrics during incipient deformation of mudrocks (Pyrenees, northern Spain). Tectonophysics 307, 1–14.

Paterson, S.R., Fowler, T.K., 1993. Re-examining pluton emplacement processes. J. Struct. Geol. 15, 191–206.

Paterson, S.R., Fowler, T.K., Schmidt, K.L., Yoshinobu, A.S., Yuan, E.S., Miller, R.B., 1998. Interpreting magmatic fabric patterns in plutons. Lithos 44, 53–82.

Paterson, S.R., Vernon, R.H., 1995. Bursting the bubble of ballooning plutons: a return to nested diapirs emplaced by multiple processes. Geol. Soc. Am. Bull. 107, 1356–1380.

Paterson, S.R., Vernon, R.H., Tobisch, O.T., 1989. A review of criteria for identification of magmatic and tectonic foliations in granitoids. J. Struct. Geol 11, 349–363.

Patočka, F., Štorch, P., 2004. Evolution of geochemistry and depositional settings of Early Palaeozoic siliciclastics of the Barrandian (Teplá–Barrandian Unit, Bohemian Massif, Czech Republic). Int. J. Earth Sci. 93, 728–741.

Paton, C., Hellstrom, J., Paul, B., Woodhead, J., and Hergt, J., 2011. Iolite: freeware for the visualisation and processing of mass spectrometric data: J. Analytical Atomic Spectrometry, 26, 2508–2518.

Paton, C., Woodhead, J. D., Hellstrom, J. C., Hergt, J. M., Greig, A., Maas, R., 2010. Improved laser ablation U–Pb zircon geochronology through robust downhole fractionation correction: Geochem. Geophys. Geosysts. 11, Q0AA06.

Pérez-Gussinyé, M., 2013. A tectonic model for hyperextension at magma-poor rifted margins: an example from the West Iberia–Newfoundland conjugate margins. Geol. Soc. London, Special Publication 369, 403–427.

Péron-Pinvidic, G., and Manatschal, G., 2019. Rifted margins: state of the art and future challenges: Frontiers Earth Sci. 7.

Peron-Pinvidic, G., Manatschal, G., Alves, T., Andersen, T., Andres-Martinez, M., Autin, J., Ball, P., Brune, S., Buiter, S., Cadenas, P., Cresswell, D., Epin, M.E., Gomez-Romeu, J., Gouiza, M., Harkin, C., Heine, C., Hopper, J., Jackson, C., Jolivet, L., Katz, R., Lescoutre, R., Lymer, G., Magee, C., Manatschal, G., Masini, M., Miro, J., Molnar, N., Mouthereau, F., Muntener, O., Naliboff, J., Norcliffe, J., Osmundsen, P.T., Diaz, L.P., Peron-Pinvidic, G., Phillips, T.P., Ramos, A., Ranero, C., Reston, T., Ribes, C., Rooney, T., Rowan, M., Snidero, M., Tugend, J., Wang, L.J., Zwaan, F., Partici, I.M.R.W., 2019. Rifted Margins: State of the Art and Future Challenges. Frontiers Earth Sci. 7, 7.

Petrakakis, K., 1997, Evolution of Moldanubian rocks in Austria: review and synthesis: J. Metamorphic Geol., 15, 203–222.

Petri, B., Duretz, T., Mohn, G., Schmalholz, S.M., Karner, G.D., Muntener, O., 2019. Thinning mechanisms of heterogeneous continental lithosphere. Earth Planet. Sci. Lett. 512, 147–162.

Petri, B., Štípská, P., Skrzypek, E., Schulmann, K., Corsini, M., and Franěk, J., 2014, Thermal and mechanical behaviour of the orogenic middle crust during the syn- to late-orogenic evolution of the Variscan root zone, Bohemian Massif: Journal of Metamorphic Geology, 32, 599–626.

Petrus, J. A., and Kamber, B. S., 2012, VizualAge: a novel approach to laser ablation ICP-MS U–Pb geochronology data reduction: Geostandards and Geoanalytical Res. 36, 247–270.

Pollock, J.C., Hibbard, J.P., Sylvester, P.J., 2009. Early Ordovician rifting of Avalonia and birth of the Rheic Ocean: U–Pb detrital zircon constraints from Newfoundland. J. Geol. Soc., London 166, 501–515.

Pollock, J.C., Hibbard, J.P., Sylvester, P.J., Tollo, R.P., Bartholomew, M.J. and Karabinos, P.M., 2010. Depositional and tectonic setting of the Neoproterozoic–early Paleozoic rocks of the Virgilina sequence and Albemarle Group, North Carolina. Geological Society of America Memoir 206, 739–772.

Potter, P.E., Pettijohn, F.J., 1977. Paleocurrent and basin analysis. Springer-Verlag. New York.

Pouclet, A., Álvaro, J.J., Bardintzeff, J.M., Imaz, A.G., Monceret, E., Vizcaïno, D., 2017. Cambrian–early Ordovician volcanism across the South Armorican and Occitan domains of the Variscan Belt in France: Continental break-up and rifting of the northern Gondwana margin. Geoscience Frontiers 8, 25-64.

Prigmore, J.K., Butler, A.J., Woodcock, N.H., 1997. Rifting during separation of Eastern Avalonia from Gondwana: evidence from subsidence analysis. Geology 25, 203–206.

Pucher, R. 1994. Pyrrhotite-induced aeromagnetic anomalies in western Germany. J. Appl. Geophys., 32, 33–42.

Rees, A. I., 1966. The effect of depositional slope of anisotropy of magnetic susceptibility of laboratory deposited sands. J. Geol. 74, 856–67.

Rees, A.I., 1965. The use of anisotropy of magnetic susceptibility in the estimation of sedimentary fabric. Sedimentology 4, 257–271.

Rees, A.I., Woodall, W.A., 1975. The magnetic fabric of some laboratory deposited sediments. Earth Planet Sci. Lett. 25, 121–30.

René, M., 2006, Provenance studies of Moldanubian paragneisses based on geochemical data (Bohemian Massif, Czech Republic): Neues Jahrbuch für Geologie and Paläntologie, Abhandlungen, 242, 83–101.

René, M., and Finger, F., 2016, The Blaník Gneiss in the southern Bohemian Massif (Czech Republic): a rare rock composition among the early palaeozoic granites of Variscan Central Europe: Mineralogy and Petrology, 110, 503–514.

Robardet, M., 2003. The Armorica ‘microplate’: fact or fiction? Critical review of the concept and contradictory palaeobiogeographical data. Palaeogeogr. Palaeoclimatol. Palaeoecol. 195, 125–148.

Rochette, P., Jackson, M., Aubourg, C., 1992. Rock magnetism and the interpretation of anisotropy of magnetic susceptibility. Rev. Geophys. 30, 209–226.

Romer, R.L., and Kroner, U., 2019. First direct evidence for a contiguous Gondwana shelf to the south of the Rheic Ocean. Geology 47, 767–770.

Rubatto, D., 2017, Zircon: the metamorphic mineral: Rev. Mineral. Geochem. 83, 261–295.

Saint-Bezar, B., Hebert, R.L., Aubourg, C., Robion, P., Swennen, R., de Lamotte, D.F., 2002. Magnetic fabric and petrographic investigation of hematite-bearing sandstones within ramp-related folds: examples from the South Atlas Front (Morocco). J. Struct. Geol. 24, 1507–1520.

Samson, S., Palmer, A.R., Robison, R.A., Secor, D.T., 1990. Biogeographical significance of Cambrian trilobites from the Carolina slate belt. Geol. Soc. Am. Bull. 102, 1459–1470.

Samsu, A., Cruden, A.R., Hall, M., Micklethwaite, S., Denyszyn, S.W., 2019. The influence of basement faults on local extension directions: Insights from potential field geophysics and field observations. Basin Res. 31, 782–807.

Sánchez-García, T., Bellido, F., Pereira, M.F., Chichorro, M., Quesada, C., Pin, C., Silva, J.B., 2010. Rift-related volcanism predating the birth of the Rheic Ocean (Ossa-Morena zone, SW Iberia). Gondwana Res. 17, 392–407.

Sánchez-García, T., Bellido, F., Quesada, C., 2003. Geodynamic setting and geochemical signatures of Cambrian–Ordovician rift-related igneous rocks (Ossa-Morena Zone, SW Iberia). Tectonophysics 365, 233–255.

Sánchez-García, T., Quesada, C., Bellido, F., Dunning, G.R., del Tanago, J.G., 2008. Two-step magma flooding of the upper crust during rifting: The Early Paleozoic of the Ossa Morena Zone (SW Iberia). Tectonophysics 461, 72–90.

Schulmann, K., Kröner, A., Hegner, E., Wendt, I., Konopásek, J., Lexa, O., Štípská, P., 2005, Chronological constraints on the pre-orogenic history, burial and exhumation of deep-seated rocks along the eastern margin of the Variscan orogen, Bohemian Massif, Czech Republic. Am. J. Sci., 305, 407–448.

Secor, D.T., Samson, S.L., Snoke, A.W., Palmer, A.R., 1983. Confirmation of the Carolina slate belt as an exotic terrane. Science 221, 649–651.

Şengör, A. M. C., 1984. The cimmeride orogenic system and the tectonics of Eurasia: Geol. Soc. Am. Special Paper 195, 82.

Sengör, A. M. C., Natal'in, B., 2004. Ribbon continents: a marginal affair of central importance. In Geol. Soc. Am. Abstr. Programs 36, 534.

Servais, T., Sintubin, M., 2009. Avalonia, Armorica, Perunica: terranes, microcontinents, microplates or palaeobiogeographical provinces? In: Bassett, M.G. (Ed.), Early Palaeozoic Peri-Gondwana Terranes: New Insights from Tectonics and Biogeography. Geol. Soc. London, Special Publications 325, 103–115.

Servais, T., Sintubin, M., 2009. Avalonia, Armorica, Perunica: terranes, microcontinents, microplates or palaeobiogeographical provinces? Geological Society, London, Special Publications 325, 103–115.

Shaw, J., Johnston, S. T., 2016. Terrane wrecks (coupled oroclines) and paleomagnetic inclination anomalies. Earth Sci. Rev. 154, 191–209.

Sisson, V.B., Pavlis, T.L., Roeske, S.M. and Thorkelson, D.J., 2003. Introduction: An overview of ridge-trench interactions in modern and ancient settings. GSA, Special Papers, 371, 1–18.

Sláma, J., Dunkley, D.J., Kachlík, V., Kusiak, M.A., 2008a. Transition from island-arc to passive setting on the continental margin of Gondwana: U–Pb zircon dating of Neoproterozoic metaconglomerates from the SE margin of the Teplá–Barrandian Unit, Bohemian Massif. Tectonophysics 461, 44–59.

Sláma, J., Košler, J., Condon, D. J., Crowley, J. L., Gerdes, A., Hanchar, J. M., Horstwood, M. S. A., Morris, G. A., Nasdala, L., Norberg, N., Schaltegger, U., Schoene, B., Tubrett, M. N., and Whitehouse, M. J., 2008b, Plešovice zircon: a new natural reference material for U–Pb and Hf isotopic microanalysis. Chem. Geol., 249, 1–35.

Soejono, I., Machek, M., Slarna, J., Janoušek, V., and Kohut, M., 2020, Cambro–Ordovician anatexis and magmatic recycling at the thinned Gondwana margin: new constraints from the Kouřim Unit, Bohemian Massif. J. Geol. Soc. 177, 325–341.

Soto, R., Larrasoaña, J.C., Beamud, E., Garcés, M., 2016. Early–Middle Miocene subtle compressional deformation in the Ebro foreland basin (northern Spain); insights from magnetic fabrics. C. R. Geosci. 348, 213–223.

Stachowska, A., Łoziński, M., Śmigielski, M., Wysocka, A., Jankowski, L., Ziółkowski, P., 2020. Anisotropy of magnetic susceptibility as an indicator for palaeocurrent analysis in folded turbidites (Outer Western Carpathians, Poland). Sedimentology 67, 3783–3808.

Stampfli, G.M., Hochard, C., Vérard, C., Wilhem, C., vonRaumer, J., 2013. The formation of Pangea. Tectonophysics 593, 1–19.

Stampfli, G.M., Von Raumer, J., Wilhem, C., 2011. The distribution of Gondwana-derived terranes in the Early Palaeozoic. In Ordovician of the World 14, 567–574. Instituto Geológico y Minero de España.

Stephan, T., Kroner, U., Hahn, T., Hallas, P., Heuse, T., 2016. Fold/cleavage relationships as indicator for late Variscan sinistral transpression at the Rheno-Hercynian–Saxo-Thuringian boundary zone, Central European Variscides. Tectonophysics 681, 250–262.

Stephan, T., Kroner, U., Romer, R.L. Rösel, D., 2019a. From a bipartite Gondwanan shelf to an arcuate Variscan belt: the early Paleozoic evolution of northern peri-Gondwana. Earth Sci. Rev. 192: 491–512.

Stephan, T., Kroner, U.W.E. Romer, R.L., 2019b. The pre-orogenic detrital zircon record of the peri-Gondwanan crust. Geol. Mag. 156: 281–307.

Stipp, M., Stünitz, H., Heilbronner, R., Schmid, S. M., 2002. The eastern Tonale fault zone: a 'natural laboratory' for crystal plastic deformation of quartz over a temperature range from 250° to 700° C. J. Struct. Geol. 24: 1861–1884.

Štorch, P., 2006, Facies development, depositional settings and sequence stratigraphy across the Ordovician–Silurian boundary: a new perspective from the Barrandian area of the Czech Republic: Geological Journal, 41, 163–192.

Štorch, P., Fatka, O., Kraft, P., 1993. Lower Palaeozoic of the Barrandian area (Czech Republic) – a review. Coloquios de Paleontología 45, 163–191.

Strnad, L., and Mihaljevič, M., 2005, Sedimentary provenance of Mid-Devonian clastic sediments in the Teplá–Barrandian Unit (Bohemian Massif): U–Pb and Pb–Pb geochronology of detrital zircons by laser ablation ICP-MS: Mineralogy and Petrology, 84, 47–68.

Sutherland, R., Collot, J., Lafoy, Y., Logan, G.A., Hackney, R., Stagpoole, V., Uruski, C., Hashimoto, T., Higgins, K., Herzer, R.H., Wood, R., Mortimer, N., Rollet, N., 2010. Lithosphere delamination with foundering of lower crust and mantle caused permanent subsidence of New Caledonia Trough and transient uplift of Lord Howe Rise during Eocene and Oligocene initiation of Tonga-Kermadec subduction, western Pacific. Tectonics 29.

Syahputra, R., Žák, J., Nance, R.D., 2022. Cambrian sedimentary basins of northern Gondwana as geodynamic markers of incipient opening of the Rheic Ocean. Gondwana Res. 105, 492–513.

Symons, D. T. A., 1967. The magnetic and petrologic properties of a basalt column. Geophys. J. R. Astr. Soc. 12, 473–90.

Taira, A., Scholle, P.A., 1979. Deposition of resedimented sandstone beds in the Pico Formation, Ventura Basin, California, as interpreted from magnetic fabric measurements. Geol. Soc. Am. Bull. 90, 952–962.

Tait, J., Schätz, M., Bachtadse, V., Soffel, H., 2000. Palaeomagnetism and Palaeozoic palaeogeography of Gondwana and European terranes, Geological Society, London, Special Publications 179, 21–34.

Tarling, D.H., Hrouda, F., 1993. The Magnetic Anisotropy of Rocks. Chapman and Hall, London.

Tasáryová, Z., Janoušek, V., Frýda, J., 2018. Failed Silurian continental rifting at the NW margin of Gondwana: evidence from basaltic volcanism of the Prague Basin (Teplá–Barrandian Unit, Bohemian Massif). Int. J. Earth Sci. 107, 1231–1266.

Taylor, B., 1995. Active margins and marginal basins of the Western Pacific. AGU, USA.

Taylor, R. N., Marlow, M. S., Johnson, L. E., Bloomer, S., & Mitchell, J., 1995. Intrusive volcanic rocks in western Pacific Forearcs. In Active margins and marginal basins of the Western Pacific 88, 31–43. American Geophysical Union, Washington, DC.

Teipel, U., Eichhorn, R., Loth, G., Rohrmuller, J., Holl, R., Kennedy, A., 2004, U-Pb SHRIMP and Nd isotopic data from the western Bohemian Massif (Bayerischer Wald, Germany): implications for Upper Vendian and Lower Ordovician magmatism: Int. J. Earth Sci., 93, 782–801.

Thompson, M. D., Grunow, A. M., Ramezani, J., 2010. Cambro-Ordovician paleogeography of the Southeastern New England Avalon Zone: Implications for Gondwana breakup. Geol. Soc. Am. Bull. 122, 76–88.

Timmermann, H., Dörr, W., Krenn, E., Finger, F., Zulauf, G., 2006. Conventional and in situ geochronology of the Teplá Crystalline unit, Bohemian Massif: implications for the processes involving monazite formation. Int. J. Earth Sci. 95, 629–647.

Tomek, F., Žák, J., Chadima, M., 2015. Granitic magma emplacement and deformation during early-orogenic syn-convergent transtension: The Stare Sedlo complex, Bohemian Massif. J Geod. 87, 50–66.

Topuz, G., Gocmengil, G., Rolland, Y., Celik, O.F., Zack, T., Schmitt, A.K., 2013. Jurassic accretionary complex and ophiolite from northeast Turkey: No evidence for the Cimmerian continental ribbon. Geology 41, 255–258.

Tunheng, A., Hirata, T., 2004. Development of signal smoothing device for precise elemental analysis using laser ablation-ICP-mass spectrometry. J. Analytical Atomic Spectrometry, 19, 932-934.

Usui, Y., Yamazaki, T., Oka, T., Kumagai, Y., 2019. Inverse magnetic susceptibility fabrics in pelagic sediment: Implications for magnetofossil abundance and alignment. J. Geophys. Res. Solid Earth 124, 10672–10686.

Vacek, F., Slavík, L., Sobień, K., Čáp, P., 2018. Refining the late Silurian sea-level history of the Prague Syncline: a case study based on the Přídolí GSSP (Czech Republic). Facies, 64, 30.

Vacek, F., Žák, J., 2019. A lifetime of the Variscan orogenic plateau from uplift to collapse as recorded by the Prague Basin, Bohemian Massif. Geological Magazine, 156, 485–509.

van Breemen, O., Aftalion, M., Bowes, D. R., Dudek, A., Mísař, Z., Povondra, P., and Vrána, S., 1982. Geochronological studies of the Bohemian Massif, Czechoslovakia, and their significance in the evolution of Central Europe: Transactions of the Royal Society of Edinburgh. Earth Sci. 73, 89–108.

van der Voo, R., 2004. Paleomagnetism, oroclines, and growth of the continental crust. Geol. Soc. Am. Today 14, 4–9.

van Staal, C.R., Barr, S.M., Waldron, J.W., Schofield, D.I., Zagorevski, A., White, C.E., 2021. Provenance and Paleozoic tectonic evolution of Ganderia and its relationships with Avalonia and Megumia in the Appalachian–Caledonide orogen. Gondwana Res. 98, 212–243.

Vejnar, Z, 1982. Regionální metamõrfoza psamiticko-pelitický chhornin domažlické oblasti. Sbor. Geol. Věd, Geol 37, 9–70 (in Czech with English summary).

Vejnar, Z., 1966. The petrogenetic interpretation of kyanite, sillimanite and andalusite in the southwestern Bohemian crystalline complexes. N Jahrb Mineral Abh 104, 172—189

Veloso, E.E., Anma, R., Ota, T., Komiya, T., Kagashima, S., Yamazaki, T., 2007. Paleocurrent patterns of the sedimentary sequence of the Taitao ophiolite constrained by anisotropy of magnetic susceptibility and paleomagnetic analyses. Sed. Geol. 201, 446–460.

Venera, Z., Schulmann, K., Kroner, A., 2000. Intrusion within a transtensional tectonic domain: the Čistá granodiorite (Bohemian Massif) - structure and rheological modelling. J. Struct. Geol. 22, 1437–1454.

Venera, Z., Schulmann, K., Kroner, A., 2000. Intrusion within a transtensional tectonic domain: the Čistá granodiorite (Bohemian Massif) - structure and rheological modelling. J. Struct. Geol. 22, 1437–1454.

Vítková, P., Kachlík, V., 2001. Petrology and geochemistry of high-Mg mafic metavolcanics sequence of the Sedlčany-Krásná Hory metamorphic “Islet”, Central Bohemian Pluton, Czech Republic. Krystalinikum 27, 7–25.

von Herzen, R., Ruppel, C., Molnar, P., Nettles, M., Nagihara, S., Ekstrom, G., 2001. A constraint on the shear stress at the Pacific-Australian plate boundary from heat flow and seismicity at the Kermadec forearc. J. Geophys. Res. 106, 6817–6833.

von Raumer, J.F., Bussy, F., Schaltegger, U., Schulz, B., Stampfli, G.M., 2013. Pre-Mesozoic Alpine basements—Their place in the European Paleozoic framework. Geol. Soc. Am. Bull. 125, 89–108.

von Raumer, J.F., Stampfli, G.M., Bussy, F., 2003. Gondwana-derived microcontinents – the constituents of the Variscan and Alpine collisional orogens. Tectonophysics 365, 7–22.

Weinberg, R.F., 1999. Mesoscale pervasive felsic magma migration: alternatives to dyking. Lithos 46, 393–410.

Weinerová, H., Bábek, O., Slavík, L., Vonhof, H., Joachimski, M. M., and Hladil, J., 2020, Oxygen and carbon stable isotope records of the Lochkovian–Pragian boundary interval from the Prague Basin (Lower Devonian, Czech Republic): Palaeogeography, Palaeoclimatology, Palaeoecology, 560.

Wendt, J.I., Kröner, A., Fiala, J., Todt, W., 1993. Evidence from zircon dating for existence of approximately 2.1 Ga old crystalline basement in southern Bohemia, Czech Republic. Geol. Rundsch. 82, 42–50.

Wernicke, B., Burchfiel, B. C., 1982. Modes of extensional tectonics. J. Struct. Geol. 4, 105–115.

White, C.E., Barr, S.M., Bevier, M.L., Kamo, S., 1994. A revised interpretation of Cambrian and Ordovician rocks in the Bourinot belt of central Cape-Breton island, Nova Scotia. Atl. Geol. 30, 123–142.

Whittaker, J.M., Williams, S.E., Halpin, J.A., Wild, T.J., Stilwell, J.D., Jourdan, F., Daczko, N.R., 2016. Eastern Indian Ocean microcontinent formation driven by plate motion changes. Earth Planet. Sci. Lett. 454, 203–212.

Wiedenbeck, M., Allé, P., Corfu, F., Griffin, W. L., Meier, M., Oberli, F., von Quadt, A., Roddick, J. C., and Spiegel, W., 1995, Three natural zircon standards for U–Th–Pb, Lu–Hf, trace element and REE analyses. Geostandards Newsletter. 19, 1–23.

Willan, R.C.R., Kelley, S.P., 1999. Mafic dike swarms in the South Shetland Islands volcanic arc: Unravelling multiepisodic magmatism related to subduction and continental rifting. J. Geophys. Res. Solid Earth 104, 23051–23068.

Winchester, J.A., Pharaoh, T.C., Verniers, J., Ioane, D., Seghedi, A., 2006. Palaeozoic accretion of Gondwana-derived terranes to the East European Craton: recognition of detached terrane fragments dispersed after collision with promontories, In: Gee, D.G., Stephenson, R.A. (Eds.), European lithosphere dynamics. Geol. Soc. London, Memoirs 32, 232–332.

Wu, J.E., McClay, K., Whitehouse, P., Dooley, T., 2009. 4D analogue modelling of transtensional pull-apart basins. Mar. Pet. Geol. 26, 1608–1623.

Xia, H.R., Platt, J.P., 2018. Quartz grainsize evolution during dynamic recrystallization across a natural shear zone boundary. J. Struct. Geol. 109, 120-126.

Žák, J., Kraft, P., Hajná, J., 2013. Timing, styles, and kinematics of Cambro–Ordovician extension in the Teplá–Barrandian Unit, Bohemian Massif, and its bearing on the opening of the Rheic Ocean. Int. J. Earth Sci. 102, 415–433.

Žák, J., Paterson, S.R., 2005. Characteristics of internal contacts in the Tuolumne Batholith, central Sierra Nevada, California (USA): implications for episodic emplacement and physical processes in a continental arc magma chamber. Geol. Soc. Am. Bull. 117, 1242–1255.

Žák, J., Schulmann, K., Hrouda, F., 2005. Multiple magmatic fabrics in the Sázava pluton (Bohemian Massif, Czech Republic): a result of superposition of wrench-dominated regional transpression on final emplacement. J. Struct. Geol. 27, 805–822.

Žák, J., Sláma, J., 2018. How far did the Cadomian terranes travel from Gondwana during early Palaeozoic? A critical reappraisal based on detrital zircon geochronology. Int. Geol. Rev. 60, 319–338.

Žák, J., Svojtka, M., Gerdjikov, I., Kounov, A., Vangelov, D. A., 2022. The Balkan terranes: a missing link between the eastern and western segments of the Avalonian–Cadomian orogenic belt? Int. Geol. Rev. 1-27.

Žák, J., Svojtka, M., Hajná, J., Ackerman, L., 2020. Detrital zircon geochronology and processes in accretionary wedges. Earth Sci. Rev. 207, 103214.

Žák, J., Verner, K., Holub, F. V., Kabele, P., Chlupáčová, M., Halodová, P., 2012. Magmatic to solid state fabrics in syntectonic granitoids recording early Carboniferous orogenic collapse in the Bohemian Massif. J. Struct. Geol. 36, 27–42.

Ziegler, P.A., Cloetingh, S., 2004. Dynamic processes controlling evolution of rifted basins. Earth Sci. Rev. 64, 1–50.

Zoubek, V., Holubec, J., Fiala, F., Pouba, Z., Chaloupský, J., 1988. Central Bohemian Region, In: Zoubek, V. (Ed.), Precambrian in younger fold belts. Wiley, Chichester, 75–118.

Zulauf, G., 1997. From very low–grade to eclogite-facies metamorphism: tilted crustal sections as a consequence of Cadomian and Variscan orogeny in the Teplá–Barrandian unit (Bohemian Massif). Geotekt. Forsch. 89,1–302.

Zulauf, G., 2001. Structural style, deformational mechanisms and paleodifferential stress along an exposed crustal section: constraints on the rheology of quartzofeldspathic rocks at supra- and infrastructural levels (Bohemian Massif). Tectonophysics 332, 211–237.

Zulauf, G., Dorr, W., Fiala, J., Vejnar, Z., 1997. Late Cadomian crustal tilting and Cambrian transtension in the Teplá-Barrandian unit (Bohemian Massif, Central European Variscides). Geol. Rundsch. 86, 571–584.

Zulauf, G., Helferich, S., 1997. Strain and strain rate in a synkinematic trondhjemitic dike: evidence for melt-induced strain softening during shearing (Bohemian Massif, Czech Republic). J. Struct. Geol. 19, 639–652.

Zulauf, G., Schitter, F., Riegler, G., Finger, F., Fiala, J., Vejnar, Z., 2000. Age constraints on the Cadomian evolution of the Teplá Barrandian unit (Bohemian Massif) through electron microprobe dating of metamorphic monazite. Zeitschrift der deutschen geologischen Gesellschaft, 627–639.

Zulauf, G., Schitter, F., Riegler, G., Finger, F., Fiala, J., Vejnar, Z., 1999. Age constraints on the Cadomian evolution of the Teplá–Barrandian unit (Bohemian Massif) through electron microprobe dating of metamorphic monazite. Z. Dtsch. geol. Gesell. 150, 627–639.

Zurbriggen, R., 2015. Ordovician orogeny in the Alps: a reappraisal. Int. J. Earth Sci. 104, 335–350.

# Appendix

Gondwana Research 105 (2022) 492–513

Contents lists available at ScienceDirect

Gondwana Research

journal homepage: www.elsevier.com/locate/gr

# Cambrian sedimentary basins of northern Gondwana as geodynamic markers of incipient opening of the Rheic Ocean

Reza Syahputra [a,b,*], Jiří Žák [a], R. Damian Nance [c,d]

[a] Institute of Geology and Paleontology, Faculty of Science, Charles University, Albertov 6, Prague 12843, Czech Republic
[b] Department of Geoscience, Faculty of Mathematics and Natural Sciences, Universitas Indonesia, Depok Campus, 16424 Jakarta, Indonesia
[c] Department of Geological Sciences, Ohio University, Athens, OH 45702, USA
[d] Department of Earth & Planetary Sciences, Yale University, New Haven, CT 06511, USA

ARTICLE INFO

*Article history:*
Received 30 June 2021
Revised 2 October 2021
Accepted 13 October 2021
Available online 18 October 2021
Handling Editor: A. Festa

*Keywords:*
Avalonian–Cadomian belt
Bohemian Massif
Lithospheric extension
Ribbon continents
Rheic Ocean

ABSTRACT

Diachronous opening of the Rheic Ocean and separation of Avalonian–Cadomian terranes from Gondwana began with a change from an active to passive margin in the late Ediacaran to early Cambrian. During the Cambrian, extension within these terranes was recorded by magmatism and by the development of sedimentary basins. However, the timing, style, and kinematics of this transformation still remain poorly understood and plate-scale models vary significantly. To address this issue, the Příbram–Jince basin in the Bohemian Massif was chosen as a case study since it preserves an excellent record of Cambrian rifting. Here, after Cadomian subduction ceased at ~527 Ma, extension initiated and a thick pile of continental siliciclastics was deposited in the basin between ~515 Ma and ~499 Ma, interrupted by marine transgression at ~506–503 Ma. Our field, paleocurrent, and rock-magnetic data suggest that the source areas were located to the ~ESE and to the ~SW of the basin during the deposition of the lower and upper formations, respectively. Sediment sources changed accordingly from distant metamorphic basement (Gondwana?) and Cadomian volcanic arcs and an accretionary wedge underlying the basin. This redirection marked a change in the tectonic evolution of the basin from orthogonal to dextral oblique extension that enlarged the basin into a pull-apart structure. Integrating this depositional and tectonic record into a large-scale picture, we suggest that strike-slip movements along the former Avalonian–Cadomian belt controlled the diachronous opening of the Rheic Ocean. An inherited suture in the Avalonian ribbon terrane facilitated complete rifting and rift–drift transition while the Cadomian terranes remained attached to Gondwana. The kinematics of this event remains controversial. Either it was opposite along the westerly (sinistral) and easterly (dextral) segments of the belt, which may be explained by interaction with an intervening spreading center, or it was the same dextral transtension.


## 1. Introduction

The mid- to late Neoproterozoic was marked by widespread convergence of lithospheric plates, culminating in the assembly of Gondwana and, in some models, the supercontinent Pannotia (e.g., Dalziel, 1997; Murphy et al., 2021; Nance et al. 2008; Nance and Murphy, 2019). Plate convergence was recorded in two types of orogenic belts, interior collisional belts that amalgamated the continental plates, and peripheral accretionary belts that were governed by subduction and accretion of oceanic material (e.g., Johnston, 2008; Linnemann et al., 2014; Morley, 2018; ÓBrien, 2001; Stampfli et al., 2013; von Raumer et al., 2013, 2003). Whereas the former, which includes the Pan-African and Brasiliano orogens, were unaffected by rifting until the Jurassic break-up of Pangea, the latter, which included the Avalonian–Cadomian, Carolinian and Terra Australis belts, were characterized by a continuous transition from subduction to extension and rifting (e.g., Cawood, 2005; Davy et al., 2008; Nance and Murphy, 1994; Nance et al., 1991; Willan and Kelley, 1999). This transition from active to passive plate margin has been studied extensively, particularly in the Avalonian–Cadomian accretionary orogen of northern Gondwana, which has been the exemplar for various geodynamic models (e.g., Díez Fernández, et al., 2012; Hajná et al., 2018; Linnemann et al., 2014; Nance et al., 1991).

It is well established that the Avalonian–Cadomian belt started to break up diachronously during the latest Neoproterozoic to early

* Corresponding author at: Institute of Geology and Paleontology, Faculty of Science, Charles University, Albertov 6, Prague 12843, Czech Republic.
*E-mail address:* syahputr@natur.cuni.cz (R. Syahputra).

https://doi.org/10.1016/j.gr.2021.10.004
1751-7311/

Ordovician and that the entire convergent/accretionary margin switched to widespread lithospheric extension resulting in the formation of a passive margin (e.g., Etxebarria et al., 2006; Hajná et al., 2018; Keppie et al., 2003; Nance et al., 2002). Extension was recorded by vigorous magmatic activity and by the development of sedimentary basins (e.g., Ballèvre et al., 2012; Crowley et al., 2000; Dörr et al., 2002; Drost et al., 2004; Garcia-Arias et al., 2018; Kemnitz et al., 2002; Pouclet et al., 2017; Žák et al., 2013), however, the timing, styles, and amount of extension varied considerably along the strike of the belt. In the west, Carolinia and the Avalonian terranes, thought to be formerly adjacent to South America, were completely rifted off Gondwana and drifted towards Laurentia (e.g., Nance et al., 2002), leading to the opening of the Rheic Ocean. In contrast, the easterly Cadomian terranes, formerly attached to Africa, likely experienced only partial separation and remained part of a broad *peri*-Gondwanan shelf throughout the Early Paleozoic (e.g., Linnemann et al., 2004; Murphy et al., 2002; Robardet, 2003; Romer and Kroner, 2019; Servais and Sintubin, 2009; Stephan et al., 2019a; Žák and Sláma, 2018). The eastward propagating rift system and scissor-like opening of the Rheic Ocean (e.g., Murphy et al., 2006; Nance and Linnemann, 2008) profoundly influenced the development of sedimentary basins in these contrasting segments of the northern Gondwana margin from at least the beginning of the Cambrian.

Cambrian sedimentary basins in the Avalonia–Carolinia terranes are interpreted as having formed in an intra-arc rift to back-arc setting (e.g., Hibbard et al., 2002; Murphy et al., 2000; Pollock et al., 2010). The Avalonian basins were initiated in a transtensional regime widely attributed to ridge–trench collision in the early Cambrian (e.g., Nance et al., 2002), following which the arc–rift transition continued with thick marine siliciclastic and carbonate deposits in fast subsiding basins (Prigmore et al., 1997). This deposition was associated with bimodal volcanism between ca. 540 and 500 Ma (e.g., Murphy et al., 1985, White et al., 1994). In Carolinia, the early Cambrian successions comprise arc-derived submarine epiclastic deposits at the base (e.g., Hibbard et al., 2002; Pollock et al., 2010; Secor et al., 1983), unconformably overlain by shallow-marine Middle Cambrian siliciclastic successions (e.g., Murphy and Nance, 1989; Nance et al., 1991; Samson et al., 1990).

Cambrian basins in the Cadomian terranes also mark the transition from active to passive margin with the opening of the Rheic Ocean (Fig. 1b; Etxebarria et al., 2006; Hajná et al., 2018). Cadomian subduction ceased at ca. 540 Ma in the Armorican Massif and Saxothuringia, but continued in the Ossa Morena Zone (Iberian Massif) and Teplá–Barrandian unit (Bohemian Massif) until at least the early to middle Cambrian. To explain the diachronous cessation of subduction and the different tectonic processes presumably occurring along the former Avalonian–Cadomian belt, Hajná et al. (2018) proposed a curved geometry for the convergent plate margin. In contrast to Avalonia, the incipient rifting in Cadomia, at least in the Teplá–Barrandian unit, is recorded in the deposition of a thick pile of continental deposits, only briefly interrupted by marine transgression, and associated with volcanic and plutonic complexes interpreted as reflecting slab-breakoff and remelting of the Cadomian arc-derived crust and mantle (e.g., Dörr et al., 2002; Zulauf, 1997; Zulauf et al., 1999).

While the tectonic processes and stratigraphic record of the Cambrian active-to-passive margin transition have been well documented in the *peri*-Gondwanan terranes, a number of issues continue to remain poorly understood, for instance, the timing and geodynamic causes of the transition. In this study, we use the well-exposed Teplá–Barrandian unit as a case study to address these issues: first, to examine changes in the depositional processes and source areas with time; second, to evaluate the tectonic controls on deposition in the Cambrian basins and to establish the styles and mechanisms of the incipient rifting; and, third, to assess the geodynamic causes of the rift–drift vs. failed-rift transition modes in the western and eastern parts of the Avalonian–Cadomian belt, respectively. All data in this study come from the Příbram–Jince basin, which is one of the best preserved and the most informative examples of a Cambrian continental–marine basin formed at the former northern Gondwana margin (Fig. 1c). We combine detailed field observations and facies and paleocurrent analysis with rock-magnetic methods (anisotropy of magnetic susceptibility, AMS) to present a refined model of the tectono-sedimentary evolution of this basin. We then compare the basin's lithostratigraphic record with correlative basins of the Avalonian–Cadomian belt and present a general model for the initial detachment of ribbon continents from Gondwana during the Cambrian.

## 2. Geology of the Příbram–Jince basin

### 2.1. Overview

At the present-day erosional level, the Příbram–Jince basin covers an area of about 400 km$^2$ along the southeastern margin of the Teplá–Barrandian unit, a large exposure of upper crust in the center of the Bohemian Massif (Fig. 1c). The basin overlies Cadomian basement made up of a late Neoproterozoic to early Cambrian accretionary wedge, referred to as the Blovice complex (e.g., Hajná et al., 2017), with a regional angular unconformity and is, in turn, overlain by basal Lower Ordovician (Tremadocian) strata of the Prague basin, also with a slight angular unconformity. The southeastern end of the basin is truncated by a system of NW–SE-trending normal faults that juxtapose the basin against Cadomian basement in the footwall (Fig. 1d). The basin axis trends ~NE–SW, which is roughly parallel to the lithotectonic belts in the underlying accretionary wedge, and aligned at an angle of approximately 20° to axis of the overlying Prague basin (Fig. 1d). The basin interior is segmented into alternating, NE–SW-trending horsts and grabens (Fig. 2a), the fault-bounded basement blocks being overlain by fill of variable thickness and spatially changing depocenters (e.g., Havlíček, 1971; Kukal, 1971). Nevertheless, the basin fill thickness generally increases from older formations along its southeastern margin to the basin center and then continuously decreases towards younger formations in the northwest.

Correlative outliers comprising Cambrian siliciclastic deposits occur to the south and southeast of the basin as narrow, faulted and folded belts and in a roof pendant enclosed by a Variscan plutonic complex (Fig. 1d), all strongly overprinted by Variscan shortening and contact metamorphism. Another graben-type basin, somewhat restricted in terms of its spatial extent, fill, and thickness, occurs about 20 km to the northwest (the Skryje–Týřovice basin; Fig. 1d). Among these Cambrian basinal relicts, the Příbram–Jince basin is the largest, provides the most complete tectonostratigraphic record, and is the least affected by younger deformation (e.g., Fatka and Mergl, 2009; Geyer et al., 2008; Kukal, 1971).

### 2.2. Lithostratigraphy

The Příbram–Jince basin is dominated by continental siliciclastic deposits interlayered with a marine horizon and capped by an intermediate to felsic volcanic complex (Strašice complex: Fig. 2; e.g., Havlíček, 1971; Kukal, 1971). The basin infill is subdivided into eight formations (Fig. 2). The contacts between adjacent formations are mostly gradational over a few meters in vertical section while lateral transitions and interdigitation are also observed, especially between the individual stratigraphic members. From

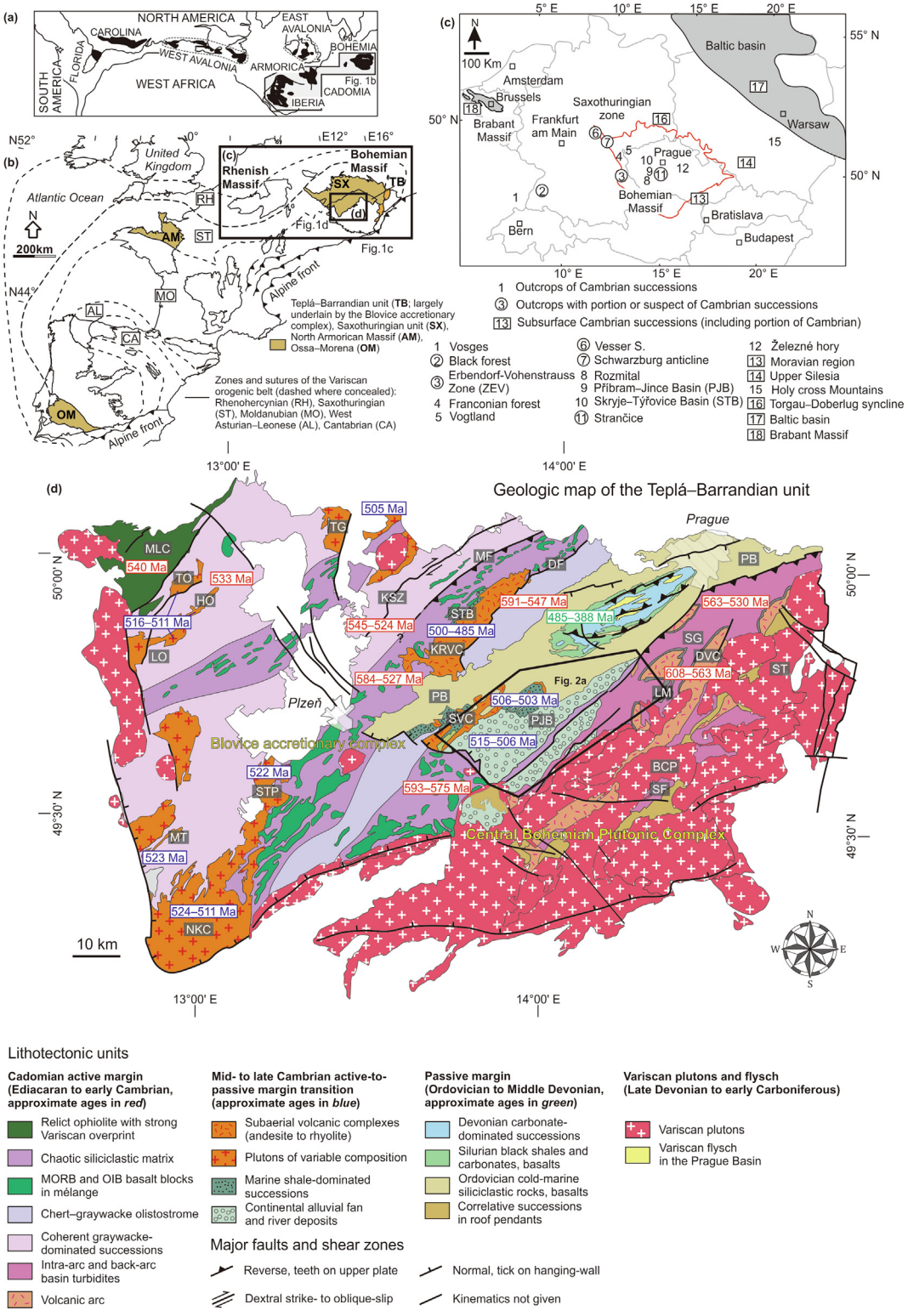


**Fig. 1.** (a) Distribution of *peri*-Gondwana terranes along the Avalonian–Cadomian orogenic belt during the Late Paleozoic (redrawn from Nance et al., 2002), (b) Cadomian crustal fragments and overlying Cambrian basins within the Variscan belt. Highlighted terranes contain well-preserved Cambrian outcrops, mostly low-grade relics of the Cadomian orogenic belt (compiled from Martínez Catalán, 2011), (c) Cambrian successions across Europe from outcrop and subsurface data (Geyer et al., 2008), (d) Geologic map of the Teplá–Barrandian unit with compilation of existing geochronologic data for the latest Neoproterozoic, Cambrian, and Ordovician in red, blue, and green rectangles, respectively (compile from Hajná et al., 2017, 2018 and geological map 1:50.000 scale from Czech Geological Survey). Cadomian units: DF Družec fault, DVC Davle volcanic complex, LM Lečice Member, MF Městečko fault, MLC Mariánské Lázně complex, SF Svrchnice Formation, SG Štěchovice Group; Cambrian–Ordovician plutons and volcanic complexes: HO Hanov orthogneiss, KRVC Křivoklát–Rokycany volcanic complex, LO Lestkov orthogneiss, MT Mračnice trondhjemite, NKC Neukirchen–Kdyně complex, STP Stod pluton, SVC Strašice volcanic complex, TG Tis pluton, TO Teplá orthogneiss; Lower Paleozoic basins: PB Prague Basin, PJB Příbram–Jince Basin, STB Skryje–Týřovice Basin. (For interpretation of the references to color in this figure legend, the reader is referred to the web version of this article.)

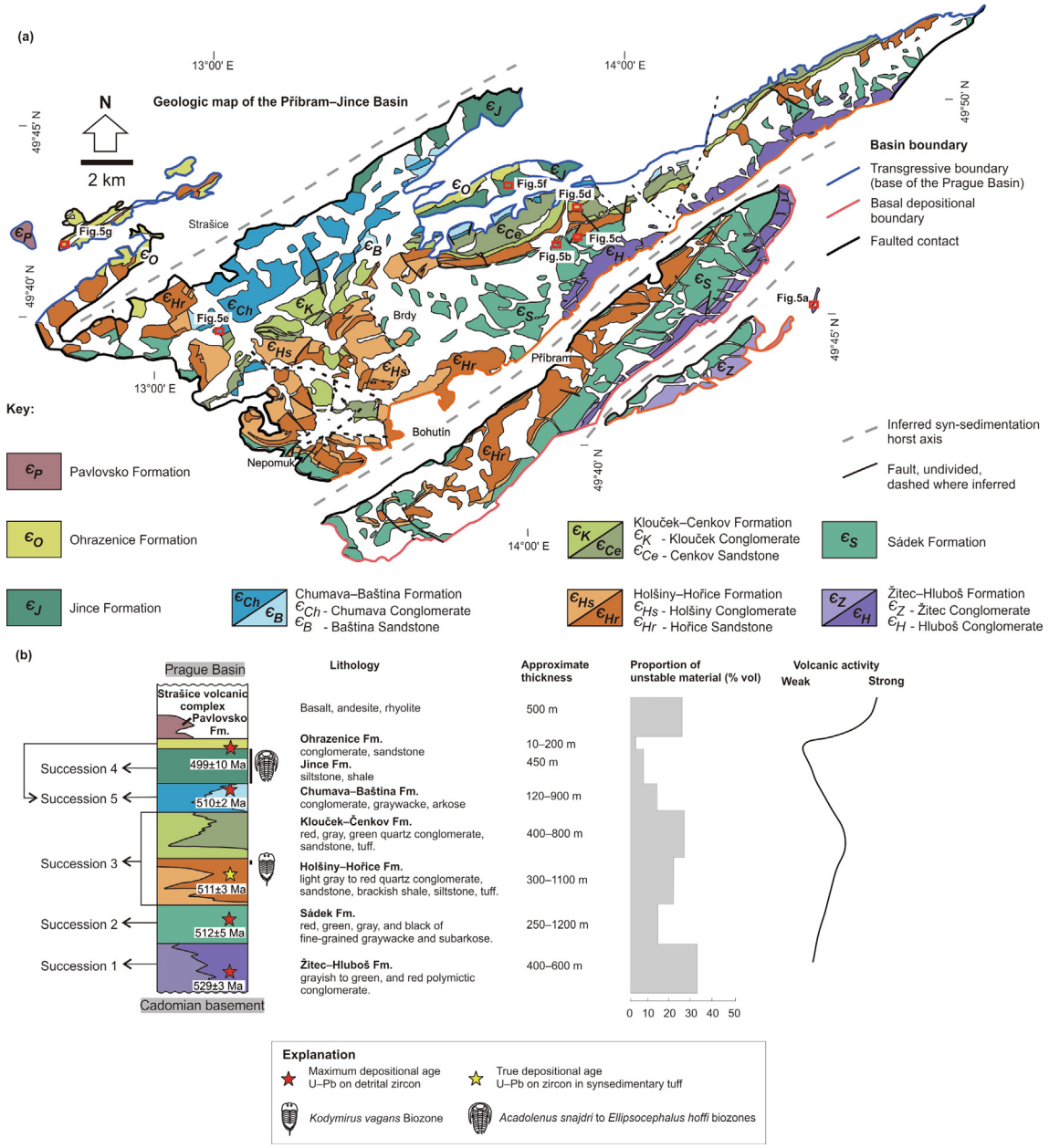


**Fig. 2.** (a) Simplified geologic map of the Příbram–Jince basin compiled from Havlíček (1971) and geological map 1:25,000 scale from Czech Geological Survey. Inferred horst axis after Havlíček (1971). (b) Lithostratigraphic scheme of the Příbram–Jince basin and graphs showing variations in the proportion of unstable material and volcanic activity across stratigraphy (Kukal, 1971). U-Pb detrital zircon ages from Drost et al. (2004, 2011) and Hajná et al. (2018) are maximum depositional ages. U-Pb detrital zircon age in synsedimentary tuff from Hajná et al. (2018).

bottom to top, the eight formations can be informally grouped into five different successions (Fig. 3). Their main characteristics are described below and depicted in a cross-section in Fig. 4.

(1) The Žitec–Hluboš Formation in the southeastern part of the basin is dominated by red and green polymictic conglomerates and sandstones. The clasts are up to 30 cm in size (boulders) and composed of quartz, Cadomian unstable material derived from a volcanic arc (granites, porphyritic plagiogranites, intermediate to felsic lavas, tuffs) and low- to medium-grade metamorphic basement (metagraywackes, phyllites, mica schists, and gneisses; Fig. 5a). Metamorphic clasts are absent at higher stratigraphic levels (Fig. 4) and have been interpreted as sourced from an unknown terrain to the southeast (present-day coordinates; Kettner, 1919, 1946). The clast size in conglomerates decreases significantly to the northwest where they are frequently overlain by a few centimeter to decimeter layers of sandstones.

(2) The Sádek Formation in the southeastern part of the basin lacks conglomerates and is dominated by graywackes to sub-graywackes or even arkoses to subarkoses interbedded with siltstones and claystones (Fig. 5b). Grain size generally decreases in the western part of the basin down to siltstone (Kukal, 1971; Havlíček, 1971). Mudstone rip-up clasts, slump structures, and several centimeter-thick lenses of conglomerates may also occur within the sandstone beds (Kukal, 1971).

(3) The overlying succession, areally the most extensive and occupying the center of the basin, is composed of monomictic conglomerates and conglomeratic sandstones with a

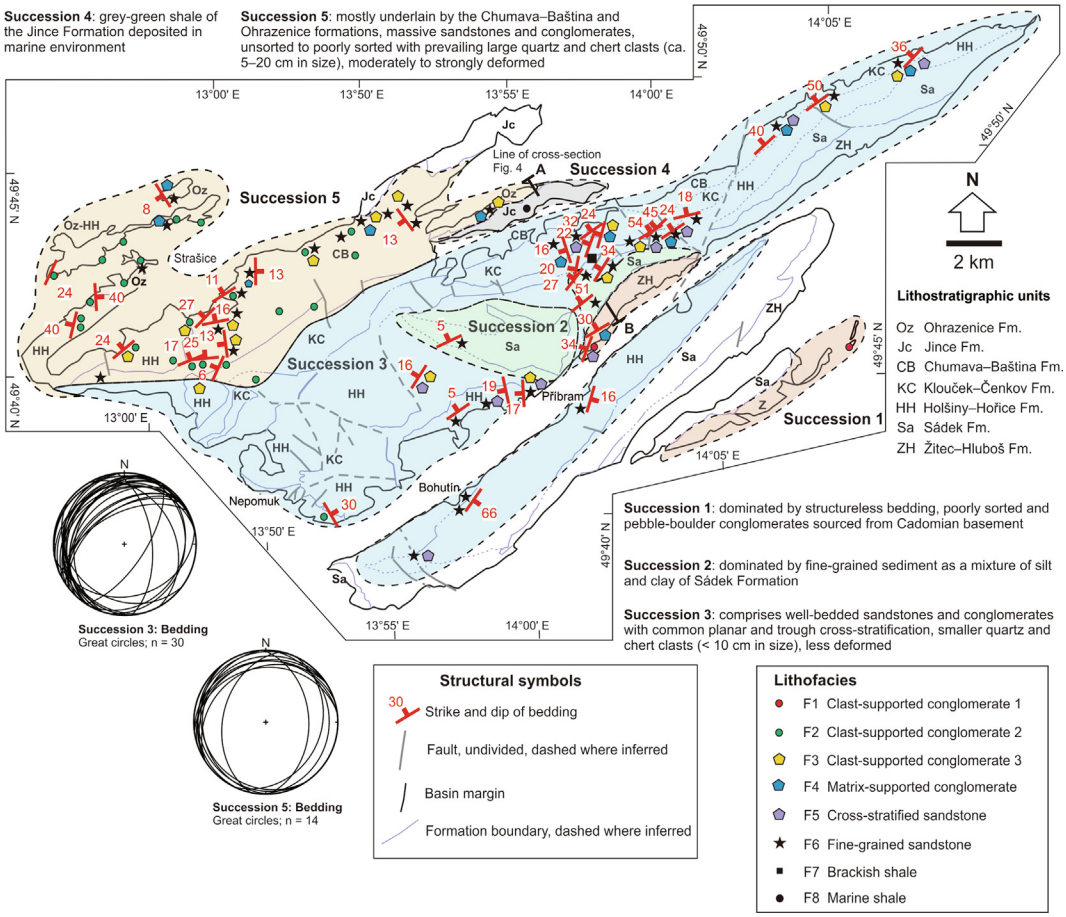


**Fig. 3.** Field measurements from the Příbram–Jince basin. The lithostratigraphy (color-coded) is divided into five successions, dominated by alluvial and fluvial depositional settings with a short-lived marine transgression (Jince Formation).

smaller clast size (typically 1–5 cm), but also includes restricted occurrences of brackish shales. This succession comprises, in stratigraphic order, the Holšiny–Hořice and Klouček–Čenkov formations and the Baština Sandstone. The conglomerates generally consist of quartz and chert clasts, but the chert proportion decreases significantly up-section (in the Klouček–Čenkov Formation). The overlying Holšiny–Hořice Formation is dominated by light gray to red sandstones and monomictic conglomerates (Fig. 5c) with a significant marker horizon of silty shales (Paseky Shale) and minor felsic tuff intercalations within the sandstones. The tuffitic material also occurs as small fragments, becoming increasingly abundant in the Klouček–Čenkov Formation (Fig. 5d). The Baština Sandstone fills the north-central part of the basin and is characterized by a decreasing abundance of tuff fragments, marking the waning of volcanic activity towards the end of continental deposition.

(4) The fourth succession, which occupies a limited area in the northern part of the basin, differs markedly from the successions above and below, and comprises finely laminated siltstones and shales of the Jince Formation, accompanied by centimeter-thick layers of sandstones (Fig. 5f). The succession's *Lingullela*, trilobite, and Agnostid Biofacies indicate sea-level rise (transgression) and deposition in a shallow to deep water marine environment (e.g., Babcock et al., 2015; Fatka and Szabad, 2014; Fatka and Mergl, 2009).

(5) The Chumava Conglomerate was deposited at the same time as the Baština Sandstone, but shares similar lithologic characteristics with the Ohrazenice Formation in the northwestern part of the basin. The lithologies include monomictic conglomerates and lithic sandstones (Fig. 5e and 5 g) with minor admixture of felsic tuffitic material in some places (Kukal, 1971). Clasts in the conglomerates range from 5 to 20 cm in size. The overlying Pavlovsko Formation contains sandstones with abundant unstable clasts and clay (Kukal, 1971), and was deposited during vigorous volcanic activity of the Strašice complex (Fig. 2b).

### 2.3. Temporal constraints on the evolution of the Příbram–Jince basin

The exact timing of deposition in the Příbram–Jince basin, a key for inter-regional correlation and the interpretation of geodynamic processes, is only broadly constrained. Drost et al. (2011) reported a maximum depositional age of 529 ± 3 Ma from U–Pb detrital zircons in the lowermost Žitec–Hluboš Formation. However, significantly younger maximum depositional ages (512 ± 5 Ma) were reported by Hajná et al. (2018) from the directly overlying Sádek graywackes. The difference in age implies either a protracted time span of deposition of the basin's basal infill or that the maximum depositional age of 529 Ma is significantly older than the true depositional age. Further up-section, a U–Pb age from a silicified tuff constrains the true depositional age of the Holšiny–Hořice Formation to

| | Ohrazenice Fm. | Jince Fm. | Chumava–Baština Fm. | Klouček–Čenkov Fm. | Holšiny–Hořice Fm. | Sádek Fm. | Žitec–Hluboš Fm. |
|---|---|---|---|---|---|---|---|
| Dominant lithology | Monomictic conglomerate | Siltsone and shale | Monomictic conglomerate | Quartz sandstone conglomerate | Quartz sandstone conglomerate | Sandstone, siltstone, shale | Polymictic conglomerate |
| Bedding | Massive to thickly bedded | Massive bedded | Massive to thickly bedded | Thin to thickly bedded | Massive to thickly bedded | Massive to thinly bedded | Massive to thickly bedded |
| Internal structures | Poorly sorted, pebbles layer | Fine-scale lamination, bedding-parallel cleavage | Poor-moderately sorted, pebbles layer | Moderately sorted, pebbles layer, cross-stratification | Moderately sorted, cross-stratification | mud strips, cross-stratification | Chaotic, cross-stratification |
| Dominant clast composition | Quartz and chert | Silt and shale (sub/graywacke) | Quartz and chert (sub/graywacke) | Quartz and chert (sub/graywacke) | Quartz and chert (sub/graywacke) | Q:F:L = 80:5:15 (subarkose) | Quartz, chert, granite, rhyolite, plagio-granite |
| Clast size | Up to 5–20 cm | Silt and shale | Up to 10–20 cm | Up to 1–5 cm | Up to 1–10 cm | Fine-grained sand | Up to 20–30 cm |
| Lithofacies | F2, F4, F6 | F8 | F2, F3, F4, F6 | F3–F6 | F2–F6 | F6 | F1 |

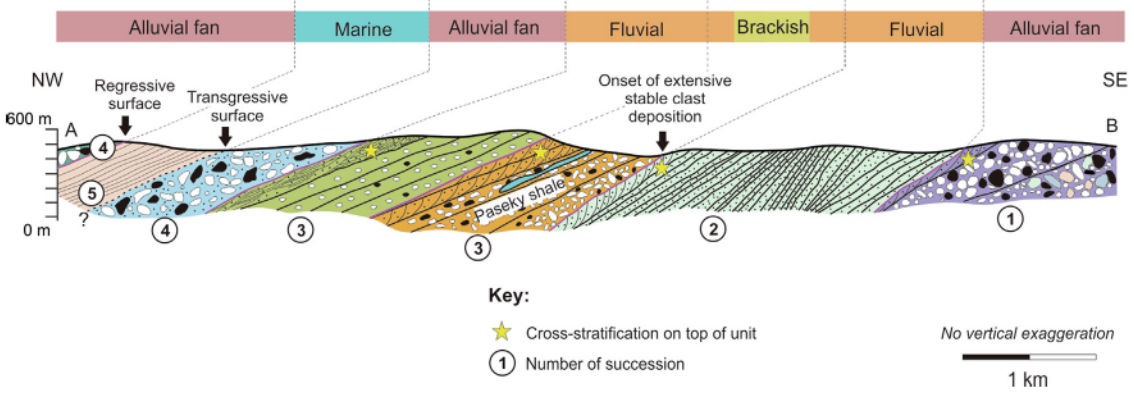


**Fig. 4.** Cross-section of the Příbram–Jince basin along the Litavka River with descriptions of each rock formation.

511 ± 3 Ma (Hajná et al., 2018), while a maximum depositional age for the overlying Chumava–Baština Formation has been estimated at 510 ± 2 Ma (Drost et al., 2011). The trangressive marine shales of the Jince Formation are dated paleontologically and were assigned to the *Acadolenus snajdri* to *Ellipsocephalus hoffi* biozones, corresponding to the time interval ca. 506–503 Ma (Fatka and Szabad, 2014). This is in agreement with the maximum depositional age of 499 ± 10 Ma determined for the uppermost levels of the Jince Formation (Drost et al., 2011). In summary, ca. 515 Ma and ca. 499 Ma may be considered the maximum and minimum time constraints for deposition within the Příbram–Jince basin (Fig. 2b).

## 3. Field observations

### 3.1. Structure of the Příbram–Jince basin

Major NE–SW-trending faults divide the Příbram–Jince basin into three segments parallel to the basin axis (Fig. 2a). These faults were active during deposition as inferred from thickness variations reflecting differential subsidence in several depocenters (Havlíček, 1998, 1971). The most notable examples are the Žitec–Hluboš and Sádek formations, which pinch out northwestwards, and the younger formations, which are spatially restricted to the northwestern margin of the basin (Fig. 2a). Otherwise, the overall structure of the basin is simple, resulting from weak Variscan shortening. Bedding dips mostly to the NW and NNW at shallow to moderate angles (between 16° and 54°) in succession 3 as a result of Variscan tilting, whereas in the northwesterly succession 5 it dips gently (mostly less than 25°) in various directions (Fig. 3). Consequently, the formations within the basin are arranged from the oldest in the SE to the youngest in the NW (Fig. 3).

### 3.2. Lithofacies

In this study, we distinguish eight main lithofacies (F1–F8) based on clast composition, clast size and sedimentary structures; these facies are attributed to four depositional environments (for detailed characteristics see Supplementary Data, Tab. 1).

#### 3.2.1. Alluvial fan facies (F1–F3)

The F1 lithofacies is represented by clast-supported, mostly non-bedded, poorly sorted polymictic conglomerates with subrounded to rounded clasts up to boulders, in places interbedded with thin sandstone beds bounded by irregular erosional contacts (Fig. 6a). Conversely, similar clast-supported conglomerates of lithofacies F2 are poorly sorted monomictic conglomerates composed of subrounded to rounded quartz pebbles to cobbles embedded in a light gray or red matrix (Fig. 6b).

The clast-supported monomictic conglomerates of lithofacies F3 comprise subrounded to rounded quartz and chert pebbles to cobbles embedded in a moderately sorted, fine- to medium-grained sandy matrix. This facies forms thin graded layers (0.1 and 1 m in thickness), each with a sharp erosional base (Fig. 6c).

#### 3.2.2. Fluvial distributary system facies (F4–F6)

Matrix-supported conglomerates of lithofacies F4 overlie the F3 facies with sharp to gradational basal contacts, forming a depositional couple. The F4 conglomerates are dominated by medium to coarse-grained, poorly to moderately sorted arkoses, subarkoses, and graywackes with scattered quartz pebbles to cobbles, fining upward (Fig. 6d).

Cross-stratified sandstones of lithofacies F5 show both planar and trough cross-stratification of low and high angle with bed thicknesses up to 30 cm (Fig. 6e). In some places, granules to pebbles of quartz are aligned within the cross-stratification.

Red or gray coarse to fine-grained sandstones of lithofacies F6 comprise bedded graywackes, subgraywackes, subarkoses, and arkoses. The sandstones show a significant compositional difference to the other facies and occur only in the Sádek Formation.

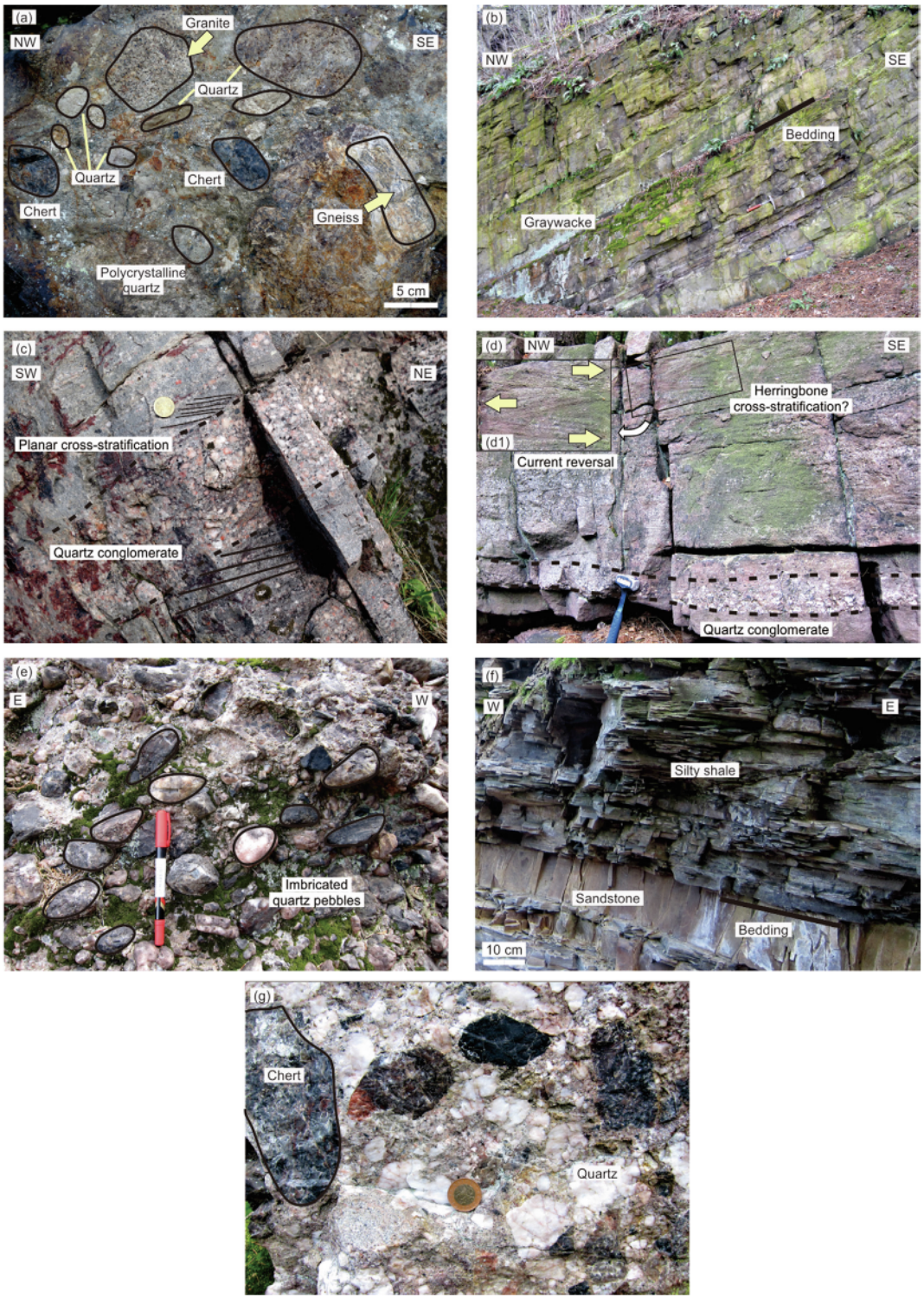


**Fig. 5.** Field photographs of Cambrian outcrops in the Příbram–Jince basin, arranged from older to younger. (a) Polymictic conglomerate of the Žitec–Hluboš Formation. Clasts were derived from a volcanic arc and metamorphic basement of the Cadomian; Tuškov [WGS84 coordinates: N49°44′26.394″, E14°10′38.363″]. (b) Graywacke of Sádek Formation. Beds dip to the NW; Bratkovice [WGS84 coordinates: N49°45′4,530″, E13°59′59,115″]. (c) Planar cross-stratification in the Holšiny–Hořice Formation with layer of quartz conglomerate interpreted as a fine-grained sheetflood fan (F3); near Hořice hill [WGS84 coordinates: N49°45′23.134″, E14°1′1.627″]. (d) The Klouček–Čenkov Formation with herringbone (?) cross-stratification implying current reversal; Bílá huť [WGS84 coordinates: N49°46′12.495″, E14°0′51.558″]. (e) Typical monomictic conglomerate with imbricated quartz pebbles in the Chumava–Baština Formation; Hlava [WGS84 coordinates: N49°43′22.272″, E13°49′23.978″]. (f) Shale with thin intercalation of sandstone from the Jince Formation; Jince [WGS84 coordinates: N49°47′3.975″, E13°59′24.791″]. (g) Ohrazenice Formation composed of quartz and cherts pebbles; Konesův vrch [WGS84 coordinates: N49°43′26.447″, E13°40′51.05″]. Scale: pen = 14 cm; hammer = 26 cm; coin diameter = 2.5 cm.

The basal sandstones have a silty and clayey matrix whereas those in the upper stratigraphic levels are accompanied by thin tuffaceous layers (Fig. 6f).

### 3.2.3. Brackish environment facies (F7)

Brackish shales of lithofacies F7 were deposited in a spatially restricted area and forms a marker horizon about 10–15 m thick

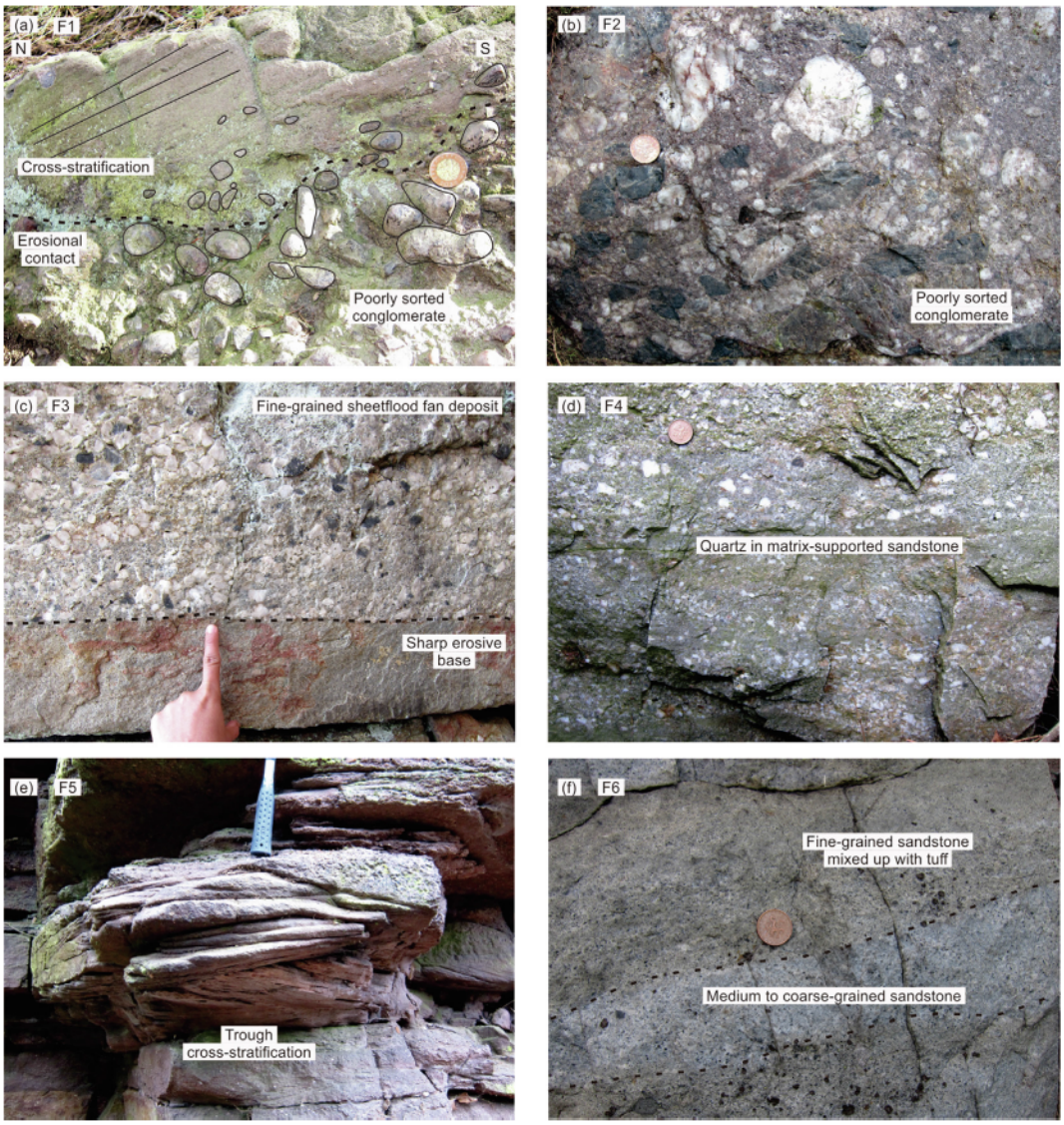


**Fig. 6.** Field photographs of Cambrian lithofacies in the Příbram–Jince basin. (a-c) Alluvial fan deposit from a debris flow. (a) F1 Clast-supported conglomerate showing chaotic internal structure with an erosional contact; between Dratovna and Valcha [WGS84 coordinates: N49°43′23.459″, E14°0′48.661″]. (b) Poorly-sorted F2 clast-supported conglomerate in a sandy matrix; Konesův vrch [WGS84 coordinates: 49°43′26.447″, E13°40′51.05″]. (c) Clast-supported conglomerate interpreted as a fine-grained sheetflood fan (F3) with sharp erosive base; Stožec [WGS84 coordinates: N49°50′7.68″, E14°8′13.311″]. (d-f) Fluvial distributary system. (d) Granule-pebble quartz in a matrix-supported sandstone (F4); Chocolatá skála [WGS84 coordinates: N49°41′44.99″, E13°47′30.718″]. (e) Trough cross-stratification in sandstone, sometimes found together with granule-pebble quartz (F5); Slonovec [WGS84 coordinates: N49°45′42.900″, E13°59′50.200″]. (f) Fine-grained sandstone (F6), sometimes associated with thin tuffaceous layers in the upper stratigraphic levels; Kazatelna [WGS84 coordinates: [N49°41′33.286″, E13°56′35.607″]. Scale: hammer = 26 cm; coin diameter = 2.5 cm.

within the Holšiny–Hořice Formation. The base of the shale horizon is an erosive boundary (Kukal, 1971). The lithofacies comprises dark-gray silty shale with reported rare endemic arthropod fossils (the Kodymirus association), representing the oldest macrofauna in the Bohemian Massif (e.g., Chlupáč et al., 1995; Chlupáč and Havlíček, 1965) and perhaps indicating a brackish environment (Kukal, 1995).

#### 3.2.4. Marine facies (F8)

The marine Jince Formation conformably overlies the continental deposits and is composed predominantly of siltstones and shales (lithofacies F8) with thin sandstone intercalations and, locally, with conglomerates (Kukal, 1971). The formation is world-famous for its rich fossil record, mostly brachiopods, trilobites, Agnostids, and an echinoderm-dominated association (Geyer et al., 2008; Fatka and Mergl, 2009; Fatka and Szabad, 2014).

### 3.3. Spatial and stratigraphic distribution of lithofacies

The alluvial fan deposits of lithofacies F1 are distributed near the southeastern edge of the basin, and are only developed in succession 1 (Žitec–Hluboš Formation). In the middle of the basin, which contains the most extensive part of succession 3, the alluvial fan was replaced by a mixture of the fine-grained sheetflood fan deposits of lithofacies F3 and the fluvial distributary system of lithofacies F4 and F5 (representing a set of bar packages in a braided stream), and F6. In detail, the lower part of the Holšiny–Hořice and Klouček–Čenkov formations is mostly dominated by lithofacies F3, changing upward to the finer grained lithofacies F4 to F6 (Fig. 7). Except for lithofacies F4, which is not present in the southwestern part of the basin, or the middle part near Příbram, the fluvial distributary system narrows from the central to the northeastern part of the basin (see Fig. 3).

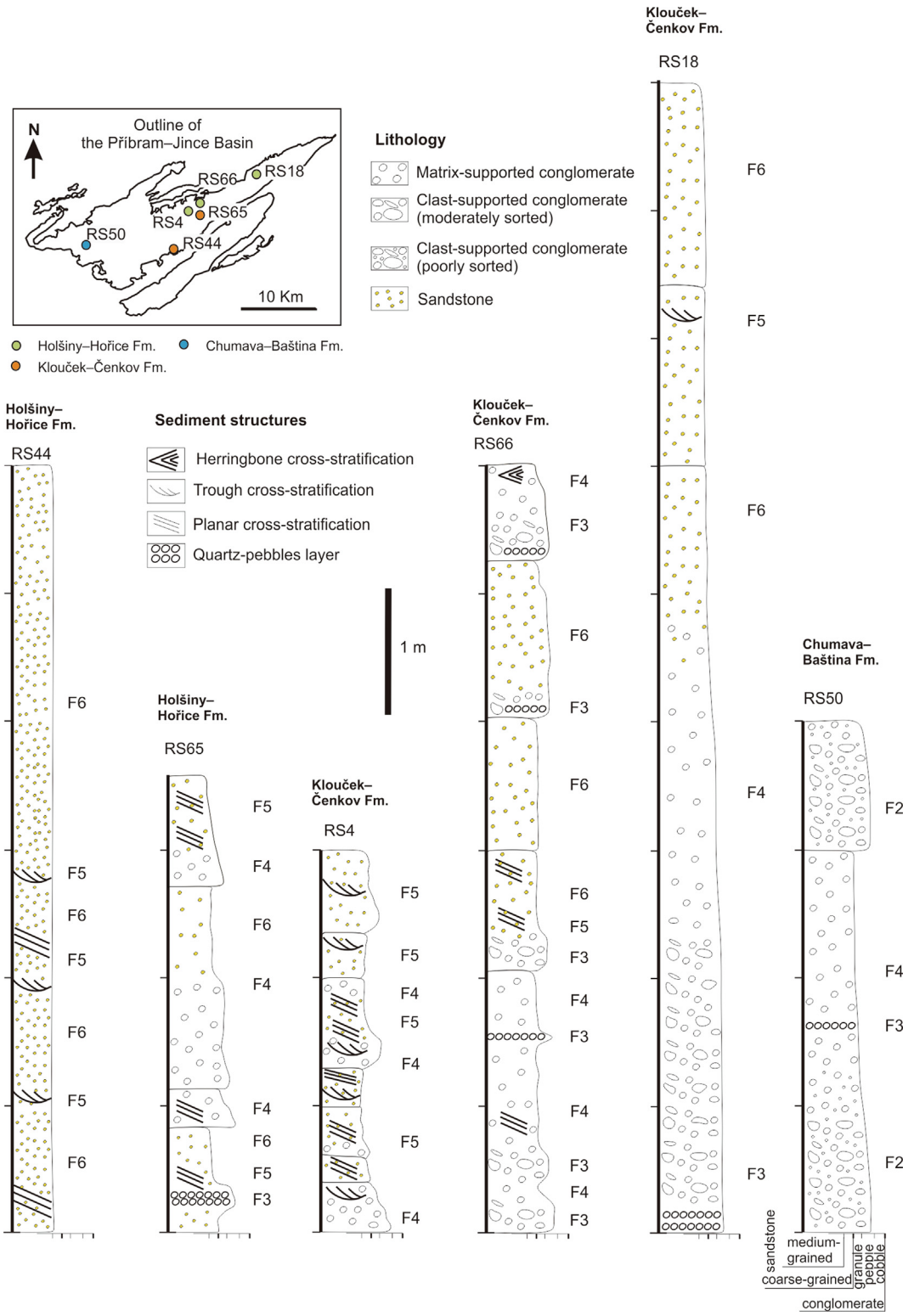


**Fig. 7.** Representative sedimentary logs of lithofacies of the fluvial distributary system and alluvial fans. A fining-upward pattern dominates the entire section, indicating waning of paleocurrents in the upper part.

In the NW part of the basin, the thickly bedded lithofacies F2 in succession 5 is frequently overlain by laminated pebbles of the F3 sheetflood fan, and conformably capped by sandstones of the F4 fluvial distributary system (see profile of Chumava–Baština Formation in Fig. 7).

The marine lithofacies F8 is limited to succession 4 and is mostly confined to the north-central part of the Příbram–Jince basin (Kukal, 1971).

## 4. Paleocurrent analysis

### 4.1. Method and description of paleocurrent indicators

Paleocurrent analysis was carried out on 15 outcrops (out of 74 stations documented in total). These outcrops expose reliable paleocurrent indicators and are mostly distributed within a 2–3 km wide belt along the southeastern margin of the basin, ranging stratigraphically from the basal Žitec–Hluboš Formation up to the Klouček–Čenkov Formation (Fig. 8). All measured paleocurrent indicators were cross-stratification structures.

Cross-stratification was most commonly preserved in the fine- to medium-grained sandstones and, occasionally, in the quartz-pebble conglomerates of succession 3 at the middle and the upper levels of the Holšiny–Hořice and the Klouček–Čenkov formations. The structures include planar, trough, and rarely bi-directional subtypes.

Planar cross-stratification is the most abundant structure, commonly present in lithofacies F5, but sometimes appearing in lithofacies F4. Fig. 8a–b shows examples of planar cross-stratification in angular and tangential foresets at high and low angles to the lower bounding surface, respectively (e.g. Blair, 2000; Herbert et al., 2020). A reactivation surface sometimes occurs within the planar cross-stratification (Fig. 8c), resulting from interaction between bedforms in unidirectional flow (e.g., Allen, 1973). The foresets have a thickness of up to 30 cm with a maximum width of 2 m, and the surface beneath and above each coset is non-erosional.

Trough cross-stratification is much less common, mostly occurring in lithofacies F5 in the Klouček–Čenkov and the Sádek formations, with coset thicknesses between 5 and 30 cm and widths from 50 to 60 cm. The foreset shape is tangential and bounded by a flat surface.

Bi-directional stratification occurs rarely in the Klouček–Čenkov and Holšiny–Hořice formations. This sedimentary structure is interpreted as herringbone cross-stratification, in which the upper and lower straight foresets have opposite dips, in Fig. 5d to the ~NE (68°) and ~SE (151°), respectively.

The paleocurrent data were collected on outcrops as dip directions of planar cross-beds and treated as a vector of unit length (e.g., Potter and Pettijohn, 1977; Nichols, 2009). The paleocurrent direction was assumed to be down dip. To remove the effect of post-depositional tectonic deformation (bedding tilt), the paleocurrent vectors have been rotated to the horizontal about a rotation axis represented by the strike of the bedding through an angle equal to the bedding dip. The rotated paleocurrent directions are presented in map view and as a rose diagram in Fig. 8c.

### 4.2. Inferred paleocurrent directions and their distribution within the basin

Statistically, the inferred paleocurrent directions scatter from ~NNW (332°) to ESE (104°) with a mean direction of 030° calculated using the method of Fisher et al. (1987). An intriguing pat-

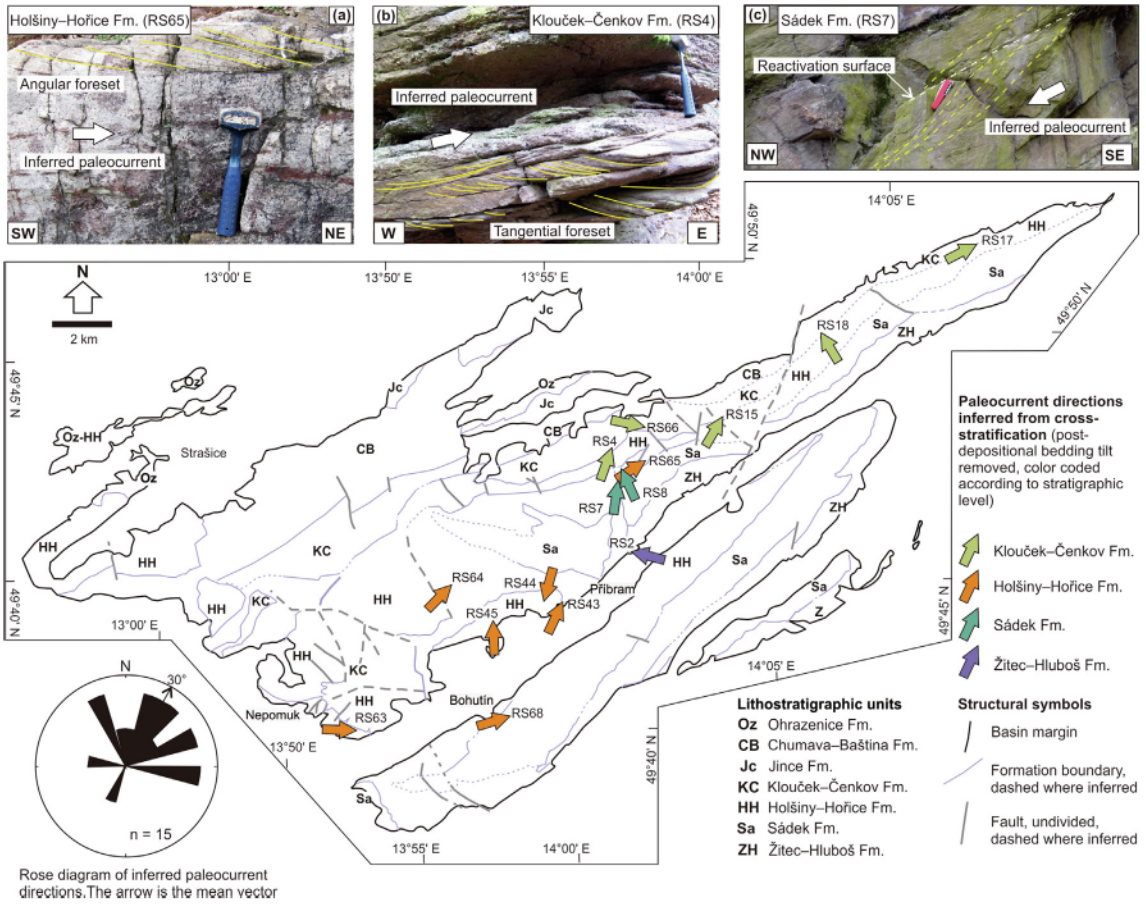


**Fig. 8.** Inferred paleocurrents from cross-stratification measurements. Mean direction of presumed paleoflowed is ~30° NE, calculated using a method by Fisher et al. (1987). Effects of tilting have been removed. Field examples of (a) angular; near Hořice hill [WGS84 coordinates: N49°45′23.134″, E14°1′1.627″] and (b) tangential foresets in planar cross-stratification; Slonovec [WGS84 coordinates: N49°45′42.900″, E13°59′50.200″]. (c) Reactivation surface indicating uniform paleoflow to the ~NNW in the Sádek Formation; Bratkovice [WGS84 coordinates: N49°45′4.530″, E13°59′59.115″]. Scale: hammer = 26 cm; folded knife = 10 cm.

tern, however, emerges when the data are viewed in stratigraphic succession and with respect to their spatial distribution across the basin (note the bedding dips generally to the NW; Fig. 2). Going up-section (and from SE to NW), the basal Žitec–Hluboš Formation shows paleocurrents to the ~WNW, changing to ~N in the overlying the Sádek Formation, and to frequent ~ENE directions in the Holšiny–Hořice and Klouček–Čenkov formations. This suggests basin axis-oblique sediment transport in the early stages of basin evolution gave way to predominantly axis-parallel transport as the basin matured. Only two localities yielded paleocurrent directions opposite to this overall trend (Fig. 8).

## 5. Microstructures

Microstructures were examined at 18 stations distributed across the basin in order to characterize the clast compositions and their relationships in the matrix, the presence or absence of volcanic admixture, and deformational features in quartz that could be used to infer the metamorphic grade of the source rocks and thus their provenance. Fig. 8 shows representative examples of microstructures within the continental successions in stratigraphic order from the oldest to the youngest.

A conglomerate sample collected from the Žitec–Hluboš Formation (Fig. 9a) comprised subrounded to subangular clasts, typically 4–5 mm in size. Fragments of volcanic rocks (lava, tuff, and volcanic glass, mostly recrystallized) are particularly abundant, with about half of the thin section area made up of skeletal plagioclase. The volcanic fragments are highly variable in size, ranging from 0.1 to 1 mm. On the other hand, the quartz grains are mostly uniform in size (ca. 0.5–0.7 mm). Polycrystalline aggregates within a single clast exhibit undulose extinction and experienced low- to high-temperature dynamic recrystallization ranging from bulging through sub-grain rotation to grain boundary migration (e.g., Blenkinsop, 2000; Stipp et al., 2002; Xia and Platt, 2018). Clastic grains of chlorite are frequent along contacts between the quartz grains, occasionally accompanied by new growth of muscovite.

A fine-grained sandstone (sub-arkose) sample collected from the overlying Sádek Formation (Fig. 9b) is dominated by angular to sub-angular quartz grains (100–250 μm in size) that generally lack undulose extinction. The quartz grains are set in a clay-rich matrix, which also contains abundant clastic grains of chlorite. Volcanic material is absent, and plagioclase occurs only in minor proportions. New growth of muscovite is sparse and crudely aligned with grain contacts. Quartz microveins are common, showing undulose extinction in some cases but no evidence of dynamic recrystallization.

The matrix in a quartz-pebble conglomerate sample from the Holšiny–Hořice Formation (Fig. 9c) is fine to medium-grained and composed of sub-angular to sub-rounded quartz clasts (0.5–2 mm in size). Most of the quartz grains within the clasts exhibit undulose extinction and evidence of low- to high-temperature dynamic recrystallization. Lamellae and other internal features, such as grain–grain contacts, are truncated by the outer clast boundaries (Fig. 9c). Volcanic fragments, mostly composed of recrystallized tuff, are rare, amounting to ca. 5% of the thin-section area. Clastic grains of chlorite occasionally delineate the clast boundaries.

Quartz-pebble conglomerate samples collected from the Klouček–Čenkov (Fig. 9d), Chumava–Baština (Fig. 9e) and Ohrazenice (Fig. 9f) formations are similar in terms of their microstructure. They exhibit a fine to coarse-grained matrix, and the quartz clasts are sub-angular to sub-rounded, 1–2 mm in size, and show undulose extinction. Most polycrystalline quartz aggregates show evidence of stretching and low- to high-temperature dynamic recrystallization (sub-grain rotation, bulging, and grain boundary migration in the smaller fragments). The modal proportion of volcanic material (mostly recrystallized tuff) increases to 10% in the Klouček–Čenkov sample (Fig. 9d), but is lower in the Chumava–Baština and Ohrazenice samples (Fig. 9 e and f). The size of volcanic clasts in the Ohrazenice sample is also generally larger than in the Klouček–Čenkov sample. Clastic grains of chlorite and new growth of muscovite (up to 3–5% modal proportion) were also observed.

## 6. Anisotropy of magnetic susceptibility (AMS)

### 6.1. Methods

Low-field (<1 mT) anisotropy of magnetic susceptibility (e.g., Borradaile and Henry, 1997; Borradaile and Jackson, 2004, 2010; Bouchez, 1997; Hrouda, 1982; Rochette et al., 1992; Tarling and Hrouda, 1993) is used here to analyze quantitatively the symmetry, intensity, and orientation of 'invisible' magnetic fabrics in sandstones and thin sandstone interbeds within the conglomerates in the Příbram–Jince basin. The main goal of applying rock-magnetic methods to these sandstones was to obtain independent quantitative information on paleocurrent directions (e.g., Felletti et al., 2016; Hrouda et al., 2009; Soto et al., 2016; Veloso et al., 2007) that would complement the field data, and to potentially reveal the 'invisible' fabric in massive lithologies that lack macroscopically discernible paleocurrent indicators (Section 5).

Magnetic susceptibility is a second-rank tensor that relates the induced magnetization of a rock linearly with the intensity of an applied magnetic field:

$$M_i = k_{ij} \times H_j$$

where $M_i$ (i = 1, 2, 3) are components of the magnetization vector, $H_j$ (j = 1, 2, 3) are components of the vector of intensity of the applied magnetic field, and $k_{ij}$ are magnetic susceptibilities (i.e., dimensionless constants of proportionality). The components $k_{11}$, $k_{22}$, $k_{33}$ are also referred to as the maximum ($k_1$), intermediate ($k_2$), and minimum ($k_3$) principal susceptibilities, respectively.

In short, several pieces of information may be retrieved from the AMS at each sampling station.

(1) The bulk susceptibility, expressed as

$$k_m = (k_1 + k_2 + k_3)/3$$

reflects the proportion and composition of mineral species in the measured rock sample and is a sum of diamagnetic, paramagnetic, and ferromagnetic components (whichever are present). Susceptibility of diamagnetic minerals (e.g., quartz, feldspar) is negative. Paramagnetic minerals, such as biotite or hornblende, have very low, slightly positive magnetic susceptibilities on the order of $10^{-5}$ to $10^{-4}$ [SI]. Ferromagnetic minerals *s.l.* (e.g., magnetite and hematite) have positive susceptibilities several orders of magnitude higher than those of paramagnetic minerals (e.g., Hrouda and Kahan, 1991). For detailed investigation of the AMS carriers, however, measurements of susceptibility variations with temperature are necessary (e.g., Hrouda, 1994).

(2) The susceptibility tensor can be geometrically represented by an ellipsoid having principal axes $k_1$, $k_2$, and $k_3$ (e.g., Hrouda, 1982; Tarling and Hrouda, 1993). The orientation of the AMS ellipsoid with respect to geographic coordinates then corresponds to the orientation of the magnetic fabric, i.e., the direction of magnetic lineation ($k_1$) and a normal (pole) to the magnetic foliation ($k_3$). The mean orientations are calculated using a method developed by Jelínek (1978) from a number of specimens at each sampling site. The

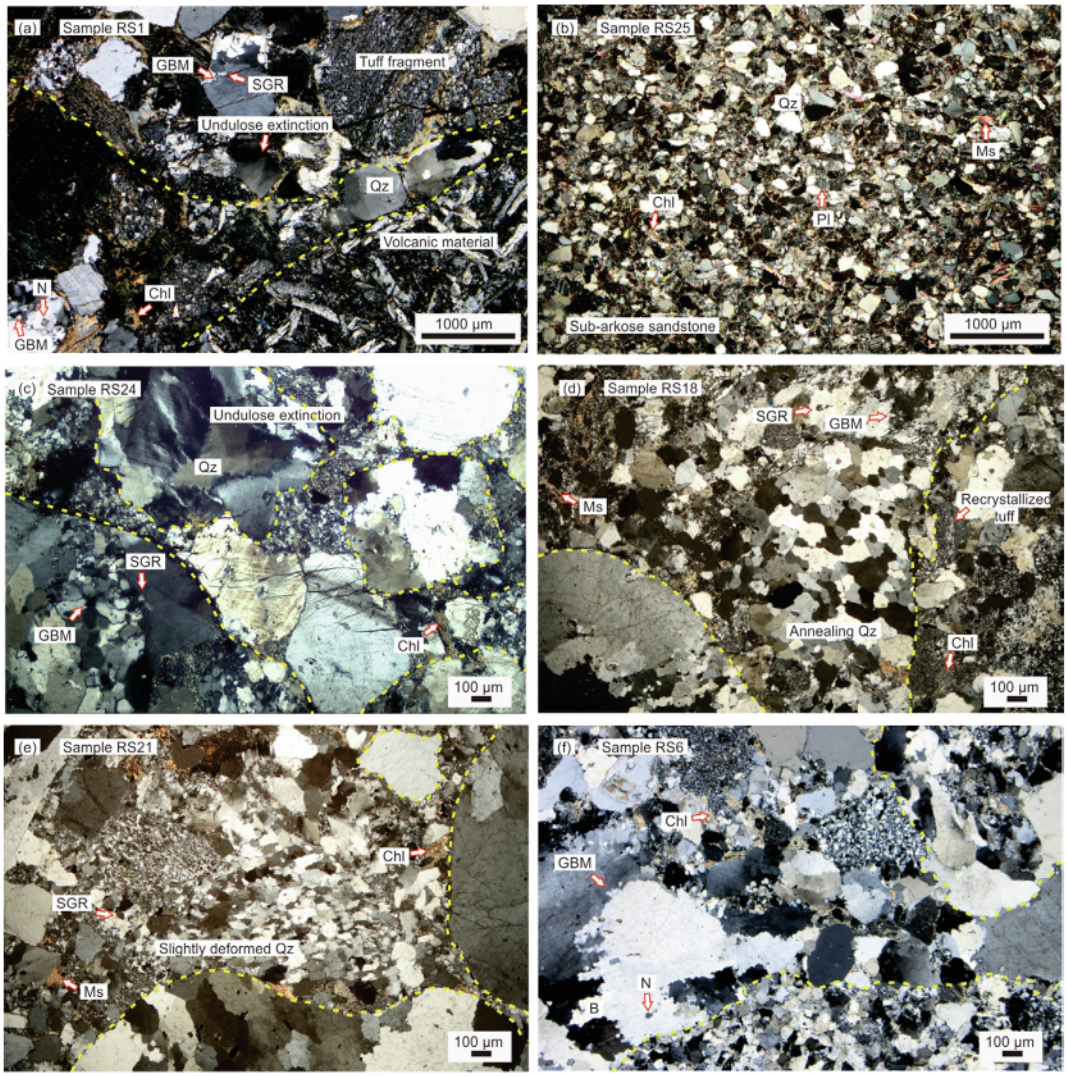


**Fig. 9.** Photomicrographs (cross polars) of conglomerates and sandstones in the Příbram–Jince basin. Yellow dashed lines outline clasts with multiple grains. Most quartz grains show undulose extinction and low- to high-temperature dynamic recrystallization. (a) Polymictic clasts with various volcanic and metamorphic grains in the Žitec–Hluboš Formation (see Fig. 5a for location). (b) Sub-arkose sandstone from the Sádek Formation with quartz embedded in a clay-rich matrix lacking undulose extinction; Bratkovice [WGS84 coordinates: N 49°44′29.404″, E 14°0′26.471″]. (c) Conglomerate sample from the Holšiny–Hořice Formation. Quartz grains have lamellae and grain to grain contact; Jezevčí skála [WGS84 coordinates: N49°42′18.539″, E13°41′55.344″]. (d–f) Polycrystalline quartz aggregates showing slight deformation. (d) Annealing resulting from grain boundary area reduction; Hradek [WGS84 coordinates: N49°48′46.26″, E14°6′28.891″]. Recrystallized tuff most abundant in the Klouček–Čenkov Formation decreases significantly in the (e) Chumava–Baština; Srážka [WGS84 coordinates: N49°42′55.868″, E13°46′50.242″] and (f) Ohrazenice formations; Koníček [WGS84 coordinates: N 49°46′33.100″, E 13°56′51.800″]. New grain (N) formed by progressive subgrain rotation (SGR). Bulging (B) resulting from grain boundary migration (GBM) that changed into a higher dislocation density. Chl = chlorite, Ms = muscovite, Pl = plagioclase, Qz = quartz. (For interpretation of the references to color in this figure legend, the reader is referred to the web version of this article.)

mean foliations and lineations are plotted on a map and summarized in stereonets to show the overall statistical orientation distribution of the principal susceptibilities.

(3) Several other statistical parameters have also been used to further describe the magnetic fabric (see review in Tarling and Hrouda, 1993, p. 17–23). Below we use the P parameter, expressed as (Nagata, 1961)

$$P = k_1/k_3.$$

Called the degree of AMS, this reflects the eccentricity of the AMS ellipsoid and thus may indicate the intensity of preferred orientation of the magnetic minerals. With some exceptions, the higher the P parameter, the stronger the preferred orientation. We also use the T parameter, expressed as (Jelínek, 1981)

$$T = 2\ln(k_2/k_3)/\ln(k_1/k_3) - 1,$$

which indicates the shape of the AMS ellipsoid. It varies from −1 (perfectly linear magnetic fabric, prolate or 'rod-shaped' ellipsoid) through 0 (transition between linear and planar magnetic fabric) to +1 (perfectly planar magnetic fabric, oblate or 'disc-shaped' ellipsoid).

### 6.2. Material and sampling strategy

The AMS samples were taken using a hand-held gasoline-powered drill at 18 stations distributed irregularly across the basin (a full list of samples is available in Supplementary Data, Tab.2). At each station, up to 10 drill cores were taken from both cross-stratified and massive lithologies. Some larger and structurally diverse outcrops were sampled in several places. In that case, the drill cores were clustered in different positions so that, if necessary, each cluster could be treated in terms of statistics as a separate

location. Orientation of bedding and cross-stratification were recorded near each cluster of drill cores. The cores were then cut into 285 standard cylindrical specimens (2.1 cm in height and 2.5 cm in diameter) in total. For each station, 7–39 specimens were taken. The specimens were measured in the Laboratory of Rock Magnetism, Institute of Geology and Paleontology, Charles University, Prague using an Agico MFK1-A Multi-function Kappabridge, which was supported by Safyr 7.0 instrument control software, and analyzed using Anisoft 5 software (written by M. Chadima, F. Hrouda, and V. Jelínek; www.agico.com). A full list of the measured AMS parameters is provided through Supplementary Data (Table 2).

### 6.3. Magnetic mineralogy

The mean (bulk) susceptibility ranges from $-10^{-3}$ to $10^{-2}$ (SI), with the highest frequency of values between $10^{-5}$ and $10^{-4}$ (Fig. 10a). About 15% of the specimens have negative (less than $10^{-7}$) susceptibility (RS15, RS21, RS36, RS45, RS50), corresponding to diamagnetic minerals. Paramagnetic ($10^{-5} \leq k_m \leq 10^{-4}$) and ferromagnetic ($k_m = 10^{-2}$) minerals carry the AMS in 74% and 2% of the specimens, respectively (Fig. 10a). Bulk susceptibility at two stations (RS45 and RS63) indicates a mixture of paramagnetic and ferromagnetic minerals.

The AMS carriers can be identified more rigorously through measurement of susceptibility variations with temperature plotted on a temperature–bulk susceptibility ($k_m$–$T$) curve. These variations were measured on 7 representative specimens using CS-L Cryostat and CS4 nonmagnetic furnace units plugged into an MFK1-A Kappabridge (Hrouda, 1994; Hrouda et al., 1997; Jelínek & Pokorný, 1997). The specimens were measured and monitored with the Cureval 8 program (www.agico.com; Hrouda et al., 1997) in three separate steps in a temperature range between −196 °C and 700 °C. The first step involved cooling to ca. −196 °C using liquid nitrogen, and subsequent heating back to room temperature of ca. 20 °C. The second step involved heating to ~700 °C, followed by immediately cooling to room temperature using argon (to prevent oxidation in minerals) at an approximate rate of 14 °C/min. The final step comprises cooling to the same temperature as the first step using liquid nitrogen.

Specimens for thermomagnetic analysis were selected as follows. Specimens RS2-1-4, RS2-3-2, RS7-1-2, RS7-2-3, RS73-1-2, and RS73-2-5 represent the most common paramagnetic massive and cross-stratified sandstones and have a bulk susceptibility of $10^{-4}$. Specimens RS2-3-2, RS7-1-2, RS7-2-3, and RS72-2-2 ($k_m = 10^{-5}$) were selected because of their medium $P$ and $T$ values. In addition, any anomaly, such as an excessively high degree of anisotropy (RS7-1-2), intermediate $P$ and slightly prolate (RS73-2-5), and an extremely low shape parameter (RS2-1-4), becomes a key characteristic for conducting the analysis.

The $k_m$–$T$ curves generally follow a hyperbolic trend (Fig. 10b). In the low temperature range, cooling curves for specimens RS2-3-2 and RS2-1-4 indicate the Verwey transition of magnetite below −150 °C. Magnetic susceptibility in the high temperature range shows a gradual increase on both the heating and cooling curves as the Curie temperature of magnetite is approached (between 520 and 560 °C). This increase in bulk susceptibility is much higher during cooling than during heating, suggesting growth of new magnetite. Magnetic susceptibility increased significantly during cooling in specimens RS73-1-2 and RS73-2-5 at a temperature of ca. 300 °C, suggesting that some ferromagnetic minerals must have been present in the rock before heating. Altogether, the thermomagnetic analyses indicate that the susceptibility is carried by paramagnetic minerals with some ferromagnetic admixture in a few cases.

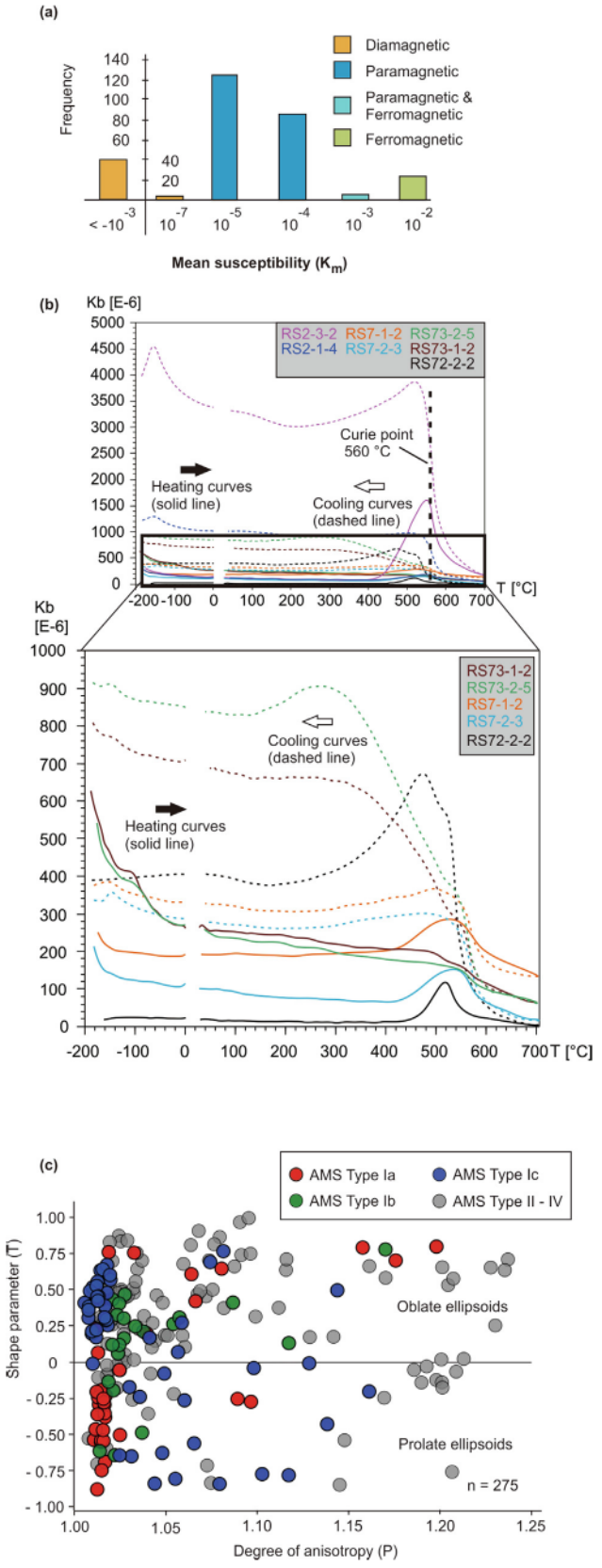


**Fig. 10.** (a) Histogram of mean (bulk) susceptibility from AMS specimens in the Příbram–Jince basin dominated with paramagnetic minerals. (b) Magnetic susceptibility variation under influence of cooling (dash lines) and heating (solid lines) in seven selected specimens. Higher magnetic susceptibility increases in the cooling processes suggest new growth of magnetite minerals (detail explanation in section 6.3. magnetic mineralogy). (c) Plot of shape parameter ($T$) versus degree of anisotropy ($P$) for all specimens. Highlighted colours represent the AMS Type I (depositional fabric).

### 6.4. Diverse magnetic fabrics in the Příbram–Jince basin

The most unexpected outcome of our analysis is that several distinct magnetic fabric types can be distinguished in the Příbram–Jince basin and that more than one fabric type may occur in a single outcrop (e.g., stations RS2 and RS7). For the purpose of this study, we classify these diverse fabrics into four end-member types (numbered here as I–IV) on the basis of orientation distribution and angular relationships of the maximum ($k_1$) and minimum ($k_3$) principal susceptibilities to bedding and/or cross-stratification (Fig. 11).

Type I fabric is the most widespread in the basin. It is characterized by strongly clustered maximum ($k_1$) and minimum ($k_3$) principal susceptibilities, a $T$ parameter scattered across both the oblate and prolate fields, and a $P$ parameter mostly not exceeding 1.15 (Fig. 10c). The Type I fabric may be further subdivided into subtypes referred to as Ia, Ib, and Ic. At two stations (RS2 and RS7), two subtypes were found in different parts of the same outcrop (distinguished as data groups).

Type Ia (data group 1 of station RS2, data group 1 of station RS7) is defined by magnetic foliations subparallel to bedding and magnetic lineations oriented down-dip or dip-oblique with respect to the cross-stratification plane (Fig. 11). This type is also characterized by a degree of anisotropy mostly less than 1.05 and by prolate AMS ellipsoids (Fig. 10c).

Type Ib (stations RS18, RS44) is represented by magnetic foliations subparallel to the bedding plane rather than the cross-stratification plane, and magnetic lineations showing a transition between clustered and girdle-like orientation distributions along the bedding/foliation plane (Fig. 11). Magnetic lineations thus tend to lie closer to the bedding plane than to the cross-stratification plane. Scalar fabric parameters indicate a transition from prolate to oblate shapes of the AMS ellipsoid ($-0.6 \leq T \leq 0.5$) and a low degree of anisotropy ($P$ = 1.02–1.17).

When cross-stratification is absent (stations RS36, RS50, RS21, RS73, RS25, RS9), we distinguish Subtype Ic since it is impossible to evaluate the relationship of the magnetic fabric to the internal bed structure (Fig. 11). Nevertheless, magnetic foliations vary from bedding-parallel to slightly bedding-oblique, while magnetic lineations are likewise oriented parallel and oblique to the bedding plane. This subtype exhibits a wide range of fabric parameters, but it is dominated by oblate AMS ellipsoids and a low degree of anisotropy (less than 1.05).

The Type I fabric is considered a depositional fabric (e.g., Rees and Woodall, 1975; Tarling and Hrouda, 1993).

In the Type II fabric, magnetic foliations are still sub-parallel to bedding/cross-stratification, but magnetic lineations scatter widely within or close to the bedding/cross-stratification plane. On a stereonet, the foliation data points are clustered close to the pole of the bedding/cross-stratification plane, whereas the lineation data points show a girdle-like orientation distribution along the great circle for bedding/cross-stratification. Oblate ($0.06 < T < 0.9$) AMS ellipsoids and low to moderate degrees of anisotropy (P between 1.0 and 1.7) are associated with this fabric

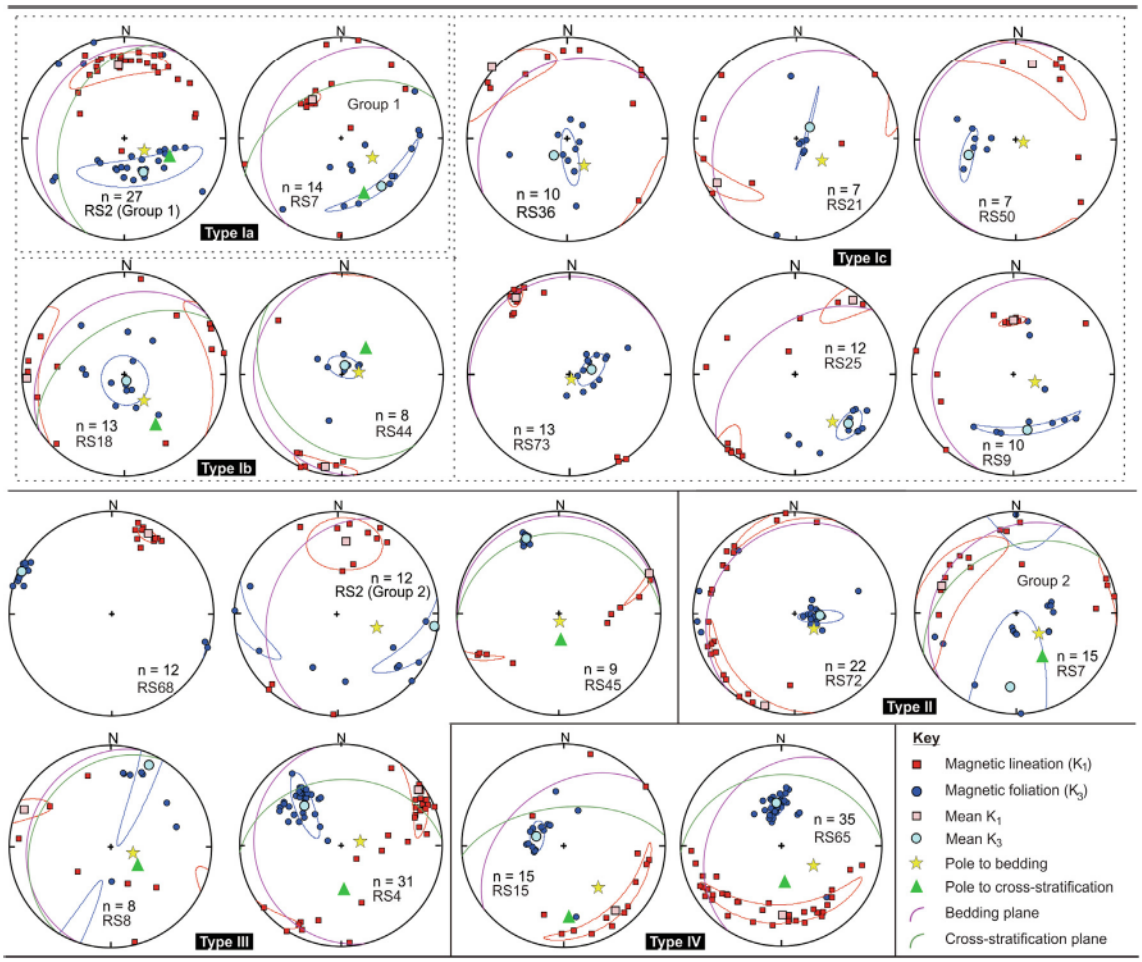


**Fig. 11.** Orientation of maximum (red squares) and minimum (blue circles) principal susceptibilities in sandstone of the Příbram–Jince basin, categorized into four different types. (For interpretation of the references to color in this figure legend, the reader is referred to the web version of this article.)

type. The Type II fabric likely records compaction strain (flattening) during burial (e.g., Hrouda et al., 2009).

The Type III fabric is characterized by steep, ~N–S to ~NE–SW-striking magnetic foliations that are at a high angle to the bedding and associated with subhorizontal magnetic lineations lying close to the bedding plane. On a stereonet, the data points for both foliations and lineations are strongly clustered. The *P* parameter ranges widely between 1.01 and 2.3 (station RS45), as does the shape parameter *T*, exhibiting both oblate and prolate AMS ellipsoids (*T* = −0.7–0.9). These characteristics suggest that Type III is a tectonic fabric (Callot et al., 2010; Parés, 2015; Parés et al., 1999; Saint-Bezar et al., 2002), closely corresponding to the regional Variscan cleavage and stretching lineation in ductile deformed domains (Casas and Murphy, 2018; Stephan et al., 2016; Žák et al., 2013).

In the Type IV fabric, both magnetic foliations and lineations are clustered at a high angle to bedding, while the $k_1$ data points plot close to the pole to bedding and cross-stratification on a stereonet. Type IV fabric is associated with a high degree of anisotropy (P = 1.3–1.5) and both oblate (0.6; RS65) and prolate (-0.37; RS15) AMS ellipsoids, and is an example of inverse magnetic fabric (e.g., Černý et al., 2020; Chadima et al., 2009; Usui et al., 2019).

### 6.5. Paleocurrent directions inferred from magnetic fabric

It is apparent from the analysis presented above that of the four magnetic fabric types found in the Příbram–Jince basin, only Type I can be used to infer paleocurrent directions. At each station where Type I fabric was detected, we applied the same approach used for the mesoscopic paleocurrent indicators. The mean magnetic lineations were rotated to horizontal about a rotation axis represented by the strike of the bedding through an angle equal to the dip of the bedding. The rotated paleocurrent directions derived from the AMS were then plotted in map view and presented as rose diagrams. The mesoscopic paleocurrent indicators are also shown for comparison (Fig. 12).

It should be noted that interpretation of the magnetic lineations is not as straightforward as that of mesoscopic paleocurrent indicators. First, in cases where lineations are subhorizontal and scattered more or less symmetrically about opposite trends, the calculated site-mean lineation, and thus the inferred paleocurrent direction, may be strongly affected by the statistical distribution of individual specimens and may easily flip by ~180°. Second, fine-grained magnetic particles may align systematically either parallel or perpendicular to flow lines during deposition, depending on the velocity gradient and depositional mechanism (e.g., Rees, 1965, Rees and Woodall, 1975; Taira and Scholle, 1979; Stachowska et al., 2020 and references therein). Hence, the AMS-derived paleocurrent directions must be interpreted with caution.

In the Příbram–Jince basin, the paleocurrent directions inferred from the magnetic lineations in most cases show a good match with those obtained from mesoscopic cross-stratification. In succession 1 (the Žitec–Hluboš Formation), the cross-stratification indicates a paleocurrent toward the ~NW, whereas the magnetic lineation points to the ~NE (station RS2; Figs. 11, 12). In the overlying succession 2 (the Sádek Formation), the mesoscopic paleocurrent directions point to the ~N to ~NNW in agreement with the magnetic lineations, which point to NNW to NW. An exception is the magnetic lineation at station RS25 (Fig. 12), which points to the SE (i.e., away from the basin) and may be a case of the statistical 'flip' effect mentioned above. In succession 3, the inferred paleocurrent directions are more varied, as are the magnetic lineations. At station RS44 (the Holšiny–Hořice Formation), the lineation is perpendicular to the cross-stratification, but both point in directions away from the basin. At station RS9 (same formation), the magnetic lineation points to the ~NE in agreement with the mesoscopic indicators, whereas in the Klouček–Čenkov Formation it points in exactly the opposite direction to the inferred paleocurrent (to the ~SE; Fig. 12). In succession 5 in the northwestern corner of the basin (stations RS21, RS36, RS50; Chumava–Baština and Ohrazenice formations), where mesoscopic paleocurrent indicators were absent, the magnetic lineations point in various directions (NE, E, SSE) but consistently into the basin (Fig. 12).

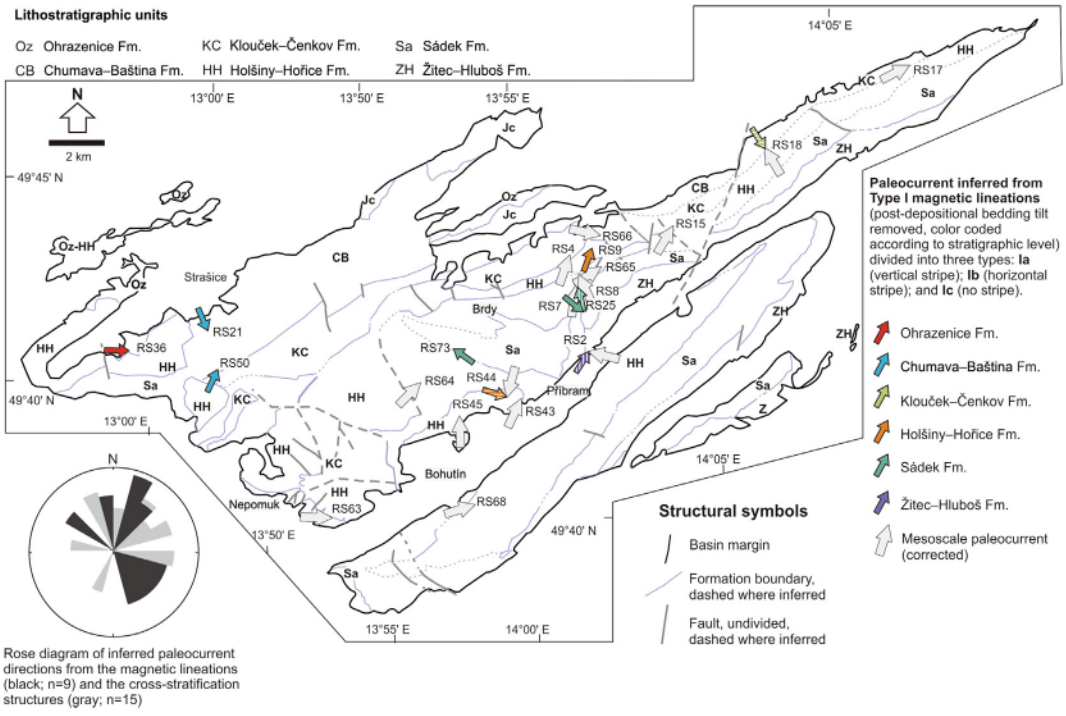


**Fig. 12.** Map of paleocurrents inferred from cross-stratification and magnetic lineations (Type I interpreted as depositional fabric).

## 7. Discussion

### 7.1. Sediment sources in the Příbram–Jince basin

As documented by clast compositions, the sediment sources in the middle Cambrian Žitec–Hluboš Formation (ca. 515 Ma) came from a volcanic arc and metamorphic basement (Fig. 4), with the source area presumably located to the ~ESE of the basin as inferred from the paleocurrent and AMS data (Figs. 8 and 12). The metamorphic sources were also reflected in the clast microstructures, with prevailing low- to high-temperature dynamic recrystallization (Fig. 9). Moreover, the published detrital zircon ages reveal that the Žitec–Hluboš Formation involved Paleoproterozoic, Neoproterozoic, and Cambrian detritus (Drost et al., 2011). The eroded material was transferred to the Příbram–Jince basin by debris flows to form alluvial fans in succession 1 that filled in the isolated depocenters in the southeastern part of the basin. The clast size indicates that they had traveled a short distance. The distal part of the alluvial fans, however, reached the main basin area (see Fig. 3), towards which the clasts become progressively smaller in size.

Subsequently (at 512 ± 5 Ma), medium- to fine-grained sediments were deposited in flood plains or braid plains (Sádek Formation), sourced from the ~SSE (transport to the ~NNW; Fig. 8). These sediments were presumably derived from a local source as shown by their sub-arkose dominated composition (Fig. 9b) and by detrital zircon ages that increasingly indicate Neoproterozoic detritus (Hajná et al., 2018). Based on the sediment distribution, the basin was almost entirely inundated by rivers except its northern part.

The deposition in succession 3, especially of the Holšiny–Hoř ice Formation (ca. 511 ± 3 Ma), is marked by a major change in the sedimentary source. The distribution of sediments in succession 3 was dominated by a fluvial distributary system (e.g., Nichols and Fisher, 2007) as axial channel belts (e.g., Gawthorpe and Leeder, 2000), interrupted by a local and short-lived brackish environment (represented by the Paseky shales). This river system, however, flowed obliquely to the underlying alluvial fan axes. A different source is indicated by a change in clast composition from unstable volcanic arc material to stable material entirely dominated by quartz and chert in the upper part of the succession (cross-section in Fig. 4 and microstructures in Fig. 9). The fluvial lithofacies in succession 3 were frequently disturbed by the fine-grained sheetflood fans (F3). The dominant paleocurrent, interpreted from mesoscale features and AMS, flowed from the western part of the basin towards the basin axis (Fig. 12), with the clasts becoming smaller to the ~NE. This re-adjustment of paleocurrent direction provides an independent argument for a change of the source area from that in the ~SE to a new one in the ~SW and ~W. This change is also demonstrated by the increasing proportion of Cambrian detrital zircon ages, which is twice that in the underlying succession (Hajná et al., 2018), perhaps as a result of faulting and recycling of some older parts of Cambrian volcano-sedimentary successions.

The Sádek and Holšiny–Hořice formations are the thickest and most areally extensive within the basin, following which the thickness of the basin fill gradually decreased (between 511 ± 3 and 510 ± 2 Ma; Hajná et al., 2018). Conversely, volcanic activity was at its peak during deposition of the overlying Klouček–Čenkov Formation, as shown by numerous recrystallized tuff grains (Fig. 2b and 9). This suggests that subsidence gradually decelerated and that the volcanic activity only occurred over a short time interval.

The conglomerates in succession 5 (Chumava–Baština and Ohrazenice formations) are again the product of alluvial fan deposition that were sourced from the ~W and ~NW. These conglomerates were interrupted periodically by sheetflood fans and, in part, were mixed with fluvial sandstones (see lithofacies distribution in Fig. 3). Interestingly, in the Chumava–Baština Formation, Neoproterozoic detrital zircon overwhelms the Cambrian detritus with a minor contribution from the Archean and Paleoproterozoic (Drost et al., 2011). Subsequently, the portion of the Cambrian detritus increased almost twofold in the overlying Ohrazenice Formation (499 ± 10 Ma; Drost et al., 2011). The sediment (and detrital zircon) transport was from the ~NW and ~SW toward the basin interior (Fig. 12).

Marine transgression occurred in succession 4 (ca. 506–503 Ma) and presumably flooded the basin above the Klouček–Čenkov Formation as depicted by the bi-directional cross-stratification (Fig. 5d).

The last volcanic activity in Cambrian was represented by the Strašice volcanic complex, which covered the NW part of the basin with subaerial, mostly andesitic lavas at ca. 500–485 Ma. The volcanism was presumably as a result of more intense rifting as shown by its alkaline composition (Štorch et al., 1993).

### 7.2. Tectonic evolution of the Příbram–Jince basin

We suggest that the above-described changes in provenance and depositional settings record changes in the tectonic regime during deposition. The tectonic regime also likely controlled the basin fill thickness and *syn*-depositional volcanic activity. We interpret the basin to have evolved kinematically in two main phases.

The first phase (at around 515 Ma) involved gravel accumulation in the SE with the basin fill younging toward the NW. We envision that small SE-side-up displacements along unconnected NE–SW-trending normal faults initially created fault scarps with river incision and thus several alluvial-fan depocenters. These faults propagated laterally and linked to form a master fault rimming the southeastern margin of the basin, now largely obscured by the Central Bohemian Plutonic Complex (Fig. 1d). Based on parallelism of the basin axis with lithotectonic belts in the underlying Cadomian basement (Fig. 1d), the initial normal faults and the master fault likely reactivated pre-existing tectonic boundaries and were active from ca. 515 Ma onwards (Fig. 13).

This first phase is interpreted to have been followed by a short period of tectonic quiescence (at around 512 Ma) as indicated by the abrupt change from gravel to the fine-grained basin fill represented by the areally extensive Sádek Formation (Fig. 13). Subsequently, faulting became active again and created a northwesterly facing half-graben system. The geometry of the basin fill and the location of depocentres suggest that the first stage of basin evolution was mainly controlled by NW–SE extension, roughly perpendicular to the basin axis (Fig. 13a, b; low obliquity rifting of Duclaux et al., 2020).

In our view, the major change in source area and in sediment transport from basin-axis-oblique (from the SE) to basin-axis-parallel (from SW or W) marks a major switch in the tectonic regime that controlled the basin evolution from ca. 511 Ma onwards (Fig. 13c). Together, the dominance of large quartz and chert pebbles at higher stratigraphic levels, the renewed alluvial fan deposition, and the inferred paleocurrent directions imply significant uplift of the local Cadomian basement to the SW and W of the basin (Fig. 13c). Hence, we suggest that the basin-axis-oblique, NW–SE-trending series of *syn*-sedimentary normal faults now bounding the southwestern end of the basin (Fig. 1c) were initiated and became a major feature during this second phase of basin development (Fig. 13c), although they were likely multiply reactivated in post-Cambrian times.

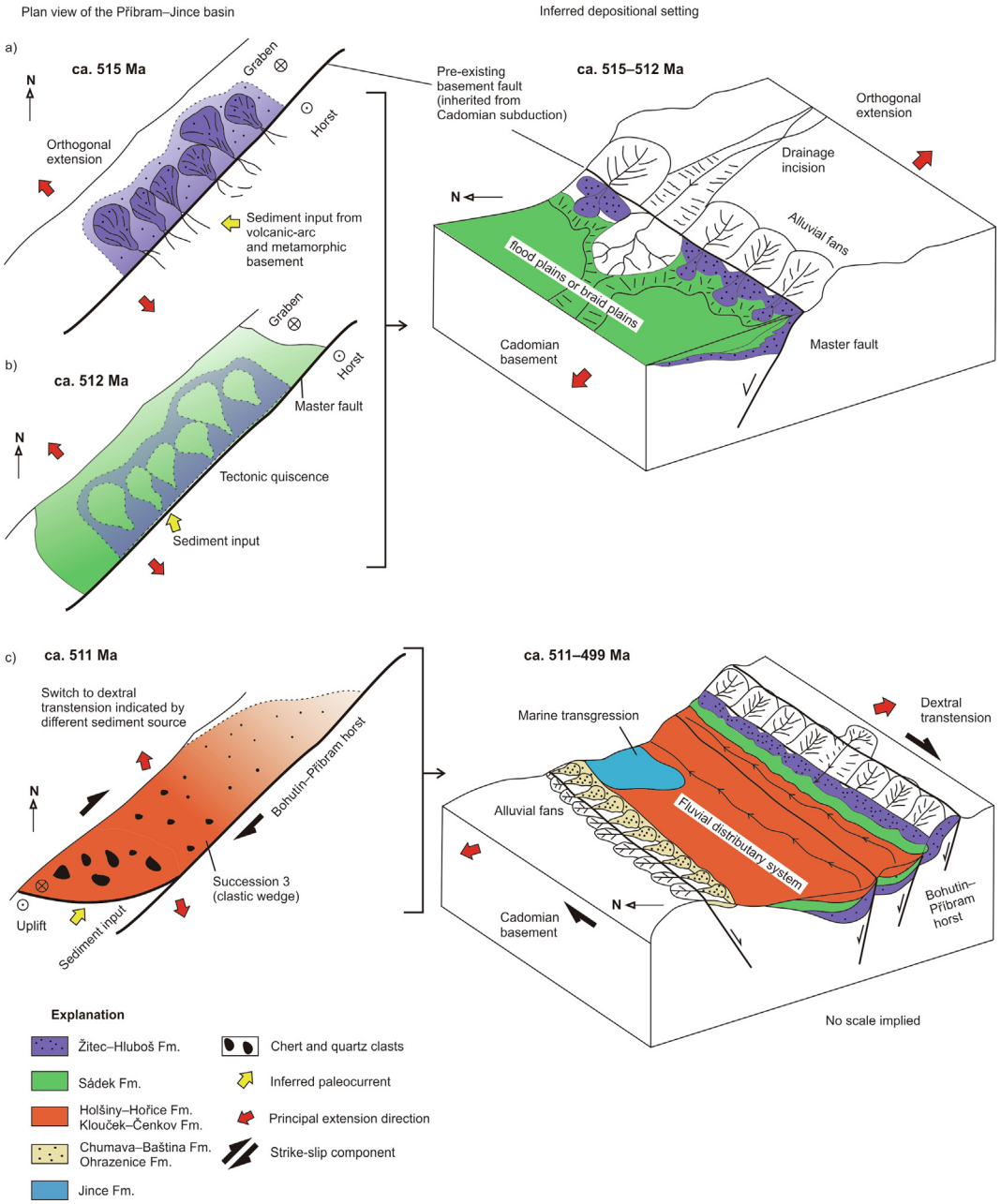


**Fig. 13.** A model of tectono-sedimentary evolution of the Příbram–Jince basin. (a) Map view showing changes in source areas, basin infill, and fault kinematics from orthogonal extension to dextral transtension. (b) Interpretation of depositional environment controlled by normal faulting.

At the same time, we propose that net displacement along the southeasterly master fault increased, leaving behind the Bohutín–Příbram zone as a NE–SW-trending horst (Havlíček, 1971; Fig. 2 and Fig. 13). The horst controlled deposition of succession 3, interpreted as deposited by an axial river, which frequently changed its course by avulsion as reflected by cross-stratifications developed during lateral accretion (see log profile; Fig. 7). The axial river produced a clastic wedge fining and pinching out toward the NE (Fig. 13c). We therefore assume that the fault bounding the Bohutin–Příbram zone had an oblique dip-slip or scissor-like displacement, increasing to the SW.

Finally, a minor normal fault in the NW controlled deposition of the alluvial fan conglomerates and sandstones in the Chumava–Baština Formation at around 510 ± 2 Ma. During this period, the basin continued to subside until a short-lived marine transgression (the Jince Formation) occurred at ca. 506–503 Ma. Subsequently, an uplifted highland probably sourced the Ohrazenice Formation in the NW of the basin.

Taken together, the geometry of the basin fill and the inferred fault geometry and kinematics suggest that the Příbram–Jince basin developed as a dextral transtensional pull-apart basin with multiple depocenters and increasing obliquity of rifting (Fig. 13; e.g., Wu et al., 2009, Duclaux et al., 2020, Autin et al., 2013, Brune et al., 2018, Farangitakis et al., 2021).

### *7.3. Cambrian sedimentary basins as precursors for opening the Rheic Ocean*

The above-developed model for the Příbram–Jince basin provides a background for comparison with other Cambrian basins along the former Avalonian–Cadomian belt. These basins represent a prelude to the opening the Rheic Ocean in the early Ordovician by

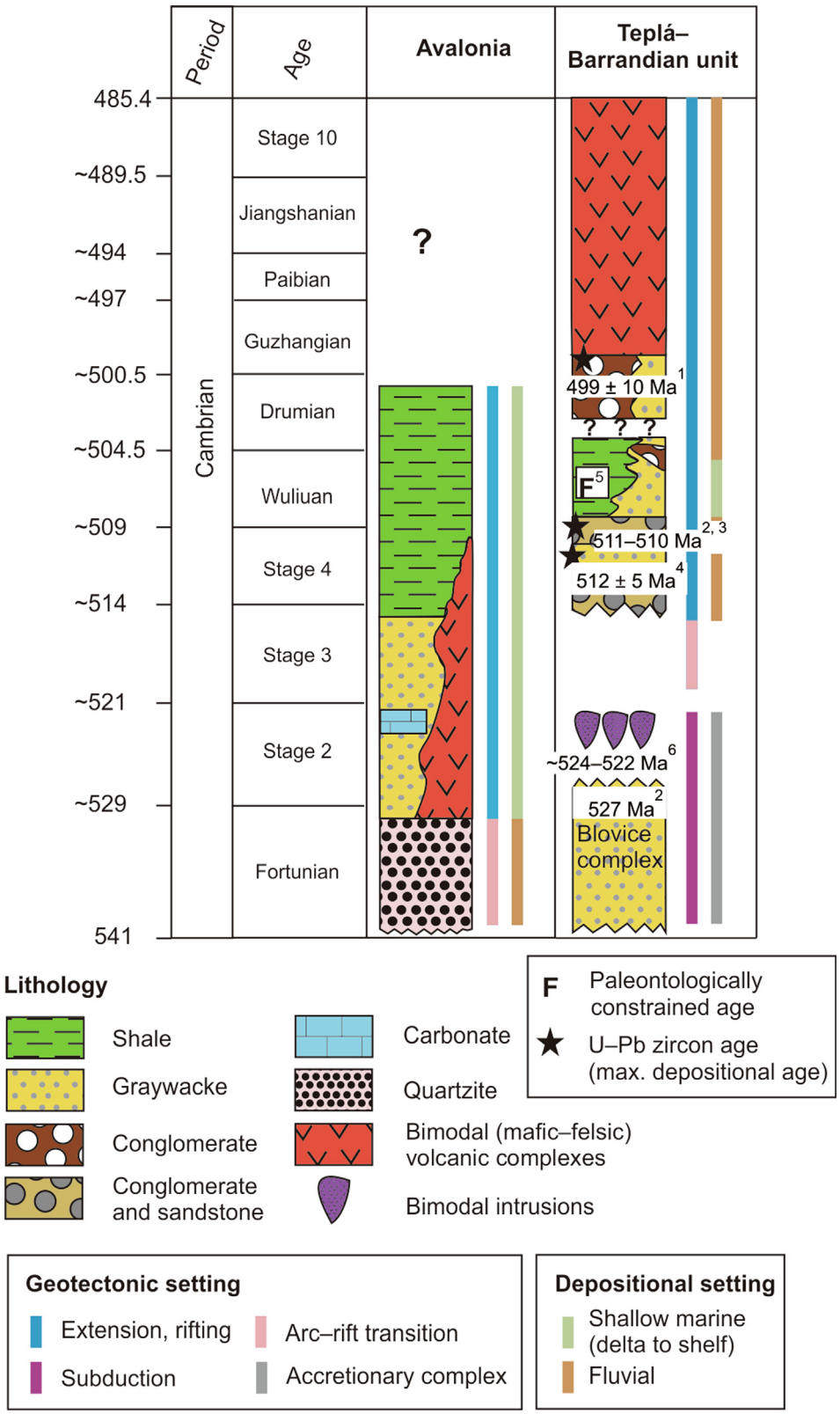


**Fig. 14.** (a) Tectono-stratigraphy of Avalonia (Nance et al., 2002, 2008) and Teplá–Barrandian unit during the Cambrian. Note difference in volcanic deposits and marine deposits indicating diachronous rifting in both terranes. Ages compiled from (1) Drost et al. (2004), (2) Drost et al. (2011), (3) Hajná et al. (2017), (4) Hajná et al. (2018), (5) Fatka and Szabad (2014), (6) Zulauf et al. (1997).

the rift–drift transition of Avalonia (e.g., Cocks et al., 1997; Murphy et al., 1999a; Nance et al., 1991; Pollock et al., 2009; Prigmore et al., 1997), and are thus key features to understand the Early Paleozoic paleogeography of Gondwana and the development of its northern passive margin. The crucial issue is whether the evolution of these basins was similar or different in the western and eastern parts of

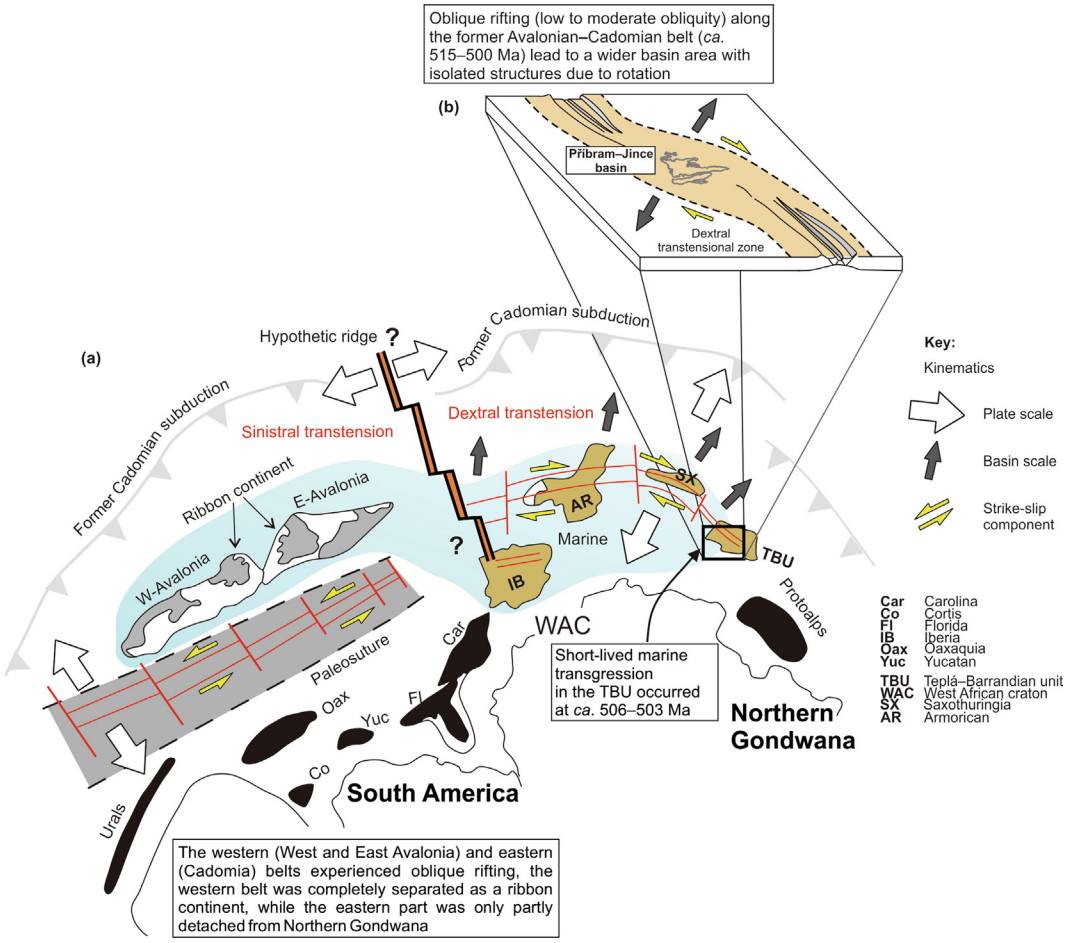


**Fig. 15.** (a) A tentative plate-tectonic reconstruction of the *peri*-Gondwana terranes during the Cambrian (*ca.* 515–500 Ma; modified from Keppie et al., 2003; Murphy and Nance, 1989; Murphy et al., 1999a,b; Gutiérrez-Alonso et al., 2003, Nance et al., 2008; and Linnemann et al., 2008, 2014). Inherited Neoproterozoic suture (after Murphy et al., 2006) is thought to have facilitated complete rifting in Avalonia. Lacking a paleosuture, the extended Cadomian terranes remained attached to the northern Gondwana margin. The kinematics of Avalonia separation has been debated. Here we examine a more complex scenario for opposing kinematics along the western and eastern segments of the former Avalonian–Cadomian belt separated by a hypothetic ridge (after Nance et al., 2002; Keppie et al., 2003, 2008; Sánchez-García et al., 2008). (b) Dextral transtension led to incipient rifting and development of a wide *peri*-Gondwanan shelf in the paleo-east (adopted from Duclaux et al., 2020). Except for the Teplá–Barrandian unit, which experienced only a short-lived marine transgression between ca. 506–503 Ma, a marine platform had already covered the other Cambrian basins.

the belt, since these two regions likely experienced different amounts of separation from Gondwana during the Ordovician (e.g., Robardet, 2003; Servais and Sintubin, 2009; Romer and Kroner, 2019; Stephan et al., 2019a, b).

For this comparison, we selected two lithotectonic units (often referred to as terranes) that are perhaps the best documented and well understood: Avalonia and the Teplá–Barrandian unit (part of Cadomia or Armorican Terrane Assemblage in some models; Tait et al., 2000). From their lithostratigraphy, tectonic setting and magmatism (Fig. 14), it can be seen that Avalonia and Cadomia differ significantly in their Cambrian evolution. Following the termination of subduction at around 540 Ma, Avalonia was overlain by a Cambrian marine platform sequence, only the basal part of which (ca. 540–530 Ma) comprises fluvial deposits (Fig. 14). In contrast, the Teplá–Barrandian unit recorded Cadomian subduction until ca. 527–524 Ma (Hajná et al., 2018). After a pulse of granitic plutonism, perhaps due to slab-breakoff, the Příbram–Jince basin was initiated at ca. 515 Ma and was filled with a thick package of alluvial and fluvial deposits (Fig. 14). Furthermore, bimodal volcanic activity was recorded in Avalonia throughout the Cambrian, whereas in the Teplá–Barrandian unit it was delayed and short-lived, lasting only from ca. 500 Ma to 485 Ma (Fig. 14).

The major differences between the Avalonian and Cadomian terranes in their Cambrian evolution were attributed by Mallard and Rogers (1997) and Murphy et al. (2006) to different tectonic inheritance, westerly Avalonia being rifted off from the previously accreted ca. 1.3–1.0 Ga juvenile crust, whereas easterly Cadomia was in contact with older, Paleoproterozoic (ca. 2.2–2.0 Ga) West African cratonic basement. In the former case, the presumed Neoproterozoic suture represented significant rheological weakness and facilitated complete separation of Avalonia from the Amazonian craton. Conversely, a similar paleosuture was absent in Cadomia and thus the rifting likely failed to form a (hyper-) extended continental shelf (Fig. 15; e.g., Romer and Kroner, 2019; Žák and Sláma, 2018).

The above inferences corroborate that the Rheic Ocean opened from west to east in a scissor-like manner by oblique rifting (e.g., Linnemann et al., 2008). However, the kinematics of this major rifting event still remains poorly understood, largely because extrapolating kinematics from local to plate scale is often not straightforward. For instance, kinematic data from Avalonia (Nova Scotia) suggest that both sinistral (Nance and Murphy, 1990) and dextral (Murphy and Hynes, 1990) strike slip were operative locally. However, on a large scale, Keppie et al. (2003) suggest the kinematics required to move Avalonia from Amazonia to Laurentia mandate a component of sinistral displacement during and following the rift–drift phase that opened the Rheic Ocean (see also Nance et al., 2008 and their Fig. 13). In contrast, Linnemann et al.

(2008) inferred dextral transtension for the Saxothuringian and Ossa Morena zones. Moreover, Zulauf and Helferich (1997) and Zulauf et al. (1997) also described dextral movements in a middle to upper continental crust of Teplá–Barrandian unit. This is being in agreement with our present study on the Příbram–Jince basin, which must have been located near the easterly tip/hinge of the opening rift.

The potentially opposing kinematics of the westerly and easterly segments of the Avalonian–Cadomian belt are difficult to reconcile with a simple, all-embrasive model for the opening of the Rheic Ocean. Yet, this conundrum may be overcome by incorporating and refining the model. For instance, Nance et al. (2002), Keppie et al. (2003, 2008), and Sánchez-García et al. (2008) postulated ridge–transform–trench interaction to explain the end of Cadomian subduction and its conversion to a passive margin during the Cambrian (see also Hajná et al., 2018). Adopting this model (Fig. 15), the mid-ocean ridge may have intersected Gondwana's northern margin at an angle and separated the contrasting segments. In this scenario, as spreading continued, the Avalonian part of the belt would experience sinistral kinematics while the Cadomian part underwent dextral movement. Furthermore, the oblique angle between the spreading ridge axis and the Avalonian continental margin would facilitate a larger magnitude of extension whereas the angle with Cadomia is more compatible with prevailing strike-slip and limited continental separation (Fig. 15). If, however, displacement during and following the rift–drift transition in Avalonia had a dextral component, as implied by Nance et al. (2002) and, more recently, by the plate reconstructions of van Staal et al. (2021), no intervening ridge would be required and a simpler, dextral model would account for the opening of the Rheic Ocean in which the kinematics of Cadomia continued westward into Avalonia with regional variations likely linked to the curvature of the margin.

If either of these inferences is correct, however, the presence of both an inherited paleosuture and a suitably oriented subducted ridge may have controlled the opening of the Rheic Ocean, leading to a rift–drift transition in Avalonia, but only to failed rifting in the eastern Cadomian segment during the late Cambrian to early Ordovician.

## 8. Conclusions

We propose the following basin history to explain the tectonostratigraphic evolution of the Příbram–Jince basin and the formation of the Avalonian ribbon continent.

1. Cadomian subduction in the Teplá–Barrandian unit ceased at ca. 527 Ma. Following bimodal magmatism at ca. 524–522 Ma, an extensional phase in the Příbram–Jince basin initiated basin infilling between ca. 515–499 Ma, accompanied by depocenter changes, rapid subsidence, and a short-lived marine transgression at ca. 506–503 Ma.
2. Bimodal volcanic activity during Avalonian rifting lasted for at least 20 m.y., whereas initial rifting in the Příbram–Jince basin was delayed and followed by magmatism lasting ca. 15 m.y.
3. Microstructures and detrital zircons indicate that the basin was initially sourced from pre-Cambrian volcanic arcs and metamorphic basement. Higher stratigraphic levels of the basin were supplied from an uplifted local source.
4. Paleocurrent data from mesoscale cross-stratification and AMS measurements suggest dynamic sediment source redirection from ~ESE to ~SW. These changes were related to the onset of dextral transtension in response to oblique rifting at ca. 511 Ma.
5. At ca. 515–500 Ma, the Příbram–Jince basin (and Teplá–Barrandian unit) occupied the rift-tip during initial rifting of the Rheic Ocean. At the same time, Avalonia left northern Gondwana as a ribbon continent. Avalonia's inherited suture played a significant role in the successful separation of the ribbon continent, followed by continental slicing due to oblique rifting. Breakup was likely initiated by the change from active to passive margin.

## CRediT authorship contribution statement

**Reza Syahputra:** Conceptualization, Investigation, Writing - original draft, Writing - review & editing. **Jiří Žák:** Conceptualization, Investigation, Writing - original draft, Writing - review & editing. **R. Damian Nance:** Conceptualization, Investigation, Writing - review & editing.

## Declaration of Competing Interest

The authors declare that they have no known competing financial interests or personal relationships that could have appeared to influence the work reported in this paper.

## Acknowledgements

We gratefully acknowledge the contribution of two anonymous reviewers and Andrea Festa for careful editorial handling. We also would like to acknowledge funding from the Grant Agency of the Charles University (GAUK) through grant No. 952220 (to Reza Syahputra) and from the Charles University projects PROGRES Q45 and Center for Geosphere Dynamics (UNCE/SCI/006). Oldřich Fatka, Václav Kachlík, and Brendan Murphy are thanked for discussions.

## Appendix A. Supplementary material

Supplementary data to this article can be found online at https://doi.org/10.1016/j.gr.2021.10.004.

## References

Allen, J.R.L., 1973. Features of cross-stratified units due to random and other changes in bed forms. Sedimentology 20, 189–202.
Autin, J., Bellahsen, N., Leroy, S., Husson, L., Beslier, M.O., d'Acremont, E., 2013. The role of structural inheritance in oblique rifting: Insights from analogue models and application to the Gulf of Aden. Tectonophysics 607, 51–64.
Babcock, L.E., Peng, S.C., Brett, C.E., Zhu, M.Y., Ahlberg, P., Bevis, M., Robison, R.A., 2015. Global climate, sea level cycles, and biotic events in the Cambrian Period. Palaeoworld 24, 5–15.
Ballèvre, M., Fourcade, S., Capdevila, R., Peucat, J.J., Cocherie, A., Fanning, C.M., 2012. Geochronology and geochemistry of Ordovician felsic volcanism in the Southern Armorican Massif (Variscan belt, France): implications for the breakup of Gondwana. Gondwana Res. 21, 1019–1036.
Blair, T.C., 2000. Sedimentology and progressive tectonic unconformities of the sheetflood-dominated Hell's Gate alluvial fan, Death Valley, California. Sed. Geol. 132, 233–262.
Blenkinsop, T., 2000. Deformation microstructures and mechanisms in minerals and rocks. Kluwer Academic Publishers, Dordrecht.
Borradaile, G., Henry, B., 1997. Tectonic applications of magnetic susceptibility and its anisotropy. Earth Sci. Rev. 42, 49–93.
Borradaile, G.J., Jackson, M., 2004. Anisotropy of magnetic susceptibility (AMS): magnetic petrofabrics of deformed rocks. Geological Society, London, Special Publications 238, 299–360.
Borradaile, G.J., Jackson, M., 2010. Structural geology, petrofabrics and magnetic fabrics (AMS, AARM, AIRM). J. Struct. Geol. 32, 1519–1551.
Bouchez, J.L., 1997. Granite is never isotropic: an introduction to AMS studies of granitic rocks. In: Bouchez, J.L., Hutton, D.H.W., Stephens, W.E. (Eds.), Granite: From segregation of melt to emplacement fabrics. Kluwer Academic Publishers, pp. 95–112.
Brune, S., Williams, S.E., Müller, R.D., 2018. Oblique rifting: the rule, not the exception. Solid Earth 9, 1187–1206.
Callot, J.P., Robion, P., Sassi, W., Guiton, M.L.E., Faure, J.L., Daniel, J.M., Mengus, J.M., Schmitz, J., 2010. Magnetic characterisation of folded aeolian sandstones: Interpretation of magnetic fabrics in diamagnetic rocks. Tectonophysics 495, 230–245.
Casas, J.M., Murphy, J.B., 2018. Unfolding the arc: The use of pre-orogenic constraints to assess the evolution of the Variscan belt in Western Europe. Tectonophysics 736, 47–61.

Cawood, P.A., 2005. Terra Australis Orogen: Rodinia breakup and development of the Pacific and Iapetus margins of Gondwana during the Neoproterozoic and Paleozoic. Earth Sci. Rev. 69, 249–279.
Černý, J., Melichar, R., Všianský, D., Drahokoupil, J., 2020. Magnetic anisotropy of rocks: A new classification of inverse magnetic fabrics to help geological interpretations. J. Geophys. Res. Solid Earth 125, e2020JB020426.
Chadima, M., Cajz, V., Týcová, P., 2009. On the interpretation of normal and inverse magnetic fabric in dikes: examples from the Eger Graben, NW Bohemian Massif. Tectonophysics 466, 47–63.
Chlupáč, I., Havlíček, V., 1965. Kodymirus n. g. a new aglaspid merostome of the Cambrian of Bohemia. J. Geol. Sci. Paleont. 6, 7–20.
Chlupáč, I., Kraft, J., Kraft, P., 1995. Geology of fossil sites with the oldest Bohemian fauna (Lower Cambrian, Barrandian area). J. Czech Geol. Soc. 40, 1–8.
Cocks, L.R.M., McKerrow, W.S., van Staal, C.R., 1997. The margins of Avalonia. Geol. Mag. 134, 627–636.
Crowley, Q.G., Floyd, P.A., Winchester, J.A., Franke, W., Holland, J.G., 2000. Early Palaeozoic rift-related magmatism in Variscan Europe: fragmentation of the Armorican Terrane Assemblage. Terra Nova 12, 171–180.
Dalziel, I.W.D., 1997. Neoproterozoic-Paleozoic geography and tectonics: Review, hypothesis, environmental speculation. Geol. Soc. Am. Bull. 109, 16–42.
Davy, B., Hoernle, K., Werner, R., 2008. Hikurangi Plateau: Crustal structure, rifted formation, and Gondwana subduction history. Geochem. Geophys. 9, Q07004.
Díez Fernández, R., Castiñeiras, P., Gómez Barreiro, J., 2012. Age constraints on Lower Paleozoic convection system: Magmatic events in the NW Iberian Gondwana margin. Gondwana Res. 21, 1066–1079.
Dörr, W., Zulauf, G., Fiala, J., Franke, W., Vejnar, Z., 2002. Neoproterozoic to Early Cambrian history of an active plate margin in the Teplá-Barrandian unit - a correlation of U-Pb isotopic-dilution-TIMS ages (Bohemia, Czech Republic). Tectonophysics 352, 65–85.
Drost, K., Linnemann, U., McNaughton, N., Fatka, O., Kraft, P., Gehmlich, M., Tonk, C., Marek, J., 2004. New data on the Neoproterozoic-Cambrian geotectonic setting of the Teplá-Barrandian volcano-sedimentary successions: geochemistry, U-Pb zircon ages, and provenance (Bohemian Massif, Czech Republic). Int. J. Earth Sci. 93, 742–757.
Drost, K., Gerdes, A., Jeffries, T., Linnemann, U., Storey, C., 2011. Provenance of Neoproterozoic and early Paleozoic siliciclastic rocks of the Teplá-Barrandian unit (Bohemian Massif): evidence from U-Pb detrital zircon ages. Gondwana Res. 19, 213–231.
Duclaux, G., Huismans, R.S., May, D.A., 2020. Rotation, narrowing, and preferential reactivation of brittle structures during oblique rifting. Earth Planet. Sci. Lett. 531, 12.
Etxebarria, M., Chalot-Prat, F., Apraiz, A., Eguíluz, L., 2006. Birth of a volcanic passive margin in Cambrian time: rift paleogeography of the Ossa-Morena Zone, SW Spain. Precambr. Res. 147, 366–386.
Farangitakis, G.P., McCaffrey, K.J.W., Willingshofer, E., Allen, M.B., Kalnins, L.M., van Hunen, J., Persaud, P., Sokoutis, D., 2021. The structural evolution of pull-apart basins in response to changes in plate motion. Basin Res. 33, 1603–1625.
Fatka, O., Mergl, M., 2009. The 'microcontinent' Perunica: status and story 15 years after conception. Geological Society, London, Special Publications 325, 65–101.
Fatka, O., Szabad, M., 2014. Cambrian biostratigraphy in the Příbram-Jince Basin (Barrandian area, Czech Republic). Bull. Geosci. 89, 413–429.
Felletti, F., Dall'Olio, E., Muttoni, G., 2016. Determining flow directions in turbidites: An integrated sedimentological and magnetic fabric study of the Miocene Marnoso Arenacea Formation (northern Apennines, Italy). Sediment. Geol. 335, 197–215.
Fisher, N. I., Lewis, T. L., Embleton, B. J., 1987. Statistical analysis of spherical data: Cambridge University Press, Cambridge.
Garcia-Arias, M., Díez-Montes, A., Villaseca, C., Blanco-Quintero, I.F., 2018. The Cambro-Ordovician Ollo de Sapo magmatism in the Iberian Massif and its Variscan evolution: A review. Earth Sci. Rev. 176, 345–372.
Gawthorpe, R.L., Leeder, M.R., 2000. Tectono-sedimentary evolution of active extensional basins. Basin Res. 12, 195–218.
Geyer, G., Elicki, O., Fatka, O., Żylińska, A., 2008. Cambrian. In: McCann T (Ed), The geology of Central Europe. Precambrian and Palaeozoic, vol 1. Geological Society, London, 155–202.
Gutiérrez-Alonso, G., Fernández-Suárez, J., Jeffries, T.E., Jenner, G.A., Tubrett, M.N., Cox, R., Jackson, S.E., 2003. Terrane accretion and dispersal in the northern Gondwana margin. An Early Paleozoic analogue of a long-lived active margin. Tectonophysics 365, 221–232.
Hajná, J., Žák, J., Dörr, W., 2017. Time scales and mechanisms of growth of active margins of Gondwana: a model based on detrital zircon ages from the Neoproterozoic to Cambrian Blovice accretionary complex, Bohemian Massif. Gondwana Res. 42, 63–83.
Hajná, J., Žák, J., Dörr, W., Kachlík, V., Sláma, J., 2018. New constraints from detrital zircon ages on prolonged, multiphase transition from the Cadomian accretionary orogen to a passive margin of Gondwana. Precambr. Res. 317, 159–178.
Havlíček, V., 1971. Stratigraphy of the Cambrian of Central Bohemia. J. Geol. Sci. Geol. 20, 7–52.
Havlíček, V., 1998. Příbram–Jince Basin. In: Chlupáč, I., Havlíček V., Kříž, J., Kukal., Z., Štorch, P., Palaeozoic of the Barrandian (Cambrian–Devonian). Czech Geological Survey, Prague, 19–38.
Herbert, C.M., Alexander, J., Amos, K.J., Fielding, C.R., 2020. Unit bar architecture in a highly-variable fluvial discharge regime: Examples from the Burdekin River, Australia. Sedimentology 67, 576–605.
Hibbard, J.P., Stoddard, E.F., Secor, D.T., Dennis, A.J., 2002. The Carolina Zone: overview of Neoproterozoic to Early Paleozoic peri-Gondwanan terranes along the eastern flank of the southern Appalachians. Earth Sci. Rev. 57, 299–339.
Hrouda, F., 1982. Magnetic anisotropy of rocks and its application in geology and geophysics. Geophys. Surveys 5, 37–82.
Hrouda, F., 1994. A technique for the measurement of thermal changes of magnetic susceptibility of weakly magnetic rocks by the CS-2 apparatus and KLY-2 Kappabridge. Geophys. J. Int. 118, 604–612.
Hrouda, F., Jelínek, V., Zapletal, K., 1997. Refined technique for susceptibility resolution into ferromagnetic and paramagnetic components based on susceptibility temperature-variation measurement. Geophys. J. Int. 129, 715–719.
Hrouda, F., Kahan, Š., 1991. The magnetic fabric relationship between sedimentary and basement nappes in the High Tatra Mountains, N. Slovakia. J. Struct. Geol. 13, 431–442.
Hrouda, F., Krejči, O., Potfaj, M., Stráník, Z., 2009. Magnetic fabric and weak deformation in sandstones of accretionary prisms of the Flysch and Klippen Belts of the Western Carpathians: Mostly offscraping indicated. Tectonophysics 479, 254–270.
Jelínek, V., 1978. Statistical processing of anisotropy of magnetic susceptibility measured on groups of specimens. Stud. Geophys. Geod. 22, 50–62.
Jelínek, V., 1981. Characterization of the magnetic fabric of rocks. Tectonophysics 79, T63–T67.
Jelínek, V., Pokorný, J., 1997. Some new concepts in technology of transformer bridges for measuring susceptibility anisotropy of rocks. Phys. Chem. Earth 22, 179–181.
Johnston, S.T., 2008. The Cordilleran ribbon continent of North America. Ann. Rev. Earth Planet Sci. 36, 495–530.
Kemnitz, H., Romer, R.L., Oncken, O., 2002. Gondwana break-up and the northern margin of the Saxothuringian belt (Variscides of Central Europe). Int. J. Earth Sci. 91, 246–259.
Keppie, J.D., Dostal, J., Murphy, J.B., Nance, R.D., 2008. Synthesis and tectonic interpretation of the westernmost Paleozoic Variscan orogen in southern Mexico: From rifted Rheic margin to active Pacific margin. Tectonophysics 461, 277–290.
Keppie, J.D., Nance, R.D., Murphy, J.B., Dostal, J., 2003. Tethyan, Mediterranean, and Pacific analogues for the Neoproterozoic-Paleozoic birth and development of peri-Gondwanan terranes and their transfer to Laurentia and Laurussia. Tectonophysics 365, 195–219.
Kettner, R., 1919. On the Precambrian granites in Bohemia. Trans. Czechoslovak Acad. Sci. Art II 27, 1–13.
Kettner, R., 1946. Některé problémy českého algonkia a kambria. J. Czech Geol. Soc. 13, 41–67.
Kukal, Z., 1971. Sedimentology of Cambrian deposits of the Barrandian area (Central Bohemia). J. Geol. Sci. Geol. 20, 53–100.
Kukal, Z., 1995. The lower Cambrian Paseky Shale: Sedimentology. J. Czech Geol. Soc. 40 (4), 67–78.
Linnemann, U., Gerdes, A., Hofmann, M., Marko, L., 2014. The Cadomian Orogen: Neoproterozoic to Early Cambrian crustal growth and orogenic zoning along the periphery of the West African Craton – constraints from U-Pb zircon ages and Hf isotopes (Schwarzburg Antiform, Germany). Precambr. Res. 244, 236–278.
Linnemann, U., McNaughton, N.J., Romer, R.L., Gehmlich, M., Drost, K., Tonk, C., 2004. West African provenance for Saxo-Thuringia (Bohemian Massif): did Armorica ever leave pre-Pangean Gondwana?– U/Pb-SHRIMP zircon evidence and the Nd-isotopic record. Int. J. Earth Sci. 93, 683–705.
Linnemann, U., Pereira, F., Jeffries, T.E., Drost, K., Gerdes, A., 2008. The Cadomian Orogeny and the opening of the Rheic Ocean: the diacrony of geotectonic processes constrained by LA-ICP-MS U-Pb zircon dating (Ossa-Morena and Saxo-Thuringian Zones, Iberian and Bohemian Massifs). Tectonophysics 461, 21–43.
Mallard, L.D., Rogers, J.J.W., 1997. Relationship of Avalonian and Cadomian terranes to Grenville and Panafrican events. J. Geodyn. 23, 197–221.
Martínez Catalán, J.R., 2011. Are the oroclines of the Variscan belt related to late Variscan strike-slip tectonics? Terra Nova 23, 241–247.
Morley, C.K., 2018. Understanding Sibumasu in the context of ribbon continents. Gondwana Res. 64, 184–215.
Murphy, J.B., Cameron, K., Dostal, J., Keppie, J.D., Hynes, A.J., 1985. Cambrian volcanism in Nova Scotia, Canada. Can. J. Earth Sci. 22, 599–606.
Murphy, J.B., Eguiluz, L., Zulauf, G., 2002. Cadomian Orogens, peri-Gondwanan correlatives and Laurentia-Baltica connections. Tectonophysics 352, 1–9.
Murphy, J.B., Gutiérrez-Alonso, G., Nance, R.D., Fernández-Suárez, J., Keppie, J.D., Quesada, C., Strachan, R.A., Dostal, J., 2006. Origin of the Rheic Ocean: rifting along a Neoproterozoic suture? Geology 34, 325–328.
Murphy, J.B., Hynes, A.J., 1990. Tectonic control on the origin and orientation of igneous layering: an example from the Greendale Complex, Antigonish Highlands, Nova Scotia, Canada. Geology 18, 403–406.
Murphy, J.B., Keppie, J.D., Dostal, J., Nance, R.D., 1999a. The Neoproterozoic–early Paleozoic evolution of Avalonia. Geol. Soc. Am. Spec. Pap. 336, 253–266.
Murphy, J.B., Keppie, J.D., Nance, R.D., 1999b. Fault reactivation within Avalonia: plate margin to continental interior deformation. Tectonophysics 305, 183–204.
Murphy, J.B., Nance, R.D., 1989. Model for the evolution of the Avalonian-Cadomian Belt. Geology 17, 735–738.
Murphy, J.B., Strachan, R.A., Quesada, C., 2021. Pannotia to Pangaea: Neoproterozoic and Paleozoic orogenic cycles in the Circum-Atlantic Region. Geological Society, London, Special Publications 503, 1–11.

Murphy, J.B., Strachan, R.A., Nance, R.D., Parker, K.D., Fowler, M.B., 2000. Proto-Avalonia: A 1.2–1.0 Ga tectonothermal event and constraints for the evolution of Rodinia. Geology 28, 1071–1074.
Nagata, T., 1961. Rock Magnetism. Maruzen, Tokyo.
Nance, R.D., Linnemann, U., 2008. The Rheic Ocean: origin, evolution, and significance. GSA Today 18, 4–12.
Nance, R.D., Murphy, J.B., 1990. Kinematic history of the Bass River Complex, Nova Scotia - Cadomian tectonostratigraphic relations in the Avalon terrane of the Canadian Appalachians. Geological Society, London, Special Publications 51, 395–406.
Nance, R.D., Murphy, J.B., 1994. Contrasting basement isotopic signatures and the palinspastic restoration of peripheral orogens: example from the Neoproterozoic Avalonian-Cadomian belt. Geology 22, 617–620.
Nance, R.D., Murphy, J.B., 2019. Supercontinents and the case for Pannotia. Geological Society, London, Special Publications 470, 65–86.
Nance, R.D., Murphy, J.B., Keppie, J.D., 2002. A Cordilleran model for the evolution of Avalonia. Tectonophysics 352, 11–31.
Nance, R.D., Murphy, J.B., Strachan, R.A., D'Lemos, R.S., Taylor, G.K., 1991. Late Proterozoic tectonostratigraphic evolution of the Avalonian and Cadomian terranes. Precambr. Res. 53, 41–78.
**Nance, R.D., Murphy, J.B., Strachan, R.A., Keppie, J.D., Gutiérrez-Alonso, G., Fernández-Suarez, J., Quesada, C., Linnemann, U., DLemos, R., Pisarevsky, S.A., 2008. Neoproterozoic–early Palaeozoic tectonostratigraphy and palaeogeography of the peri-Gondwanan terranes: Amazonian v. West African connections. Geological Society, London, Special Publications 297, 345–383.**
Nichols, G., 2009. Sedimentology and stratigraphy. Wiley-Blackwell, West Sussex, UK.
Nichols, G.J., Fisher, J.A., 2007. Processes, facies and architecture of fluvial distributary system deposits. Sed. Geol. 195, 75–90.
**ÓBrien, P.J., 2001. Subduction followed by collision: Alpine and Himalayan examples. Phys. Earth Planet Inter. 127, 277–291.**
Parés, J.M., 2015. Sixty years of anisotropy of magnetic susceptibility in deformed sedimentary rocks. Front. Earth Sci. 3, 1–13.
Parés, J.M., van der Pluijm, B.A., Dinarés-Turell, J., 1999. Evolution of magnetic fabrics during incipient deformation of mudrocks (Pyrenees, northern Spain). Tectonophysics 307, 1–14.
Pollock, J.C., Hibbard, J.P., Sylvester, P.J., 2009. Early Ordovician rifting of Avalonia and birth of the Rheic Ocean: U-Pb detrital zircon constraints from Newfoundland. J. Geol. Soc. London 166, 501–515.
Pollock, J.C., Hibbard, J.P., Sylvester, P.J., Tollo, R.P., Bartholomew, M.J., Karabinos, P. M., 2010. Depositional and tectonic setting of the Neoproterozoic–early Paleozoic rocks of the Virgilina sequence and Albemarle Group, North Carolina. Geol. Soc. Am. Mem. 206, 739–772.
Potter, P.E., Pettijohn, F.J., 1977. Paleocurrent and basin analysis. Springer-Verlag, New York.
Pouclet, A., Álvaro, J.J., Bardintzeff, J.M., Imaz, A.G., Monceret, E., Vizcaïno, D., 2017. Cambrian–early Ordovician volcanism across the South Armorican and Occitan domains of the Variscan Belt in France: Continental break-up and rifting of the northern Gondwana margin. Geosci. Front. 8, 25–64.
Prigmore, J.K., Butler, A.J., Woodcock, N.H., 1997. Rifting during separation of Eastern Avalonia from Gondwana: evidence from subsidence analysis. Geology 25, 203–206.
Rees, A.I., 1965. The use of anisotropy of magnetic susceptibility in the estimation of sedimentary fabric. Sedimentology 4, 257–271.
Rees, A.I., Woodall, W.A., 1975. The magnetic fabric of some laboratory deposited sediments. Earth Planet Sci. Lett. 25, 121–130.
Robardet, M., 2003. The Armorica 'microplate': fact or fiction? Critical review of the concept and contradictory palaeobiogeographical data. Palaeogeogr. Palaeoclimatol. Palaeoecol. 195, 125–148.
Rochette, P., Jackson, M., Aubourg, C., 1992. Rock magnetism and the interpretation of anisotropy of magnetic susceptibility. Rev. Geophys. 30, 209–226.
Romer, R.L., Kroner, U., 2019. First direct evidence for a contiguous Gondwana shelf to the south of the Rheic Ocean. Geology 47, 767–770.
Saint-Bezar, B., Hebert, R.L., Aubourg, C., Robion, P., Swennen, R., de Lamotte, D.F., 2002. Magnetic fabric and petrographic investigation of hematite-bearing sandstones within ramp-related folds: examples from the South Atlas Front (Morocco). J. Struct. Geol. 24, 1507–1520.
Samson, S., Palmer, A.R., Robison, R.A., Secor, D.T., 1990. Biogeographical significance of Cambrian trilobites from the Carolina slate belt. Geol. Soc. Am. Bull. 102, 1459–1470.
Sánchez-García, T., Quesada, C., Bellido, F., Dunning, G.R., del Tanago, J.G., 2008. Two-step magma flooding of the upper crust during rifting: The Early Paleozoic of the Ossa Morena Zone (SW Iberia). Tectonophysics 461, 72–90.
Secor, D.T., Samson, S.L., Snoke, A.W., Palmer, A.R., 1983. Confirmation of the Carolina slate belt as an exotic terrane. Science 221, 649–651.
Servais, T., Sintubin, M., 2009. Avalonia, Armorica, Perunica: terranes, microcontinents, microplates or palaeobiogeographical provinces? Geological Society, London, Special Publications 325, 103–115.
Soto, R., Larrasoaña, J.C., Beamud, E., Garcés, M., 2016. Early-Middle Miocene subtle compressional deformation in the Ebro foreland basin (northern Spain); insights from magnetic fabrics. C. R. Geosci. 348, 213–223.
Stachowska, A., Łoziński, M., Śmigielski, M., Wysocka, A., Jankowski, L., Ziółkowski, P., 2020. Anisotropy of magnetic susceptibility as an indicator for palaeocurrent analysis in folded turbidites (Outer Western Carpathians, Poland). Sedimentology 67, 3783–3808.
Stampfli, G.M., Hochard, C., Vérard, C., Wilhem, C., vonRaumer, J., 2013. The formation of Pangea. Tectonophysics 593, 1–19.
Stephan, T., Kroner, U., Romer, R.L., Rösel, D., 2019a. From a bipartite Gondwanan shelf to an arcuate Variscan belt: the early Paleozoic evolution of northern peri-Gondwana. Earth Sci. Rev. 192, 491–512.
Stephan, T., Kroner, U.W.E., Romer, R.L., 2019b. The pre-orogenic detrital zircon record of the peri-Gondwanan crust. Geol. Mag. 156, 281–307.
Stephan, T., Kroner, U., Hahn, T., Hallas, P., Heuse, T., 2016. Fold/cleavage relationships as indicator for late Variscan sinistral transpression at the Rheno-Hercynian–Saxo-Thuringian boundary zone, Central European Variscides. Tectonophysics 681, 250–262.
Stipp, M., Stünitz, H., Heilbronner, R., Schmid M., S., 2002. The eastern Tonale fault zone: a 'natural laboratory' for crystal plastic deformation of quartz over a temperature range from 250° to 700° C. J. Struc. Geol. 24, 1861–1884.
Štorch, P., Fatka, O., Kraft, P., 1993. Lower Palaeozoic of the Barrandian area (Czech Republic) – a review. Coloquios de Paleontología 45, 163–191.
Taira, A., Scholle, P.A., 1979. Deposition of resedimented sandstone beds in the Pico Formation, Ventura Basin, California, as interpreted from magnetic fabric measurements. Geol. Soc. Am. Bull. 90, 952–962.
Tait, J., Schätz, M., Bachtadse, V., Soffel, H., 2000. Palaeomagnetism and Palaeozoic palaeogeography of Gondwana and European terranes. Geological Society, London, Special Publications 179, 21–34.
Tarling H., D., Hrouda, F., 1993. The Magnetic Anisotropy of Rocks. Chapman and Hall, London.
Usui, Y., Yamazaki, T., Oka, T., Kumagai, Y., 2019. Inverse magnetic susceptibility fabrics in pelagic sediment: Implications for magnetofossil abundance and alignment. J. Geophys. Res. Solid Earth 124, 10672–10686.
van Staal, C.R., Barr, S.M., Waldron, J.W., Schofield, D.I., Zagorevski, A., White, C.E., 2021. Provenance and Paleozoic tectonic evolution of Ganderia and its relationships with Avalonia and Megumia in the Appalachian-Caledonide orogen. Gondwana Res. 98, 212–243.
Veloso, E.E., Anma, R., Ota, T., Komiya, T., Kagashima, S., Yamazaki, T., 2007. Paleocurrent patterns of the sedimentary sequence of the Taitao ophiolite constrained by anisotropy of magnetic susceptibility and paleomagnetic analyses. Sed. Geol. 201, 446–460.
von Raumer, J.F., Bussy, F., Schaltegger, U., Schulz, B., Stampfli, G.M., 2013. Pre-Mesozoic Alpine basements—Their place in the European Paleozoic framework. Geol. Soc. Am. Bull. 125, 89–108.
von Raumer, J.F., Stampfli, G.M., Bussy, F., 2003. Gondwana-derived microcontinents – the constituents of the Variscan and Alpine collisional orogens. Tectonophysics 365, 7–22.
White, C.E., Barr, S.M., Bevier, M.L., Kamo, S., 1994. A revised interpretation of Cambrian and Ordovician rocks in the Bourinot belt of central Cape-Breton island, Nova Scotia. Atl. Geol. 30, 123–142.
Willan, R.C.R., Kelley, S.P., 1999. Mafic dike swarms in the South Shetland Islands volcanic arc: Unravelling multiepisodic magmatism related to subduction and continental rifting. J. Geophys. Res. Solid Earth 104, 23051–23068.
Wu, J.E., McClay, K., Whitehouse, P., Dooley, T., 2009. 4D analogue modelling of transtensional pull-apart basins. Mar. Pet. Geol. 26, 1608–1623.
Xia, H., Platt P., J., 2018. Quartz grainsize evolution during dynamic recrystallization across a natural shear zone boundary. J. Struct. Geol. 109, 120–126.
Žák, J., Kraft, P., Hajná, J., 2013. Timing, styles, and kinematics of Cambro-Ordovician extension in the Teplá-Barrandian Unit, Bohemian Massif, and its bearing on the opening of the Rheic Ocean. Int. J. Earth Sci. 102, 415–433.
Žák, J., Sláma, J., 2018. How far did the Cadomian terranes travel from Gondwana during early Palaeozoic? A critical reappraisal based on detrital zircon geochronology. Int. Geol. Rev. 60, 319–338.
Zulauf, G., 1997. From very low–grade to eclogite-facies metamorphism: tilted crustal sections as a consequence of Cadomian and Variscan orogeny in the Teplá-Barrandian unit (Bohemian Massif). Geotekt. Forsch. 89, 1–302.
Zulauf, G., Dorr, W., Fiala, J., Vejnar, Z., 1997. Late Cadomian crustal tilting and Cambrian transtension in the Teplá-Barrandian unit (Bohemian Massif, Central European Variscides). Geol. Rundsch. 86, 571–584.
Zulauf, G., Helferich, S., 1997. Strain and strain rate in a synkinematic trondhjemitic dike: evidence for melt-induced strain softening during shearing (Bohemian Massif, Czech Republic). J. Struct. Geol. 19, 639–652.
Zulauf, G., Schitter, F., Riegler, G., Finger, F., Fiala, J., Vejnar, Z., 1999. Age constraints on the Cadomian evolution of the Teplá-Barrandian unit (Bohemian Massif) through electron microprobe dating of metamorphic monazite. Z. Dtsch. geol. Gesell. 150, 627–639.